Graphene Oxide-Based Gene Delivery Strategies for Cancer-Specific Elimination in 3D Lung Tumor Models

Francesca Grilli

Thesis submitted to the University of Ottawa in partial fulfillment of the requirements for the

Doctor of Philosophy degree in Biomedical Engineering

Supervisors: Dr. Shan Zou, Dr. Fabio Variola

Department of Biomedical Engineering

Faculty of Engineering

University of Ottawa

uOttawa

ACKNOWLEDGMENTS

First and foremost, I would like to sincerely thank my supervisor, Dr. Shan Zou, for her constant mentorship, scientific rigor, and trust in my independence as a researcher. Her ability to challenge me while encouraging creativity pushed me to refine my thinking and strengthen this work at every stage. I am equally grateful to my co-supervisor, Dr. Fabio Variola, for his support throughout my doctoral studies and for his guidance within the university framework. His assistance in navigating academic milestones and institutional processes was greatly appreciated. Working under your joint supervision has been an invaluable experience.

I would also like to thank my collaborators and colleagues at the National Research Council Canada. The stimulating discussions, technical assistance, and shared problem-solving moments greatly enriched this research. I am especially grateful to Sadman Sakib and Eman Hassan for their significant support in the laboratory. Their guidance, help, and thoughtful discussions were instrumental in advancing this work. A special thank you also goes to Zeina Maan, who was not only a colleague at NRC but, above all, a true friend. Her encouragement and positivity brightened many demanding days, both at work and beyond.

Beyond the laboratory, I owe deep gratitude to my family. To my parents, thank you for your unconditional love, sacrifices, and unwavering belief in me, even when I moved across countries to follow this path. Your support has been my constant foundation. To my partner, Shreyas Dhokte, thank you for your patience, constant encouragement, and steady belief in me at every step. Your support made the difficult days manageable and the successes even more meaningful.

Finally, to my friends, thank you for your presence, encouragement, and support, even when distance kept us apart. To Elena Rainone, I am so grateful to have had you here during this chapter of my life. Your constant presence, support, and readiness to help have meant more than I can express.

This thesis represents years of work, persistence, and growth, but it is also the result of a collective effort. I am deeply grateful to everyone who contributed, directly or indirectly, to this journey.

ABSTRACT

Solid tumors develop within highly complex three-dimensional (3D) microenvironments, in which cancer cells interact dynamically with stromal cells, immune populations, and extracellular matrix (ECM) components. These interactions critically regulate tumor progression, immune evasion, and therapeutic resistance, yet are not adequately captured by conventional two-dimensional (2D) *in vitro* models. Despite significant advances in anticancer therapies, the clinical translation of many promising strategies remains limited by the lack of selectivity for cancer cells. As a result, therapeutic efficacy is often overestimated, while resistance mechanisms and effects on non-target cell populations remain insufficiently understood.

Gene therapy has emerged as a powerful approach to modulate cancer-associated pathways, particularly those governing immune evasion and apoptosis. By controlling gene expression in cancer cells, gene-based strategies can suppress tumor growth and enhance immune-mediated cancer cell elimination while reducing impacts on healthy tissues. Among emerging nanomaterials, graphene oxide (GO) has attracted increasing interest as a nanocarrier platform for gene delivery due to its high loading capacity, tunable surface functionalization, and promising biocompatibility.

The goal of this doctoral work was to establish an integrated platform combining GO-based gene delivery with progressively complex 3D lung cancer models, enabling the rational design, evaluation, and refinement of cancer-specific therapeutic strategies. This work is structured around three interrelated pillars: nanocarrier engineering, tumor microenvironment modeling, and therapy strategy design, which are explored iteratively throughout the thesis.

First, GO nanocarrier formulations were systematically engineered and evaluated to identify those providing optimal biocompatibility and transfection efficiency. The effects of nanocarrier size and surface modification with polyethylene glycol (PEG) and polyamidoamine (PAMAM) were assessed for small interfering RNA (siRNA) delivery in both conventional 2D cultures and 3D lung cancer

spheroids. Cellular viability, apoptosis, and target protein modulation were analyzed to elucidate how nanocarrier physicochemical properties influence delivery performance.

Building on this optimized delivery system, an increasingly physiologically relevant multicellular 3D lung tumor model was developed by integrating cancer cells, stromal fibroblasts, and macrophages within an ECM-mimetic scaffold. GO nanocarriers delivered distinct therapeutic cargos, including siRNA and plasmid DNA (pDNA), targeting immune evasion and apoptotic pathways through single-gene and co-delivery strategies. Analysis of nanocarrier uptake, gene and protein modulation, and cancer cell viability demonstrated that co-delivery approaches enhance cancer cell elimination while limiting off-target effects within a tumor-stroma-immune-rich microenvironment.

Finally, the optimized nanocarrier and advanced 3D tumor model were unified into a single platform, enabling multi-gene delivery targeting cancer cells, stromal support, and immune-mediated responses simultaneously. To further enhance cancer cell specificity, GO was functionalized with an epidermal growth factor receptor (EGFR)-targeting peptide. Therapeutic outcomes were evaluated through cell type-specific nanocarrier uptake, targeted gene modulation, macrophage activation, stromal remodeling, and apoptosis induction. Coordinated modulation of multiple tumor components led to enhanced cancer-specific elimination, compared to single-target approaches.

This thesis demonstrates that effective cancer-specific gene therapy requires the concurrent optimization of nanocarrier design, tumor model complexity, and multi-target therapeutic strategies. By integrating these elements within a unified 3D evaluation framework, this work establishes GO-based gene delivery systems as versatile, microenvironment-aware tools for preclinical evaluation and rational development of next-generation cancer therapies.

STATEMENT OF ORIGINALITY

I, Francesca Grilli, state that the content of this thesis is entirely original. The research and the corresponding manuscripts were done under the supervision of Dr. Shan Zou, senior research officer at National Research Council Canada and adjunct professor at Carleton University, and co-supervision of Dr. Fabio Variola, cross-appointed professor in both the Department of Mechanical Engineering and the Department of Cellular and Molecular Medicine at the University of Ottawa. This Thesis consists of an introductory background and rationale chapter (Chapter 1), followed by a review paper (Chapter 2) and three experimental research manuscripts, either published (Chapter 3 and Chapter 4) or submitted for peer-reviewed scientific journals (Chapter 5). All co-authors' contributions are highlighted at the start of each chapter. The general thesis conclusions and future directions are discussed in Chapter 6.

Manuscripts included in this Thesis:

- Grilli, F.; Gohari, P. H.; Zou, S. Characteristics of Graphene Oxide for Gene Transfection and Controlled Release in Breast Cancer Cells. *Int J Mol Sci* **2022**, *23* (12), 6802. DOI: 10.3390/ijms23126802
- Grilli, F.; Hassan, E. M.; Variola, F.; Zou, S. Harnessing graphene oxide nanocarriers for siRNA delivery in a 3D spheroid model of lung cancer. *Biomater Sci* **2023**, *11* (19), 6635-6649. DOI: 10.1039/d3bm00732d
- Grilli, F.; Sakib, S.; Variola, F.; Zou, S. Graphene Oxide-Based Gene Modulation in Preferential Elimination of Lung Cancer Cells in a 3D Tumor Microenvironment Model. *Adv Nanobiomed Res* **2025**, *5* (7), 2500028. DOI: 10.1002/anbr.202500028
- Grilli, F.; Sakib, S.; Variola, F.; Zou, S. Dual Graphene Oxide-Based Multi-Gene Delivery for Cancer Elimination via Stromal and Immune Reprogramming (submitted to *International Journal of Biomaterials*)

STATEMENT OF CONTRIBUTIONS

I, Francesca Grilli, contributed to the majority of the work presented in this thesis. I conceived and designed the experimental strategies underlying all studies, with guidance and supervision from my supervisors. While the graphene oxide nanocarrier platform was originally developed and characterized within the research group, I significantly advanced this system by designing and implementing multi-gene delivery strategies and, in the final study (Chapter 5), by independently developing and executing the functionalization protocol with a cancer-targeting molecule.

All cell culture work, including the development, optimization, and execution of two-dimensional and advanced three-dimensional tumor models, was performed by me. I independently conceptualized, established, and validated the 3D tumor microenvironment models used throughout this thesis. I conducted all biological experiments, including gene delivery, functional assays, imaging analyses, and quantitative evaluations, and I performed all data processing, statistical analyses, and interpretation of results. Limited assistance was received for specific sample preparation steps related to imaging.

I also took a primary role in the drafting of the scientific papers that are included in this Thesis.

STRUCTURE OF THE THESIS

Chapter 1 establishes the general background and scientific rationale of the thesis. It introduces the key challenges in cancer-specific therapy and explains the rationale for the selection of the nanocarrier material, targeted genes, biological models, and the overall and chapter-specific objectives.

Chapter 2 presents a focused review of graphene oxide as a nanocarrier for gene delivery in cancer. This chapter provides detailed insight into the structure, toxicity, and controlled release behavior of graphene oxide, supporting the experimental studies, which primarily investigate its application for gene delivery.

Chapter 3 presents the first experimental study of the thesis, in which graphene oxide is evaluated as a material for gene delivery. This chapter investigates how the physicochemical properties of the nanocarrier influence gene delivery performance across different cancer models, establishing key design principles for subsequent studies.

Chapter 4 reports the second experimental study, which aims at developing a more physiologically relevant cancer model. Using the optimized material and transfection strategies previously identified in Chapter 3, this chapter focuses on evaluating cancer-specific elimination within a complex 3D tumor microenvironment.

Chapter 5 presents the final experimental study, which integrates the optimized nanocarrier material and the advanced cancer model developed in earlier chapters. This chapter focuses on enhancing cancer specificity and therapeutic efficacy by refining gene therapy strategies based on the combined understanding of material behavior and tumor model complexity.

Chapter 6 summarizes the main findings of the thesis, integrates insights across all experimental studies, and discusses their broader implications. Future research directions and potential translational pathways are also outlined.

TABLE OF CONTENTS

Chapter 2

LIST OF FIGURES

Chapter 1

Chapter 2

Chapter 3

Chapter 4

Chapter 5

Appendix

LIST OF TABLES

Chapter 1

Chapter 2

Chapter 4

Appendix

Chapter 1: Background and Rationale for Cancer-Specific Gene Therapy

This chapter presents the conceptual basis of the thesis by introducing the key limitations of current cancer treatments, motivating the exploration of gene-based strategies that can more precisely modulate cancer survival. Within this framework, the chapter introduces the molecular targets investigated in this thesis and briefly summarizes foundational studies supporting the selection of graphene oxide (GO) as a non-viral nanocarrier platform. A comprehensive discussion of GO design, functionalization, and performance is presented in Chapter 2.

The chapter further introduces advanced three-dimensional (3D) cancer models, emphasizing the importance of stromal components, immune populations, and 3D architecture in regulating tumor behavior and therapeutic response. The related topics are addressed in greater detail in subsequent research chapters, where directly relevant to avoid redundancy. The chapter concludes by defining the objectives of each research chapter.

1.1 General Overview and Rationale

Lung cancer remains one of the leading causes of cancer-related mortality worldwide, largely because current therapies often fail to eradicate malignant cells selectively while sparing healthy tissues. Conventional treatment modalities, including chemotherapy, radiotherapy, and targeted agents, are frequently constrained by systemic toxicity, incomplete tumor specificity, and the emergence of therapeutic resistance. These limitations are intensified by the complex lung tumor microenvironment, in which stromal and immune components actively regulate disease progression and treatment response.

Gene therapy has emerged as a promising strategy to overcome these challenges by enabling precise modulation of cancer-relevant genetic pathways. Through the selective silencing or expression of disease-driving genes, gene-based approaches offer the potential for cancer-specific intervention. However, their effective application in lung cancer is hindered by delivery inefficiency, poor cellular selectivity, and microenvironment-mediated barriers characteristic of solid tumors.

Advances in nanomaterials and non-viral delivery systems have enabled the rational design of gene carriers with tunable physicochemical properties, high nucleic acid loading capacity, and modular surface functionalization. In parallel, increasing recognition of the tumor microenvironment as a central determinant of therapeutic outcome has underscored the need for experimental platforms that capture the multicellular and structural complexity of lung tumors.

Accordingly, 3D *in vitro* lung cancer models have emerged as essential tools for evaluating gene- and nanotherapy strategies in physiologically relevant contexts. These systems better recapitulate tumor architecture, cell-cell interactions, and stromal barriers than conventional two-dimensional (2D) cultures, providing a more predictive platform for assessing cancer specificity and therapeutic efficacy.

Within this context, this doctoral work focuses on the development of GO-based non-viral gene delivery systems evaluated in advanced multicellular 3D lung tumor microenvironment models. By integrating rational nanocarrier engineering with biologically relevant co-culture platforms, this thesis aims to elucidate how material properties and microenvironmental context jointly regulate cancer-specific gene modulation, ultimately contributing to design principles for more effective lung cancer gene therapies.

1.2 Limitations in Cancer-Specificity of Current Cancer Therapies

1.2.1 Non-selective Cytotoxic Therapies

The foundations of modern cancer therapy were established through chemotherapy and radiotherapy as the first non-surgical approaches capable of controlling malignant disease at the systemic and local levels, respectively [1]. While these modalities represented transformative advances, their mechanisms of action were intrinsically non-selective (Table 1.1). As a consequence, therapeutic efficacy became fundamentally constrained by toxicity to normal proliferating tissues [2, 3]. This limitation remains evident in clinical practice, where improved tumor control achieved through intensified chemotherapy is frequently offset by dose-limiting adverse effects [4-6]. Such strategies typically produce modest gains in tumor response or progression-free survival, while reproducibly leading to substantial increases in severe off-target toxicities, including myelosuppression, neurotoxicity, nephrotoxicity, and gastrointestinal adverse events [2, 3]. These findings underscore a fundamental limitation of conventional chemotherapy: its core mechanisms of action, which disrupt DNA replication and cell division, are not biologically selective for malignant cells. As a result, intensifying treatment primarily amplifies injury to rapidly proliferating normal tissues rather than enhancing tumor-specific elimination.

In parallel, radiotherapy underwent substantial technological refinement, evolving from primary external beam approaches to highly conformal techniques such as intensity-modulated radiotherapy and stereotactic body radiotherapy [7]. These advances enhanced spatial precision and allowed dose escalation within defined tumor volumes, reducing exposure of adjacent normal tissues. Nevertheless, radiotherapy remains inherently limited by its inability to address disseminated or microscopic disease beyond the irradiated field. Consequently, durable tumor control for many solid malignancies, including lung cancer, has continued to rely on systemic chemotherapy, either alone or in combination with radiation [7]. This convergence led to the widespread adoption of combined chemoradiotherapy regimens for cancers such as lung, breast, and head-and-neck malignancies, where chemotherapy augments radiation-induced DNA damage but also compounds systemic toxicity [8, 9]. Although such dual-modality strategies improved locoregional control and survival in selected settings, their efficacy has remained constrained by cumulative toxicity [10-12].

Systemic toxicity, therefore, persists as the dominant barrier limiting the clinical effectiveness of conventional chemotherapeutics, even as they have evolved mechanistically. This is exemplified in some lung cancer studies, where more myelosuppressive regimens improve objective response rates, yet significantly increase bone marrow toxicity [6, 13]. Moreover, these gains are accompanied by a measurable risk of late toxicities, including therapy-related acute myeloid leukemia [14]. This central limitation has driven the development of more selective therapeutic paradigms.

1.2.2 Molecular Targeting and Partial Specificity

The development of targeted small-molecule therapies marked a conceptual departure from the indiscriminate cytotoxicity of conventional chemotherapy toward molecularly defined cancer intervention [15]. Traditional systemic agents primarily eliminate rapidly dividing cells with limited discrimination between malignant and healthy tissues, resulting in narrow therapeutic windows and substantial off-target toxicity. Advances in cancer genetics instead revealed that many tumors are

driven by discrete oncogenic alterations, most commonly dysregulated protein kinases, that are not equivalently required for normal cell survival [16]. Protein kinases function as central regulatory nodes, controlling proliferation, metabolism, and signaling through ATP-dependent phosphorylation events, and their aberrant activation through mutation, amplification, or chromosomal rearrangement is closely linked to tumor initiation and maintenance. This biological dependency rendered oncogenic kinases particularly attractive targets for selective cancer elimination. The clinical feasibility of this approach was first established in chronic myeloid leukemia (CML) through targeting the BCR-ABL fusion kinase [17]. Because BCR-ABL is both constitutively active and largely restricted to malignant cells, its inhibition produced deep and durable remissions with comparatively limited systemic toxicity, validating the principle of tumor-selective kinase targeting. This success catalyzed the rapid development of small-molecule tyrosine kinase inhibitors (TKIs) and set a benchmark for precision oncology [17]. Importantly, however, the exceptional cancer specificity observed in CML reflected the presence of a single, dominant oncogenic driver with minimal physiological redundancy, a condition less common in solid tumors.

When this paradigm was extended to epithelial malignancies, molecular selection emerged as a critical determinant of therapeutic efficacy. In non-small cell lung cancer (NSCLC), early EGFR inhibitors such as gefitinib and erlotinib showed that dramatic tumor regression was largely confined to patients harboring activating EGFR mutations, firmly establishing genotype-dependent response [18]. Subsequent third-generation EGFR inhibitors further refined this balance between efficacy and toxicity. For example, in EGFR-mutant NSCLC, Osimertinib improved progression-free and overall survival compared with earlier TKIs, while maintaining comparable rates of high-grade adverse events despite longer treatment duration [19, 20]. In curative-intent settings, adjuvant Osimertinib after complete surgical resection reduced disease recurrence, highlighting how molecular specificity can enhance residual disease suppression without proportionally increasing systemic toxicity.

Targeted small-molecule therapies persist in systemic toxicities and vulnerability to resistance, highlighting the incomplete nature of kinase-level targeting alone (Table 1.1). These limitations have motivated complementary precision strategies, including antibody-based and other biologic modalities, which aim to refine cancer-specific elimination by exploiting extracellular targets, immune mechanisms, and modular engineering approaches beyond intracellular kinase inhibition.

1.2.3 Immune and Biologic Approaches to Cancer Selectivity

Antibody-based and other biologic therapies emerged as complementary precision strategies aimed at addressing key limitations of small-molecule inhibitors, particularly their incomplete selectivity, off-target toxicities, and frequent development of resistance. Their advance was driven by a central challenge in oncology: achieving durable tumor elimination while minimizing collateral damage to normal tissues [21]. Monoclonal antibodies are intrinsically well suited to this objective because of their high affinity and specificity for defined extracellular or cell-surface antigens, enabling selective targeting of malignant cells [21]. However, in lung cancer, antibody-targeted chemotherapies do not yet consistently outperform standard untargeted chemotherapy on overall survival in unselected populations, though some agents offer modest progression-free survival gains and better overall tolerability with a trade-off of increased interstitial lung disease risk, underscoring that antibody targeting attenuates but does not abolish off-target toxicity [4, 22].

The modern era of biologic therapy builds on earlier immunotherapeutic concepts but advanced decisively with the clinical success of immune checkpoint blockade inhibitors, such as CTLA-4 and PD-1, which demonstrated that durable tumor control could be achieved by releasing endogenous antitumor immunity rather than directly targeting cancer cells [23, 24]. For example, in previously treated advanced NSCLC, PD-1/PD-L1 antibody inhibitors improve overall survival relative to standard chemotherapy, while reducing the incidence of treatment-related adverse events from ~45-50% with chemotherapy to ~10-20% with immunotherapy, demonstrating a substantially improved

therapeutic index [25]. Importantly, these benefits are achieved at the cost of immune-related toxicities rather than broad cytotoxic injury, marking a fundamental shift in both efficacy and side-effect profiles.

Table 1.1. Advantages and limitations in cancer-specificity of current cancer therapies [7, 21, 26].

Therapy	Mechanism	Advantages	Limitations
Chemotherapy	Induces DNA damage or disrupts cell division in rapidly proliferating cells	Broad cytotoxic efficacy; effective against fast-growing tumors	Poor cancer specificity; damages normal proliferating tissues (bone marrow, gut, hair follicles); high systemic toxicity; resistance
Radiotherapy	Causes DNA double-strand breaks via ionizing radiation	Spatial targeting to tumor site; high local tumor control	Limited molecular specificity; damages surrounding normal tissue; induces fibrosis and can promote pro-metastatic signaling
Targeted Small Molecules	Inhibit oncogenic proteins or signaling pathways (e.g., kinases)	Higher molecular specificity than chemo; oral administration; effective in biomarker-defined tumors	Off-target effects due to shared pathways in normal cells; rapid resistance; limited efficacy in heterogeneous tumors
Antibody-based therapy	Bind tumor-associated surface antigens or ligands; block signaling or recruit immune effectors	High target specificity; long half-life; immune engagement	Target expression is often not tumor-exclusive; poor penetration in solid tumors; immune-related toxicities
Biologic/ Immunotherapy	Reactivate or modulate immune responses against cancer cells	Functional cancer specificity via immune recognition; durable responses in responders	Dependence on pre-existing immunity; immune-related adverse events; immune-excluded tumors limit efficacy

These observations demonstrate that while antibody and immune therapies have markedly improved cancer specificity, they do so by shifting toxicity into the immune domain and remain fundamentally limited by target accessibility and adaptive resistance mechanisms (Table 1.1).

Despite progressive improvements in molecular and immune selectivity, durable cancer-specific elimination remains limited, highlighting the need for strategies that act upstream of protein function and immune activation. Gene delivery therapies address this gap by enabling direct, programmable control of gene expression and therapeutic localization, providing a natural transition toward approaches designed to enhance specificity while limiting systemic toxicity.

1.3 Gene-Based Therapeutic Strategies for Cancer-Specific Intervention

Gene therapy is a medical approach that treats diseases by correcting or manipulating a person's genetic makeup, aiming to fix underlying genetic alterations rather than just managing symptoms, often by re-expressing a healthy gene, disabling a faulty one, or editing existing DNA to restore normal cell function [27]. Gene-based cancer therapies arose from genomic insights establishing cancer as a disease driven by somatic genetic alterations, motivating direct intervention at the level of gene expression rather than downstream protein function [27]. Although initially developed for inherited disorders, gene delivery rapidly shifted toward oncology, which now accounts for nearly two-thirds of all gene therapy clinical trials, reflecting both tumor genetic complexity and the limitations of existing treatments, positioning gene therapy as a central component of modern, genomically informed multimodal cancer therapy [27].

Despite being a relatively recent clinical field, cancer gene therapy has already led to the approval of innovative treatments such as the oncolytic virus T-VEC in 2015 and CAR-T cell therapies starting in 2017, where patient T cells are genetically engineered to recognize and eliminate cancer cells. These approaches have shown remarkable success, particularly in hematologic malignancies such as leukemia and lymphoma, highlighting the strong therapeutic potential of gene-based cancer treatments.

1.3.1 Rationale for Gene Therapy in Cancer Specificity

Gene therapy enables programmable modulation of tumor biology by targeting oncogenic dependencies through controlled genetic delivery and expression. By integrating target selection with spatial and regulatory restriction, therapeutic activity can be concentrated within malignant tissue while minimizing effects on normal cells.

Clinical experience with gene-engineered immune cells illustrates the upper bound of what highly selective targeting can achieve: CD19-directed CAR-T therapies induce overall remission rates of ~70-80% and complete remissions in ~50-60% of adults with B-cell acute lymphoblastic leukemia, with ~50% of patients remaining event-free at 12 months and relatively low rates of severe cytokine-release syndrome (~2-7%) [28-31]. These outcomes reflect highly selective targeting enabled by lineage-restricted antigen expression, but they come at the cost of permanent on-target toxicity (B-cell aplasia) and have limited applicability to solid tumors, including lung cancer. In solid malignancies, shared antigen expression with healthy tissues, heterogeneous target density, and physical barriers sharply constrain therapeutic delivery, selectivity, and efficacy.

Together, these limitations motivate the development of gene delivery systems that seek to reproduce CAR-T–like specificity through spatially and molecularly restricted delivery of genetic payloads, rather than immune-cell engineering [32-34]. By concentrating gene modulation within tumor tissue and cancer-relevant cellular contexts, such approaches aim to maximize malignant cell elimination while preserving normal tissue function, providing a strong rationale for continued development of cancer-specific gene therapy strategies in solid tumors.

1.3.2 Genetic Payload Delivery

Depending on the therapeutic goal, genetic payloads may encode functional proteins, induce degradation of specific messenger RNAs, or introduce precise genomic modifications. The process by which these nucleic acids are introduced into cells is referred to as *transfection* in non-viral systems (or *transduction* when viral vectors are used) [35]. During transfection, genetic payloads are transported across the cell membrane and subsequently released into the cytoplasm or nucleus, where they engage endogenous molecular machinery. Through this controlled delivery and intracellular processing of genetic information, gene therapy enables precise and programmable modulation of

cellular functions that cannot be achieved with conventional small-molecule or protein-based drugs [27].

In non-viral gene therapy, the functional outcome of transfection depends on the nature of the delivered genetic payload. Small interfering RNAs (siRNAs) mediate post-transcriptional gene silencing by engaging the endogenous RNA interference machinery in the cytoplasm, where they are incorporated into the RNA-induced silencing complex (RISC), which directs sequence-specific cleavage and degradation of target mRNAs, resulting in a transient reduction in protein expression (Figure 1.1) [36]. In contrast, plasmid DNA (pDNA) enables gene addition by introducing exogenous coding sequences that traffic to the nucleus and are transcribed by the host machinery into messenger RNA, which is subsequently translated into functional proteins (Figure 1.1) [37]. Together, siRNA- and pDNA-based transfection strategies provide complementary and highly controllable approaches for modulating cellular pathways, allowing gene therapy to selectively suppress pathogenic signals or restore therapeutic functions within target cells.

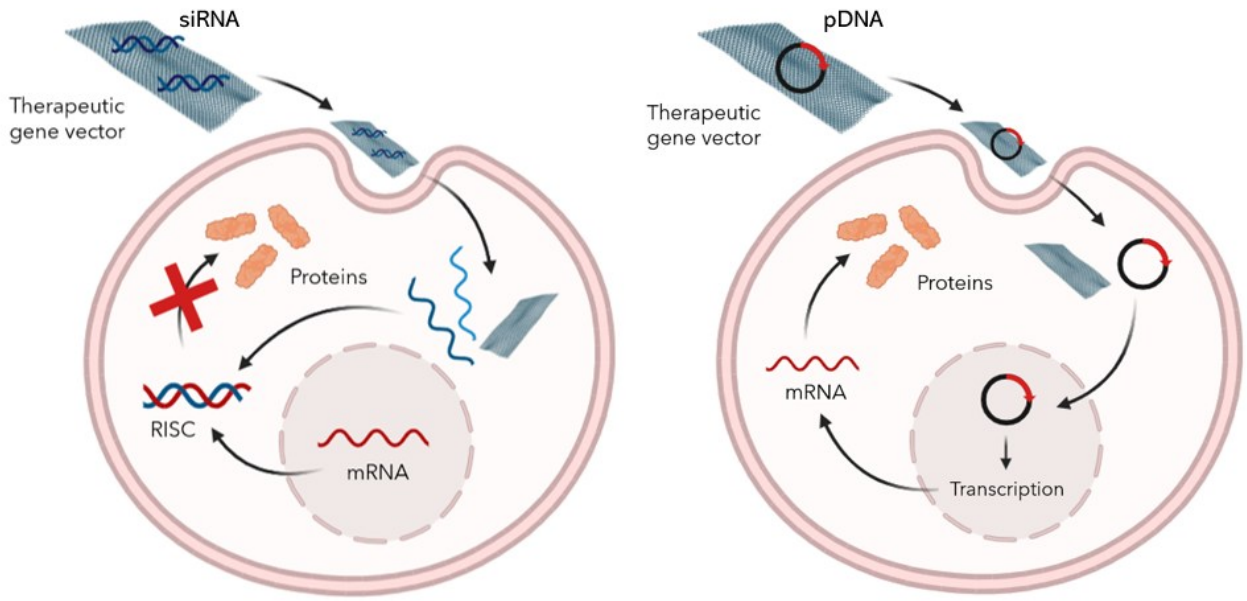

Figure 1.1. Transfection mechanisms. Schematic representation of the siRNA (left) and pDNA (right) transfection processes inside a cell. *Illustration created with BioRender.com.*

1.3.2.1 Targeting Cluster of Differentiation 47 (CD47)

CD47 is a ubiquitously expressed transmembrane glycoprotein that functions as a central regulator of innate immune self-recognition. Its primary role is to inhibit macrophage-mediated phagocytosis through binding to signal regulatory protein alpha (SIRPα), an inhibitory receptor expressed on myeloid cells. Under physiological conditions, this “don’t eat me” signal protects healthy cells from inappropriate clearance, particularly when cells transiently acquire stress signals, such as during inflammation or cytokine stimulation, thereby increasing their probability of survival during immune activation [38]. In this context, CD47 acts as a conditional self-preservation signal rather than a constitutive immune shield.

Cancer cells exploit this physiological pathway by constitutively overexpressing CD47, converting a transient protective mechanism into a persistent immune-evasion strategy. Studies in acute myeloid leukemia (AML) first demonstrated that leukemia stem cells and blast populations uniformly display elevated CD47 compared to normal hematopoietic counterparts, with high CD47 expression correlating with aggressive disease and poor clinical outcome [39]. Functional blockade of CD47 using monoclonal antibodies restored macrophage-mediated phagocytosis of AML cells *in vitro* and eliminated leukemia *in vivo* without inducing apoptosis or depleting normal hematopoietic stem cells [39, 40]. These findings revealed the initially counterintuitive principle that, despite CD47 expression on normal cells, its therapeutic blockade preferentially targets malignant cells, implying the involvement of additional determinants of macrophage selectivity.

The mechanistic basis for this cancer specificity was clarified with the identification of calreticulin (CRT) as the dominant pro-phagocytic “eat-me” signal expressed on malignant cells [41]. CRT is an endoplasmic reticulum chaperone that is frequently translocated to the cancer cell surface or becomes extracellularly available, where it promotes phagocytosis through interaction with low-density lipoprotein receptor-related protein (LRP) on macrophages. CRT expression is high across many hematologic and solid tumors but remains low on most normal cells under homeostatic conditions

[41]. CD47 and CRT therefore function as a signal pair: CRT provides a constitutive or stress-induced phagocytic cue, while CD47 counterbalances this signal to prevent engulfment. Blockade or genetic suppression of CD47 unmasks pre-existing CRT-mediated phagocytic pressure, resulting in selective cancer cell elimination while sparing normal tissues that present low CRT expression [41]. Importantly, even when cancer cells express low surface CRT, macrophages can supply CRT themselves, enabling labeling and clearance of adjacent tumor cells once CD47-mediated inhibition is removed [42, 43].

This macrophage-driven modulation of the CD47/CRT axis is directly supported by a study from my research group, which demonstrated that LPS activation of THP-1–derived macrophages selectively downregulated CD47 while concomitantly upregulating CRT on AML cells, but not on normal peripheral blood mononuclear cells (Figure 1.2A and B) [44]. This coordinated shift correlated with dose-dependent leukemia elimination and robust M1 cytokine secretion, providing experimental evidence that macrophage activation can drive cancer-specific phagocytosis without damaging normal cells (Figure 1.2C and D).

Subsequent studies extended this paradigm beyond hematologic malignancies, demonstrating that CD47 is broadly overexpressed across solid tumors and that its inhibition restores innate immune surveillance. In multiple solid tumor models, including lung cancers, CD47 blockade enabled macrophage phagocytosis, suppressed tumor growth, and prolonged survival *in vivo*, with toxicity largely limited to transient hematologic effects [45]. Notably, small-cell lung cancer (SCLC) was shown to uniformly overexpress CD47 across primary tumors, patient-derived xenografts, and circulating tumor cells, and CD47 blockade markedly reduced tumor burden and extended survival in orthotopic lung cancer models [46].

Despite this therapeutic promise, CD47 blockade presents some limitations. Chemotherapy and radiotherapy can increase CRT exposure on both malignant and normal cells, potentially reducing selectivity when combined with systemic CD47 inhibition [41]. Moreover, monoclonal anti-CD47

antibodies are associated with hematologic toxicity, particularly anemia, due to on-target interactions with CD47 on red blood cells, creating both safety concerns and an antigen sink that limits effective tumor dosing [45]. These challenges have motivated the development of gene-based strategies to suppress CD47 expression selectively within tumor cells. CRISPR-Cas9-mediated CD47 gene disruption has been shown to silence CD47 expression, restore macrophage-mediated phagocytosis, and inhibit tumor growth *in vivo* while avoiding continuous systemic receptor blockade [46]. Importantly, CD47 gene suppression displays enhanced efficacy when combined with inhibition of additional innate immune checkpoints, such as CD24, which signals through Siglec-10 on macrophages, reinforcing the concept that cancer cells rely on layered "don't eat me" signals for immune evasion [46].

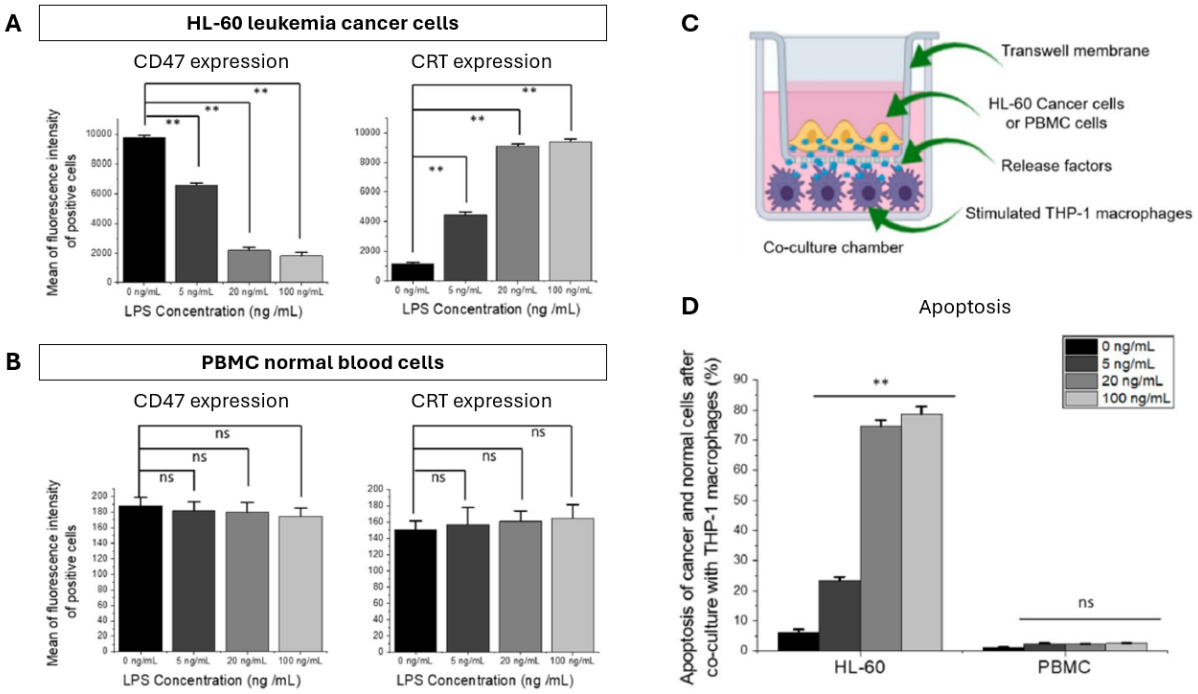

Figure 1.2. Levels of CD47, CRT, and apoptosis in HL-60 and PBMC after co-culturing with stimulated THP-1 macrophages. Flow cytometric analysis of CD47 and CRT in (A) HL-60 cells and (B) PBMC cells after co-culturing with THP-1 macrophages activated using 0, 5, 20, and 100 ng/mL of LPS 24 h before flow cytometry measurements. (C) Scheme of the THP-1 macrophages co-culturing with HL60 or PBMC in a co-culture chamber. (D) Bar graph showing the percentage (%) of apoptosis of cancer and normal cells after co-culturing with THP-1 macrophages. Values in the graph are shown as means ± SEM of three trials of duplicate samples. The statistical significance was determined by one-way ANOVA (OriginPro 2019); * $P < 0.05$, ** $P < 0.01$, *ns* non-significant ($P > 0.05$). *Panels compiled and adapted from (Cancer Immunol Immun, 70, 787-801 (2021)) [44].*

1.3.2.2 Targeting Adenine Nucleotide Translocase 1 (ANT1)

ANT1 is a major inner mitochondrial membrane carrier belonging to a family of four ANT isoforms that display distinct tissue- and proliferation-dependent expression patterns. In humans, ANT1 is predominantly expressed in terminally differentiated, energy-demanding tissues such as heart, skeletal muscle, and brain, whereas ANT2 is enriched in proliferating cells and is frequently up-regulated in tumors [47], ANT3 is ubiquitously expressed, and ANT4 is largely restricted to the testis [48]. Functionally, ANT1 catalyzes the exchange of mitochondrial ATP for cytosolic ADP, constituting the final step of oxidative phosphorylation [47]. Beyond nucleotide transport, ANT1 also serves as a multifunctional regulator of mitochondrial homeostasis [48]. Importantly, both experimental depletion and pathological dysregulation of ANT1 have been demonstrated to induce oxidative stress and cell death, underscoring its homeostatic role in non-malignant contexts [48]. In cancer, however, ANT1 expression is frequently suppressed in favor of ANT2, a shift that supports proliferative capacity and resistance to mitochondrial apoptosis. This altered isoform balance creates a cancer-specific vulnerability, as re-expression or overexpression of ANT1 in tumor cells is sufficient to trigger intrinsic apoptosis independently of its canonical transport function [47]. ANT1 overexpression induces collapse of mitochondrial membrane potential, apoptosis through caspase-9 and caspase-3 activation and cytochrome c release, and DNA fragmentation, largely through MPTP-dependent mechanisms [49], while simultaneously suppressing oncogenic survival pathways by inactivating NF-κB and Bcl-2 signaling [47, 50, 51]. Notably, because NF-κB and Bcl-2 family overexpression are key drivers of chemoresistance and tumor progression, ANT1 modulation offers a way to simultaneously hit multiple cancer survival axes. Importantly, this death-inducing activity is isoform-specific: ANT1 (and ANT3), but not ANT2, promotes apoptosis despite high sequence homology, highlighting a unique functional specialization exploitable for therapy [49, 50, 52]. In multiple cancer models, ANT1 overexpression selectively reduces tumor cell viability, sensitizes cells to retinoid- and chemotherapy-induced mitochondrial apoptosis, and suppresses tumor growth *in vivo* [50, 52], while sparing normal cells that either already express ANT1 at homeostatic levels or

rely predominantly on ANT2 [47]. These findings position ANT1 as a compelling cancer-specific therapeutic target: its differential expression across normal and malignant tissues, its direct control over mitochondrial apoptosis, and its capacity to simultaneously disable multiple oncogenic survival pathways define a wide therapeutic window in which selective modulation of ANT1 can drive cancer-specific elimination while minimizing damage to healthy tissues.

1.3.2.3 Targeting Transforming Growth Factor-β (TGFβ)

TGFβ is a family of secreted cytokines, primarily TGF-β1, -β2, and -β3, that regulate cell proliferation, differentiation, apoptosis, extracellular matrix (ECM) remodeling, and immune function [53]. In normal tissues, TGFβ is abundant in platelets and sites of tissue turnover, where it plays a central role in wound healing, stromal remodeling, and immune homeostasis by coupling epithelial, stromal, and immune cell behavior to local environmental cues [54]. It enforces cytostatic and apoptotic programs in many epithelial and hematopoietic cells, restrains excessive immune activation, and transiently activates fibroblasts to promote controlled ECM deposition and tissue repair, thereby acting as a context-dependent regulator rather than a constitutive growth factor [53, 55, 56]. A defining feature of TGFβ biology, however, is its functional plasticity. Early work established that TGFβ can act as a tumor suppressor during the initial stages of carcinogenesis [53, 54]. As a result, the notion of TGFβ inhibition as cancer therapy emerged primarily in the context of advanced and metastatic disease, where malignant cells have escaped TGFβ-mediated growth inhibition and instead exploit its signaling to promote progression [53, 54]. In established cancers, elevated TGFβ signaling drives epithelial-mesenchymal transition (EMT), invasion, stem-like phenotypes, and resistance to therapy in malignant cells, while simultaneously activating cancer-associated fibroblasts (CAFs) to generate a dense, fibrotic ECM that compresses vasculature, limits drug and immune-cell penetration, and fosters hypoxia [53, 55-58]. In parallel, TGFβ profoundly reprograms anti-tumor immunity by suppressing cytotoxic T-cell differentiation and function,

promoting regulatory T cells, and polarizing macrophages and myeloid-derived suppressor cells toward immunosuppressive phenotypes, collectively producing immune-excluded tumors in which effector cells are physically and functionally restrained [53, 56, 59, 60]. This convergence explains why TGFβ emerges as a coordinator of malignant progression, particularly metastasis and immune evasion, rather than primary tumor initiation. Therapeutically, multiple strategies have been developed to inhibit TGFβ signaling, including neutralizing antibodies, receptor kinase inhibitors, and anti-TGFβ siRNA, many of which demonstrate robust suppression of invasion, circulating tumor cell survival, and distant metastasis without markedly reducing primary tumor burden [53, 56, 61, 62]. These findings highlight a limitation of TGFβ inhibition as monotherapy: while highly effective at halting progression and metastatic dissemination, it rarely achieves complete tumor elimination on its own. Crucially, however, TGFβ blockade demonstrates strong cancer-selective value as a sensitizing strategy by targeting tumor-specific vulnerabilities that emerge from aberrant stromal activation and immune suppression. When combined with other cancer treatments, TGFβ inhibition prevents therapy-induced metastatic acceleration, reverses cancer stem-cell enrichment, normalizes vasculature and ECM architecture, restores immune infiltration, and markedly improves durable therapeutic responses [53, 57, 60-62]. Thus, TGFβ represents a cancer-contextual vulnerability whose inhibition enhances treatment specificity and efficacy by dismantling tumor-exclusive stromal and immunological barriers to cancer cell elimination (Table 1.2). This strategy is particularly relevant in the context of conventional therapies, such as radiotherapy and chemotherapeutic agents including doxorubicin and paclitaxel, which can increase local and systemic TGFβ levels and thereby promote stromal activation, immune suppression, and metastatic potential [57].

From a therapeutic perspective, these features provide a strong rationale for targeting TGFβ at the genetic level rather than through systemic pathway inhibition. Gene therapy approaches, particularly siRNA-mediated silencing of TGFβ ligands or receptors, enable localized and cell-type-selective suppression of aberrant TGFβ signaling within tumor and stromal compartments, exploiting the cancer-specific overproduction and activation of this pathway while minimizing interference with its

essential homeostatic functions in normal tissues [53, 56, 58, 60]. By directly reducing TGFβ synthesis, gene-based inhibition circumvents compensatory ligand accumulation and non-canonical pathway activation often observed with pharmacological inhibitors, thereby creating a more permissive tumor microenvironment that enhances other treatments.

Table 1.2. Summary of representative studies comparing therapeutic outcomes of standard cancer treatments administered alone or in combination with TGFβ pathway inhibition.

Therapy	Monotherapy Results	Combined Therapy Results
siRNA (dual-target) [60] (Bifunctional ppp-TGFβ siRNA)	ppp-RNA only: reduces cancer cell viability to ≈ 35 % and ≈ 6 % complete regressions. TGFβ-RNA only: shows no significant viability loss and 0 % regressions.	Cancer cell viability drops to ≈ 25 %, triggers profound tumor-cell apoptosis and 33 % complete regressions.
siRNA (dual-target) + immune-checkpoint antibody [53] (TGFβ + COX2 siRNA + anti-PD-L1)	Dual siRNA reduces tumor-growth rate more than anti-PD-L1 alone, but does not achieve complete regression	100 % survival with durable complete remission
Neutralizing antibody + radiation [63, 64] (pan-TGFβ antibody + radiation)	Radiation alone increases circulating tumor cells (CTC) and induces a 17-fold rise in lung metastases	CTC colony formation is reduced by ~70 %
Bispecific antibody [62] (Siglec-15/TGFβ antibody)	Anti-Siglec-15 alone slows tumor growth but metastases are still detected in lung and liver	Strongly suppresses tumor growth and no lung or liver metastases are observed
Small-molecule + immune-checkpoint antibody [65] (Galunisertib + anti-PD-L1)	Galunisertib alone: 3/14 complete regressions (CR). Anti-PD-L1 alone: 5/15 CRs.	9/14 CRs (all animals respond)
Small-molecule + immune-checkpoint antibody [66] (Galunisertib-loaded sonodynamic nanodrug + anti-PD-L1)	Anti-PD-L1 alone produces reduced tumor volume from ≈1055 mm^3 to ≈ 800 mm^3	Metastatic tumor volume drops to ≈ 256 mm^3

1.3.3 Gene Delivery Vectors

Cancer specificity in gene therapy is determined largely by how, where, and in which cells therapeutic nucleic acids become active. Naked nucleic acids lack intrinsic tumor selectivity and are rapidly degraded or cleared after systemic administration, leading to broad biodistribution, negligible tumor

accumulation, and off-target effects [36, 37]. By contrast, nanocarrier-mediated delivery can shield nucleic acids during circulation, control cellular uptake, and regulate intracellular availability, effectively defining the spatial and cellular context of gene expression [67]. Well-designed carriers can bias payload delivery toward malignant cells and tumor-associated stromal or immune populations, transforming gene therapy from a broadly distributed intervention into a spatially constrained, cancer-specific strategy.

1.3.3.1 Viral Vectors

Viral vectors are engineered viruses used to deliver therapeutic genetic material into target cells and currently represent the most efficient gene delivery systems, yet their systemic use for cancer-specific therapy is constrained by targeting precision, safety, and controllability (Table 1.3) [68]. Integrating vectors such as retroviruses and lentiviruses provides durable expression but lacks intrinsic tumor selectivity and carries persistent risks of insertional mutagenesis, restricting their use primarily to *ex vivo* applications. Non-integrating platforms, including adenoviral and adeno-associated viral vectors (AAV), achieve high transduction efficiency *in vivo* but exhibit broad tissue tropism, leading to off-target gene expression and dose-limiting toxicities [69]. In particular, immune recognition, pre-existing neutralizing antibodies, and vector-driven inflammation restrict repeat dosing and narrow the therapeutic window, while attempts to escalate dose for tumor penetration risk hepatotoxicity, vascular injury, or systemic immune activation. Within this broad category of viral vectors, oncolytic viruses constitute a specialized subgroup designed not only to deliver genes (Table 1.3), but also to selectively replicate within and destroy tumor cells while stimulating anti-tumor immune responses. However, efficacy remains heterogeneous due to antiviral responses and dependence on permissive tumor biology rather than absolute cancer specificity [70].

Table 1.3. Summary of major viral vector platforms used in cancer gene therapy and their principal advantages and limitations [69-71].

Viral Vector	Therapy	Main Advantages	Main Limitations
Adenovirus	Gene delivery, oncolytic virotherapy	High transduction efficiency, strong gene expression, effective tumor cell killing	Strong immune response, limited long-term delivery
Adeno-associated virus (AAV)	Gene delivery/editing	Low immunogenicity, good safety profile, efficient *in vivo* delivery	Small cargo capacity, limited tumor penetration, limited long-term delivery
Retrovirus	Gene delivery/editing	Long-term gene expression through genome integration, used in CAR-T therapies	Only infects dividing cells, risk of insertional mutagenesis
Lentivirus	Gene delivery/editing	Efficient long-term expression, infects dividing and non-dividing cells, widely used in CAR-T therapies	Complex manufacturing, insertional mutagenesis risk
Herpes simplex virus (HSV)	Oncolytic virotherapy	Selective tumor infection and lysis, stimulates anti-tumor immunity	Limited systemic delivery, antiviral immune clearance
Vaccinia virus	Oncolytic virotherapy	Large cargo capacity, strong tumor replication	Immune clearance, safety concerns in immunocompromised patients
Measles virus	Oncolytic virotherapy	Efficient tumor cell killing, immune activation	Pre-existing immunity can reduce efficacy

1.3.3.2 Non-Viral Vectors

Non-viral nucleic acid-based therapies rely primarily on delivery control rather than inherent tropism to achieve cancer specificity. The principal non-viral platforms include lipid-based nanocarriers, polymer- and carbon-based systems, inorganic nanomaterials, and engineered extracellular vesicles (EVs), which offer safer, less immunogenic, and more tunable alternatives to viral vectors [72].

- EVs represent one of the most intrinsically cancer-relevant non-viral delivery systems, as they exploit endogenous cellular communication pathways [68, 73]. Surface engineering or cytosolic delivery enhancements can further bias the payload toward malignant populations. Limitations include scalable production, cargo-loading consistency, and potential off-target signaling from native vesicle components.
- Lipid-based nanocarriers, including liposomes and lipid nanoparticles (LNPs), are the most clinically advanced non-viral vectors [73-75]. They protect nucleic acids and promote cellular

uptake but preferentially accumulate in the liver after systemic administration. Targeting ligands such as antibodies or peptides are therefore critical to impose tumor selectivity.

- Polymer-based nanocarriers offer a higher degree of structural and chemical tunability, enabling more precise control over cancer-selective delivery [76, 77]. Cationic polymers and dendrimers can be engineered with degradable backbones, pH-sensitive linkages, or tumor-targeting moieties to release cargo preferentially in the tumor microenvironment or specific intracellular compartments. Polypeptide-based systems further exploit biological cues, such as enzymatic activity or acidic tumor conditions, to bias gene expression toward malignant tissue [78]. Challenges include non-specific interactions and dose-dependent toxicity, emphasizing that cancer specificity depends on precise material design rather than polymer class alone.
- Carbon-based and inorganic nanocarriers (e.g., graphene-derived materials, metallic nanoparticles) provide high-density nucleic acid loading and modular surface functionalization, allowing selective targeting of cancer cells through ligand-mediated uptake [79]. These strategies leverage spatial confinement of physicochemical activity to selectively impact tumor tissue, coupling gene modulation with local cytotoxic stress [80]. However, their clinical translation is constrained by challenges related to long-term biodistribution and biodegradability.

Collectively, these non-viral vector classes demonstrate that cancer specificity in gene therapy is not an intrinsic property of any single platform, but rather an emergent feature dictated by delivery design, biodistribution control, and context-dependent gene activation. Continued optimization of targeting strategies, tumor-selective release mechanisms, and manufacturability is therefore central to advancing non-viral gene delivery toward truly cancer-specific therapeutic applications in precision oncology.

1.3.3.3 Rationale for Graphene Oxide for Cancer-Specific Delivery

Engineered nanomaterials can induce cytotoxicity through multiple, often overlapping mechanisms, including oxidative stress, membrane disruption, physical damage, and interference with intracellular organelles, whose severity depends strongly on particle size, shape, surface chemistry, aggregation state, dose, exposure time, and cellular context [81-83]. Within this broad landscape, GO flakes exhibit a comparatively well-defined and tunable toxicity profile that makes them particularly attractive for gene-delivery applications. Across systematic studies using controlled GO sources and interference-resistant assays, GO toxicity is demonstrated to be consistently dose- and cell-type-dependent, with adherent epithelial and fibroblast cells tolerating higher concentrations than suspension or highly phagocytic cells, thereby defining predictable and experimentally manageable safety windows [82]. Flake size and morphology emerge as the dominant determinants of GO cytotoxicity: GO flakes with lateral dimensions of ~50-150 nm (small-GO) show higher cytotoxic potential due to increased membrane interactions and internalization, whereas larger flakes (~800-1200 nm lateral size; big-GO) are generally better tolerated.[82, 84] Highly wrinkled or folded morphologies further intensify cytotoxic responses, while more planar flakes exhibit reduced membrane damage [85]. Importantly, GO toxicity correlates more strongly with physical structure than with bulk oxygen content or trace impurities, in contrast to high-aspect-ratio nanomaterials such as carbon or boron nitride nanotubes, whose fiber-like geometry raises asbestos-like safety concerns and complicates biological clearance [81]. Compared with LNPs, which are generally well tolerated but require tight control of surface charge and composition, GO offers a distinct advantage through its large surface area, 2D geometry, and intrinsic capacity for versatile surface functionalization, enabling nucleic acid loading without relying on highly cationic cores that often drive non-specific toxicity [83, 86]. Although the functionalization of GO with cationic polymers to promote gene delivery can increase its cytotoxicity, this effect can be effectively mitigated through rational control of flake size, dosing, and shielding strategies such as PEGylation [86].

Beyond its favorable toxicity profile, graphene oxide has demonstrated robust and reproducible performance as a nanocarrier for gene transfection across a wide range of cellular systems. These conclusions are drawn from a series of systematic studies from my research group that directly compared multiple nanocarrier platforms for the delivery of CD47_siRNA under standardized conditions, enabling direct evaluation of efficiency, selectivity, and cytocompatibility [86-88]. Among GO-based formulations, small-GO flakes that are further modified with PEG and PAMAM dendrimers consistently outperform big-GO flakes and less functionalized GO variants, underscoring the critical role of both nanoscale size and surface chemistry in intracellular delivery (Figure 1.3) [86]. Importantly, in both suspension and adherent cancer cell models, these optimized small-modified-flake GO carriers achieve substantially higher gene-silencing efficiency than conventional commercial transfection reagents, which often perform poorly in hematopoietic cells, co-culture systems, and 3D models (Table 1.4).

Notably, the same comparative studies revealed that nanocarrier-mediated CD47_siRNA delivery resulted in minimal transfection in normal cells, with knockdown efficiency remaining very low (<10%) in primary peripheral blood mononuclear cells (PBMCs) and NIH3T3 fibroblasts [86]. This observation indicates a pronounced functional preference of GO-based carriers for cancer cells and, concurrently, underscores the high transfection specificity of CD47-targeted gene-editing strategies toward malignant populations (Figure 1.3E and F). Importantly, in complex biological architectures such as multicellular co-cultures and intestinal organoids, small-GO nanocarriers maintain high transfection efficiency, demonstrating effective penetration and functional nucleic acid delivery in structured tissues where standard reagents are limited, highlighting the potential of GO in efficiently transfecting 3D models (Table 1.4) [87, 88].

When benchmarked against other nanocarrier classes, lipid nanoparticles generally represent the upper bound of transfection efficiency but require precise formulation to balance efficacy and toxicity, while short boron nitride nanotubes exhibit efficiencies comparable to small-GO flakes and

long nanotubes consistently underperform [87]. Importantly, differences in transfection efficiency must be interpreted alongside cytocompatibility: GO nanocarriers achieve high gene silencing at concentrations that preserve cell viability, whereas unconjugated cationic polymers and some alternative nanomaterials exhibit narrower safety margins [86]. As a result, GO occupies a balance between delivery efficiency and tolerability. These attributes support the use of graphene oxide as the nanocarrier platform in this work, particularly for applications requiring efficient, versatile, and microenvironment-compatible gene modulation.

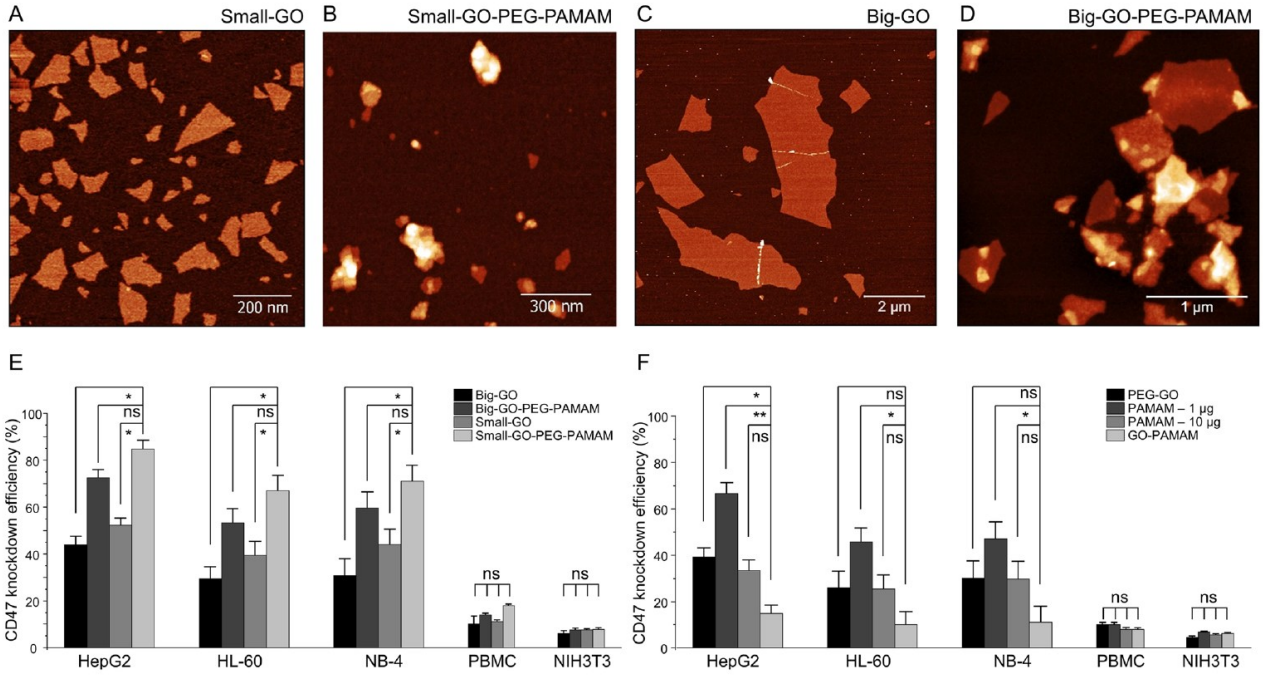

Figure 1.3. Morphology and CD47_siRNA knockdown efficiency comparison of four GO-based formulations. (A)-(D) AFM topography images of (A) small-GO, (B) small-GO-PEG-PAMAM, (C) big-GO and (D) big-GO-PEG-PAMAM. (E, F) Calculated CD47_siRNA knockdown efficiency in cells with GO and PAMAM formulations. Values in the graphs are shown as mean ± SEM of three trials of duplicate samples (n = 6). The statistical significance of CD47 knockdown efficiency of small-GO-PEG-PAMAM to other formulations (big-GO, big-GO-PEG-PAMAM and small-GO), and GO-PAMAM to other formulations (PEG-GO, PAMAM-1 µg and PAMAM-10 µg) in all cell lines (HepG2, HL-60, NB4, PBMC and NIH3T3) was determined by one-way ANOVA, respectively, with the notes of *P < 0.05, **P < 0.01, and "ns" not significant. *Reproduced from (Colloids Surf B Biointerfaces, 217, 112609s (2022)).[86]*

Table 1.4. Transfection efficiency results obtained using GO nanocarriers compared to other nanomaterials.

Nanocarrier	Cells/Model	Transfection Efficiency	Ref.
GO (small-GO-PEG-PAMAM)	AML monocultures	67-71%	[86]
	HepG2 monoculture	84%	[86]
	A549, HepG2 and AML in co-culture	84-95%	[87]
	3D organoids (enteroids and colonoids)	92-94%	[88]
Lipid Nanoparticles (LNPs)	A549, HepG2 and AML in co-culture	90-98%	[87]
Short Boron-Nitride Nanotubes (short BNPs)	A549, HepG2 and AML in co-culture	84-94%	[87]
Long Boron-Nitride Nanotubes (long BNPs)	A549, HepG2 and AML in co-culture	73-85 %	[87]
Lipofectamine RNAiMAX	AML monocultures	30-33 %	[86]
	HL-60 monoculture	46%	[87]
	3D organoids (enteroids and colonoids)	63-69%	[88]

*AML: HL-60 and NB4 cells.

1.4 *In Vitro* Cancer Models

To generate reliable and translatable insights into cancer biology and therapeutic response, *in vitro* models must recapitulate the key structural, biochemical, and functional features of *in vivo* tumors. This is particularly critical for solid tumors, where dense extracellular matrices, elevated interstitial pressure, and limited diffusion impose physical barriers that strongly influence drug and gene-therapy delivery [89].

Conventional 2D cultures offer simplicity, low cost, and reproducibility, but fail to reproduce 3D architecture, spatial heterogeneity, and dynamic cell-cell and cell-ECM interactions. As a result,

cancer cells grown in 2D often display altered morphology, gene expression, and exaggerated therapeutic sensitivity, limiting predictive value [90, 91]. These limitations have driven the development of 3D cancer models that better emulate tumor organization and microenvironmental cues. Common 3D platforms include multicellular spheroids, organoids, and scaffold-based systems, each offering distinct advantages and limitations.

- Multicellular spheroids are self-assembled tumor aggregates that develop gradients of oxygen, nutrients, pH, and metabolites, reproducing features of avascular tumor regions and enabling studies of drug penetration, heterogeneous sensitivity, and resistance [92, 93]. However, spheroids are structurally simple, lack cellular heterogeneity and defined ECM components, and are not compatible with all cancer cell types.
- Organoids, derived from stem cells or patient tissues, preserve tissue architecture, genetic heterogeneity, and cellular diversity, providing powerful platforms for disease modeling and personalized therapy testing, but their technical complexity, specialized matrices, and long culture times limit scalability and routine use [94, 95].
- Scaffold-based 3D models employ natural or synthetic biomaterials to provide an ECM-like framework that supports multicellular growth and spatial organization, allowing controlled incorporation of stromal and immune cells, although careful material selection is required to minimize variability and unintended effects on cellular behavior [96, 97].

Importantly, faithfully modeling tumor behavior requires more than 3D structure alone, as tumor progression, therapeutic resistance, and treatment response emerge from dynamic interactions between cancer cells, stromal populations, immune cells, and the ECM. By capturing these interactions *in vitro*, advanced 3D models provide a predictive, ethically responsible platform for evaluating cancer therapies, enabling more informed and targeted use of animal models.

1.4.1 Importance of the Stroma

Within solid tumors, the stromal compartment is a critical determinant of therapeutic outcome because it shapes the biological and physical context in which anticancer strategies operate, a complexity that cannot be captured by conventional 2D cultures. The tumor microenvironment comprises malignant cells together with fibroblasts, endothelial cells, immune populations, an extensively remodeled ECM, and a diverse repertoire of soluble mediators that collectively regulate tumor growth, invasion, immune evasion, and treatment sensitivity (Figure 1.4) [89].

By providing a 3D architecture and dynamic cellular interactions, stromal-inclusive models more accurately reflect the conditions under which clinical therapies must function *in vivo*. Stromal incorporation also preserves key tumor features that directly influence therapeutic performance, such as cellular heterogeneity, stem-like subpopulations, and invasive behavior. Fibroblasts and endothelial cells enhance tumor proliferation and alter malignant phenotype, while stromal-derived signals promote EMT and matrix-guided invasion [97-99]. At the same time, stromal remodeling generates dense ECM and abnormal vasculature that restrict the delivery of cytotoxic agents, targeted drugs, antibodies, and nucleic-acid therapeutics, while fostering immunosuppressive niches dominated by regulatory immune cells and tumor-promoting macrophages [56, 100]. Central mediators, such as TGFβ, integrate these effects by coupling stromal activation, immune suppression, and tumor plasticity, thereby influencing the durability of responses across multiple therapeutic modalities [56, 59]. Importantly, therapeutic interventions themselves can perturb these stromal circuits, for example by inducing compensatory signaling pathways that promote resistance, underscoring that treatment efficacy cannot be evaluated independently of microenvironmental feedback [57].

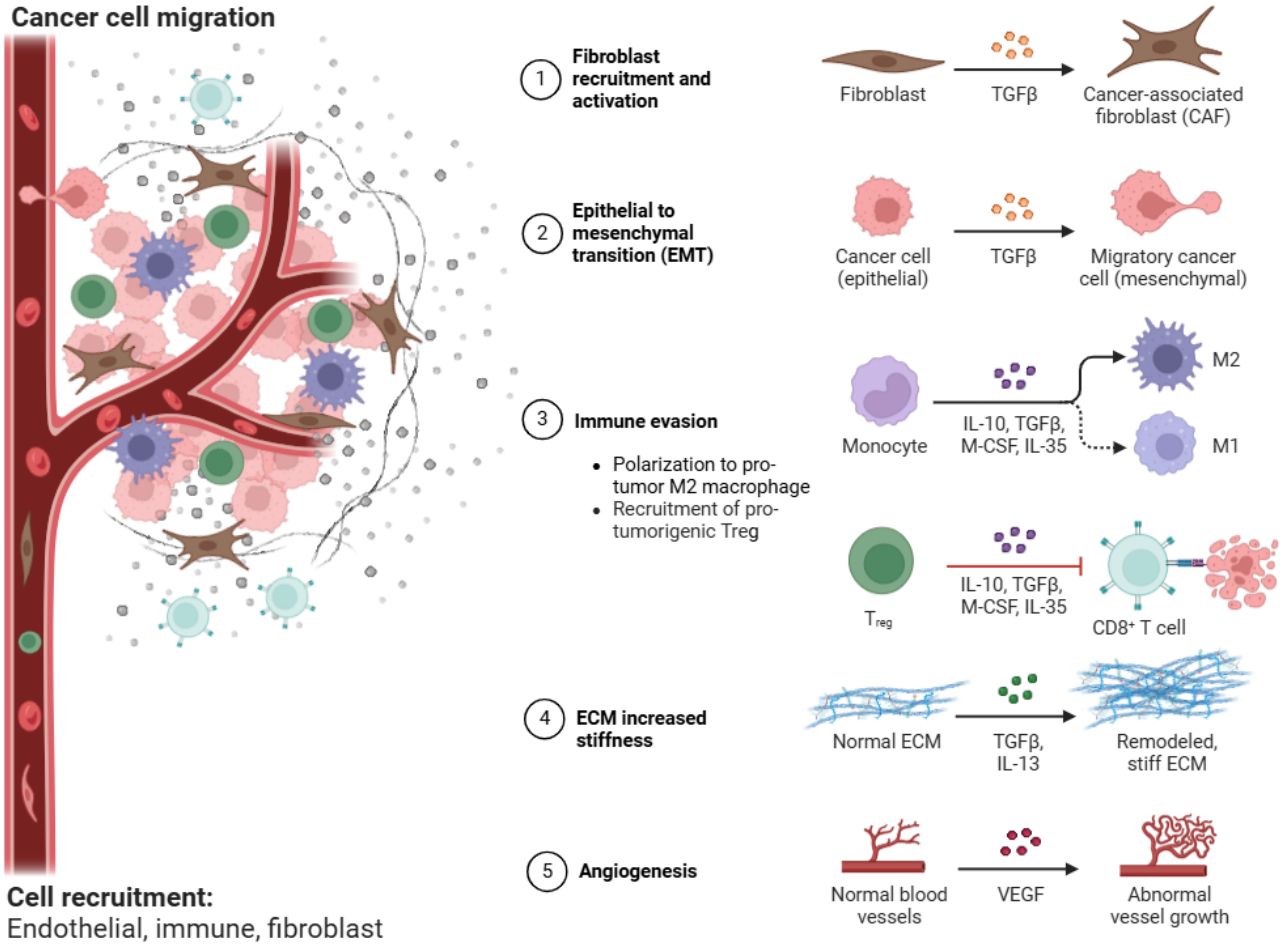

Figure 1.4. Influence of the tumor microenvironment on cancer progression. Schematic representation of the tumor microenvironment highlighting reciprocal interactions between cancer cells, stromal and immune populations, extracellular matrix, and vasculature, and illustrating how soluble factors and cell-cell signaling reprogram surrounding components toward tumor-supportive, pro-invasive, and immunosuppressive functions. *Illustration created with BioRender.com.*

Because cancer specificity and therapeutic resistance are emergent properties of tumor-microenvironment interactions, the predictive value of any anticancer strategy depends critically on the model system used to assess it. Stromal-inclusive 3D cancer models, therefore, provide an essential platform for evaluating not only whether a therapy is cytotoxic, but whether it can achieve selective, durable tumor control under physiologically relevant conditions that mirror those encountered *in vivo*.

1.4.2 Rationale for Model Selection in 3D Cancer Therapeutic Studies

The *in vitro* cancer models employed in this work were selected through a stepwise strategy designed to progressively increase biological complexity while maintaining experimental control, thereby enabling meaningful evaluation of therapeutic strategies as they encounter increasingly realistic tumor constraints. The initial platform used in Chapter 3 consisted of cancer-cell-only spheroids, which serve as a critical intermediate between 2D monolayers and animal models. Spheroids spontaneously establish a 3D architecture and physiological gradients of oxygen, nutrients, and growth factors, resulting in spatially organized proliferative, quiescent, and hypoxic or necrotic regions that resemble avascular tumor domains [90, 91, 101]. This organization drives gene-expression and proteomic profiles that more closely reflect *in vivo* tumors, including endogenous ECM deposition, and confers therapeutic response kinetics that differ markedly from 2D cultures [90, 102]. Consequently, spheroids provide a valuable system for studying drug penetration, nanoparticle uptake, and time-dependent cytotoxic responses, with imaging-based approaches enabling kinetic monitoring of viability and apoptosis rather than reliance on single end-point assays [92, 93, 103]. These features make spheroids well suited for establishing baseline cancer-cell-intrinsic responses to therapeutic agents under controlled 3D conditions.

Despite these advantages, spheroid models present important technical and biological limitations that restrict their predictive value for complex therapeutic strategies. Variability in spheroid size and maturation can introduce experimental heterogeneity, while their physical thickness complicates automated imaging and high-throughput analysis [93, 103]. Diffusion limitations in large spheroids may induce premature necrosis that does not reflect all tumor stages, and standard viability assays often underestimate cell survival due to incomplete probe penetration [101]. Most importantly, simple spheroids lack key components of the tumor microenvironment, including fibroblasts, immune cells, and a defined ECM, limiting their ability to capture stromal-driven invasion, immune suppression, and therapy resistance. These shortcomings are particularly relevant for evaluating delivery-

dependent therapies, such as nanocarrier-based systems, which are often excluded at the spheroid boundaries and therefore behave differently than *in vivo*.

To overcome these constraints, in Chapters 4 and 5, the model was subsequently expanded into a 3D multicellular matrix-based system incorporating cancer cells together with fibroblasts and immune cells. Introduction of an ECM at this stage was intended to provide the structural and biochemical framework required for multicellular self-organization, stromal activation, and immune plasticity. Matrix-supported 3D models allow cells to adopt *in vivo*-like morphologies and establish dynamic reciprocal interactions that can override cancer cell intrinsic oncogenic programs [96]. For example, co-culture studies have shown that CAFs can suppress epithelial dysplasia while simultaneously promoting invasion, highlighting the context-dependent nature of tumor behavior [99, 104]. These systems also enable reproduction of immunosuppressive microenvironments, including recruitment and polarization of macrophages toward tumor-promoting phenotypes in the absence of exogenous cytokines, thereby capturing emergent properties of tumor-immune crosstalk [100].

From a therapeutic standpoint, multicellular matrix models offer substantially improved predictive value. Unlike 2D cultures, which frequently show immediate and unrealistic tumor eradication, 3D stromal-inclusive models reproduce gradual treatment responses and adaptive resistance patterns observed in xenografts and patients [96]. For instance, PEG-fibrin hydrogel models of lung adenocarcinoma accurately mirrored *in vivo* responses to oncolytic adenovirus therapy, whereas 2D systems exhibited complete and rapid oncolysis [96]. These platforms are also well-suited for evaluating immunotherapies, as bio-printed or encapsulated models permit controlled spatial organization and analysis of immune-cell infiltration, as well as combinatorial drug testing [100, 105]. Notably, fibrin-Matrigel co-culture systems have demonstrated that anti-fibrotic agents can enhance chemotherapy efficacy by suppressing stromal programs associated with invasion and matrix remodeling, illustrating how therapeutic outcomes emerge from tumor-stroma interactions rather than cancer cells alone [106].

Within this framework, Matrigel and type I collagen were selected as complementary matrix components to support multicellular growth and self-organization. Matrigel provides a permissive environment for epithelial organization and stable assembly of cancer, stromal, and immune populations, facilitating reproducible long-term co-culture [107]. However, because Matrigel alone can suppress invasion, it was combined with collagen I, which supplies a fibrillar architecture compatible with cell migration, stromal remodeling, and fibroblast-guided invasion mechanisms, including the formation of migration "tracks" along elongated fibroblast protrusions [107]. Therefore, the use of mixed matrices represents a pragmatic compromise that balances experimental tractability with biological relevance, enabling evaluation of therapeutic strategies in an environment that incorporates structural constraint, immune modulation, and delivery barriers.

Overall, the progression from ECM-free cancer spheroids to ECM-supported multicellular tumor models reflects a deliberate escalation in model complexity aligned with the evolving experimental questions addressed in this work. By matching each model to a specific level of biological organization, this approach enables systematic assessment of therapeutic performance as cancer specificity and resistance emerge from tumor-microenvironment interactions, providing a more predictive context for evaluating advanced cancer therapies, including gene- and nanocarrier-based strategies.

1.5 Specific Objectives

1.5.1 Objective 1 (Chapter 3)

Despite growing interest in non-viral gene therapy for lung cancer, the efficient delivery of nucleic acids remains a major challenge. Nanocarrier performance depends strongly on physicochemical and surface properties, including particle size, surface charge, and chemical functionalization. These parameters govern nanocarrier stability, cellular uptake, cytotoxicity, and intracellular trafficking.

However, the influence of such material properties is often evaluated under simplified 2D culture conditions, limiting the ability to predict nanocarrier behavior in tumor-relevant environments where physical diffusion barriers and transport constraints play a dominant role.

The primary objective of this study was to determine how key design parameters of GO nanocarriers, specifically lateral flake size and surface functionalization, affect siRNA delivery efficiency in lung cancer models. To this end, GO formulations with distinct lateral dimensions and surface chemistries, ranging from unmodified flakes to PEG- and PAMAM-functionalized formulations, were systematically evaluated for siRNA delivery. A549 lung cancer spheroids were employed as a simplified yet physiologically relevant 3D model to recapitulate key physical barriers to gene delivery, including limited diffusion and spatial heterogeneity. Delivery performance was directly compared between conventional 2D monolayers and 3D spheroids. siRNA targeting the immune checkpoint protein CD47 served as a functional readout, with delivery efficiency assessed through target protein downregulation.

By systematically linking GO size and surface functionalization to delivery outcomes in both 2D and 3D systems, this work establishes a foundation for the rational optimization of GO-based nanocarriers for gene delivery under tumor-relevant conditions.

1.5.2 Objective 2 (Chapter 4)

Tumor response to therapy is increasingly recognized as an emergent consequence of interactions within the tumor microenvironment. Nevertheless, many preclinical gene therapy studies continue to rely on simplified culture systems that do not fully capture the complexity of cancer-stroma-immune communication. While numerous co-culture models incorporate either stromal or immune compartments, relatively few integrate both simultaneously, thereby overlooking critical regulatory interactions that influence therapy sensitivity, immune function, and cancer cell elimination.

The objective of this study was to develop a multicellular 3D lung tumor microenvironment model for evaluating gene-therapy-driven cancer elimination under physiologically relevant conditions, and to determine how tumor cellular composition modulates therapeutic response. To achieve this, a 3D lung cancer model incorporating A549 cancer cells, human lung fibroblasts, and THP-1-derived macrophages embedded within a Matrigel-collagen matrix was established. This multicellular system was systematically compared with models containing only one or two cell types in order to isolate the contributions of stromal and immune compartments to therapeutic outcomes. Building upon the optimized GO formulation identified in Chapter 3, GO-based nanocarriers were employed to deliver immune checkpoint-related siRNAs (CD47 and CD24) and an apoptosis-inducing plasmid DNA (ANT1). This enabled the evaluation of macrophage-dependent and macrophage-independent mechanisms of cancer elimination, as well as assessment of single- versus multi-gene delivery strategies.

Overall, this study establishes a physiologically relevant 3D tumor microenvironment platform for assessing gene therapy responses in lung cancer and highlights GO as a versatile non-viral nanocarrier capable of mediating gene delivery and cancer elimination within multicellular tumor models.

1.5.3 Objective 3 (Chapter 5)

Despite advances in nanocarrier engineering and tumor modeling, achieving efficient and selective cancer cell elimination remains a central challenge in gene-based cancer therapy. Many therapeutic strategies focus primarily on cancer-intrinsic pathways without addressing the supportive and resistance-promoting roles of the tumor microenvironment. In addition, off-target delivery and unintended gene modulation in non-malignant cells remain important barriers to therapeutic specificity.

The objective of this study was to enhance the efficacy and cancer selectivity of the gene therapy strategy developed in Chapter 4 by integrating tumor microenvironment modulation, immune regulation, and delivery targeting into a unified therapeutic framework. To this end, a combinatorial GO-based delivery platform was designed to co-deliver a microenvironment-modulating siRNA targeting TGFβ together with cancer-directed therapeutic genes, including the immune checkpoint CD47 and the apoptosis-inducing ANT1, optimized in the previous study. In parallel, the EGFR-targeting peptide GE11 was incorporated as a targeting ligand to promote preferential uptake in EGFR-expressing lung cancer cells.

Through this integrated strategy, this study demonstrates that effective cancer-directed gene therapy is not determined by a single therapeutic target or delivery vehicle, but instead arises from coordinated modulation of cancer cells, stromal support pathways, and immune-mediated responses. By jointly optimizing payload selection, microenvironmental regulation, and targeted nanocarrier design, this work aims to establish a system-level strategy to enhance cancer cell elimination while minimizing off-target effects.

References

(1) DeVita, V. T.; Chu, E. A History of Cancer Chemotherapy. *Cancer Res* **2008**, *68*, 8643-8653.
(2) Jordan, B.; Margulies, A.; Cardoso, F.; Cavaletti, G.; Haugnes, H. S.; Jahn, P.; Le Rhun, E.; Preusser, M.; Scotté, F.; Taphoorn, M. J. B.; Jordan, K.; Comm, E. G.; Comm, E. G.; Grp, E. E. W.; Grp, E. E. W.; Comm, E. G. Systemic anticancer therapy-induced peripheral and central neurotoxicity: ESMO-EONS-EANO Clinical Practice Guidelines for diagnosis, prevention, treatment and follow-up. *Ann Oncol* **2020**, *31*, 1306-1319.
(3) Lustberg, M. B.; Kuderer, N. M.; Desai, A.; Bergerot, C.; Lyman, G. H. Mitigating long-term and delayed adverse events associated with cancer treatment: implications for survivorship. *Nat Rev Clin Oncol* **2023**, *20*, 527-542.
(4) Ahn, M. J.; Tanaka, K.; Paz-Ares, L.; Cornelissen, R.; Girard, N.; Pons-Tostivint, E.; Baz, D. V.; Sugawara, S.; Cobo, M.; Perol, M.; Mascaux, C.; Poddubskaya, E.; Kitazono, S.; Hayashi, H.; Hong, M. H.; Felip, E.; Hall, R.; Juan-Vidal, O.; Brungs, D.; Lu, S.; Garassino, M.; Chargualaf, M.; Zhang, Y.; Howarth, P.; Uema, D.; Lisberg, A.; Sands, J.; Investigators, T.-L. T. Datopotamab Deruxtecan Versus Docetaxel for Previously Treated Advanced or Metastatic Non-Small Cell Lung Cancer: The Randomized, Open-Label Phase III TROPION-Lung01 Study. *J Clin Oncol* **2025**, *43*, 260-272.
(5) Ferry, D.; Billingham, L.; Jarrett, H.; Dunlop, D.; Woll, P. J.; Nicolson, M.; Shah, R.; Thompson, J.; Spicer, J.; Muthukumar, D.; Skailes, G.; Leonard, P.; Chetiyawardana, A. D.; Wells, P.; Lewanski, C.; Crosse, B.; Hill, M.; Gaunt, P.; O'Byrne, K. Carboplatin versus two doses of cisplatin in combination with gemcitabine in the treatment of advanced non-small-cell lung cancer: Results from a British Thoracic Oncology Group randomised phase III trial. *Eur J Cancer* **2017**, *83*, 302-312.
(6) Gronberg, B. H.; Bremnes, R. M.; Flotten, O.; Amundsen, T.; Brunsvig, P. F.; Hjelde, H. H.; Kaasa, S.; von Plessen, C.; Stornes, F.; Tollali, T.; Wammer, F.; Aasebo, U.; Sundstrom, S. Phase III Study by the Norwegian Lung Cancer Study Group: Pemetrexed Plus Carboplatin Compared With Gemcitabine Plus Carboplatin As First-Line Chemotherapy in Advanced Non-Small-Cell Lung Cancer. *J Clin Oncol* **2009**, *27*, 3217-3224.
(7) Zafar, A.; Khatoon, S.; Khan, M. J.; Abu, J.; Naeem, A. Advancements and limitations in traditional anti-cancer therapies: a comprehensive review of surgery, chemotherapy, radiation therapy, and hormonal therapy. *Discov Oncol* **2025**, *16*, 607.
(8) Haddad, R.; O'Neill, A.; Rabinowits, G.; Tishler, R.; Khuri, F.; Adkins, D.; Clark, J.; Sarlis, N.; Lorch, J.; Beitler, J. J.; Limaye, S.; Riley, S.; Posner, M. Induction chemotherapy followed by concurrent chemoradiotherapy (sequential chemoradiotherapy) versus concurrent chemoradiotherapy alone in locally advanced head and neck cancer (PARADIGM): a randomised phase 3 trial. *Lancet Oncol* **2013**, *14*, 257-264.
(9) Chung, S. W.; Cho, Y. S.; Choi, J. U.; Kim, H. R.; Won, T. H.; Kim, S. Y.; Byun, Y. Highly potent monomethyl auristatin E prodrug activated by caspase-3 for the chemoradiotherapy of triple-negative breast cancer. *Biomaterials* **2019**, *192*, 109-117.
(10) Jiang, Y. Y.; Martin, J.; Alkadhimi, M.; Shigemori, K.; Kinchesh, P.; Gilchrist, S.; Kersemans, V.; Smart, S.; Thompson, J. M.; Hill, M. A.; O'Connor, M. J.; Davies, B. R.; Ryan, A. J. Olaparib increases the therapeutic index of hemithoracic irradiation compared with hemithoracic irradiation alone in a mouse lung cancer model. *Brit J Cancer* **2021**, *124*, 1809-1819.
(11) Motea, E. A.; Huang, X. M.; Singh, N.; Kilgore, J. A.; Williams, N. S.; Xie, X. J.; Gerber, D. E.; Beg, M. S.; Bey, E. A.; Boothman, D. A. NQO1-dependent, Tumor-selective Radiosensitization of Non-small Cell Lung Cancers. *Clin Cancer Res* **2019**, *25*, 2601-2609.
(12) Bradley, J. D.; Hu, C.; Komaki, R. R.; Masters, G. A.; Blumenschein, G. R.; Schild, S. E.; Bogart, J. A.; Forster, K. M.; Magliocco, A. M.; Kavadi, V. S.; Narayan, S.; Iyengar, P.; Robinson, C. G.; Wynn, R. B.; Koprowski, C. D.; Olson, M. R.; Meng, J.; Paulus, R.; Curran, W.; Choy, H. Long-Term Results of NRG Oncology RTOG 0617: Standard- Versus High-Dose Chemoradiotherapy With or Without Cetuximab for Unresectable Stage III Non-Small-Cell Lung Cancer. *J Clin Oncol* **2020**, *38*, 706-714.
(13) Hanna, N.; Shepherd, F. A.; Fossella, F. V.; Pereira, J. R.; De Marinis, F.; von Pawel, J.; Gatzemeier, U.; Tsao, T. C. Y.; Pless, M.; Muller, T.; Lim, H. L.; Desch, C.; Szondy, K.; Gervais, R.; Manegold, C.; Paul, S.; Paoletti, P.; Einhorn, L.; Bunn, P. Randomized Phase III Trial of Pemetrexed Versus Docetaxel in Patients With Non-Small-Cell Lung Cancer Previously Treated With Chemotherapy (Reprinted from vol 22, pg 1589-1597, 2004). *J Clin Oncol* **2023**, *41*, 2682-2690.
(14) Ghersi, D.; Willson, M. L.; Chan, M. M. K.; Simes, J.; Donoghue, E.; Wilcken, N. Taxane-containing regimens for metastatic breast cancer. *Cochrane Db Syst Rev* **2015**, CD003366.
(15) Min, H. Y.; Lee, H. Y. Molecular targeted therapy for anticancer treatment. *Exp Mol Med* **2022**, *54*, 1670-1694.
(16) Hunter, T.; Sefton, B. M. Transforming gene product of Rous sarcoma virus phosphorylates tyrosine. *Proc Natl Acad Sci U S A* **1980**, *77*, 1311-1315.
(17) Cohen, P.; Cross, D.; Jänne, P. A. Kinase drug discovery 20 years after imatinib: progress and future directions. *Nat Rev Drug Discov* **2021**, *20*, 551-569.
(18) Yun, C. H.; Mengwasser, K. E.; Toms, A. V.; Woo, M. S.; Greulich, H.; Wong, K. K.; Meyerson, M.; Eck, M. J. The T790M mutation in EGFR kinase causes drug resistance by increasing the affinity for ATP. *Proc Natl Acad Sci U S A* **2008**, *105*, 2070-2075.

(19) Ramalingam, S. S.; Vansteenkiste, J.; Planchard, D.; Cho, B. C.; Gray, J. E.; Ohe, Y.; Zhou, C.; Reungwetwattana, T.; Cheng, Y.; Chewaskulyong, B.; Shah, R.; Cobo, M.; Lee, K. H.; Cheema, P.; Tiseo, M.; John, T.; Lin, M. C.; Imamura, F.; Kurata, T.; Todd, A.; Hodge, R.; Saggese, M.; Rukazenkov, Y.; Soria, J. C.; Investigators, F. Overall Survival with Osimertinib in Untreated, EGFR-Mutated Advanced NSCLC. *New Engl J Med* **2020**, *382*, 41-50.
(20) Wu, Y. L.; Tsuboi, M.; He, J.; John, T.; Grohe, C.; Majem, M.; Goldman, J. W.; Laktionov, K.; Kim, S. W.; Kato, T.; Vu, H. V.; Lu, S.; Lee, K. Y.; Akewanlop, C.; Yu, C. J.; de Marinis, F.; Bonanno, L.; Domine, M.; Shepherd, F. A.; Zeng, L. M.; Hodge, R.; Atasoy, A.; Rukazenkov, Y.; Herbst, R. S.; Investigators, A. Osimertinib in Resected-Mutated Non-Small-Cell Lung Cancer. *New Engl J Med* **2020**, *383*, 1711-1723.
(21) Paul, S.; Konig, M. F.; Pardoll, D. M.; Bettegowda, C.; Papadopoulos, N.; Wright, K. M.; Gabelli, S. B.; Ho, M.; van Elsas, A.; Zhou, S. B. Cancer therapy with antibodies. *Nat Rev Cancer* **2024**, *24*, 399-426.
(22) Paz-Ares, L. G.; Juan-Vidal, O.; Mountzios, G. S.; Felip, E.; Reinmuth, N.; de Marinis, F.; Girard, N.; Patel, V. M.; Takahama, T.; Owen, S. P.; Reznick, D. M.; Badin, F. B.; Cicin, I.; Mekan, S.; Patel, R.; Zhang, E. R.; Karumanchi, D.; Garassino, M. C. Sacituzumab Govitecan Versus Docetaxel for Previously Treated Advanced or Metastatic Non-Small Cell Lung Cancer: The Randomized, Open-Label Phase III EVOKE-01 Study. *J Clin Oncol* **2024**, *42*, 2860-2872.
(23) Leach, D. R.; Krummel, M. F.; Allison, J. P. Enhancement of antitumor immunity by CTLA-4 blockade. *Science* **1996**, *271*, 1734-1736.
(24) Iwai, Y.; Ishida, M.; Tanaka, Y.; Okazaki, T.; Honjo, T.; Minato, N. Involvement of PD-L1 on tumor cells in the escape from host immune system and tumor immunotherapy by PD-L1 blockade. *Proc Natl Acad Sci USA* **2002**, *99*, 12293-12297.
(25) Armoiry, X.; Tsertsvadze, A.; Connock, M.; Royle, P.; Melendez-Torres, G. J.; Souquet, P. J.; Clarke, A. Comparative efficacy and safety of licensed treatments for previously treated non-small cell lung cancer: A systematic review and network meta-analysis. *PLoS One* **2018**, *13*, e0199575.
(26) O'Reilly, D.; O'Leary, C. L.; Reilly, A.; Teo, M. Y.; O'Kane, G.; Hendriks, L.; Bennett, K.; Naidoo, J. Toxicity of immune checkpoint inhibitors and tyrosine kinase inhibitor combinations in solid tumors: a systematic review and meta-analysis. *Front Oncol* **2024**, *14*, 1380453.
(27) Youssef, E.; Fletcher, B.; Palmer, D. Enhancing precision in cancer treatment: the role of gene therapy and immune modulation in oncology. *Front Med* **2025**, *11*, 1527600.
(28) Roddie, C.; Sandhu, K. S.; Tholouli, E.; Logan, A. C.; Shaughnessy, P.; Barba, P.; Ghobadi, A.; Guerreiro, M.; Yallop, D.; Abedi, M.; Pantin, J. M.; Yared, J. A.; Beitinjaneh, A. M.; Chaganti, S.; Hodby, K.; Menne, T.; Arellano, M. L.; Malladi, R.; Shah, B. D.; Mountjoy, L.; O'Dwyer, K. M.; Peggs, K. S.; Lao-Sirieix, P.; Zhang, Y. Y.; Brugger, W.; Braendle, E.; Pule, M.; Bishop, M. R.; DeAngelo, D. J.; Park, J. H.; Jabbour, E. Obecabtagene Autoleucel in Adults with B-Cell Acute Lymphoblastic Leukemia. *New Engl J Med* **2024**, *391*, 2219-2230.
(29) Kalos, M.; Levine, B. L.; Porter, D. L.; Katz, S.; Grupp, S. A.; Bagg, A.; June, C. H. T Cells with Chimeric Antigen Receptors Have Potent Antitumor Effects and Can Establish Memory in Patients with Advanced Leukemia. *Sci Transl Med* **2011**, *3*, 95ra73.
(30) Porter, D. L.; Levine, B. L.; Kalos, M.; Bagg, A.; June, C. H. Chimeric Antigen Receptor-Modified T Cells in Chronic Lymphoid Leukemia. *New Engl J Med* **2011**, *365*, 725-733.
(31) Zhang, J. Q.; Hu, Y. X.; Yang, J. X.; Li, W.; Zhang, M. M.; Wang, Q. C.; Zhang, L. J.; Wei, G. Q.; Tian, Y.; Zhao, K.; Chen, A.; Tan, B. H.; Cui, J. Z.; Li, D. Q.; Li, Y.; Qi, Y. L.; Wang, D. R.; Wu, Y. X.; Li, D. L.; Du, B.; Liu, M. Y.; Huang, H. Non-viral, specifically targeted CAR-T cells achieve high safety and efficacy in B-NHL. *Nature* **2022**, *609*, 369-374.
(32) Nie, H. F.; Xie, X. D.; Zhang, D. D.; Zhou, Y.; Li, B. F.; Li, F. Q.; Li, F. Y.; Cheng, Y. L.; Mei, H.; Meng, H.; Jia, L. Use of lung-specific exosomes for miRNA-126 delivery in non-small cell lung cancer. *Nanoscale* **2020**, *12*, 877-887.
(33) Dubey, S.; Chen, Z.; Jiang, Y. J.; Talis, A.; Molotkov, A.; Ali, A.; Mintz, A.; Momen-Heravi, F. Small extracellular vesicles (sEVs)-based gene delivery platform for cell-specific CRISPR/Cas9 genome editing. *Theranostics* **2024**, *14*, 2777-2793.
(34) Shi, Y. N.; Zhang, H. Q.; Chen, H.; Guo, J. W.; Yuan, R. R.; Tian, Y.; Xin, Q. L.; Mu, Z.; Tao, Y. P.; Chu, Y. C.; Wang, A. P.; Zhang, Z. W.; Tian, J. W.; Wang, H. B. Cetuximab-Immunoliposomes Loaded with TGF-β1 siRNA for the Targeting Therapy of NSCLC: Design, and In Vitro and In Vivo Evaluation. *Int J Mol Sci* **2025**, *26*, 1196.
(35) Chong, Z. X.; Yeap, S. K.; Ho, W. Y. Transfection types, methods and strategies: a technical review. *PeerJ* **2021**, *9*, e11165.
(36) Hu, B.; Zhong, L. P.; Weng, Y. H.; Peng, L.; Huang, Y. Y.; Zhao, Y. X.; Liang, X. J. Therapeutic siRNA: state of the art. *Signal Transduct Target Ther* **2020**, *5*, 101.
(37) Andreev, D. E.; Terenin, I. M.; Dmitriev, S. E.; Shatsky, I. N. Pros and cons of pDNA and mRNA transfection to study mRNA translation in mammalian cells. *Gene* **2016**, *578*, 1-6.
(38) Jaiswal, S.; Jamieson, C. H. M.; Pang, W. W.; Park, C. Y.; Chao, M. P.; Majeti, R.; Traver, D.; van Rooijen, N.; Weissman, I. L. CD47 Is Upregulated on Circulating Hematopoietic Stem Cells and Leukemia Cells to Avoid Phagocytosis. *Cell* **2009**, *138*, 271-285.
(39) Majeti, R.; Chao, M. P.; Alizadeh, A. A.; Pang, W. W.; Jaiswal, S.; Gibbs, K. D.; van Rooijen, N.; Weissman, I. L. CD47 Is an Adverse Prognostic Factor and Therapeutic Antibody Target on Human Acute Myeloid Leukemia Stem Cells. *Cell* **2009**, *138*, 286-299.

(40) Chao, M. P.; Alizadeh, A. A.; Tang, C.; Jan, M.; Weissman-Tsukamoto, R.; Zhao, F. F.; Park, C. Y.; Weissman, I. L.; Majeti, R. Therapeutic Antibody Targeting of CD47 Eliminates Human Acute Lymphoblastic Leukemia. *Cancer Res* **2011**, *71*, 1374-1384.
(41) Chao, M. P.; Jaiswal, S.; Weissman-Tsukamoto, R.; Alizadeh, A. A.; Gentles, A. J.; Volkmer, J.; Weiskopf, K.; Willingham, S. B.; Raveh, T.; Park, C. Y.; Majeti, R.; Weissman, I. L. Calreticulin Is the Dominant Pro-Phagocytic Signal on Multiple Human Cancers and Is Counterbalanced by CD47. *Sci Transl Med* **2010**, *2*, 63ra94.
(42) Feng, M. Y.; Chen, J. Y.; Weissman-Tsukamoto, R.; Volkmer, J. P.; Ho, P. Y.; McKenna, K. M.; Cheshier, S.; Zhang, M.; Guo, N.; Gip, P.; Mitra, S. S.; Weissman, I. L. Macrophages eat cancer cells using their own calreticulin as a guide: Roles of TLR and Btk. *Proc Natl Acad Sci USA* **2015**, *112*, 2145-2150.
(43) Feng, M. Y.; Marjon, K. D.; Zhu, F. F.; Weissman-Tsukamoto, R.; Levett, A.; Sullivan, K.; Kao, K. S.; Markovic, M.; Bump, P. A.; Jackson, H. M.; Choi, T. S.; Chen, J.; Banuelos, A. M.; Liu, J.; Gip, P.; Cheng, L.; Wang, D. N.; Weissman, I. L. Programmed cell removal by calreticulin in tissue homeostasis and cancer. *Nat Commun* **2018**, *9*, 3194.
(44) Hassan, E. M.; Walker, G. C.; Wang, C.; Zou, S. Anti-leukemia effect associated with down-regulated CD47 and up-regulated calreticulin by stimulated macrophages in co-culture. *Cancer Immunol Immun* **2021**, *70*, 787-801.
(45) Willingham, S. B.; Volkmer, J. P.; Gentles, A. J.; Sahoo, D.; Dalerba, P.; Mitra, S. S.; Wang, J.; Contreras-Trujillo, H.; Martin, R.; Cohen, J. D.; Lovelace, P.; Scheeren, F. A.; Chao, M. P.; Weiskopf, K.; Tang, C.; Volkmer, A. K.; Naik, T. J.; Storm, T. A.; Mosley, A. R.; Edris, B.; Schmid, S. M.; Sun, C. K.; Chua, M. S.; Murillo, O.; Rajendran, P.; Cha, A. C.; Chin, R. K.; Kim, D.; Adorno, M.; Raveh, T.; Tseng, D.; Jaiswal, S.; Enger, P. O.; Steinberg, G. K.; Li, G.; So, S. K.; Majeti, R.; Harsh, G. R.; van de Rijn, M.; Teng, N. N. H.; Sunwoo, J. B.; Alizadeh, A. A.; Clarke, M. F.; Weissman, I. L. The CD47-signal regulatory protein alpha (SIRPa) interaction is a therapeutic target for human solid tumors. *Proc Natl Acad Sci USA* **2012**, *109*, 6662-6667.
(46) Weiskopf, K.; Jahchan, N. S.; Schnorr, P. J.; Cristea, S.; Ring, A. M.; Maute, R. L.; Volkmer, A. K.; Volkmer, J. P.; Liu, J.; Lim, J. S.; Yang, D.; Seitz, G.; Nguyen, T.; Wu, D.; Jude, K.; Guerston, H.; Barkal, A.; Trapani, F.; George, J.; Poirier, J. T.; Gardner, E. E.; Miles, L. A.; de Stanchina, E.; Lofgren, S. M.; Vogel, H.; Winslow, M. M.; Dive, C.; Thomas, R. K.; Rudin, C. M.; van de Rijn, M.; Majeti, R.; Garcia, K. C.; Weissman, I. L.; Sage, J. CD47-blocking immunotherapies stimulate macrophage-mediated destruction of small-cell lung cancer. *J Clin Invest* **2016**, *126*, 2610-2620.
(47) Jang, J. Y.; Choi, Y.; Jeon, Y. K.; Aung, K. C. Y.; Kim, C. W. Over-expression of adenine nucleotide translocase 1 (ANT1) induces apoptosis and tumor regression. *Bmc Cancer* **2008**, *8*, 160.
(48) Lena, A.; Rechichi, M.; Salvetti, A.; Vecchio, D.; Evangelista, M.; Rainaldi, G.; Gremigni, V.; Rossi, L. The silencing of adenine nucleotide translocase isoform 1 induces oxidative stress and programmed cell death in ADF human glioblastoma cells. *Febs J* **2010**, *277*, 2853-2867.
(49) Bauer, M. K. A.; Schubert, A.; Rocks, O.; Grimm, S. Adenine nucleotide translocase-1, a component of the permeability transition pore, can dominantly induce apoptosis. *J Cell Biol* **1999**, *147*, 1493-1501.
(50) Zamora, M.; Meroño, C.; Viñas, O.; Mampel, T. Recruitment of NF-κB into mitochondria is involved in adenine nucleotide translocase 1 (ANT1)-induced apoptosis. *J Biol Chem* **2004**, *279*, 38415-38423.
(51) Schubert, A.; Grimm, S. Cyclophilin D, a component of the permeability transition-pore, is an apoptosis repressor. *Cancer Res* **2004**, *64*, 85-93.
(52) Zamora, M.; Ortega, J. A.; Alañna, L.; Viñas, O.; Mampel, T. Apoptotic and anti-proliferative effects of all-trans retinoic acid. Adenine nucleotide translocase sensitizes HeLa cells to all-trans retinoic acid. *Exp Cell Res* **2006**, *312*, 1813-1819.
(53) Kim, W.; Ye, Z.; Simonenko, V.; Shahi, A.; Malikzay, A.; Long, S. Z.; Xu, J. J.; Lu, A.; Horng, J. H.; Wu, C. R.; Chen, P. J.; Lu, P. Y.; Evans, D. M. Codelivery of TGFβ and Cox2 siRNA inhibits HCC by promoting T-cell penetration into the tumor and improves response to Immune Checkpoint Inhibitors. *Nar Cancer* **2024**, *6*, zcad059.
(54) Sporn, M. B. The early history of TGF-β, and a brief glimpse of its future. *Cytokine Growth Factor Rev* **2006**, *17*, 3-7.
(55) Garcia-Cuellar, C. M.; Santibanez-Andrade, M.; Chirino, Y. I.; Quintana-Belmares, R.; Morales-Barcenas, R.; Quezada-Maldonado, E. M.; Sanchez-Perez, Y. Particulate Matter (PM) Promotes Cell Invasion through Epithelial-Mesenchymal Transition (EMT) by TGF-β Activation in A549 Lung Cells. *Int J Mol Sci* **2021**, *22*, 12632.
(56) Yang, M.; Qin, C.; Tao, L.; Cheng, G.; Li, J.; Lv, F.; Yang, N.; Xing, Z.; Chu, X.; Han, X.; Huo, M.; Yin, L. Synchronous targeted delivery of TGF-beta siRNA to stromal and tumor cells elicits robust antitumor immunity against triple-negative breast cancer by comprehensively remodeling the tumor microenvironment. *Biomaterials* **2023**, *301*, 122253.
(57) Bhola, N. E.; Balko, J. M.; Dugger, T. C.; Kuba, M. G.; Sánchez, V.; Sanders, M.; Stanford, J.; Cook, R. S.; Arteaga, C. L. TGF-β inhibition enhances chemotherapy action against triple-negative breast cancer. *J Clin Invest* **2013**, *123*, 1348-1358.
(58) Moore, L. D.; Isayeva, T.; Siegal, G. P.; Ponnazhagan, S. Silencing of transforming growth factor-β1 by RNA interference for breast cancer: Implications for proliferation and migration and metastasis. *Clin Cancer Res* **2008**, *14*, 4961-4970.
(59) Zhang, F.; Wang, H. S.; Wang, X. F.; Jiang, G. M.; Liu, H.; Zhang, G.; Wang, H.; Fang, R.; Bu, X. Z.; Cai, S. H.; Du, J. TGF-β induces M2-like macrophage polarization via SNAIL-mediated suppression of a pro-inflammatory phenotype. *Oncotarget* **2016**, *7*, 52294-52306.

(60) Ellermeier, J.; Wei, J. W.; Duewell, P.; Hoves, S.; Stieg, M. R.; Adunka, T.; Noerenberg, D.; Anders, H. J.; Mayr, D.; Poeck, H.; Hartmann, G.; Endres, S.; Schnurr, M. Therapeutic Efficacy of Bifunctional siRNA Combining TGF-β1 Silencing with RIG-I Activation in Pancreatic Cancer. *Cancer Res* **2013**, *73*, 1709-1720.
(61) Rej, A.; Paladhi, A.; Daripa, S.; Sarkar, D.; Bhattacharyya, S.; Mondal, I.; Hira, S. K. Galunisertib synergistically potentiates the doxorubicin-mediated antitumor effect and kickstarts the immune system against aggressive lymphoma. *Int Immunopharmacol* **2023**, *114*, 109521.
(62) Shen, L. M.; Schaefer, A. M.; Tiruthani, K.; Wolf, W.; Lai, S. K. Siglec15/TGF-β bispecific antibody mediates synergistic anti-tumor response against 4T1 triple negative breast cancer in mice. *Bioeng Transl Med* **2024**, *9*, e10651.
(63) Biswas, S.; Guix, M.; Rinehart, C.; Dugger, T. C.; Chytil, A.; Moses, H. L.; Freeman, M. L.; Arteaga, C. L. Inhibition of TGF-β with neutralizing antibodies prevents radiation-induced acceleration of metastatic cancer progression. *J Clin Invest* **2007**, *117*, 1305-1313.
(64) Biswas, S.; Guix, M.; Rinehart, C.; Dugger, T. C.; Chytil, A.; Moses, H. L.; Freeman, M. L.; Arteaga, C. L. Inhibition of TGF-β with neutralizing antibodies prevents radiation-induced acceleration of metastatic cancer progression (vol 117, pg 1305, 2007). *J Clin Invest* **2017**, *127*, 1116-1116.
(65) Holmgaard, R. B.; Schaer, D. A.; Li, Y. X.; Castaneda, S. P.; Murphy, M. Y.; Xu, X. H.; Inigo, I.; Dobkin, J.; Manro, J. R.; Iversen, P. W.; Surguladze, D.; Hall, G. E.; Novosiadly, R. D.; Benhadji, K. A.; Plowman, G. D.; Kalos, M.; Driscoll, K. E. Targeting the TGFβ pathway with galunisertib, a TGFβRI small molecule inhibitor, promotes anti-tumor immunity leading to durable, complete responses, as monotherapy and in combination with checkpoint blockade. *J Immunother Cancer* **2018**, *6*, 47.
(66) Huang, S.; Ding, D.; Lan, T.; He, G.; Ren, J.; Liang, R.; Zhong, H.; Chen, G.; Lu, X.; Shuai, X.; Wei, B. Multifunctional nanodrug performs sonodynamic therapy and inhibits TGF-beta to boost immune response against colorectal cancer and liver metastasis. *Acta Biomater* **2023**, *164*, 538-552.
(67) Geng, G. N.; Xu, Y. X.; Hu, Z. Y.; Wang, H.; Chen, X. Y.; Yuan, W.; Shu, Y. L. Viral and non-viral vectors in gene therapy: current state and clinical perspectives. *Ebiomedicine* **2025**, *118*, 105834.
(68) Zhuang, J. L.; Tan, J. Z.; Wu, C. L.; Zhang, J.; Liu, T.; Fan, C. H.; Li, J. P.; Zhang, Y. Q. Extracellular vesicles engineered with valency-controlled DNA nanostructures deliver CRISPR/Cas9 system for gene therapy. *Nucleic Acids Res* **2020**, *48*, 8870-8882.
(69) Wang, J. H.; Gessler, D. J.; Zhan, W.; Gallagher, T. L.; Gao, G. P. Adeno-associated virus as a delivery vector for gene therapy of human diseases. *Signal Transduct Target Ther* **2024**, *9*, 78.
(70) Lin, D. N.; Shen, Y. A.; Liang, T. B. Oncolytic virotherapy: basic principles, recent advances and future directions. *Signal Transduct Target Ther* **2023**, *8*, 156.
(71) Matsunaga, W.; Gotoh, A. Adenovirus as a Vector and Oncolytic Virus. *Curr Issues Mol Biol* **2023**, *45*, 4826-4840.
(72) Nzila, M. M.; Koehl, U.; Ivics, Z. Non-viral vectors as beacons of hope for reducing genotoxic risks of gene therapy. *Nat Biomed Eng* **2026**, in press.
(73) Lee, D. Y.; Amirthalingam, S.; Lee, C.; Rajendran, A. K.; Ahn, Y. H.; Hwang, N. S. Strategies for targeted gene delivery using lipid nanoparticles and cell-derived nanovesicles. *Nanoscale Adv* **2023**, *5*, 3834-3856.
(74) G Gregoriadis, B. E. R. Liposomes as carriers of enzymes or drugs: a new approach to the treatment of storage diseases. *Biochem Eng J* **1971**, *124*, 58P.
(75) Akkewar, A.; Mahajan, N.; Kharwade, R.; Gangane, P. Liposomes in the Targeted Gene Therapy of Cancer: A Critical Review. *Curr Drug Deliv* **2023**, *20*, 350-370.
(76) Boussif, O.; Lezoualch, F.; Zanta, M. A.; Mergny, M. D.; Scherman, D.; Demeneix, B.; Behr, J. P. A versatile vector for gene and oligonucleotide transfer into cells in culture and in vivo: polyethylenimine. *Proc Natl Acad Sci USA* **1995**, *92*, 7297-7301.
(77) Zhang, J.; Yang, X.; Chang, Z.; Zhu, W.; Ma, Y.; He, H. Polymeric nanocarriers for therapeutic gene delivery. *Asian J Pharm Sci* **2025**, *20*, 101015.
(78) Chen, J.; Guan, X.; Hu, Y.; Tian, H.; Chen, X. Peptide-Based and Polypeptide-Based Gene Delivery Systems. *Top Curr Chem (Cham)* **2017**, *375*, 32.
(79) Yazdani, S.; Mozaffarian, M.; Pazuki, G.; Hadidi, N.; Villate-Beitia, I.; Zárate, J.; Puras, G.; Pedraz, J. L. Carbon-Based Nanostructures as Emerging Materials for Gene Delivery Applications. *Pharmaceutics* **2024**, *16*, 288.
(80) Song, W. L.; Jia, P. F.; Zhang, T.; Dou, K. K.; Liu, L. B.; Ren, Y. P.; Liu, F. J.; Xue, J. M.; Hasanin, M. S.; Qi, H. Z.; Zhou, Q. H. Cell membrane-camouflaged inorganic nanoparticles for cancer therapy. *J Nanobiotechnol* **2022**, *20*, 289.
(81) Augustine, J.; Cheung, T.; Gies, V.; Boughton, J.; Chen, M. H.; Jakubek, Z. J.; Walker, S.; Martinez-Rubi, Y.; Simard, B.; Zou, S. Assessing size-dependent cytotoxicity of boron nitride nanotubes using a novel cardiomyocyte AFM assay. *Nanoscale Adv* **2019**, *1*, 1914-1923.
(82) Gies, V.; Zou, S. Systematic toxicity investigation of graphene oxide: evaluation of assay selection, cell type, exposure period and flake size. *Toxicol Res* **2018**, *7*, 93-101.
(83) Syama, K.; Jakubek, Z. J.; Chen, S.; Zaifman, J.; Tam, Y. Y. C.; Zou, S. Development of lipid nanoparticles and liposomes reference materials (II): cytotoxic profiles. *Sci Rep* **2022**, *12*, 18071.
(84) Coleman, B. R.; Knight, T.; Gies, V.; Jakubek, Z. J.; Zou, S. Manipulation and Quantification of Graphene Oxide Flake Size: Photoluminescence and Cytotoxicity. *Acs Appl Mater Inter* **2017**, *9*, 28911-28921.
(85) Gies, V.; Lopinski, G.; Augustine, J.; Cheung, T.; Kodra, O.; Zou, S. The impact of processing on the cytotoxicity of graphene oxide. *Nanoscale Adv* **2019**, *1*, 817-826.

(86) Hassan, E. M.; Zou, S. Novel nanocarriers for silencing anti-phagocytosis CD47 marker in acute myeloid leukemia cells. *Colloid Surface B* **2022**, *217*, 112609.
(87) Hassan, E. M.; McWhirter, S.; Walker, G. C.; Martinez-Rubi, Y.; Zou, S. Elimination of Cancer Cells in Co-Culture: Role of Different Nanocarriers in Regulation of CD47 and Calreticulin-Induced Phagocytosis. *Acs Appl Mater Inter* **2023**, *15*, 3791-3803.
(88) Sakib, S.; Zou, S. Attenuation of Chronic Inflammation in Intestinal Organoids with Graphene Oxide-Mediated Tumor Necrosis Factor-α_Small Interfering RNA Delivery. *Langmuir* **2024**, *40*, 3402-3413.
(89) Zhang, C. Y.; Sui, Y. X.; Liu, S.; Yang, M. In vitro and in vivo experimental models for cancer immunotherapy study. *Curr Res Biotechnol* **2024**, *7*, 100210.
(90) Juarez-Moreno, K.; Chavez-Garcia, D.; Hirata, G.; Vazquez-Duhalt, R. Monolayer (2D) or spheroids (3D) cell cultures for nanotoxicological studies? Comparison of cytotoxicity and cell internalization of nanoparticles. *Toxicol In Vitro* **2022**, *85*, 105461.
(91) Hurrell, T.; Lilley, K. S.; Cromarty, A. D. Proteomic responses of HepG2 cell monolayers and 3D spheroids to selected hepatotoxins. *Toxicol Lett* **2019**, *300*, 40-50.
(92) Morgan, R. G.; Chambers, A. C.; Legge, D. N.; Coles, S. J.; Greenhough, A.; Williams, A. C. Optimized delivery of siRNA into 3D tumor spheroid cultures. *Sci Rep* **2018**, *8*, 7952.
(93) Singh, M.; Close, D. A.; Mukundan, S.; Johnston, P. A.; Sant, S. Production of Uniform 3D Microtumors in Hydrogel Microwell Arrays for Measurement of Viability, Morphology, and Signaling Pathway Activation. *Assay Drug Dev Techn* **2015**, *13*, 570-583.
(94) Barker, N.; Huch, M.; Kujala, P.; van de Wetering, M.; Snippert, H. J.; van Es, J. H.; Sato, T.; Stange, D. E.; Begthel, H.; van den Born, M.; Danenberg, E.; van den Brink, S.; Korving, J.; Abo, A.; Peters, P. J.; Wright, N.; Poulsom, R.; Clevers, H. Lgr5+ve Stem Cells Drive Self-Renewal in the Stomach and Build Long-Lived Gastric Units In Vitro. *Cell Stem Cell* **2010**, *6*, 25-36.
(95) Lv, J. J.; Du, X.; Wang, M. M.; Su, J. C.; Wei, Y.; Xu, C. Construction of tumor organoids and their application to cancer research and therapy. *Theranostics* **2024**, *14*, 1101-1125.
(96) Del Bufalo, F.; Manzo, T.; Hoyos, V.; Yagyu, S.; Caruana, I.; Jacot, J.; Benavides, O.; Rosen, D.; Brenner, M. K. 3D modeling of human cancer: A PEG-fibrin hydrogel system to study the role of tumor microenvironment and recapitulate the effect of oncolytic adenovirus. *Biomaterials* **2016**, *84*, 76-85.
(97) Takahashi, H.; Kikuchi, Y. 3D co-culture disc for spatiotemporal image analysis of cancer-stromal cell interaction. *Biomater Sci* **2021**, *9*, 4448-4458.
(98) Lee, S.; Hong, J. H.; Kim, J. S.; Yoon, J. S.; Chun, S. H.; Hong, S. A.; Kim, E. J.; Kang, K.; Kang, J. L.; Ko, Y. H.; Ahn, Y. H. Cancer-associated fibroblasts activated by miR-196a promote the migration and invasion of lung cancer cells. *Cancer Lett* **2021**, *508*, 92-103.
(99) Miyazaki, K.; Oyanagi, J.; Hoshino, D.; Togo, S.; Kumagai, H.; Miyagi, Y. Cancer cell migration on elongate protrusions of fibroblasts in collagen matrix. *Sci Rep* **2019**, *9*, 292.
(100) Rebelo, S. P.; Pinto, C.; Martins, T. R.; Harrer, N.; Estrada, M. F.; Loza-Alvarez, P.; Cabeçadas, J.; Alves, P. M.; Gualda, E. J.; Sommergruber, W.; Brito, C. 3D-3-culture: A tool to unveil macrophage plasticity in the tumor microenvironment. *Biomaterials* **2018**, *163*, 185-197.
(101) Sambale, F.; Lavrentieva, A.; Stahl, F.; Blume, C.; Stiesch, M.; Kasper, C.; Bahnemann, D.; Scheper, T. Three dimensional spheroid cell culture for nanoparticle safety testing. *J Biotechnol* **2015**, *205*, 120-129.
(102) Qiu, X. F.; Zhang, Y. T.; Zhao, X. Z.; Zhang, S. W.; Wu, J. H.; Guo, H. Q.; Hu, Y. Q. Enhancement of endothelial differentiation of adipose derived mesenchymal stem cells by a three-dimensional culture system of microwell. *Biomaterials* **2015**, *53*, 600-608.
(103) Kessel, S.; Cribbes, S.; Bonasu, S.; Rice, W.; Qiu, J.; Chan, L. L. Y. Real-Time Viability and Apoptosis Kinetic Detection Method of 3D Multicellular Tumor Spheroids Using the Celigo Image Cytometer. *Cytom Part A* **2017**, *91a*, 883-892.
(104) Chen, S.; Giannakou, A.; Wyman, S.; Gruzas, J.; Golas, J.; Zhong, W. Y.; Loreth, C.; Sridharan, L.; Yamin, T. T.; Damelin, M.; Geles, K. G. Cancer-associated fibroblasts suppress SOX2-induced dysplasia in a lung squamous cancer coculture. *Proc Natl Acad Sci USA* **2018**, *115*, E11671-E11680.
(105) Domenici, G.; Lopes, N. F.; Trindade, G.; Gal, I. R.; Minard, J. M.; Rebelo, S. P.; Freitas, C.; Duarte, N.; Brito, C. Assessing Novel Antibody-Based Therapies in Reconstructive 3D Cell Models of the Tumor Microenvironment. *Adv Biol* **2024**, *8*, e2400431.
(106) Pan, H. J.; Lee, C. W.; Wu, L. Y.; Hsu, H. H.; Tung, Y. C.; Liao, W. Y.; Lee, C. H. A 3D culture system for evaluating the combined effects of cisplatin and anti-fibrotic drugs on the growth and invasion of lung cancer cells co-cultured with fibroblasts. *Apl Bioeng* **2023**, *7*, 016117.
(107) Anguiano, M.; Morales, X.; Castilla, C.; Pena, A. R.; Ederra, C.; Martínez, M.; Ariz, M.; Esparza, M.; Amaveda, H.; Mora, M.; Movilla, N.; Aznar, J. M. G.; Cortés-Domínguez, I.; Ortiz-de-Solorzano, C. The use of mixed collagen-Matrigel matrices of increasing complexity recapitulates the biphasic role of cell adhesion in cancer cell migration: ECM sensing, remodeling and forces at the leading edge of cancer invasion. *PLoS One* **2020**, *15*, e0220019.

Chapter 2: Characteristics of Graphene Oxide for Gene Transfection and Controlled Release in Breast Cancer Cells

This chapter presents a review of GO-based nanocarriers for cancer gene delivery, with an emphasis on structure, functionalization strategies, biocompatibility, and delivery performance. While the reviewed studies primarily focus on breast cancer models, the underlying design principles governing GO-mediated gene delivery, including the influence of flake size, surface chemistry, charge, and environmental responsiveness on cellular uptake, toxicity, and controlled payload release, are broadly applicable across solid tumors.

My specific contribution to this review centers on the analysis of GO toxicity and controlled release mechanisms, examining how physicochemical properties and microenvironmental stimuli regulate biocompatibility. These insights provide a background for translating GO design strategies to lung cancer and other epithelial malignancies, enabling rational engineering of nanocarriers that balance delivery efficiency, biocompatibility, and tumor specificity.

Reference:

Grilli, F.; Hajimohammadi, P. G.; Zou, S. Characteristics of Graphene Oxide for Gene Transfection and Controlled Release in Breast Cancer Cells. Int. J. Mol. Sci., 2022, 23, 6802

Abstract

Functionalized graphene oxide (GO) nanoparticles are being increasingly employed for designing modern drug delivery systems because of their high degree of functionalization, high surface area with exceptional loading capacity, and tunable dimensions. With intelligent controlled release and gene silencing capability, GO is an effective nanocarrier that permits the targeted delivery of small drug molecules, antibodies, nucleic acids, and peptides to the liquid or solid tumor sites. However, the toxicity and biocompatibility of GO-based formulations should be evaluated, as these nanomaterials may introduce aggregations or may accumulate in normal tissues while targeting tumors or malignant cells. These side effects may potentially be impacted by the dosage, exposure time, flake size, shape, functional groups, and surface charges. In this review, the strategies to deliver the nucleic acid via the functionalization of GO flakes are summarized to describe the specific targeting of liquid and solid breast tumors. In addition, we describe the current approaches aimed at optimizing the controlled release towards a reduction in GO accumulation in non-specific tissues in terms of the cytotoxicity while maximizing the drug efficacy. Finally, the challenges and future research perspectives are briefly discussed.

2.1 Introduction

Breast cancer is one of the most frequent malignant tumors that affects women globally. Even though standard breast cancer treatments, including surgery, radiotherapy, and chemotherapy, have been relatively effective, significant limitations and side effects still jeopardize the quality of patients' lives [1]. There are currently two FDA-approved drugs to alleviate the side effects of chemotherapy, Doxil and Abraxane, which are based on doxorubicin (DOX) and paclitaxel, respectively [2]. However, the detrimental effects of chemotherapy strategies on normal tissues due to the multidrug resistance (MDR) effect and high concentration of the drug used cannot be eliminated [3]. In order to address the shortcomings of chemotherapy, breast cancer treatment strategies based on polymers [4-6],

dendrimers [7,8], carbon-derivatives [9,10], and liquid metal and metal–organic framework nanoparticles [11,12] have been developed to deliver small drug molecules, antibodies, and nucleic acids to the targeted sites [13].

Over the years, gene transfection by carriers has become an alternative treatment because it is based on inducing or replacing overexpressed genes or proteins in tumor cells, leading to cancer cell death and a reduction in tumor growth [13]. Among these carriers, GO has recently drawn the interest of researchers due to its unique properties, including its controllable 2-dimensional structure, high surface area, and versatile functional groups. Interestingly, these features not only give this material the capability of being rationally functionalized, but also to respond to the stimuli from its surrounding environment. Thus, these characteristics provide GO with the distinctive capability to be tailored in multifunctional nanocarriers for various applications [14]. Nonetheless, engineering a drug/gene carrier that can ideally meet all of the essential requirements of a delivery system and finally reach clinical trials is still challenging. According to the existing definitions [15], a potential drug/gene carrier must be capable of (1) protecting the drug/gene from degradation upon transfer; (2) retaining it in the circulation system for more than a few hours; (3) facilitating cell internalization and drug release at the desired sites; (4) being non-toxic and biodegradable. All of the mentioned criteria are highly dependent on the carrier's physicochemical properties (such as its morphology, including shape, size, and aspect ratio, ionic strength, and charges, and its chemical functionality), determining its potential to pass through the biological compartments. Furthermore, the chemical modification of GO provides the opportunity to improve the performance of GO-based nanocarriers in terms of their toxicity, specific targeting, cell internalization, and drug release. The conjugation of these biocompatible materials enables the carrier to associate with nucleic acids, and at the same time preserves them from cleavage in biological fluids [16].

Once the carriers are internalized into cells, gene derivatives are released in the desirable cell compartment. Subsequently, the nucleic acids can direct the formation of the mutated genes, with the

alternation of their nature resulting in the expression or inhibition of specific proteins. Obviously, this ability to manipulate gene expression or inhibition is highly affected by the release of gene derivatives from the carriers [17]. Taking advantage of the readiness for GO functionalization, this material is responsive to stimuli such as pH, temperature, and near-infrared irradiation (NIR) [18]. This susceptibility and the possibility of being functionalized with stimuli-responsive agents through specific linkages can lead to multi-responsive GO carriers being engineered for a controlled and efficient release.

In this review, we describe the characteristics of GO and functionalized GO as nanocarriers, their modification for nucleic acid delivery, their toxicity, and their controlled release of payloads with the aim of providing a breast cancer treatment by summarizing the most recent publications (before October 2021). The following combination of words, such as GO, modification, toxicity, gene/drug delivery, controlled release, and breast cancer, was applied when searching papers using the Science Direct and PubMed engines.

2.2 Characteristics of GO as a Nanocarrier

Among all nanocarriers, carbon-based materials display various structures, such as a tetrahedral sp^3 network, planar sp^2, and linear sp configurations [19], which result in the presence of allotropes, including 0-dimensional (0D) fullerene, 1-dimensional (1D) carbon nanotubes, and 3-dimensional (3D) graphite [20]. As a carbon derivative, graphene comprises a monolayer of sp^2 carbon atoms aligned in a honeycomb-like two-dimensional (2D) network. Despite its optical properties and large surface area, the hydrophobic nature of graphene has caused aggregations that have hindered its functionality in solution- processed applications. In order to overcome this limitation, the synthesis of GO and reduced GO (rGO) was introduced and has improved the solubility and processability of graphene-based materials [21,22]. In comparison with other carbon-based materials, GO has a large surface area with theoretical and measured values of around 2418 and 2391 m^2/g, respectively [23],

an order of magnitude more than that of the majority of other nanomaterials [24]. Unlike the hydrophobic nature of graphene, GO has both hydrophobic regions and hydrophilic peripheries, giving this material an amphiphilic character [25]. This composition is responsible for the good aqueous dispersibility and the exceptional ability to cross cell membranes easily. These unique structures allow biological molecules to be associated with GO flakes, facilitating the efficient loading of drugs and genes or a combination of them.

The synthesis of GO has developed over the years [26-28] after the original protocol was proposed [29]. Recently, the modified Hummers method has been used to produce exfoliated graphene oxide flakes with the potential for additional modification in biomedical applications [22,25,28,30,31]. As a result, graphene is highly oxidized, leaving hydroxyl and epoxy functional groups on the planar surface, while the carboxylic groups are found at the edges [32]. Depending on the post-processing step after the synthesis and purification, a wide range of exfoliation [25] and oxidation degrees can be obtained, with the possibility for size distribution control [33].

2.2.1 Size and Two-Dimensional Structure

When nanoparticles are in the body, they must pass through several barriers to reach the targeted site and successfully release the therapeutic chemicals into the appropriate biological compartment. The journey of the nanoparticle initiates within the blood vessels, and if the targeted cells are out of blood circulation (e.g., solid tumors), the nanoparticle encounters three primary barriers prior to reaching the malignant tissue: (1) the endothelium of the vessel walls; (2) the extracellular matrix (ECM); (3) the cell membrane [34]. In the case of breast cancer therapy, the carrier needs to pass through the mentioned barriers, but it should not penetrate the blood–brain barrier (BBB) to avoid potential brain toxicity [35]. The BBB separates the brain from the blood circulation with a continuous layer over the thick basement membrane.

The size of the drug carriers determines their potential to pass through the biological compartments. Larger carriers (in the micron range) are likely to be cleared by reticuloendothelial macrophages through phagocytosis before reaching the targeted site of the body. Carriers at the nanoscale can circulate in the body for a more extended period without being recognized by macrophages as invaders [36-39]. Specifically, small carriers (<200 nm) are required for endothelial penetration when the targeted tissue is positioned outside the bloodstream [15]. The size of the endothelial fenestrations for carrier penetration relies on the pathological conditions that the carrier is dealing with [40]. Almost all solid tumors have leaky angiogenesis and impaired lymphatic function, differentiating them from other tissues. A growing tumor creates an excessive network of blood vessels to increase oxygen and nutrition transfer. This property allows particles of 10 to 100 nm in size to pass through the voids of blood vessel walls and to accumulate in tumor locations instead of normal tissues, which is known as enhanced permeability and retention (EPR) [41], while it was also reported that even larger carriers (200−800 nm) could penetrate through the endothelium barrier and accumulate in the targeted tumor [42]. These results indicate the easier and more efficient diffusion of smaller particles (<100 nm), while the penetration of the larger ones (<800 nm) is not entirely prevented. Subsequent to successfully passing through the endothelium, the nanoparticle should be capable of going through the collagen fibers, which is the primary component of the ECM. The gaps between the fibrils and the intra-fibrillar spacing are 20−40 and 75−130 nm, respectively [43]. For this reason, the ideal size of a carrier was reported to be less than 200 nm to not only prevent its clearance from the circulation [43], but also to facilitate its diffusion throughout the ECM. All of the reported information regarding nanoscale carriers raises the demand for an appropriate range of carrier sizes as one of the criteria to achieve adequate drug or gene transportation. Therefore, a material with unique size and dimension characteristics is more advantageous as a drug or gene carrier.

Compared to all of its counterparts, GO can meet the required criteria mentioned above due to its tunable lateral size from a few nanometers to tens of microns [45,46] and its monolayer thickness at the sub-nanometer scale. The reported thickness (vertical size) of a GO monolayer ranged from

approximately 0.5 to 1.2 nm (measured by atomic force microscopy topography imaging), while larger reported scales are associated with multilayer GO [28,47,48]. On the other hand, the wide range of lateral sizes is advantageous to meet different requirements for biological applications [49,50]. GO nanoparticles ranging from 50 to 200 nm have consistently been demonstrated in multiple investigations to bypass immune cells, diffuse through vessel walls and the ECM, and infiltrate breast cancer cells effectively [51-55].

GO cell penetration occurs through three different mechanisms, depending on the carrier size. Smaller particles, ranging from 20 to 100 nm, internalize cells through caveolin- dependent endocytosis, while clathrin-dependent endocytosis occurs for larger particles of 100–500 nm. Additionally, carriers possessing a much larger size (0.5−1.5 μm) are absorbed by micropinocytosis [34]. According to the research findings, GO nanoparticles are more likely to be taken up by cancer cells via clathrin-mediated endocytosis than other nanoparticles because of the planar 2D shape of the GO flakes, which possess sharp edges [56,57].

According to the literature, various approaches have been conducted to obtain GO with specific lateral dimensions applicable before, during, or after the synthesis. The approaches used prior to the synthesis include adopting a suitable graphite as the starting material with a suitable particle size, or increasing the mass of the oxidative agent and the time of oxidation, while post-processing methods are based on ultrasonication, centrifugation, and dialysis/filtration [33]. These strategies cause GO breakage, which initiates from defected sites with sp3 bonds. Consequently, if the size reduction procedure continues, it will ultimately lead to the removal of functional groups at the edges. By applying a range of ultrasonication energy, the diameters of two types of commercial graphene oxide flakes could be tuned from about 2 microns to around 150 nm [58]. In another study, utilizing the centrifugation of 0.01 mg/mL GO in a mixture of water and glycerol at 8000 g for 3 h could decrease the GO flake size to 150−850 nm [59], as shown in Figure 2.1.

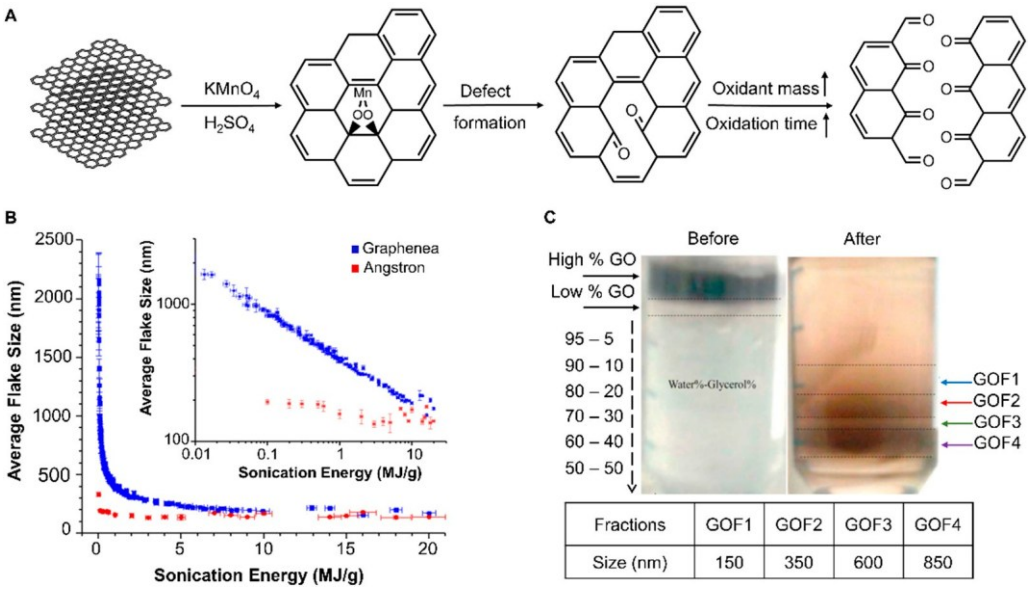

Fractions	GOF1	GOF2	GOF3	GOF4
Size (nm)	150	350	600	850

Figure 2.1. Approaches to reduce the lateral size of GO through (A) increasing the oxidant mass and the time of oxidation during synthesis, which causes ruptures in defected regions of GO flakes. The figure is adapted from [33,58] with open access permission. Copyright © 2020 Tufano, Vecchione, and Netti. (B) Increasing the ultrasonication time and energy, leading to a decrease in the size of GO from 2 µm to 150 nm. The figure is reprinted with permission from [58]. Copyright 2017 American Chemical Society. (C) Centrifugation and fractionation of 0.01 mg/mL GO in water–glycerol mixture at 3000× g for 1 h. The figure is reprinted with permission from [59] Elsevier.

It was also reported that the lateral width of GO is highly influenced by the initial size of the raw graphite flakes used for synthesis. By breaking down graphite as a starting material, GO with a 10−300 nm lateral size can be obtained 60]. Using graphite nanofibers with a 130 nm diameter as a precursor, Luo et al. could scale down the average lateral width of GO flakes to 100 nm for cancer drug release [61]. These results indicated that, depending on the application, fabricating a carrier that can diffuse the mentioned barriers to reach the targeted site of the body raises the demand for achieving a uniform size of GO particles using the mentioned approaches. In addition, different sizes of functionalized GO have been utilized for breast cancer therapy [17,51,53,62-69].

Ultrasonication has been used not only to reduce the flake size to 30−500 nm, but also to exfoliate graphite into monolayer GO. Furthermore, increases were found in the average lateral dimension and height of GO after functionalization, which were considered the result of successful modifications [51,62-67,70-72]. Although the mentioned methods reduce the lateral dimension of GO, it should be

noted that the ultimate nanoparticle that interacts with breast cancer cells has a different size compared to GO alone, depending on the amount of functionalization and the payload mass [51,62-67,70-72].

As explained above, an ideal carrier needs to have a long blood circulation time and bypass the phagocytosis by macrophages to reach the targeted site, and at the same not diffuse past the blood–brain barrier [35]. Zhang et al. focused on the effect of lateral dimension of GO on the blood circulation time and clearance by macrophages. They synthesized GO particles ranging from 10−800 nm and evaluated the blood circulation times *in vivo*. It was shown that considering the wide size distribution, GO particles with a larger size are likely to be eliminated more readily, and the half-life of the blood circulation was reported to be about 5.3 h, which was higher than for single-walled carbon nanotubes and fullerene, according to previous findings [73-76]. This suggested that GO can be a promising candidate for gene delivery due to its distinctive size characteristics. Additionally, the polymer modification of GO was shown to slow down phagocytosis. Other parameters, such as the cell type, dosage, and exposure time, are also involved in the clearance and cellular uptake of GO, which will be discussed in the next section.

2.2.2 Functionalization

GO can be considered as a form of functionalized graphene, encompassing abundant oxygen-containing groups, which enable the nanocarrier to be specifically modified and loaded with therapeutic agents [77,78]. With the polar basal plane and hydrophilic -OH and -COOH groups, GO is dispersible in water, similar to an amphiphilic molecule that can be used as a surfactant to stabilize hydrophobic species in water (e.g., drugs) [79,80].

GO typically has a negative surface charge when dispersed in water, mainly due to the ionization of the carboxylic acid and hydroxyl groups. This negative charge could provide electrostatic repulsion,

allowing a stable GO dispersion. The ability of GO to disperse in aqueous environments has been demonstrated as an advantage for targeting and release mechanisms and imaging in cancer therapy [63,81,82].

GO is more hydrophilic in acidic environments, affecting GO suspensions' zeta potentials [63,79,80]. Alkaline pH causes the ionizable groups (carboxylic and hydroxyl groups) of GO to dissociate, resulting in a greater negative charge [81,82]. This suggests that GO can be made into a smart drug delivery system due to its controlled release properties in diverse biological environments by fine-tuning its one-of-a-kind pH characteristics. Those functional groups are, in fact, highly affected by the pH level of the surrounding medium due to the affinity to accept or give out protons. The hydrophilicity of GO increases with pH due to the protonation of carboxyl groups on GO [81,82].

Even though GO disperses in cell culture and physiological environments due to its hydrophilic characteristics, in order to avoid aggregation and overcome the π-π stacking and van der Waals forces between sheets, it is necessary to functionalize it through various methods to sustain its single-layer structure [83]. These modifications are categorized into covalent and non-covalent methods [84,85], which are utterly dependent on the loading strategy of the drug or gene, as summarized in Table 2.1.

Table 2.1. Graphene oxide modifications with the objective of gene transfection.

GO Modification	Modification Mechanism	Agents
Covalent	Amidation	PEG [62, 63, 77, 86]
		PAMAM [16, 17, 87]
		PEI [88, 89]
		Chitosan [64-66]
		DEX [90]
	Ring-opening reaction	PEG [91]
		APTES [53]
	Esterification	PEG [91]
Non-covalent	π-π stacking	MUC1 aptamer [72]
	Electrostatic interactions	PEG [67, 70]
		PEI [67]
	Hydrophobic interactions	Phospholipids [52, 70]

2.2.2.1 Covalent Modification

Polymer materials, such as polyethylene glycol (PEG) [86], polyethyleneimine (PEI) [92], polyvinyl alcohol (PVA) [93], dextran (DEX) [90], polyacrylic acid (PAA) [94], and chitosan [95], have been covalently bonded to enhance the biocompatibility and stability of GO-based delivery systems. Covalent modification routes are generally carried out using three different reactions: (1) a ring-opening reaction of epoxide groups present on the basal plane of GO via nucleophilic attacks; (2) amidation, where COOH groups at the edges of GO flakes are replaced by NH2 in polymer groups; (3) esterification, in which carboxylic groups of GO directly react with hydroxyl groups of the polymer in the absence of NH2 as a mediator agent [17,77,91], as illustrated in Figure 2.2.

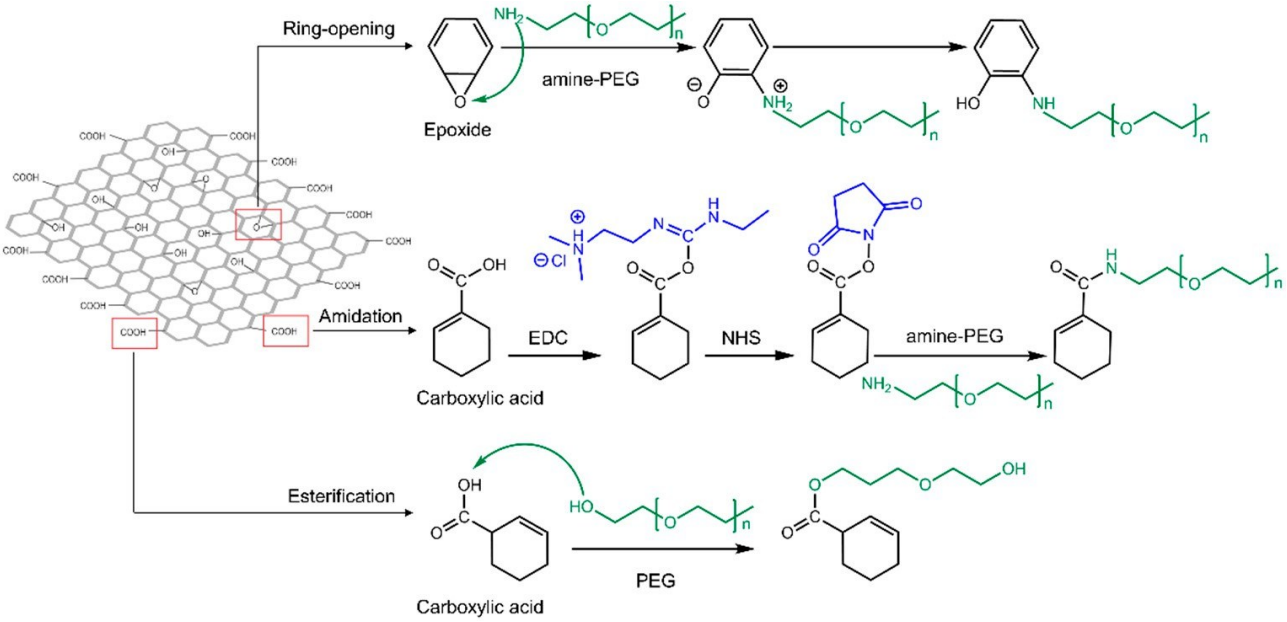

Figure 2.2. Commonly used modification methods to functionalize GO for drug/gene delivery applications, including the ring-opening of epoxide, amidation using EDC-NHS chemistry, and esterification in the absence of NH2 in carboxylic acid regions.

The most commonly utilized polymers to assist in the loading of genes for breast cancer treatment include PEG [17,62,88], polyamidoamine (PAMAM) [16,17,87], PEI [88], and chitosan [64–66]. Due to the negative charges of GO and gene derivatives, these cationic mediators form a stable interaction

between the GO and the genes. To covalently modify GO with these polymers, 1-ethyl-3-(3-dimethylaminopropyl) carbodiimide (EDC) and N-hydroxysuccinimide (NHS) were used as key agents to expose reactive C=O in carboxylic groups of GO to form amide bonds with primary amine (NH2) moieties. The reason for using both agents is that when EDC reacts with a carboxyl group of GO, it will generate amine-reactive O-acyl isourea. If this product does not interact with an amine, it will hydrolyze and renew the carboxylic acid. NHS is added to generate amine-reactive NHS esters, leading to a more stable amide bond between the polymer and GO [96] (Figure 2.2). In some studies, all epoxide groups of GO have been altered to carboxylic groups to increase the polymer modification, thereby generating a more positive charge through the primary amine content for higher gene loading efficiency [64,65]. It is worth noting that the amide bonds formed between −COOH and the amine-terminated agents are sensitive to pH alterations. In acidic environments such as cancerous cells, the amide bond weakens, leading to the dissociation of the cationic agent containing the payload from GO because of protonation [17,64,97,98]. This shows the essential role of GO functionalities in delivering genes to the desired cell compartment.

Among these polymers, PEG has attracted particular interest for biocompatibility enhancement because it increases the blood circulation time without being recognized by macrophages and alleviates GO particle aggregation in the biological medium [21]. Subsequent to PEGylation, GO is functionalized with other polymers, such as PEI and PAMAM, to load gene derivatives for breast cancer treatments to enhance the gene loading efficiency due to their outstanding capability for encapsulating gene derivatives [17,67,88]. It was shown that PEI had an essential role in binding siRNA to cell-penetrating peptide (CPP)-modified GO-PEI-PEG. By increasing only the GO/PEI mass ratio from 60 to 100 in the carrier system, the complete siRNA protection by the carrier and its binding were confirmed by gel retardation assay [67]. This might be due to PEI's ability to alter the surface charge of GO to positive values to a certain extent, since it has been reported that PEI could increase the zeta potential of GO to +47.2 mV due to its primary amines, while this value for bare GO was −28.9 mV [99]. The results demonstrated the same trend for PAMAM in terms of the zeta

potential, except that PAMAM is a dendrimer and its amine functionalities depend on the number of its generations, defined as the number of reaction sequences. As a result, its branched structure plays an essential role in encapsulating drugs and genes [17,100]. Yadav et al. [17] reported that PEGylation was necessary for the carrier's stability, as bonding PAMAM individually to GO causes precipitation. The presence of two or more polymers along with PEG improves the drug or gene encapsulation and provides protection against enzyme-induced degradation. Chen et al. [64] demonstrated that the presence of chitosan in the GO-based carrier could efficiently protect siRNA from degradation. Likewise, Wang et al. [51] showed that bare GO could not retard the migration of siRNA, and the GO modification with octaarginine (R8), a cell-penetrating peptide, was essential to protect the payload.

It should be noted that in some studies, PEGylation was carried out through the ring-opening reaction of epoxide groups and nucleophilic attacks on carbonyls [17], while in other studies the amidation strategy was used to modify GO with polymers and peptides [62,67,88].

2.2.2.2 Non-covalent Modification

In addition to covalent modifications, hydrogen bonding, π-π stacking, and electrostatic interactions were the major driving forces for small drug molecules [16,65], phospholipids [70], and oligonucleotides [68,72] to interact with GO, suggesting that gene derivatives can be directly loaded on GO.

The aromatic rings that exist in the bases of genes enhance such short-range π-π interactions, which are sensitive to the pH level of the surrounding medium. It was reported that miRNAs, siRNAs, and some short-stranded DNA strands dissociate from GO when the medium becomes acidic. This might weaken the π-π stacking interactions [101], which is beneficial to the cancerous cells, where the environment is often acidic. These forces are not only limited to gene derivatives but to most drugs,

including DOX, Dinaciclib, and Xanthohumol, which have also been loaded on GO through the same interactions for breast cancer treatment [65,86,88].

In addition to pH, these aromatic C-C bonds can respond to NIR irradiation. Pulsed laser irradiation NIR activates photosensitizing agents with an affinity for optical wavelengths. When the NIR light or photons interact with GO, this can lead to a forced resonance vibration mechanism, resulting in heat production at around 50 ◦C. This phenomenon has been demonstrated to weaken π-π interactions between drugs and genes by applying an NIR laser at 808 nm [62,66,102–104]. The effect of pH and NIR irradiation on the release is described thoroughly in Section 4.

On the other hand, the challenges associated with transferring naked nucleic acids to the targeted cells are their negative charge, high molecular weight, enzymatic degradation, instability, and low cellular uptake [51,62]. Therefore, most nucleic acids such as plasmid DNA, DNA aptamers, siRNAs, and miRNAs transfected to cancer cells are loaded on GO via intermediaries through electrostatic interactions. As a result, the surface charge (zeta potential) is altered to cationic (positive), promoting electrostatic interactions with anionic oligonucleotides [105].

Although polymers and all materials with a positive charge interact with GO through electrostatic interactions [67,70], covalent modifications are more desirable due to their stronger bonding, protecting the GO carrier system from degradation before reaching the targeted site of the body [16,17,62,63,77,86–89].

2.2.2.3 Targeting Strategy

After bypassing macrophages and degradation enzymes of the body, the carriers must reach the desired region of the body. The recruited strategies for a carrier to find its way to the cancerous part are active and passive targeting. The former uses EPR to reach malignant tissues, while the latter is based on the ligand–receptor approach to internalize individual cancer cells [106]. Although GO

carriers can be internalized in cells depending on their size, shape, charge, and functional groups, the presence of an active targeting agent can further assist the carriers to distinguish breast cancer cells from healthy ones.

Similar to other cancers, breast cancer cells produce overexpressed proteins or receptors, such as glycosaminoglycans (GAGs) [62], hyaluronic acid (HA) [65], and folic acid (FA) [66] binding receptors on the cell membrane. In addition, there are also HER2 proteins, which are responsible for the growth and division of healthy breast cells but are overexpressed on the membranes of cancerous ones [107]. Epithelial cell adhesion molecule (EpCAM) is also another transmembrane glycoprotein, which is overexpressed in cancerous epithelial cells with fast proliferation and can be found in breast cancer cells [64]. These proteins can be directly recognized by targeting molecules added to GO-based carriers. After being combined with polymers or biocompatible agents, the covalent or non-covalent modification of GO with peptides, antibodies, aptamers, or hyaluronic and folic acids enhances its cell penetration potential to target the specific breast cancer cells. Table 2.2 represents the GO modifications, payload types, targeting agents, and breast cancer cell types.

Covalent modifications are the most common strategies to bind targeting agents to functional groups on GO through the formation of amide bonds between carboxylic groups and the amine moieties. Nonetheless, these modifications were not limited to covalent bonding and GO could form different kinds of interactions with targeting agents [72].

In recent studies, GO was covalently linked to cell-penetrating peptides such as poly- L-arginine (PLA) and octaarginine (R8) through an amidation reaction [51]. On the other hand, another study applied electrostatic interactions for R8 modifications [67]. Whether using covalent or non-covalent interactions, these studies have shown that the negative zeta potential values of the GO-based carriers were altered to positive values, resulting in tunable gene–carrier interactions. The presence of arginine in peptides plays an essential role in cell internalization, and the guanidine groups are vital for the

targeting of cancer cells, which interact with overexpressed GAGs on cancer cell membranes [51,62,67,70].

Table 2.2. The effects of the surface functionalization and N/P ratio of GO-based carriers on gene silencing in breast cancer cells.

GO Modification	Payload Type (Targeting Agent)	N/P Ratio (w/w)	Gene Silencing	Cell Type
PEG	[a] miRNA 101 (PLA) [62]	1-3.8	-	MCF-7, MDA-MB-231
	[a] cd-siRNA (R8) [70]	10	-	
	[a] P-gp siRNA (FA) [88]	4	70%	
	[b] Rictor siRNA (R8) [67]	0.5	70%	
	[a] EPAC1-siRNA [17]	2	62%	MDA-MB-231
PAMAM	[a] EPAC1-siRNA [17]	2	62%	MDA-MB-231
	[b] miR-21i [16]	-	-	
	[b] MMP-9 shRNA [87]	10	52%	MCF-7
PEI	[a] P-gp siRNA (FA) [88]	4	70%	MCF-7, MDA-MB-231
	[b] Rictor siRNA (R8) [67]	0.5	70%	
Chitosan	[b] Survivin siRNA (anti-EpCAM) [51]	30	44%	MCF-7
	[a] HIF-1α siRNA (HA) [65]	6.5	62%	4T1
	[a] EGFR siRNA (FA) [66]	-	-	MCF-7, MDA-MB-231
Peptide	[a] cd-siRNA (R8) [70]	10	-	MCF-7, MDA-MB-231
	[b] Rictor siRNA (R8) [67]	0.5	70%	
	[b] Survivin siRNA (anti-HER2) [51]	40	50%	MCF-7

[a] *in vitro*; [b] *in vitro* and *in vivo*.

Similarly, aptamers, such as MUC1 and AS1411, have also been used to functionalize GO to target breast cancer cells [72,90]. MUC1 has a high affinity to Mucin MUC1 glycoproteins that are overexpressed on MCF-7 and MDA-MB-231 cells. The MUC1 aptamer has been immobilized on GO along with the cytochrome C aptamer through π-π stacking interactions. In addition to the synergic effect of MUC1 on targeting, none of the aptamers has been demonstrated to migrate from GO due to the strong π-π stacking interactions with GO. This indicates the ability of GO to protect aptamers

in the absence of any other mediator [72]. Unlike MUC1, the synthetic 26-base DNA aptamer AS1411 [108] was con- jugated to GO through hydroxyl groups of DEX and showed affinity towards nucleolin proteins on the 4T1 and MCF-7 cells [90].

On the other hand, antibodies such as anti-HER2 and anti-EpCAM have been associated with GO and interacted explicitly with overexpressed HER2 and EpCAM, respectively. The former was bound to GO through amidation in hydroxyl groups, while the latter was immobilized on GO through electrostatic interactions. These receptors were considered to be responsible for the fast proliferation of MCF-7 cells [51,64]. In addition, Antwi-Boasiako et al. [109] developed a GO-based Raman probe, which was tested on SKBR3 breast cancer cells with the overexpression of HER2. The results demonstrated that bioconjugated graphene oxide can selectively recognize cancer cells. Another targeting agent HA was covalently bonded on GO and showed an improved targeting efficiency to 4T1 breast cancer cells through its interaction with CD44 receptors [65,71]. At the same time, the presence of FA enhanced the targeting effect on MCF-7 and MDA-MB-231 cells through an interaction with folate receptors [63,66,88].

These targeting strategies of GO have also been adopted in biosensing to detect breast cancer cells, in which protein receptors can bind to GO through electrostatic and hydrophobic interactions. As an example, for the early detection of breast cancer, ERBB2, human epidermal growth factor receptor 2 was functionalized through EDC-NHS chemistry on the surface of a graphene foam modified with electrospun carbon-doped titanium dioxide nanofibers (nTiO2) and GO–gold nanoparticles. The results showed that these sensors have the potential to detect specific biomarkers in breast cancer cells [110,111].

2.2.2.4 Gene Loading Efficiency of GO-Based Carriers

The loading efficiency of GO carriers depends on the ability of the whole gene carrier system to protect and simultaneously deliver genes. This ability is directly influenced by the type, structure, concentration, and magnitude of positive charges of modified GOs, which affects the gene silencing efficiency in breast cancer cells. In order to engineer an efficient GO-based gene carrier, optimal concentrations of the modification agents should be selected to completely preserve genes. The protection level of GO carriers to genes has been determined by using gel retardation assays. In these tests, different nanocarrier/gene weight ratios were used to investigate the optimal ratio at which the carrier can retard gene migration [51,62,64,70]. Table 2.2 shows a summary of the most recent studies based on GO modification approaches, as well as the N/P ratio, in which N defines the nitrogen content of the amine-terminated polymers and peptides, while P presents the phosphorous present in the nucleic acids.

PEGylation is a well-known GO modification approach due to its ability to make GO flakes stable in biological dispersions. It assists GO carriers in bypassing the body's immune system [70]. The colloidal stability of GO-PEG in aqueous solution is due to the steric hindrance of PEG's hydrophilic chains and the repulsion between its amine groups [70]. For this reason, amine–PEG has been used to functionalize GO with the purpose of delivering various miRNAs and siRNAs to breast cancer cells, including: (1) miRNA 101 and Rictor siRNA, which are regulators of the PI3K/AKT pathway and responsible for cell metabolism and proliferation; (2) EPAC1 siRNA to inhibit EPAC1 protein, which is responsible for cell metastasis; (3) cell death (cd) siRNA to induce apoptosis; (4) P-gp siRNA to inhibit multidrug resistance protein (P-gp) [17,62,67,70,88]. Despite its capability, PEG is commonly combined with other polymers to functionalize GO. It has been shown that PEG maintained the stability of gold nanoparticles associated with GO for four weeks without any aggregation. The results showed that the zeta potential of the gold nanoparticle–GO shifted to negative with PEGylation and could only retard miRNA 101 at the GO–carrier/miRNA ratio of 3.8.

On the other hand, adding PLA to the carrier could alter the negative charge of the carrier to positive and retard the migration of miRNA at all GO–carrier/miRNA ratios lower than 3.8 (e.g., 2.8, 1.5, and 1). As a result, the release of miRNA-101 in MCF-7 and MDA-MB-231 cells could induce apoptosis by activating apoptotic pathways after 24 h, and it decreased the cell viability of MCF-7 and MDA-MB-231 to 62% and 64% with gold nanorods and nanoparticles, respectively [62].

In addition, Yadav et al. [17] reported that in their GO-based carrier functionalized with the dendrimer PAMAM, PEGylation was necessary to avoid precipitation. As mentioned earlier in Section 2.2.1, the branched structure of PAMAM can bring about a large number of positive charges on GO, followed by gene encapsulation. As a result, the efficient loading of EPAC1 siRNA on GO-PEG in the presence of PAMAM could lead to 62% gene silencing in MDA-MB-231 cells *in vitro*. These results indicated that even if PEGylated GO maintained the stability of GO, the presence of another mediator on GO was essential to form a sufficient electrostatic interaction, and thereby effective gene loading. A similar approach was used by Zeng et al. [88] to load P-gp siRNA on GO functionalized with both PEG and PEI, where PEI assisted GO-PEG in protecting the siRNA with its rich amine groups. The results showed that combining the siRNA and DOX with GO-PEG-PEI can increase protein inhibition by 70%.

On the other hand, there are studies that have focused on loading gene derivatives and functionalizing GO with PAMAM in the absence of PEG. PAMAM has been grafted on GO to deliver MMP-9 shRNA and miR-21i to breast cancer cells [16,87]. MMP-9 shRNA is a short hairpin RNA responsible for cancer metastasis, while miR-21i is an inhibitor of miR-21 with the capability for preventing cancer cell growth [16,87].

To prevent the overexpression of Survivin protein, an inhibitor of apoptosis, Survivin siRNA, was delivered to breast cancer cells through GO-modified chitosan and R8 [51,64]. Both studies showed that according to the Tyndall phenomenon, the covalent modification of GO with either chitosan or R8 increased the carrier stability in aqueous solutions, which might have been due to the electrostatic

shielding effect. Their result demonstrated that GO–chitosan and GO–R8 loaded with Survivin siRNA induced 44% and 50% inhibition of the related-protein expression *in vitro* and *in vivo*, respectively. Therefore, the polymer modification was essential, and a 30:40 (w/w) N/P ratio was required to protect the siRNA in the GO carrier system [51,64].

Figure 2.3A illustrates the capability of the GO/R8/anti-HER2/Survivin-siRNA nanocarrier to inhibit the relative protein expression of MCF-7 cells. The same phenomenon can be observed for MMP-9 shRNA loaded on GO modified only with PAMAM, where 10 mg of the carrier system was required to deliver 1 mg of the shRNA in breast cancer cells *in vitro* and *in vivo* to cause 52% gene silencing (Figure 2.3B) [87]. Additionally, Izadi et al. [65] and Maheshwari et al. [66] reported that the functionalization of GO with trimethyl chitosan (TMC) and chitosan oligosaccharide changed the zeta potentials of GO from −29 to +38 mV and from −43 to +31 mV, respectively. This result was beneficial for the homogenous dispersion and effective interactions with gene derivatives. The combination of GO-TMC loaded with Dinaciclib and HIF-1α siRNA, which is defined as a hypoxia-inducible factor, resulted in 62% gene silencing in 4T1 cells *in vitro*. Moreover, this approach could protect the siRNA for 18 h, while GO grafted with chitosan oligosaccharides loaded with EGFR siRNA caused protein inhibition in MCF-7 and MDA-MB-231 cells. Other studies have reported on the delivery of siRNAs using R8-grafted GO, and the links were through either amidation or electrostatic interactions, which provided sufficient positive charges with its -NH2 terminals for siRNAs to be absorbed [51,67,70].

Among gene derivatives that have been loaded on GO carriers for breast cancer treat- ment, fewer studies have focused on plasmids. Recently, GO was covalently functionalized with (3-aminopropyl) triethoxysilane (APTES)/spermine and hydroxyapatite (HAp) to deliver gene p53 and with Survivin–green fluorescent protein–HSV-TK plasmid, respectively. These plasmids can induce the expression of specific genes, such as P53, which is a tumor suppressor. HSV-TK is a herpes simplex virus thymidine kinase gene, also known as the suicide gene. The results have shown that the

functionalization APTES/Spermine and HAp completely retarded the migration of these plasmids, with 50- and 1.5-fold gene expression increases, respectively, leading to cancer cell death by apoptosis [14,31].

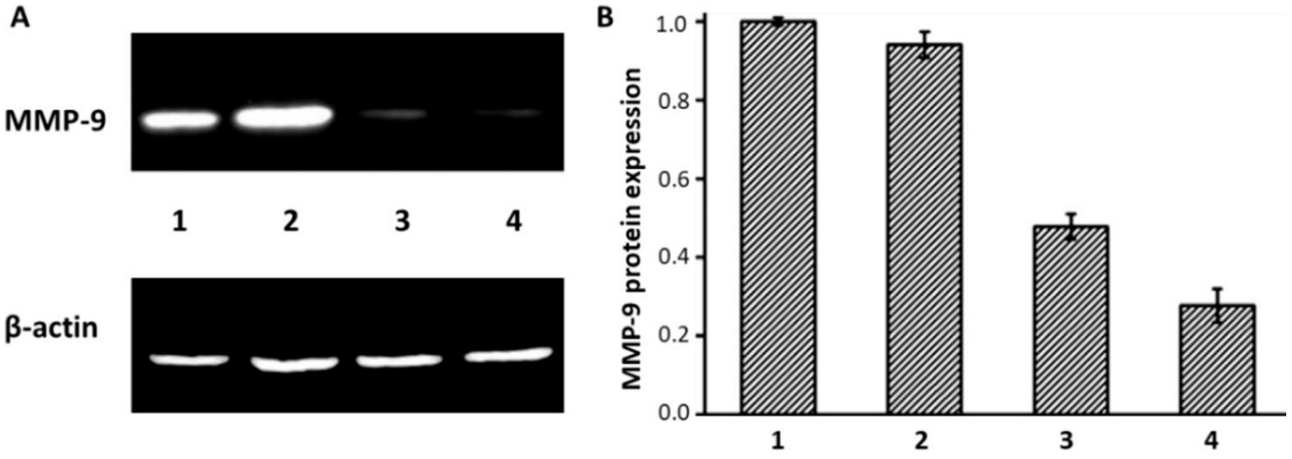

Figure 2.3. MMP-9 protein expression determined by Western blot analysis (A) and intensity analysis of (B) MMP-9 expression as the ratio of MMP-9 to β-actin from Western blot results: (1) PBS; (2) GO- PAMAM; (3) GO-PAMAM/MMP-9 (weight ratio of 10:1); (4) PEI-25k/MMP-9 (weight ratio of 4:3) [87]. Figures are reprinted with permission from Elsevier.

As presented in Table 2.2, regardless of the payload type, GO-based carriers modified by combined agents showed a carrier/payload ratio of less than 5, indicating that the presence of more positive charges (i.e., amine groups) on the GO surface led to more efficient loading and the protection of genes. Although GO flakes can easily penetrate cancer cells, the cellular internalization was enhanced by adding CPPs, providing more positive charges for gene derivatives to be absorbed.

On the other hand, it was shown that NAS-24 and cytochrome C aptamers were loaded directly on GO through π-π stacking interactions in the absence of mediators. The interaction between the NAS-24 aptamer and vimentin, an intermediate filament protein overexpressed in cancer cells, can cause cell apoptosis, which can be detected by the fluorescence-labeled cytochrome C aptamer. Immobilizing both aptamers on bare GO could completely prevent aptamer migration due to strong π-π interactions. This implies that it is possible to fabricate GO carriers without polymer modifications, which can also be as effective as functionalized GO [72].

2.3 Toxicity

A comprehensive analysis of the *in vitro* and *in vivo* cytotoxicity and biocompatibility of graphene oxide is an essential aspect to consider for the development of nanoparticles for drug and gene delivery. Graphene-based materials can induce cytotoxicity through a few different mechanisms: (1) interactions with the lipid tails of cell membranes, which induce the extraction of hydrophobic cholesterol and the creation of pores that damage the integrity of the membrane; (2) direct physical contact interactions of the sharp edges of GO flakes with cells, causing the rupture of the plasma membrane [112]; (3) penetration inside the cells and stimulation of excessive production of ROS, which cause dysfunction at the mitochondrial level; (4) the release of lactate dehydrogenase (LDH), which causes damage to the cell membrane [113,114]; (5) intranuclear penetration and an interaction with DNA, which induce genotoxic effects [115]; (6) the induction of an immune or inflammatory response, which activates apoptotic pathways (IKK/IκBα/NF-κB and BAX/BCL-2) [116].

Numerous studies have analyzed characteristics of GO to determine its potential use for biomedical applications [69,117,118]. These studies have shown that the toxicity depends on the complex interactions of several intrinsic characteristics of GO and extrinsic factors. The physiochemical properties, such as the shape, size, oxidation, and functionalization [69,119,120], are some of the main characteristics of GOs that can influence their interaction with the biological system. In addition, other experimental parameters, such as the dose of administration, time of exposure of GOs to cells, and type of cell line, represent important discriminating factors that can result in variable toxicity responses [118,119,121]. Therefore, to evaluate the toxicity of GO carriers, it is necessary to consider all of these parameters and to find the right ranges and combinations that allow the minimum cytotoxic response to be obtained on normal cells and the maximum one to be obtained on cancerous cells for breast cancer detection and elimination. Although the GO toxicity can be beneficial for the death of cancer cells, it raises the demand for the control of GO's functionalization to avoid the death of non-specific cells in targeted drug and gene delivery.

2.3.1 In vitro Toxicity

In vitro cell viability tests are the common steps taken to study and verify the influence of various intrinsic and extrinsic parameters on the material itself in order to understand its cytotoxicity, before continuing to more complex and expensive tests performed *in vivo* [121]. The structure, morphology, and size of GOs are the major parameters that can influence their interaction with cells. Through *in vitro* experiments, it is also possible to expose specific concentrations of GOs to different cell lines for defined periods of time and to test the influence of the time and concentration on the cytotoxicity in different cell types [118,122]. Following the exposure of cells to GOs, internalization studies highlight the mechanisms of cellular uptake and intracellular distribution that are influenced by the surface charge of the nanocarriers and their exposed functional groups [114,117]. The observation of the nanoparticle's journey inside cells allows an understanding of the fate following payload release. It shows where the GO carriers accumulate and whether they are biodegraded within specific intracellular organelles (e.g., endosomes, lysosomes) or excreted by exocytosis and captured by phagocytic cells (i.e., macrophages) [123].

2.3.1.1 Dose-, Time-, and Cell-Line-Dependent Cytotoxicity

GO is known to induce a dose- and time-dependent cytotoxicity [124,125]. Yue et al. [117] demonstrated that naked GO exposed to MCF-7 cells could induce dose-dependent cyto- toxicity in the range of 0–20 μg/mL, decreasing the cell viability by about 20% within 48 h. However, these results proved the non-toxicity of GO in these concentrations. The same trend was reported by Ribeiro et al. [114], in which MCF-7 cells showed a decrease of about 12% in viability when exposed for 72 h to 48 μg/cm2 GO. However, other studies found a different behavior of GO on breast cancer cells. Alibolandi et al. [90] showed that bare GO showed high cytotoxicity after 24 and 48 h, even at low concentrations (<70% cell viability with concentrations > 10 μg/mL and 20 μg/mL in 4T1 and MCF-7 cells, respectively).

Regarding the time-dependency of the cytotoxicity, the literature has reported conflicting results. Some studies did not find any relationship between the exposure time to GO and the decrease in viability [90,114], while others observed time-dependent cell death [118,119,122]. Chowdhury et al. [122] stated that GO nanoribbons decorated with amphiphilic lipid 1,2-distearoyl-sn-glycero-3-phosphoethanolamine-PEG (DSPE-PEG) could cause a time- and dose-dependent cytotoxicity, even though the cell viability measured in MCF-7 cells for the highest concentration tested (i.e., 400 μg/mL) showed only decreases of 15% and 20% after 24 and 48 h treatments, respectively. Thus, there is no clear agreement regarding the influence of the concentration and exposure time of GO on its cytotoxicity to breast cells. In addition, Chatterjee et al. [126] showed that GO could cause dose-dependent cytotoxicity and apoptosis due to damage and a consequent loss of structural integrity of the plasma membrane. This phenomenon can be explained by the strong physical interaction that forms between GO and the phospholipid bilayer.

Some studies have investigated the possibility of using rGO, which is characterized by a higher hydrophobicity that leads to a higher affinity for the cell membrane [127]. In the work by Kretowski et al. [118], the cytotoxicity of rGO nanoplatelets was analyzed on different breast cancer cell lines (T-47D, MCF-7, MDA-MB-231, ZR-75, Hs 578T) through LDH and propidium iodide staining (PI) tests. The cells were incubated with different amounts of rGO, ranging between 25 and 300 μg/mL, and with two different exposition times (24 and 48 h). The results showed that rGO can cause an increased time- and dose-dependent cytotoxicity with respect to MDA-MB-231 and ZR-75-1 breast cell lines. The results showed that after 48 h of exposure to 50 μg/mL of rGO, 30% of the cultured MDA-MB-231 cells and 50% of ZR-75-1 cells were apoptotic, while 8% of the former and 2% of the latter were necrotic. Equivalent results were obtained in the study by Farell et al. [119], in which lipid–rGO-nanocarrier-treated MDA-MB-231 cells showed an increase in cytotoxicity by about 3-fold with respect to the controls when exposed to a lower concentration (i.e., 10 μg/mL). The results were not the same for MCF-10A and MCF-7 cells. For these cell lines, there was no variation observed in the cell death level during the treatment period with increased concentrations (i.e., 10, 50

and 100 μg/mL) of bare and lipid–rGO compared to the control samples. These results proved that rGO is more cytotoxic than GO, demonstrating a strong interaction between the graphene and cells within a limited period of time. Since the toxicity depends on the physicochemical properties of the materials, the use of reducing agents to deoxygenate GO can lead to the formation of materials with different characteristics (i.e., particles size, density of functional groups on the surface) and different toxicity levels. In fact, following some reduction treatments, rGO has been shown to aggregate due to van der Waals interactions and has exhibited different sizes. This characteristic is known to be a major cause of increased toxicity, as will be discussed in the following sections.

Table 2.3. Dose- and time-dependent cytotoxicity of GO-based nanocarriers in different cell lines.

Nanoparticle	Cell Type	Dose (μL/mL)/Dependency		Time (Day)/Dependency	
GONR (PEG-DSPE) [122]	HeLa; MCF-7; SKBR; NIH3T3	10-400	Y	0.5-2	Y
GO	PMO; J774A.1; LLC; MCF-7; HepG2; HUVEC [117]	0-20	Y	1, 2, and 4	-
	HDF [129]	5, 10, 20, 50, and 100	Y	1, 2, 3, 4, and 5	Y
	A549 [130,131]	10, 25, 50, 100, and 200	N	1, 2, and 3	N
	HepG2 [132]	4, 8, and 16	Y	1 and 3	Y
GO, GOD and GOP [a] [114]	MCF-7	2.4, 24, and 48 (μg/cm^2)	Y	1, 2, and 3	N
GO-DEX-Apt-CUR [b] [90]	4T1; MCF-7	Up to 300	Y	1 and 2	N
Lipid-rGO [119]	MDA-MB-231	10, 50, and 100	Y	1 and 2	Y
	MCF-7; MCF 10-A		N		N
rGO [118]	MDA-MB-231; ZR-75-1	25-300	Y	1-24h	Y
	MCF-7; Hs 578T; T-47D		N		N
Graphene/SWCNT [128]	PC12	0.01, 0.1, 1, 10, and 100	Y	1-24h	Y

[a] GO modified with DAB-AM-16 and PAMAM dendrimers. [b] Dextran, ssDNA aptamer, and curcumin.

More clarification is needed to better understand in which conditions dose and time influence the toxicity of the GO carriers. The differences between the results found in the literature can be attributed to the different physicochemical properties of graphene-based nanomaterials, such as the surface functional groups, the shape and size of the flakes, and the unique characteristics of the treated cell lines (Table 2.3). For instance, MCF-7 cells are not affected by the dose or time of exposure to GO

with respect to other breast cell lines (i.e., MDA-MB-231, 4T1, ZR-75-1) [90,114,118,119]. The lower sensitivity of this cell line to GO can be caused by its different responsive expression levels of apoptotic and autophagic genes when exposed to the material. Different cell lines are characterized by distinctive characteristics, such as their morphology, dimensions, apoptotic genes, cell cycle activity, and expression of estrogen receptors [118]. Nonetheless, Chowdhury et al. [122] tested the dose- and time-dependent cytotoxicity of GO on all studied cell lines, including MCF-7 cells, while in other studies MCF-7 cells demonstrated only dose-dependent cytotoxicity [90,114].

Even though the dosage and time were proven to highly influence the cytotoxicity of GO in several studies, the dependency was not found in others (Table 2.3). Instead, it was noticed that other parameters can be modulated, allowing decreased cytotoxicity in similar experimental conditions, such as by modifying the biocompatible functionalization and size of the GO [113,114,128].

2.3.1.2 Charge- and Functionalization-Dependent Cytotoxicity

Cellular interactions are profoundly affected by the charge and chemical composition of GO, having a high negative charge density due to its numerous oxygenated functional groups. While it is well known that the cellular membrane has a net negative or neutral electrical charge, the negative zeta potential of GO measured in different studies (Table 2.4) reduces the cytotoxicity due to the same charge of the cellular membrane that reduces their interactions [133]. However, electrostatic interactions between GO and membrane lipids may arise due to the presence of some positively charged lipids on the plasma membrane. In addition, hydrophobic interactions between negatively charged GO and lipids can lead to GO adsorption and membrane damage [134]. Nevertheless, even if GO was shown to induce a certain degree of cytotoxicity, the possibility of modifying its surface with biocompatible polymers (e.g., PLA, PLGA, PAMAM) could significantly decrease its toxicity, both *in vivo* and *in vitro* [135]. Moreover, it has been seen that GO tends to aggregate in cell culture medium and biological fluids, due to the presence of serum [34]. The formation of GO aggregates is

detrimental to its function, as once the aggregates are formed, the GO carriers will no longer have the same initial structural characteristics, reducing their ability to penetrate the cells and to release the payload. Furthermore, aggregates of GO carriers could have large dimensions, making them unable to cross biological barriers and accumulate inside cells and tissues, increasing the toxic effect [57].

Thus, GO in physiological solutions induces unfavorable reactions for putative applications in the biomedical field, limiting its use without further surface modifications [92]. As previously said in Section 2, studies have demonstrated that the use of polymers, such as PEG [86], PEI [92], PVA [93], DEX [90], PAA [94], and chitosan [95], which were covalently bonded to GO functional groups, can enhance the biocompatibility and stability of GO- based drug or gene delivery systems. However, care must be taken, as many of the polymers that are often used are cationic and can increase the zeta potential of the carriers to positive values (see Table 2.4). Excessively high positive charges can induce higher cytotoxicity due to the strong physical interactions with the cell membrane, which can casue its damage and breakage [64].

Table 2.4. Size and zeta potential values of GO-based nanocarriers used in cytotoxicity studies.

Nanocarrier	Size (nm)	Zeta Potential (mV)	
		GO	NP
GO-PEI [133]	250−500	−53	+50
GO-DOTAP [52]	100−150	−30	+15
rGO-MPAH-FA [136]	100−230	−45	+40
GO-anti HER2-R8 [51]	120−260	−49	+26
GO-anti EpCAM-Chitosan [64]	70−350	−42	+38
GO-PEG-PAMAM [17]	54−220	−30	+10

GO can induce toxicity due to its different properties; however, the toxic effects are also likely to be highly dependent on its accumulation in certain tissues and the time of exposure to cells. Therefore, the functionalization of the nanocarriers with targeting molecules (e.g., antibodies specific to certain cells) is the main approach to control the accumulation and exposure time of the nanomaterials to

specific sites. Targeting molecules, which can specifically recognize the tumoral cells, allow nanoparticles to accumulate in the cancer site, inducing the cytotoxic effect mainly only in the circumscribed area of the tumor [69]. In addition, functionalization can increase the specificity and recognition potential of the nanocarriers from the body [137].

2.3.1.3 Size-Dependent Cytotoxicity

GO can induce cell death via various pathways. In general, the greater toxicity of small flakes is recognized [112,138], even if other studies have not found this correspondence [117]. Different sizes can induce different cytotoxicity effects (Figure 2.4). The toxicity pathways induced by GO can be of various types: (1) chemical induction of intracellular stress (ROS production) [122,138]; (2) mechanical induction by the physical interaction of GO with cell membranes, which can lead to their damage and breakage [112]; (3) genetic induction through the interaction with cellular DNA in the nucleus and its fragmentation or production of chromosomal aberrations [138,139]. The first pathway is observed in several studies [122]. Small GO flakes (i.e., ~10 nm) have been shown to induce increased oxidative stress [138]. The cause could be found in the procedure of breaking GO flakes to produce smaller ones. During this process, more edge defects are inserted, which can turn into active sites for ROS production [112]. The influence of the GO thickness on ROS production was also investigated in one study [138]. Single-layer and 4-layer GOs were assessed on MCF-7 cells. Again, smaller dimensions (i.e., single layer GO) induced greater oxidative stress with consequent greater cell death. Although this phenomenon seems to have been recently recognized as the main effect of nanomaterial-induced toxicity, other mechanisms seem to appear as the size of the GO flakes varies. As the size decreases, the nanoparticles present a lower surface-to-perimeter ratio, thereby exposing more of their irregular edges to cells.

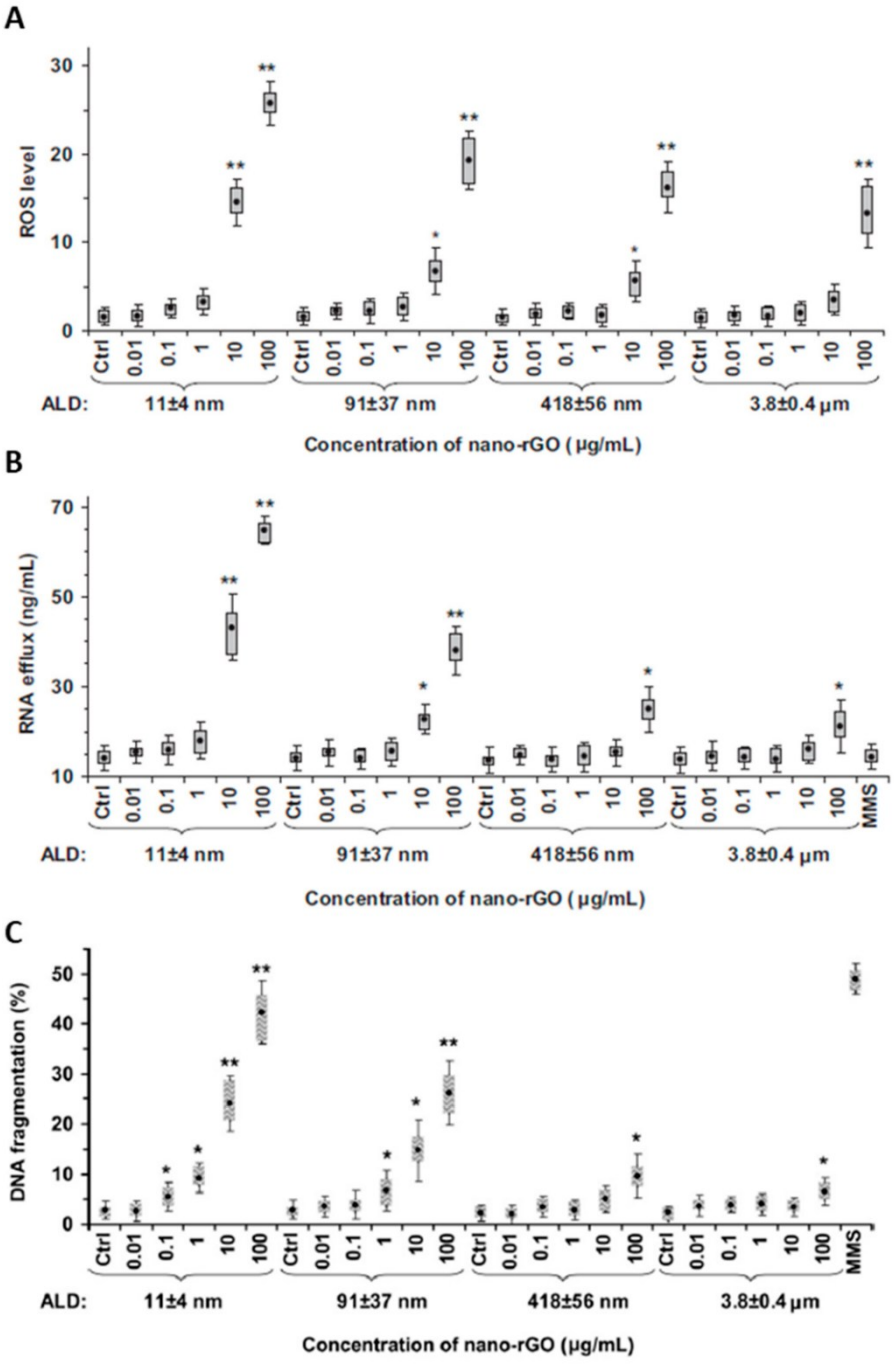

Figure 2.4. (A) ROS-generation-, (B) RNA-efflux-, and (C) DNA-fragmentation-induced toxicity of rGO flakes of different sizes (ALD: average lateral dimension; *: $p < 0.05$, **: $p < 0.01$) [112]. Figures are reprinted with permission from Elsevier.

This phenomenon could induce the second pathway of cytotoxicity. The interaction of cells with the sharp edges of flakes may cause the damage and rupture of the plasma membranes. When the size is small, the mobility of the GO is high, which may increase the probability and number of interactions

that a single flake has with the cell. Akhavan et al. [112] observed this phenomenon by studying the efflux of RNA from cells. They found that GO flakes of 11 ± 4 nm were shown to induce much greater RNA efflux from cells than graphene measuring 418 ± 56 nm, for which no significant RNA efflux was recorded, except for higher concentrations (i.e., 100 μg/mL). In some cases, despite inducing cell death, GO flakes are not responsible for damaging the cell membrane (i.e., no RNA efflux or significant levels of LDH have been recorded) [112,140], nor for the significant production of ROS [138]. These studies suggest the presence of other mechanisms capable of inducing necrosis. Among these mechanisms is genotoxicity. GO flakes can penetrate the nuclear membrane and interact with the cellular DNA inside the nucleus [139,141]. Following this interaction, DNA fragmentation and chromosomal aberrations can occur and induce apoptosis [138,142].

These considerations reveal the importance of producing and defining the size of the manufactured particles accurately. Predicting the main pathway of cellular toxicity, combined with the possibility of adequately functionalizing such GO flakes, could allow apoptosis to be driven in target cells in a highly controlled way.

2.3.1.4 Oxidative Stress

As mentioned above, oxidative stress is a phenomenon that normally occurs inside the body [118]. An imbalance in the regulation of the production and elimination of these reactive oxygen species within cells can lead to cell mutations, such as the emergence and development of tumors [143]. They are usually characterized by their ROS production in much higher concentrations and by a limited antioxidant enzymatic activity compared to healthy cells [119]. Various compounds can be used to induce this oxidative stress, such as lipid peroxides, oxidized proteins, and sugars. These are normally compensated by the presence of reduced compounds, such as the reduced form of glutathione (GSH) [118]. It plays a fundamental role in protecting cellular activities that can be affected by the presence of free radicals.

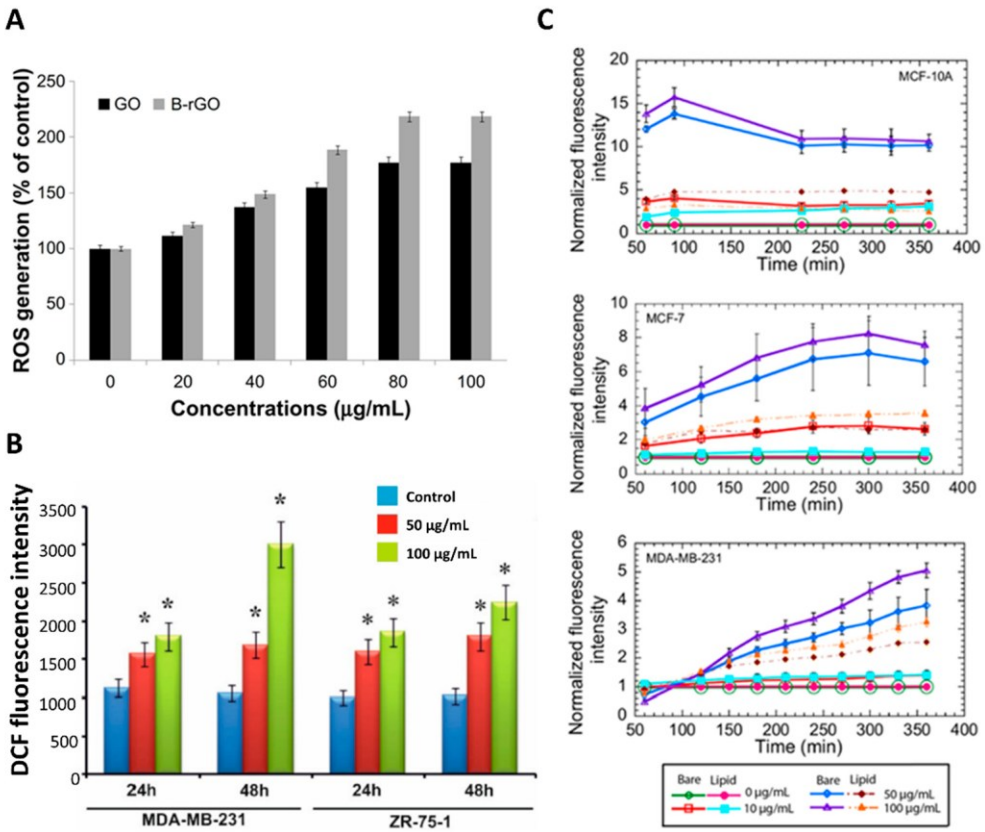

Figure 2.5. The effect of GO on the production of ROS in breast cancer cells. (A) Generation of ROS in MCF-7 cells induced by GO and bacteria-reduced GO (B-rGO) (treated groups showed statistically significant higher ROS production with respect to the control (*: $p < 0.05$)). The figure is adapted from [147], copyright 2013 Gurunathan et al., originally published by and used with permission from Dove Medical Press Ltd. (B) ROS production induced by rGO in MDA-MB-231 and ZR-75-1 cells with different concentrations of nanoparticles. The figure is adapted with open-access permission from [118], copyright 2021 Kretowski et al., publisher and licensee MDPI. (C) Oxidative stress caused by different concentrations of rGO and measured through DCFDA assay on MCF-7 and MDA-MB- 231 breast cancer cells and MCF-10A normal breast cells. Figures are reprinted and adapted with permission from [119], copyright 2020 American Chemical Society.

A decrease in the antioxidant GSH and a consequent increase in the ROS level have typically been observed following the administration of GO and rGO [121]. The increase in oxidative stress can cause lipid peroxidation, DNA and protein fragmentation, and mutation due to their oxidation [121]. This process can lead to the breakage, modification, or further cross-linking of the molecular chains. Cellular proteins and DNA can, therefore, undergo modification or even a complete loss of their biological activities [144].

Two possible explanations for ROS-induced cell death following GO internalization can be found in the literature [118,145,146]. The first signaling pathway that can be activated is due to the interaction of GO with the electron transport system that induces the overexpression of H2O2 and hydroxyl radicals, resulting in the oxidation of cardiolipin and its release into the cytoplasm of the hemoprotein contained in the mitochondria. This mechanism consequently induces the release of the cytochrome C complex, which stimulates the release of Ca2+ from the endoplasmic reticulum. This process in turn activates the caspase cascade, resulting in cell death [146]. The other possible mechanism involved may be the GO-driven induction of mitogen-activated protein kinase (MAPK) (i.e., JNK, ERK, p38) and transforming growth factor-beta (TGF-β) signaling pathways, resulting in the activation of Bcl-2 proteins. The latter could be directly responsible for the initiation of mitochondria-induced apoptosis [145].

Therefore, it may be possible to exploit GO-based nanocarriers to selectively induce an increase in oxidative stress at the oncological site to induce cancer cell death [119]. In several studies performed on breast cancer cells (i.e., MCF-7, MDA-MB-231 and 4T1 cells) [119,135,147,148], naked and functionalized GO have demonstrated the ability to induce cell death in such pathological cells by inducing the generation of ROS species. Farell et al. showed different trends of oxidative stress in two cancerous (i.e., MCF-7 and MDA-MB-231) and one non-cancerous (i.e., MCF-10A) cell line (Figure 2.5) [119] when exposed to naked and lipid-functionalized rGO carriers. However, the ROS levels recorded in all cell lines in response to naked rGO administration were remarkably high. This could indicate that non-functionalized rGO is not an adequate material for breast cancer treatment, as such high ROS concentrations could result in an increased risk of mutations of normal breast cells into tumor tissue. Even when tested in lower doses than GO, rGO was shown to induce the same or higher levels of cell death, depending on the time and dose of exposure to cells. This phenomenon can be related to the higher affinity of rGO to the cell membrane, which increases the hydrophobic interactions between them. In addition, some chemical agents used for GO reduction can generate

metallic impurities and organic contamination, causing alterations in the interaction with cells, leading to cell membrane damage and apoptosis.

2.3.1.5 GO Clearance from Cells and Biodegradation

As mentioned previously, the GO concentration is one of the parameters that plays a key role in regulating the toxicity of GO [90,118,119]. When a high dose of GO accumulates in cells, it causes their death more rapidly [114]. Therefore, a particularly important aspect to consider is the fate of GO flakes following the delivery of therapeutic agents. Most of the studies in the literature investigate the efficiency of GO in loading, transporting, and delivering payloads specifically into pathological cells, and few studies so far have focused on the disposal of such nanocarriers once they have accomplished their task. This aspect is critical to understand the efficiency of GO as a transporter for gene therapy. It must not exhibit toxicity on its way to the target site in its complete laboratory-prepared form, but it must also be completely disposable without causing toxicity once disassembled [123]. As explained in Section 2, it is usually decorated with other molecules, typically PEG or cationic polymers, to increase its stability and half-life within the bloodstream before being recognized by macrophages during the cargo delivery [34,86]. Once the payload is administered, the separation of the GO from the polymer chains may allow it to be more easily recognized by phagocytic cells and degraded.

The degradation of GO can be catalyzed by peroxidase enzymes, which are naturally occurring in plants and humans [149–151]. They are responsible for the oxidative biodegradation of graphene driven in living beings by the presence of reactive intermediates formed during their catalytic cycloadditions, such as plant horseradish peroxidase (HRP) [150], inflammatory human myeloperoxidase (hMPO) [149], and eosinophil peroxidase [151]. These reactive species can convert halides into strong oxidants (i.e., hypochlorous acid, HOCl) that can induce GO biodegradation [152]. HOCl produced by peroxidase from H2O2 could be a major cause of the biodegradation of carbon nanomaterials [149–151]. Several studies have confirmed that recombinant hMPO is able to degrade

single-layer and multi-layer GOs [153,154], and that the degradation products are non-toxic [155]. Through other studies, researchers have shown that graphene-based materials can be degraded by hMPO [153], recombinant eosinophil peroxidase [156], and HRP [153,157].

Macrophages activated by the presence of GO begin to secrete MPO, which converts H2O2 and chloride ions into HOCl. Notably, during this oxidative process, the epoxide groups of GO were transformed into carbonyl groups, causing C-C bond breakage and the fragmentation of GO into sp2 aromatic domains [158]. Therefore, macrophages can degrade GO flakes after their internalization [123]. As small GO fragments (i.e., a few tens of nm) have been shown to exhibit photoluminescence properties [159], these properties can be exploited to investigate the effective disassembly and degradation of GO-based nanocarriers [123]. In the study by Kim et al. [123], the photoluminescence of GO, both naked and functionalized with PEG and PEI, was measured after treatment with HRP and H2O2 to simulate the intracellular environment of macrophages. The intensity was increased, indicating that fragmentation of the GO had occurred. Moreover, even if it has been reported that the cell internalization of GO is size-dependent in different cell lines [52,53], different studies have proven that macrophages (i.e., PM8 and J774A.1) are not always affected by the size and dosage during GO uptake [117]. All of these findings may demonstrate the potential for naked graphene-based materials to be degraded within phagocytic cells after the payload delivery [69,123].

On the other hand, micro-sized GO flakes (i.e., lateral dimension < 1 μm) have been shown to be internalized more readily by mammalian cells through endocytic mechanisms (i.e., clathrin-dependent, caveolin-dependent, or clathrin- and caveolin-independent endocytosis; phagocytosis; micropinocytosis) compared to larger GO [24,34,160]. All of these mechanisms are due to the fact that once internalized, GOs were found to be accumulated and confined within intracellular vesicles (i.e., endosomes, lysosomes, phagosomes, and macropinosomes) [161]. Inside lysosomes, GO can be degraded through acid hydrolases, which include proteases, lipases, nucleases, glycosidases,

phosphatases, and sulfolipases [24,160]. Several studies have simulated the co-localization of GO flakes within lysosomes, even after payload release [54,117,160,162].

2.3.2 In Vivo Toxicity

In general, the *in vivo* fate of nanomaterials is influenced by several factors. In addition to the characteristics and parameters we have discussed in the previous section, there are also the routes of administration, the physiological environment that is tested, the interactions with the blood, the proteins and immune system of the host, and the presence of many different barriers [163].

The protein corona is one of the first factors to be addressed, which causes the rapid change of GO in the bloodstream [164]. This protein coating induces the size change of GO that substantially influences the interactions with the cells [34]. These interactions include internalization, biodegradation, biodistribution, and delivery to target sites. Although preliminary *in vitro* studies are essential to set the basic parameters and perform a first screening of the tested materials, *in vivo* studies are equally essential to fully understand the behavior of the designed systems in living organisms. In fact, results obtained *in vitro* are not always reproducible within a biological system, due to several peculiar responses that cannot be predicted or simulated, such as the inflammatory response, the biodistribution, and the clearance from the body.

2.3.2.1 Inflammatory Response

The body's non-specific immune defense relies on phagocytosis of foreign molecules via macrophages, providing a significant barrier to intravenous injections of GO nanocarriers. In addition, GO nanocarriers have a high probability of being removed by macrophages before reaching their destination and may initiate an inflammatory reaction [24,164]. In particular, when in the bloodstream, larger nanoparticles (>200 nm) have a higher risk of being recognized and sequestered

by the phagocytosing cells of the immune system (i.e., macrophages, dendritic cells, neutrophils, and B lymphocytes), which are responsible for recognizing the foreigner and destroying it via enzymatic digestion, as explained previously [31,44,53,123,137]. When macrophages are activated by invader molecules, they start to release cytokines and chemokines, resulting in the accumulation of neutrophils and monocytes. Like all foreign materials, GO could also cause the secretion of cytokines, such as IL-1α, IL-6, IL-10, and tumor necrosis factor-alpha (TNF-α), as well as chemokines, including monocyte chemoattractant protein-1 (MCP-1), macrophage inflammatory protein- 1α (MIP-1α), and MIP-1β. This leads to cell internalization and removal by macrophages via phagocytosis [165,166].

In the study by Yue et al. [117], GO flakes with lateral sizes of 2 μm and 350 nm were brought into contact with phagocytic and non-phagocytic cells and their responses were compared. The results showed that macrophages have a higher ability to internalize GOs than non-phagocytic cells. The motivation might lie in the fact that macrophages are able to overcome the strong electrostatic repulsions that are generated between the negatively charged surfaces of the GO and the cell membrane. This recognition may be mediated by the phagocytosis receptor Fcγ [117]. As previously mentioned, it has also been shown that GO flakes with lateral sizes from nanometers to microns can be similarly internalized by macrophages. However, GO (with micron size) activates stronger inflammatory responses, characterized by significant increases in cytokine levels (i.e., IL-6, IL-12, TNF-α, MCP-1, and IFN-γ) [117]. One possible explanation for this size-dependent phenomenon is the strong steric effects caused by larger GO when it encounters cells [117]. This result has also been proven in other studies, in which larger GO flakes have been revealed to induce increased cytokine and chemokine production and immune cell recall due to increased interaction with phagocytic cell membrane receptors, which induce the activation of the immune response via the NF-kB pathway. This mechanism was demonstrated to induce programmed cell death in MCF-7 breast cancer cells [167].

It can be concluded that GO flakes with lateral sizes at the nanoscale may induce a decreased inflammatory response, resulting in a more efficient solution to deliver therapeutic agents to the human body. For examples, some studies [168,169] have shown that GO recognition by macrophages could be kept under control by injecting GO flakes with a size smaller than about 150 nm. Another important aspect to avoid recognition by phagocytic cells is functionalization with hydrophilic molecules, which weaken the opsonin–protein interaction. Since the recognition and elimination of nanoparticles by phagocytes is mediated by opsonization (i.e., adsorption of immunoglobulins, serum proteins, and complement proteins on the surfaces of nanoparticles, causing the formation of the protein corona), the inhibition of opsonization is generally taken as a possible solution [170]. A highly utilized approach is PEGylation [171], or functionalization of the nanocarriers with target molecules. Hydrophilic PEG generates a shield through its extended molecules, inducing a repulsive barrier between the GO and circulating proteins, while targeting molecules increase the specificity and recognition potential of the NPs from the body [137]. However, making GO smaller than 200 nm in size would be preferred to limit their recognition by immune cells when administered intravenously and by the inflammatory response [17,44,123].

2.3.2.2 GO Biodistribution and Clearance from the Body

Another fundamental aspect to determine the effective toxicity of graphene-based nanomaterials is their biodistribution and excretion from the biological environment as assessed via *in vivo* measurements. Generally, GO was found to distribute in tissues and organs, inducing different response to cells cultured *in vitro*. In one study, PEG-enhanced functionalized monolayer carbon nanotubes were found to be non-toxic when injected *in vivo* into animal models (i.e., rats and rabbits), although the results showed some level of toxicity when used in *in vitro* models [163]. This result may indicate that the toxicity of a material could be concentration- and time-dependent, as analyzed in Section 3.1. In fact, for concentrations of nanomaterials localized in cultured cells, a certain toxicity

can be found, which on the contrary was not detected when carriers were injected into an organism where they were dynamically transported in the blood and continuously circulated in different tissues and organs [163].

However, it has been confirmed by several studies that GO injected intravenously tends to accumulate preferentially in some tissues and organs [166,172]. Through *in vivo* studies, it has been shown that most intravenously administered nanoparticles tend to accumulate in the liver and spleen [173,174]. Nevertheless, these studies also showed that toxicity was not observed, as predicted from the *in vitro* studies (Figure 2.6) [64,166]. More- over, only a small fraction of the total number of injected nanocarriers were demonstrated to accumulate at the target pathological site (i.e., approximately 1−10%) [172].

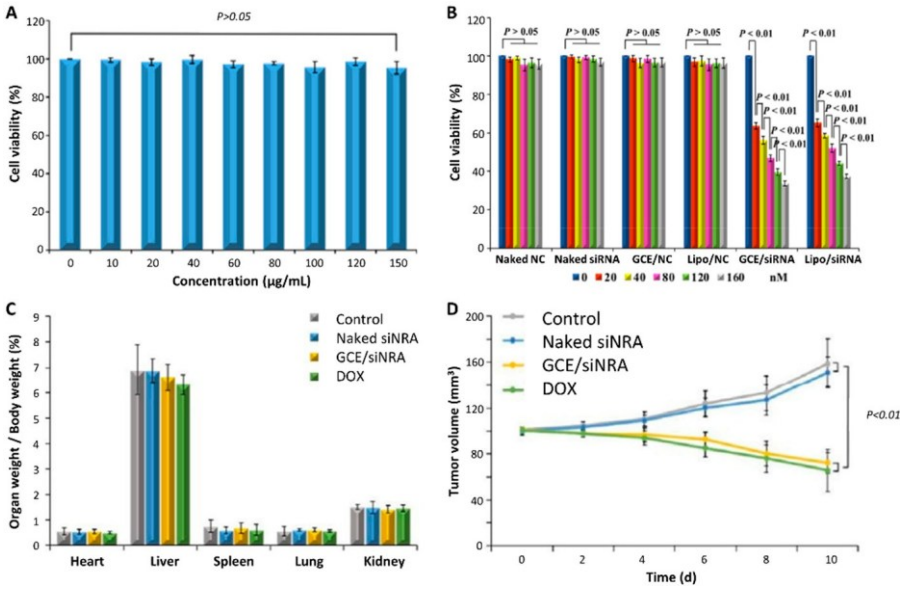

Figure 2.6. Cytotoxicity of GO and antiproliferation effect of GO-siRNA *in vitro* and *in vivo*. (A) Cyto- toxicity of GCE and (B) antiproliferation of GCE-siRNA on MCF-7 cells *in vitro*. (C) Cytotoxicity on normal tissues and (D) on breast cancer tumor of GCE-siRNA *in vivo*. Figures are reprinted with open access permission from [64], copyright 2021 Shenyang Pharmaceutical University, published by Elsevier.

The size plays an essential role in the journey of GO in *in vivo* tests. After the injection, the circulating GO nanoparticles start to diffuse through tissues and accumulate in organs. In the same report, Zhang

et al. [76] investigated the biodistribution of intravenously administered GO-based particles in mice, showing that GO usually accumulates preferentially in organs, such as the liver, spleen, lungs, and bone marrow. As explained in the previous section, biological barriers are present inside the body, which can limit the circulation of GO within the body. Sometimes it is also possible for GO to pass through them and accumulate in different compartments. One study illustrated that GO particles with a size of 54.9 ± 23.1 nm were unlikely to cross the blood–testicular and hemato-epidymal barriers after intra-abdominal injection. Interestingly, further tests showed that the sperm of mice analyzed after GO treatment was unaffected, even when administered at a high dose (i.e., 300 mg/kg) [175]. Other barriers such as placental and blood–brain barriers were also evaluated. In both cases, nanoscale GOs were able to pass through these membranes and diffuse into the compartment, affecting the fetus and the nervous system, respectively [176]. These observations highlight the need to control the characteristics of graphene-based particles in such a way that efficient targeting of the disease site will be achieved, with the aim of minimizing their interaction with healthy tissues as much as possible.

In general, when a non-degradable nanomaterial is too large to be filtered out of the body and then excreted through the kidneys, it accumulates in the tissues. The estimated time spent inside them is about 8 months [163]. GO-based nanomaterials are usually considered to be poorly degradable *in vivo*. Therefore, their functionalization by adding hydrophilic functional groups on the surface represents a possible strategy to optimize their biocompatibility and degradability *in vivo*. However, there are no prolonged studies (i.e., over 1 year) regarding the distribution and maintenance of GO within the body. This aspect raises the need for further *in vivo* analyses to better understand its toxicity over time. In addition to size, the surface functionalization of graphene flakes via biocompatible polymers also influences their biodistribution *in vivo*. For example, GO modified with FA or heparin could increase the ability of nanocarriers to target and penetrate 4T1 breast cancer cells *in vivo* by recognizing FA receptors or receptors for advanced glycation end products (RAGE), respectively [177].

In the study by Yang et al. [178], PEG modified GO-based nanoparticles with a monoclonal antibody modification were tested against follicle-stimulating hormone receptor (FSHR) to specifically target metastatic nodules of MDA-MB-231 breast cancer cells within the lungs. The metastatic tumor targeting the efficiency of GO conjugates was investigated in a mouse model. The obtained results showed that GO nanomaterials have excellent stability and high specificity for FSHR, which was demonstrated by the rapid tumor uptake of the GO conjugates. The accumulation of these GO-based materials was very low in healthy tissues, and their elimination from the bloodstream was much faster than that detected from tumor nodules. These results demonstrated the efficiency of such nanocarriers to specifically target the tumor site and accumulate in it (Figure 2.7A).

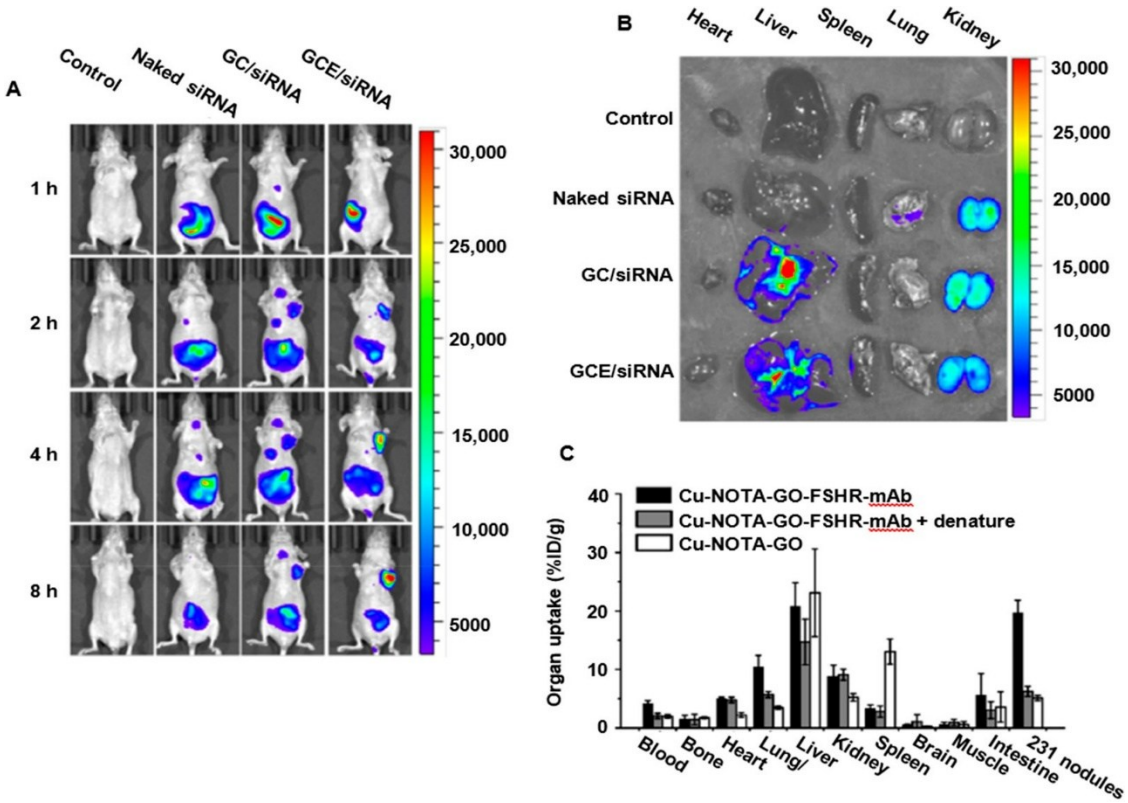

Figure 2.7. *In vivo* human breast cancer xenograft model in nude mice to observe the Survivin-siRNA biodistribution via fluorescence imaging. (A) Images taken at 1, 2, 4, and 8 h after injection of all formulations. (B) Fluorescent images obtained after dissection of the main organs from each formulation group. Figures in (A,B) are reprinted with open access permission from [64], copyright 2021 Shenyang Pharmaceutical University, published by Elsevier. (C) Biodistribution of Cu-labeled GO nanocarriers evaluated in *ex vivo* mice organs after 24 h of intravenous injection (NOTA: 2- S-(4-isothiocyanatobenzyl)-1,4,7-triazacyclononane-1,4,7-triacetic acid). Figures are reprinted with permission from [178], copyright 2016 Elsevier.

In the study by Chen et al. [64], GO was functionalized with chitosan (GC) and the Ep- CAM antibody (GCE) as a targeting agent for delivering Survivin-siRNA in MCF-7 *in vitro* and *in vivo*. The targeting effect of the antibody and the biodistribution *in vivo* were analyzed in nude mice, as a model of a human breast cancer xenograft. The test was conducted by injecting GO nanocarriers intravenously followed by *in vivo* fluorescence imaging after 1, 2, 4, and 8 h. The results showed that the fluorescence intensity of functionalized GO was higher than the control, demonstrating the specific targeting effect of the EpCAM antibody on MCF-7 cells. In addition, through the dissection of the main organs (i.e., heart, lungs, livers, kidneys, and spleen), it was observed that a higher accumulation occurred in kidney and liver (Figure 2.7B). Moreover, comparing the nanoparticles functionalized with the antibody (GCE/siRNA) and a non-targeted control (GC/siRNA), it was evidenced that the targeting agent was effective in increasing the accumulation potency of the nanocarriers (Figure 2.7C) [178].

Regarding the excretion of GO from an organism, there are several possible pathways, depending on the organ in which the particles are located. For example, the nanoparticles accumulated in the lungs have shown greater difficulty in being eliminated. Furthermore, they have often been shown to cause cellular infiltration, inflammation, and the onset of granulomas and pulmonary edema with greater ease [179]. In the liver, GO-based nanomaterials can be eliminated via the hepatobiliary pathway via the duodenal bile duct [172]. It was pointed out that GO was able to overcome these barriers and be excreted even with larger flakes. This is probably due to its ability to fold [180]. However, large GO particles (i.e., >200 nm) usually appear to accumulate via physical splenic filtration, as well as being prone to being cleared more rapidly from the circulation by macrophages [172], as explained in the GO biodegradation section. Conversely, small GOs, with dimensions under the cutoff for renal filtration (i.e., about 5 nm), can enter the renal tubules to be rapidly excreted without any toxicity via the urine [24]. Yang et al. [178] observed that when injected intravenously, a high fraction of GO particles was excreted through the hepatobiliary route, as the size of the nanomaterials was greater than 5 nm. Some studies have also observed that the urinary elimination of GO was size-independent

and influenced its excretion rate. In order to confirm this hypothesis, large GO flakes (1−35 μm) were tested and were excreted more slowly than small (30 nm–1.9 μm) and ultra-small (10−500 nm) GOs [181].

The elimination pathways of GO *in vivo* are not yet clear and defined. Nevertheless, the renal and fecal pathways appear to be the main pathways of excretion. However, the results published to date have shown conflicting results regarding the biodistribution and excretion of GO from organisms *in vivo* [172].

2.4 Controlled Release Strategies

The controlled release of drugs and genes from delivery nanocarriers is a mechanism that has been extensively studied in recent years. One of the main limitations to overcome is the non-specific treatment that results from the uncontrolled release of the payload inside the body during the circulation of the nanomaterials in the bloodstream [88]. The goal to be achieved is the specific accumulation of the nanoparticles in the tumor site and the release of the drug/gene only once internalized within the pathological cells [182]. This would allow an increase in treatment efficiency, as a high percentage of nanocarriers would transport the therapeutic agent directly to the oncological sites [123]. This mechanism would lead to a decrease in the dose of nanocarriers necessary to administer, with consequent advantages of low toxicity and limited side effects [53,168].

Several approaches have been devised to achieve payload release in a controlled manner. Some of these mechanisms exploit factors intrinsic to the human body, such as changes in pH [65,95,162], temperature [183,184], or the presence of reducing [123,185,186] or enzyme-rich [186] environments. Other mechanisms can instead be induced externally to guide and control the behavior of the injected nanoparticles once the target site is reached. Some examples of these extrinsic mechanisms are the administration of near-infrared radiation [53,123,136] to induce the photothermal

effect on the GO and the controlled injection of specific molecules able to compete with the payload for the bonds on the surface of GO [187,188]. Table 2.5 summarizes the primary mechanisms used to date to induce a controlled release of the therapeutic agent from graphene-based nanoparticles. Some studies have presented the use of these mechanisms individually, while others have also proposed the possibility of fabricating multimodal carriers capable of responding to several different triggers to maximize the transport and release efficiency.

Table 2.5. Release mechanisms of GO nanocarriers for gene delivery.

Release Trigger	Responsive Molecules	Responsive Functional Groups/Bonds	Mechanism
pH	GO + cationic molecules, pH-sensitive hydrogels	Amide [162], imine [189], hydrazone [190], ester [191], and oxime [192]	Protonation
Reducible intracellular environment	GO + molecules containing disulfide bonds	Disulfide bonds	Redox [123, 185, 193]
Enzymes	Phosphatase, collagenase, cathepsin	Peptide bonds	Degradation [186, 194]
NIR irradiation	GO	Aromatic C-C bonds	PDT and PTT [168, 195, 196]
Temperature treatment	Thermo-sensitive hydrogels	Hydrogen bonds between the polymer molecules and/or water	Phase-volume transition [197, 188]
Competitive molecules	GO + polyaromatic cationic molecules	Hydrophobic and electrostatic interactions between GO and the polyaromatic cationic molecules	Desorption of genes [187, 188]
	GO + cellular DNA	Hydrogen bonds between nitrogenous bases of the two DNA strands	Desorption of genes [187]

2.4.1 pH-Sensitive Platforms for Control Release

In Section 2.2, we described that GO has a unique surface structure due to its large number of hydrophilic and pH-sensitive groups, which confer a highly anionic charge given the negative surface charges deriving from their ionization. It is well known that the tumor environment has a higher acidity level, as tumor cells have a high rate of glycolysis and excrete lactic acid [91,199], lowering

the pH (pH = 5.7–7.8) compared to the physiological level (pH = 7.4) [162,182]. In addition, some intracellular compartments also exhibit an acidic surrounding, which can be exploited to release the payload only when the nanoparticles are internalized into the specific cancer cells. Late endosomes and lysosomes show pH values of around 4.5–5.5, in contrast to the pH of the cytosol, which is about 7 [199]. This pH gradient is an excellent trigger that can be used to stabilize the payload at physiological pH and to perform the selective release when the nanocarriers are tuned to a pH environment below a certain trigger threshold [97].

Many experiments have been carried out by exploiting GO and pH for smart drug delivery. The efficient loading of various anticancer drugs onto GOs via π-π stacking and hydrophobic interactions and their pH-controlled release has been widely demonstrated (Table 2.6). Many studies have assessed the efficiency of this mechanism when hydrophobic

drugs are to be delivered in hydrophilic body fluids [88]. Under basic pH conditions, such drugs are usually deprotonated and can be readily loaded onto GO flakes, which are also hydrophobic under the same neutral pH conditions. Conversely, in an acidic environment, such drugs protonate and become more hydrophilic and more soluble in water and less attracted to GO, facilitating their release from the nanoparticle surface [88,200]. DOX is one of the most widely used drugs that has been used to treat several types of cancer, particularly against breast cancer [18]. At low pH, it becomes more hydrophilic due to the protonation of the daunosamine group, which weakens the hydrophobic π-π stacking interaction, causing the release from GO-based nanoparticles [88].

To stabilize genes on GO, pH-sensitive bonds can be a way to exploit this trigger in gene therapy. Such pH-cleavable covalent bonds can be formed between the cationic molecules and the GO, thanks to its large surface rich in reactive functional groups. Once it reaches the tumor or intracellular site, the bond is broken, leading to the disassembly of the nanoparticles and the release of the gene. Some of the most important pH-cleavable bonds are shown in Figure 2.8, which were used in the production of nanocarriers for the transport of pH-sensitive genes [97]. The amide bond, formed between the

amine group (−NH2) of cationic molecules and the carboxylic group (−COOH) of GO, is the most widely used acid-sensitive linker in GO-based systems for the delivery of genes against tumors [17,64,98].

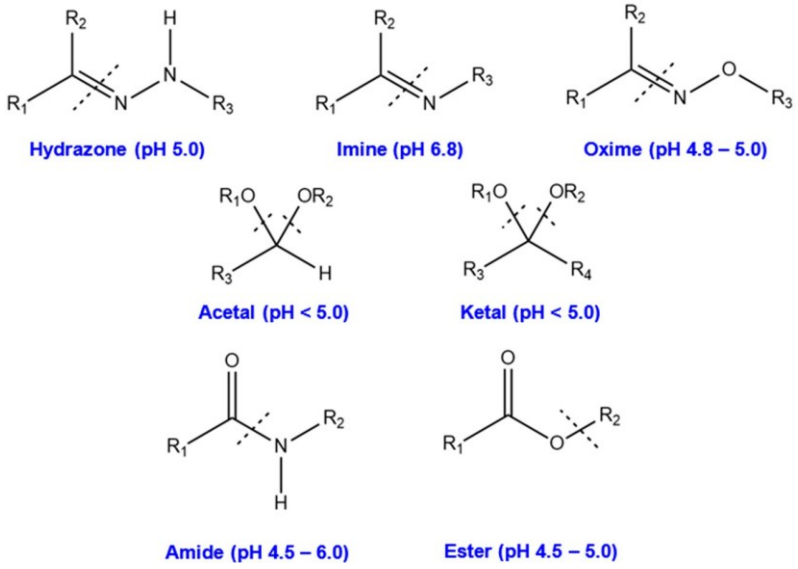

Figure 2.8. Acid-sensitive cleavable linkers used in designing smart nanoparticles [97,192]. Figures are reprinted with permission from Elsevier.

Chen et al. [64] and Xu et al. [162] explained the functionalization of GO with chitosan through amide bonds and found that the release efficiency of siRNA is significantly higher at acidic pH (5.0) compared to physiological pH (7.4) in breast cancer cells. However, the majority of studies in the literature have reported a low gene release efficiency when using chitosan. This could attribute to the further protonation of chitosan, which may increase the positive charge of the GO-based carriers, which would increase the electrostatic binding force to the transported genes [201]. In these studies, it has been shown that the pH response was given by the pH-sensitive molecule attached to GO instead of by GO itself. Hence, when the nanocarrier disassembles in acidic pH, the efficient delivery of the therapeutic agent is due to the ability of the functional molecules to release genes. Izadi et al. [65] functionalized carboxylate GO with chitosan and hyaluronic acid to transport HIF-1α-siRNA (i.e., Hypoxia Inducible Factor-1) and Dinaciclib. The aim was to silence HIF-1α, a factor that influences the spread of the tumor by regulating the expression of genes involved in cellular growth and in the blockade of cyclin-dependent kinases (CDKs) in CD44-expressing cells, including 4T1 breast cancer

cells. The results showed a non-significant difference in the gene release in neutral and acidic pH values. Similar observations were made in other studies on different cells lines [182,201], demonstrating the presence of contradiction in the efficiency of chitosan in its pH-sensitive functionalization for gene delivery. Similar conclusions were observed by Yadav et al. [17], who decorated GO flakes with PEG and the cationic dendrimer PAMAM to deliver siRNA in MDA-MB-231 cells. The release efficiency of the nanocarrier was assessed after 72 h of incubation at pH 6.5, 7.0, 7.5, and 8.0, obtaining results of 11.8, 38.9, 60.9, and 38.4%, respectively. Therefore, it was seen that at pH 7.5–8, the percentage of primary amines was lower, while at pH = 6–7, the quantity of ammonium ions increased, generating a higher net positive charge of the dendrimer. This phenomenon led to a more strongly complexed oligonucleotide due to the greater electrostatic interactions that were formed. This resulted in a slower release rate, which can interfere with the processing of genes within the cell and their transcription [201].

Table 2.6. The pH-sensitive platforms using GO nanocarriers for drug and gene delivery in breast cancer cells.

pH	Efficiency	GO Functionalization	Drug/Gene	Time	Cell Type
<7	20%	GO-PAMAM [87]	DOX	144	MCF-7
7.4	17%				
<7	40%	PPG-FA [a] [88]	DOX	48	MCF-7/ADR
7.4	10%				
<7	60%	CS-g-PMAA/GO [b] [202]	DOX	220	MCF-7
7.4	25%				
<7	71%	GO [200]	DOX	30	-
7.4	11%				
<7	95%	FA-rGO/ZnS:Mn [c] [203]	DOX	70	MDA-MB-231
7.4	150%				
<7	28%	GO-Gel-BSA [186]	DOX	-	MCF-7
7.4	10%				
<7	58%	CGO-TMC-HA[d] [64]	Dinaciclib	36	4T1
7.4	50%				
<7	90%	Chitosan [64]	Survivin_siRNA	200	MCF-7
7.4	30%				
<7	80%	Chitosan-HA [64]	HIF-1α_siRNA and Dinaciclib	32	4T1, CT26, B16-F10, TM3
7.4	70%				
<7	12%	PAMAM [17]	siRNA	72	MDA-MB-231
7.4	61%				

[a] FA-conjugated high molecular weight branched polyethyleneimine modified PEGylated nanographene; [b] chitosan-graft-poly(methacrylic acid); [c] chemically reduced graphene oxide combined with manganese-doped zinc sulfide quantum dots and functionalized with folic acid; [d] carboxylate graphene oxide (CGO) conjugated with trimethyl chitosan (TMC) and hyaluronate (HA) nanoparticles.

It can be noted that in the literature, there are some contradictions about the efficiency of the pH-stimulated gene release using cationic molecules as an intermediate for the functionalization between GO and nucleotides (Table 2.6). Further studies may be necessary to better understand this modification approach, as exploiting the pH gradients naturally presented in biological and tumor environments and the ability of the GO to respond to them could be a potentially advantageous approach.

2.4.2. Reducible Intracellular Environment

Tumor intracellular microenvironments are characterized by unique features compared to non-pathological tissues. In addition to their higher acidity, cancer cells also present a highly reducing environment due to their high intracellular concentration of glutathione [204]. GSH is the most abundant antioxidant in the cells, playing a major role in regulating intracellular oxidative stress by buffering ROS, as explained in the previous section [118]. It is synthesized from the amino acids glutamate, cysteine, and glycine through the controlled action of intracellular enzymes. Nonetheless, it was observed that the expression of these enzymes that drive the production of the three GSH precursors was upregulated within cancer cells [205]. The level of GSH was higher in cancer cells than in normal cells (i.e., 10 μM and 10 mM, respectively) [206]. Therefore, the presence of GSH and its activity in terms of redox buffering had a strong influence on tumor development. Several studies showed the selective release of drug/gene within the tumor's intracellular environment by using GO-based nanocarriers. Indeed, it is known that the disulfide chemical bond (S-S) is sensitive to reducing environments. When molecules containing this bond are close to reducing species, they undergo cleavage [207]. On the other hand, GO offers a large surface area that is capable of assembling numerous molecules containing disulfide groups and that respond to the tumor environment for controlled payload release. We have not found specific studies in the literature that

have exploited this mechanism in graphene-based nanoparticles to transport genes in breast cancer cells. For example, one study [186] designed a GO nanocarrier functionalized with bovine serum albumin (BSA) in the presence of gelatin to transport DOX into MCF-7 cells and release it in a controlled manner via pH, redox, and enzymatic treatment mechanisms. To assess the redox sensitivity of such nanoparticles, the drug release triggered by the presence of 10 mM GSH was evaluated and compared to the release obtained in its absence. Each BSA molecule has 17 disulfide bond pairs, which demonstrate high sensitivity to the intracellular tumor-reducing environment. Specifically, in the presence of GSH, DOX release was faster and 1.6-fold greater than in the absence of GSH, achieving the release of 44.3% of the total drug loaded.

In addition, Kim et al. [123] made GO nanocarriers decorated with PEG-NH2 and PEI via intermediate disulfide bonding using the cysteine molecule. Such a system was used to load and transport pDNA, as it can form electrostatic interactions with the positively charged amine groups of the polymer chains. The ability to release the gene via disulfide bond degradation once internalized into tumor cells was preliminarily verified by incubation in DTT (i.e., a small molecule antioxidant) in order to simulate the intracellular reducing environment [207]. The results showed that after treatment in DTT, the disulfide bonds between the polymer chains and GO were broken, resulting in the release of pDNA. As a control, nanoparticles of GO/PEG/PEI linked via amide bonds were also fabricated and incubated in DTT. No significant release of pDNA was observed in the systems.

Other studies in the literature have exploited this mechanism to control the payload release, but most of them have focused on drug transport [186,208] or have used different nanoparticles [207,209]. Nevertheless, there is evidence that once the GO is functionalized by molecules containing disulfide bonds, oligonucleotide chains can also be loaded onto such systems. Therefore, further studies could be conducted in this field to increase the efficiency of gene transfection in breast cancer treatment.

2.4.3 Enzyme-Induced Tumor Initiation

Earlier reports and findings support the theory that the enzymatic action of extracellular proteases, such as matrix metalloproteinases (MMPs), mediates various physiological processes and signaling pathways in the intra- and extracellular microenvironments during tumor progression [199]. By regulating various changes in the intracellular biochemical factors, these enzymes play a key role in tumor initiation and development. Therefore, the tumor microenvironment shows an overpressure of these enzymes with respect to physiological tissues [186]. For this reason, the creation of specific bonds that can be recognized by the metalloproteinases between the payload and the nanocarriers could be used to achieve an enzymatically controlled release in the tumor site. To our knowledge, there are no studies that exploit this mechanism for the transport of genes. However, several attempts can be found in the literature on GO-based nanocarriers for drug delivery.

Wu et al. [186] developed biodegradable multimodal carriers with a pH-, redox-, and enzyme-triggered drug release capacity, using GO modified with bovine serum albumin (approximately 5 nm) and gelatin (GGB) in MCF-7 breast cancer cells. The results showed that gelatin, being extremely sensitive to MMP-2, undergoes degradation, promoting DOX release and cleaving BSA-DOX complexes into small sizes. Thus, it increased the amount of drug released and enhanced its penetration efficiency within the tumor cells. As a result, after enzymatic pretreatment, the cumulative DOX released from GGBD nanoparticles reached 36.4%, which was 1.8-fold higher than the release obtained without enzyme treatment.

Other studies have evaluated the drug release and transport upon bond cleavage by enzymes [78,194,210], which was carried out on different cell lines. When it is not possible to attach the drug directly to GO, specific linkages can be formed using peptides or polysaccharide molecules. In this case, the release of the drug is due to the action of enzymes that can break the bond between two monomers of the linker instead of between the GO and the drug [210]. Trusek et al. [78] attached DOX on the surface of GO through the Gly-Gly-Leu tripeptide linker. The metalloendopeptidase

thermolysin enzyme catalyzes the hydrolysis of the peptide bond between Gly and Leu. Consequently, DOX is released with leucine attached to its NH2 group. The results also revealed that this molecular modification did not affect the therapeutic properties of DOX, while the release efficiency was satisfied. In another study of the same group [210], the same linker was exploited to attach amoxicillin to GO. A bromelain enzyme was added to the solution at concentrations of 0.04, 0.10, 0.20, and 0.40 mg/mL and the release efficiency measured was around 19% for the lower dose, 62% for the next dose, and reaching 90% within 24 h for the two higher doses.

Although drug delivery is highly dependent on the enzyme concentration achieved by hydrolysis of the specific links, high efficiency values can be achieved. Regarding the use of this approach for the controlled release of genes, the formation of permanent linkages between linkers and nucleotides could compromise the function of the gene itself. It could be further exploited as an intermediate link between GO and another molecule capable of interacting with the gene, or by encapsulating the nucleotide within biomaterials that undergo enzymatic degradation. The possibility of encapsulating RNA and DNA within the gelatin hydrogel has been attested [211,212]. Once internalized into cells, gelatin has been shown to undergo degradation in the endo-lysosomal complex, which contains many types of hydrolases (i.e., phosphatases, cathepsins), including collagenase, to which gelatin is highly sensitive [194]. The promising results obtained in studies on controlled drug delivery through the intervention of enzymes could be an encouragement to assess this possibility for the transport of genes.

2.4.4 Near IR Stimuli and Treatment

In recent years, GO has also attracted a lot of attention as a photothermal sensitizer nanomaterial. GO in fact holds great promise for its ability to convert absorbed light into localized heat through plasmon resonance, taking advantage of its wide absorption spectrum ranging from UV to NIR [195,213]. GO was explored in cancer phototherapies, mainly including photothermal therapy (PTT) and

photodynamic therapy (PDT), upon specific light irradiation on the cancer site. Table 2.7 reports some recent GO-based studies using NIR against breast cancer. These approaches are particularly advantageous because the specific targeting of cancer cells with high selectivity reduced the side-effects compared to the undesired treatment of healthy cells [168]. Zhang et al. [169] suggested that a significant increase in temperature was found to be proportional to the GO concentration and the applied irradiation. The maximum temperature was reached at approximately 48−50 ◦C. Such temperatures proved to be sufficient to generate a heat shock in the targeted cancer cells capable of blocking their rapid growth.

Table 2.7. Optical treatments for breast cancer using GO materials.

Trigger	NPs	Cell Type	Effect
439 nm laser (100 J/cm^2)	GO-Ag	MCF-7	ROS production [214]
NIR	GO-FA	MDA-MB-231	PTT [195]
	nGO-CuSQDs	MCF-7	Apoptosis [148]
	rGO-nZVI	MCF-7	PTT [215]
LED (660 nm)	GO-MB	MDA-MB-231	PDT [168]
	GQDs-MB	MCF-7	ROS production and apoptosis [213]

Moreover, it was also shown that the photothermal conversion of GO could increase its payload release efficiency, allowing a multimodal treatment of cancer cells using NIR radiation. Gadeval et al. [195] studied GO nanoparticles reduced and stabilized by quercetin and functionalized with FA as a therapy against triple-negative breast cancer (i.e., MDA- MB-231 cells). In addition to a PTT effect, the nanocarrier showed a pH-dependent and NIR- dependent quercitin release trend. At acidic pH (5.5), higher release values (35% in 48 h) were obtained than at physiological pH (7.4; 20% in 48 h), while after NIR irradiation, the release rates were significantly higher for both pH values (40% at pH 7.4 vs. 70% at pH 5.5).

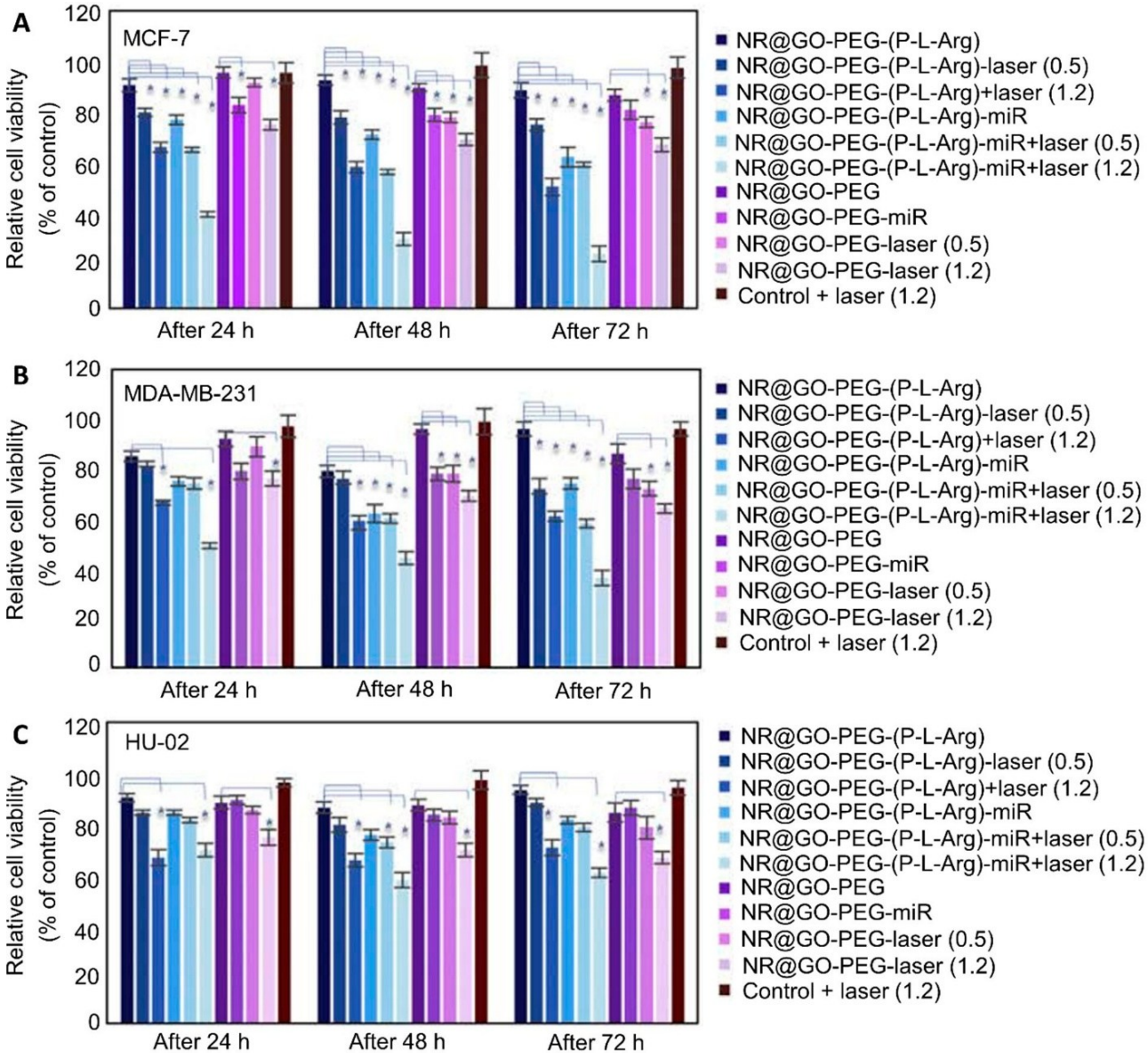

Figure 2.9. Cell viability of (A) HU-02 primary cell line and (B) MDA-MB-231 and (C) MCF-7 breast cancer cell lines. The results show the vitality of the cells treated with GO and GO-miRNA nanocarri- ers with respect to the control and exposed or not to laser irradiation (0.5 and 1.2 W/cm2) for 10 min, *: $p < 0.05$. The figures are reprinted with permission from Elsevier [62].

This phenomenon can be explained by the increased kinetic energy generated by the NIR laser irradiation. By increasing the kinetic energy, the vibrations of the atoms increase, which in turn induces an easier breakage of the π-π stacking between GO and quercitin, resulting in the release of the payload [195]. Comparable results were also obtained by Roy et al. [136], whereby rGO was functionalized by the modified poly(allylamine hydrochloride (MPAH) and FA. This nanocarrier

showed that the release of pDNA from the nanocomposites in the solution increased with NIR irradiation (35%) compared to without NIR irradiation (5%), as observed by the increased fluorescence intensities of the supernatants collected. The rGO can represent an interesting solution for the cellular transfection process due to its higher affinity for the cell membrane and higher cellular uptake. In addition, rGO has a higher conductivity that enhances its photothermal response upon light absorption in the NIR range. This characteristic could, therefore, be an advantage in terms of the endosome escape, controlled release of the therapeutic agent, and PTT and PDT treatments of cancer. Nevertheless, rGO is characterized by a lower density of functional groups on its surface, which can be detrimental from the point of view of the drug/gene loading efficiency, affecting the transfection results. Moreover, a higher toxicity of rGO was recorded compared to GO under the similar experimental conditions, which may limit its application in further transfection steps.

As previously mentioned in Section 2.2, Assali et al. [62] studied a multimodal GO-based nanoparticle functionalized with gold nanorods, PEG as a stabilizer, and PLA as a targeting agent to treat breast cancer cells (i.e., MCF-7, MDA-MB-231 and HU-02) with miRNA-101 and NIR thermal therapy. NIR radiation was used to induce a photothermal effect combined with an enhanced gene release in cancerous breast cells. The results showed low breast cancer cell viability (<20% in 72 h, Figure 2.9) when performing NIR radiation with or without miRNA. In addition, the NIR laser showed no toxicity on normal cells.

Zeng et al. [88] exploited GO's responsiveness to NIR radiation to develop a nanocarrier system for the joint delivery of genes and drugs to solve the big challenge of the drug resistance for breast anticancer treatment. The system was composed of an FA-conjugated, PEI-modified PEGylated graphene (PPG-FA/siRNA/Dox) for the dual delivery of DOX and siRNA. The heat generated by the PPG-FA was analyzed to confirm the actual ability of the system to convert light energy into thermal energy. The results confirmed that the temperature increased over time to a maximum of about 43 ◦C after 10 min for NGO concentrations of 15 µg/mL. Therefore, despite the numerous functionalization

strategies, the high NIR absorbance of the GO allowed the support of a remarkable photothermal ability. Furthermore, the release of DOX was studied at two different pH levels (7.4 and 5.0), with and without NIR radiation.

As previously demonstrated by Gadeval et al. [195], the lowest release rate was recorded at physiological pH and without radiation (about 20% in 48 h). In the presence of acidic pH or NIR, the release values increased, reaching a maximum with the combination of these two stimuli (about 60% in 48 h). Finally, the presence of siRNA confirmed the ability to efficiently transport the gene, as the drug resistance effect was significantly decreased compared to the DOX-only control.

2.4.5 Heat Treatment

In addition to the high acidity and imbalance in the levels of proteins and intracellular enzymes, the tumor environment was reported to present a higher temperature of about 2−5 ◦C more than the physiological temperature [206]. This characteristic represents another stimulus that can be exploited to engineer nanoparticles for the controlled release of drugs and genes in the pathological site.

GO has exhibited high thermal conductivity (i.e., about 5300 W/mK at room temperature) [184]. Other materials known for their sensitivity to temperature changes are thermo-responsive polymers, such as poly(N-isopropylacrylamide) (PNIPAM), with a phase transition temperature of around 32 ◦C [197]. It can be combined with natural polymers, such as chitosan or HA, to form smart hydrogels with a similar transition temperature [198]. When these polymers were linked to GO, the volume phase transition temperature (VPTT) of the polymers decreased due to the high heat conductivity of GO. For instance, the PVA/PNIPAM hydrogel normally exhibits a VPTT of around 35 ◦C, but when combined with GO, this temperature decreases to 34 ◦C [184]. In this case, the hydro- gel exhibited an excellent temperature response due to the increased sensitivity caused by the rapid thermal conduction of the GO. Another plausible reason is that the presence of GO induces the formation of a denser hydrogel network, leading to low adsorption of water. As a result, the material would have

a lower swelling ratio and a higher volume change in response to temperature variations [184]. Most of the published efforts were focused on building smart hydrogels to realize a nanoscale system that can tune their properties once they reach the tumor to release the payload.

Wang et al. [183] prepared a thermo-sensitive delivery system by functionalizing the 2D GO flakes with PNIPAM-polyehylene oxide (PEO) through 1-pyrenebutyric acid N-hydroxysuccinimide ester. The GO complex was previously loaded with Adriamycin, an aromatic drug used for treating tumors. Polymer chains form hydrogen bonds with water when the temperature is above the specific critical solution temperature (LCST). Once the temperature is lower than the LCST, the hydrogen bonds break and the material shrinks, releasing the drug from the GO-based carriers [197].

Although there are few studies using this approach for gene transport, we found that GO-based hydrogels were exploited for drug/gene delivery. With an LCST lower than body temperature, such temperature-sensitive smart hydrogels were used to make a gel containing GO flakes. During the preparation at room temperature, they were kept in liquid form and could be injected in a mini-invasive way in the tumor site. At 37 ◦C, the hydrogel tended to go through gelation, supporting the accumulation of GO carriers in the target site and their sustained release over time in accordance with the degradation time of the hydrogel [216]. Fong et al. [198] fabricated a GO nanoparticle decorated with FA to load and deliver DOX to MCF-7 breast cancer cells. Subsequently, these nanocarriers were loaded into a thermo-sensitive hydrogel made of hyaluronic acid–chitosan-g–PNIPAM that presented an LCST range of around 30−32 ◦C. This material allowed the injection and accumulation of nanoparticles into the tumor site due to the in situ formation of the hydrogel in response to the higher temperature, supporting their release concomitant with its degradation. A similar approach was explored for the gene delivery [216].

2.4.6 Competitive Molecules

Another approach for GO-based gene delivery in targeting breast cancer cells is through a mechanism of competition between the oligonucleotide and other molecules. Inside cells, the given specific molecules that have high affinity towards GO tend to bind together to reach a more stable form. As a result, the payload associated with GO could be "replaced" with these molecules on the graphene surface. This approach would form GO nanocarriers without additional functionalization, leading to a limited fabrication step, which may increase the reproducibility and make them non-toxic [117]. The use of molecules that compete for the binding to the GO surface may be a solution to induce the release of genes from graphene flakes. These molecules include small polyaromatic molecules, such as methylene blue (MeB) and rhodamine 6G (R6G). They possess extended aromatic systems that allow the formation of π-π stacking interactions with graphene, similar to that of DNA [187,188]. Therefore, they have the potential to competitively desorb DNA molecules bound on the GO surface. Another possibility could be to exploit the cellular DNA. A single-stranded DNA molecule loaded on the GO could be influenced by its higher affinity with the DNA in the cell, which would then compete with the GO for binding of the strand complementary to itself [187]. These approaches are schematically illustrated in Figure 2.10.

These mechanisms have been tested by Chen and Zhang [187], who loaded oligonucleotides and ss-DNA onto SWNTs. Binding occurred through a mechanism of wrapping DNA around the nanotubes, as DNA possesses a negatively charged chain due to sugar-phosphate bonds, which can impart a large degree of hydrophilicity to the SWNTs by preventing them from aggregating in aqueous solutions. Furthermore, such binding was facilitated by the tendency of the four nitrogenous bases of DNA to form attractive π-π stacking interactions due to their extended π structures. MeB and R6G were used as competitive molecules and compared with creatinine and fluorescein to understand the key feature of achieving efficient competition with GO. Interestingly, amino and amino groups on creatinine are similar to those found in R6G and MeB, which are positively charged. However, creatinine does not

have an extended aromatic structure, whereas fluorescein has the opposite characteristics. The results showed that the extended aromatic structure was a key feature, with the positive charges facilitating the process. In this study, the results obtained through gel electrophoresis confirmed the formation of the double-stranded DNA (dsDNA) from the ssDNA loaded on the GO. In this case, the driving force for the release of the oligonucleotide from the nanocarrier was probably the affinity between the strands. The possibility of creating hydrogen bonds with the complementary nitrogenous bases was also thermodynamically favored with respect to the π-π stacking interactions with graphene.

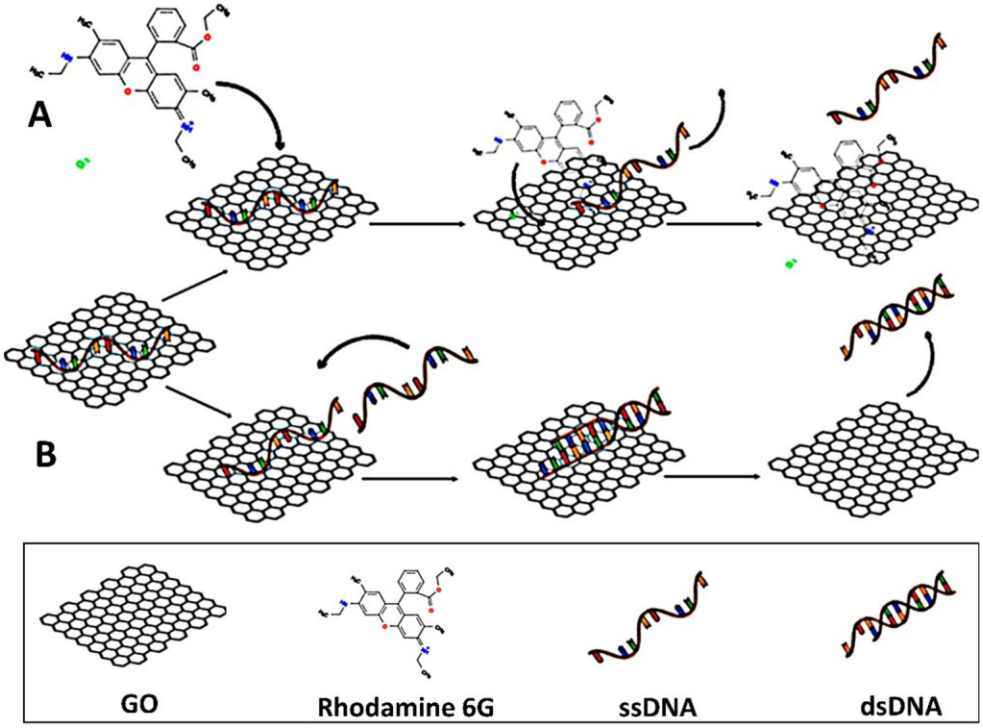

Figure 2.10. Schematic representation of the gene release from GO through the association of (A) competitive molecules (rhodamine 6G is reported as an example) and (B) ssDNA.

The same approach was also evaluated by Hsieh et al. [188], in which the dye R6G was used to visualize and induced DNA release from GO nanocarriers. In addition to competing for bonds on GO, rhodamine is pH-sensitive and protonated under acidic conditions, emitting fluorescence at around 588 nm. Therefore, R6G was used to stimulate the controlled release of the dT30 gene when GO nanocarriers were internalized into RAW 264.7 cells. Simultaneously, the binding formed between

rhodamine and the graphene surface led to the quenching of R6G's fluorescence by GO, which was used to visually confirm the actual internalization of graphene nanoparticles and their gene release within the cell.

In addition, directly linking genes to the GO surface was explored using non-covalent bonds. Although some difficulties related to this mechanism can be found in the literature [160], several studies have demonstrated the possibility of achieving such direct binding [160,187,188]. On the other hand, it was pointed out that once the gene was linked on GO, it showed almost no tendency to separate from the graphene surface, demonstrating stable binding but discouraging its application for gene therapy [160]. Therefore, in the case of loading genes on GO through π-π stacking interactions, applying an external driving force for the release can be beneficial.

The possibility of using an external molecule could represent a potential approach. Nevertheless, there are no recent studies in this field, probably due to the difficulties encountered in the procedure of loading and releasing genes in the absence of further functionalization [160]. Either way, the results obtained in these studies seem promising, although it would be necessary to extend these studies to highlight the release efficiency on tumor cell lines to understand the true potential of this mechanism.

2.5 Challenges and Perspectives

Graphene-oxide-based nanocarriers have shown great potential in gene transfection and could be used in breast cancer treatments by overcoming the limitations and side effects of chemotherapy. This carbon-based material allows a facile surface modification to enhance its biological application and gene delivery efficiency. Although GO is controllable in terms of its lateral size, achieving a narrow size distribution with cost-effective and less time-consuming approaches remains a challenge. As-synthesized GO flakes without size control (ranging from microns to nanoscale) highlight the importance of reaching a uniform size of GO flakes for drug/gene delivery purposes to facilitate

passing through the barriers. Polymer–cationic agent modifications have been widely exploited to create GO carrier formulations. Nevertheless, the possibility of enhancing the biocompatibility and stability in the absence of cationic agents is yet to be investigated. In most studies, nucleic acids were primarily loaded on a polymer, dendrimer, or peptide-modified GO, while fewer studies have focused on non-covalent interactions between genes and GO. In addition, studies have widely shown the successful delivery and release of siRNAs and miRNAs with the purpose of gene silencing through binding these genes to mRNA, while fewer studies have reported on the delivery of plasmids that can internalize nuclei of the cell, causing specific gene expression in breast cancer cells.

Since versatile factors affect the journey of GO-based carriers in the body, it is crucial to reach a comprehensive understanding of GO's characteristics. Despite the contradictions regarding the toxicity of GO in the literature, it should be noted that the function and toxic effect of GO in biological applications are profoundly affected by the synthesis route, purification, post-processing, size distribution, shape, functionalization, charge, dose, and time of exposure to biological compartments. The production of GO is one key aspect impacting its performance. Although modifying the synthesis conditions can increase the production yield, post-processing approaches play a complementary role in achieving a stable, consistent, and reproducible material. The methods, including exfoliation, purification, and size separation, can be further improved to be less time-consuming than conventional methods (e.g., ultrasonication, centrifugation, and filtration), as reported in the literature. In other words, by modifying the post-synthesis methods, not only can a uniform material be obtained, but also a larger quantity of GO can be processed efficiently, which at the same time will have consistent features. It is also noteworthy that although successful *in vitro* and *in vivo* results regarding gene transfection using GO-based carriers have been reported, the lack of consensus in the research findings raises the need to better understand the characteristics of this material prior to clinical investigation.

In addition, the capability of GO to respond to various stimuli, including pH, the reducible intracellular environment, enzymes, NIR irradiation, and the presence of competitive molecules, allows the engineering of smart drug/gene carriers with controlled release for cancer therapy. Several studies can be found in the literature regarding the exploitation of pH and NIR radiation for the controlled release of genes from GO carriers for breast cancer treatment. Other stimuli such as redox, enzyme, and heat treatments, however, have not been fully assessed for this application so far, although several examples were exploited for drug release.

Moreover, some of these stimuli, such as pH and temperature, do not directly act on the GO but rather on moieties that can be efficiently loaded on it. This may have led to the contradictory findings in the literature, as the efficiency of cargo release would unlikely depend on the GO but rather on the functional molecules used. Therefore, it is clear that additional challenges have to be overcome to achieve an adequate gene delivery system, such as accomplishing the efficient loading of oligonucleotides onto the GO and their controlled release into the right cellular compartment. This applies especially to the transport of DNA segments. In the case of efficient transfection, GO must be able to penetrate inside the cell nucleus to release the gene onsite. For this purpose, these approaches could represent potential mechanisms to increase the transfection efficiency in target cancer cells.

References

(1) Singh, S.K.; Singh, S.; Lillard, J.W., Jr.; Singh, R. Drug delivery approaches for breast cancer. *Int. J. Nanomed.* **2017**, *12*, 6205–6218.
(2) Wu, D.; Si, M.; Xue, H.Y.; Wong, H.L. Nanomedicine applications in the treatment of breast cancer: Current state of the art. *Int. J. Nanomed.* **2017**, *12*, 5879–5892.
(3) Xue, H.-Y.; Bendayan, R.; Wong, H.-L. Chapter 5—MDR reversal for effective chemotherapy in breast cancer. In *Drug Efflux Pumps in Cancer Resistance Pathways: From Molecular Recognition and Characterization to Possible Inhibition Strategies in Chemotherapy*; Sosnik, A., Bendayan, R., Eds.; Academic Press: Cambridge, MA, USA, 2020; Volume 7, pp. 121–147.
(4) Herdiana, Y.; Wathoni, N.; Shamsuddin, S.; Joni, I.M.; Muchtaridi, M. Chitosan-Based Nanoparticles of Targeted Drug Delivery System in Breast Cancer Treatment. *Polymers* **2021**, *13*, 1717.
(5) Luo, L.; Xu, F.; Peng, H.; Luo, Y.; Tian, X.; Battaglia, G.; Zhang, H.; Gong, Q.; Gu, Z.; Luo, K. Stimuli-responsive polymeric prodrug-based nanomedicine delivering nifuroxazide and doxorubicin against primary breast cancer and pulmonary metastasis. *J. Control. Release* **2020**, *318*, 124–135.
(6) Tahir, N.; Madni, A.; Correia, A.; Rehman, M.; Balasubramanian, V.; Khan, M.M.; Santos, H.A. Lipid-polymer hybrid nanoparticles for controlled delivery of hydrophilic and lipophilic doxorubicin for breast cancer therapy. *Int. J. Nanomed.* **2019**, *14*, 4961–4974.
(7) Xiong, H.; Liu, S.; Wei, T.; Cheng, Q.; Siegwart, D.J. Theranostic dendrimer-based lipid nanoparticles containing PEGylated BODIPY dyes for tumor imaging and systemic mRNA delivery in vivo. *J. Control. Release* **2020**, *325*, 198–205.Zhang, X.; Pan, J.; Yao, M.; Palmerston Mendes, L.; Sarisozen, C.; Mao, S.; Torchilin, V.P. Charge reversible hyaluronic acid- modified dendrimer-based nanoparticles for siMDR-1 and doxorubicin co-delivery. *Eur. J. Pharm. Biopharm.* **2020**, *154*, 43–49.
(8) Kong, T.; Hao, L.; Wei, Y.; Cai, X.; Zhu, B. Doxorubicin conjugated carbon dots as a drug delivery system for human breast cancer therapy. *Cell Prolif.* **2018**, *51*, e12488.
(9) Pardo, J.; Peng, Z.; Leblanc, R.M. Cancer Targeting and Drug Delivery Using Carbon-Based Quantum Dots and Nanotubes. *Molecules* **2018**, *23*, 378.
(10) Kim, D.; Hwang, J.; Choi, Y.; Kwon, Y.; Jang, J.; Yoon, S.; Choi, J. Effective Delivery of Anti-Cancer Drug Molecules with Shape Transforming Liquid Metal Particles. *Cancers* **2019**, *11*, 1666.
(11) Lei, J.; Wang, H.; Zhu, D.; Wan, Y.; Yin, L. Combined effects of avasimibe immunotherapy, doxorubicin chemotherapy, and metal-organic frameworks nanoparticles on breast cancer. *J. Cell Physiol.* **2020**, *235*, 4814–4823.
(12) Ahmadzada, T.; Reid, G.; McKenzie, D.R. Fundamentals of siRNA and miRNA therapeutics and a review of targeted nanoparticle delivery systems in breast cancer. *Biophys. Rev.* **2018**, *10*, 69–86.
(13) Cheang, T.Y.; Lei, Y.Y.; Zhang, Z.Q.; Zhou, H.Y.; Ye, R.Y.; Lin, Y.; Wang, S. Graphene oxide-hydroxyapatite nanocomposites effectively deliver HSV-TK suicide gene to inhibit human breast cancer growth. *J. Biomater. Appl.* **2018**, *33*, 216–226.
(14) Crommelin, D.J.A.; Hennink, W.E.; Storm, G. Chapter 5: Drug Targeting Systems: Fundamentals and Applications to Parenteral Drug Delivery. In *Drug Delivery and Targeting: For Pharmacists and Pharmaceutical Scientists*, 1st ed.; Hillery, A.M., Lloyd, A.W., Swarbrick, J., Eds.; Taylor & Francis Publishing: New York, NY, USA, 2001; pp. 105–130.
(15) Wu, C.; Tian, Y.; Zhang, Y.; Xu, J.; Wang, Y.; Guan, X.; Li, T.; Yang, H.; Li, S.; Qin, X.; et al. Acid-Triggered Charge-Convertible Graphene-Based All-in-One Nanocomplex for Enhanced Genetic Phototherapy of Triple-Negative Breast Cancer. *Adv. Healthc. Mater.* **2020**, *9*, e1901187.
(16) Yadav, N.; Kumar, N.; Prasad, P.; Shirbhate, S.; Sehrawat, S.; Lochab, B. Stable Dispersions of Covalently Tethered Polymer Improved Graphene Oxide Nanoconjugates as an Effective Vector for siRNA Delivery. *ACS Appl. Mater. Interfaces* **2018**, *10*, 14577–14593.
(17) Ma, K.; Li, W.; Zhu, G.; Chi, H.; Yin, Y.; Li, Y.; Zong, Y.; Guo, Z.; Wang, L.; Xu, W.; et al. PEGylated DOX-coated nano graphene oxide as pH-responsive multifunctional nanocarrier for targeted drug delivery. *J. Drug Target.* **2021**, *29*, 884–891.
(18) Bandopadhyay, S.; Manchanda, S.; Chandra, A.; Ali, J.; Deb, P.K. Chapter 5—Overview of different carrier systems for advanced drug delivery. In *Drug Delivery Systems*; Tekade, R.K., Ed.; Academic Press: Cambridge, MA, USA, 2020; pp. 179–233.
(19) Mendes, R.G.; Bachmatiuk, A.; Büchner, B.; Cuniberti, G.; Rümmeli, M.H. Carbon nanostructures as multi-functional drug delivery platforms. *J. Mater. Chem. B* **2013**, *1*, 401–428.

(20) McCallion, C.; Burthem, J.; Rees-Unwin, K.; Golovanov, A.; Pluen, A. Graphene in therapeutics delivery: Problems, solutions and future opportunities. *Eur. J. Pharm. Biopharm.* **2016**, *104*, 235–250.
(21) Shariare, M.H.; Masum, A.A.; Alshehri, S.; Alanazi, F.K.; Uddin, J.; Kazi, M. Preparation and Optimization of PEGylated Nano Graphene Oxide-Based Delivery System for Drugs with Different Molecular Structures Using Design of Experiment (DoE). *Molecules* **2021**, *26*, 1457.
(22) Zhang, S.; Wang, H.; Liu, J.; Bao, C. Measuring the specific surface area of monolayer graphene oxide in water. *Mater. Lett.* **2020**, *261*, 127098.
(23) Kiew, S.F.; Kiew, L.V.; Lee, H.B.; Imae, T.; Chung, L.Y. Assessing biocompatibility of graphene oxide-based nanocarriers: A review. *J. Control. Release* **2016**, *226*, 217–228.
(24) Zhang, Z.; Schniepp, H.C.; Adamson, D.H. Characterization of graphene oxide: Variations in reported approaches. *Carbon* **2019**, *154*, 510–521.
(25) Staudenmaier, L. Verfahren zur Darstellung der Graphitsäure. *Ber. Dtsch. Chem. Ges.* **1898**, *31*, 1481–1487.
(26) Hummers, W.S.; Offeman, R.E. Preparation of Graphitic Oxide. *J. Am. Chem. Soc.* **1958**, *80*, 1339.
(27) Marcano, D.C.; Kosynkin, D.V.; Berlin, J.M.; Sinitskii, A.; Sun, Z.; Slesarev, A.; Alemany, L.B.; Lu, W.; Tour, J.M. Improved synthesis of graphene oxide. *ACS Nano* **2010**, *4*, 4806–4814.
(28) Brodie, B.C. XIII. On the atomic weight of graphite. *Phil. Trans. R. Soc.* **1859**, *149*, 249–259.
(29) Shirvalilou, S.; Khoei, S.; Khoee, S.; Raoufi, N.J.; Karimi, M.R.; Shakeri-Zadeh, A. Development of a magnetic nano-graphene oxide carrier for improved glioma-targeted drug delivery and imaging: In vitro and in vivo evaluations. *Chem. Biol. Interact.* **2018**, *295*, 97–108.
(30) Mariadoss, A.V.A.; Saravanakumar, K.; Sathiyaseelan, A.; Wang, M.H. Preparation, characterization and anti-cancer activity of graphene oxide–silver nanocomposite. *J. Photochem. Photobiol. B* **2020**, *210*, 111984.
(31) Rawal, A.; Che Man, S.H.; Agarwal, V.; Yao, Y.; Thickett, S.C.; Zetterlund, P.B. Structural Complexity of Graphene Oxide: The Kirigami Model. *ACS Appl. Mater. Interfaces* **2021**, *13*, 18255–18263.
(32) Tufano, I.; Vecchione, R.; Netti, P.A. Methods to Scale Down Graphene Oxide Size and Size Implication in Anti-cancer Applications. *Front. Bioeng. Biotechnol.* **2020**, *8*, 613280.
(33) Donahue, N.D.; Acar, H.; Wilhelm, S. Concepts of nanoparticle cellular uptake, intracellular trafficking, and kinetics in nanomedicine. *Adv. Drug Deliv. Rev.* **2019**, *143*, 68–96.
(34) Tabish, T.A.; Narayan, R.J. Crossing the blood–brain barrier with graphene nanostructures. *Mater. Today* **2021**, *51*, 393–401.
(35) Kawaguchi, H.; Koiwai, N.; Ohtsuka, Y.; Miyamoto, M.; Sasakawa, S. Phagocytosis of latex particles by leucocytes. I. Dependence of phagocytosis on the size and surface potential of particles. *Biomaterials* **1986**, *7*, 61–66.
(36) Champion, J.A.; Walker, A.; Mitragotri, S. Role of particle size in phagocytosis of polymeric microspheres. *Pharm. Res.* **2008**, *25*, 1815–1821.
(37) Yue, H.; Wei, W.; Yue, Z.; Lv, P.; Wang, L.; Ma, G.; Su, Z. Particle size affects the cellular response in macrophages. *Eur. J. Pharm. Sci.* **2010**, *41*, 650–657.
(38) Zhi, F.; Dong, H.; Jia, X.; Guo, W.; Lu, H.; Yang, Y.; Ju, H.; Zhang, X.; Hu, Y. Functionalized graphene oxide mediated adriamycin delivery and miR-21 gene silencing to overcome tumor multidrug resistance in vitro. *PLoS ONE* **2013**, *8*, e60034.
(39) Hirano, A.; Kawanami, T.; Llena, J.F. Electron microscopy of the blood-brain barrier in disease. *Microsc. Res. Tech.* **1994**, *27*, 543–556.
(40) Ventola, C.L. Progress in Nanomedicine: Approved and Investigational Nanodrugs. *Pharm. Ther.* **2017**, *42*, 742–755.
(41) Hobbs, S.K.; Monsky, W.L.; Yuan, F.; Roberts, W.G.; Griffith, L.; Torchilin, V.P.; Jain, R.K. Regulation of transport pathways in tumor vessels: Role of tumor type and microenvironment. *Proc. Natl. Acad. Sci. USA* **1998**, *95*, 4607–4612.
(42) Engin, A.B.; Nikitovic, D.; Neagu, M.; Henrich-Noack, P.; Docea, A.O.; Shtilman, M.I.; Golokhvast, K.; Tsatsakis, A.M. Mechanistic understanding of nanoparticles' interactions with extracellular matrix: The cell and immune system. *Part. Fibre Toxicol.* **2017**, *14*, 22.
(43) Prokop, A.; Davidson, J.M. Nanovehicular intracellular delivery systems. *J. Pharm. Sci.* **2008**, *97*, 3518–3590.
(44) Singh, S.K.; Singh, M.K.; Nayak, M.K.; Kumari, S.; Grácio, J.J.A.; Dash, D. Size distribution analysis and physical/fluorescence characterization of graphene oxide sheets by flow cytometry. *Carbon* **2011**, *49*, 684–692.
(45) Chen, J.; Zhang, X.; Zheng, X.; Liu, C.; Cui, X.; Zheng, W. Size distribution-controlled preparation of graphene oxide nanosheets with different C/O ratios. *Mater. Chem. Phys.* **2013**, *139*, 8–11.
(46) Shao, G.; Lu, Y.; Wu, F.; Yang, C.; Zeng, F.; Wu, Q. Graphene oxide: The mechanisms of oxidation and exfoliation. *J. Mater. Sci.* **2012**, *47*, 4400–4409.
(47) Shearer, C.J.; Slattery, A.D.; Stapleton, A.J.; Shapter, J.G.; Gibson, C.T. Accurate thickness measurement of graphene. *Nanotechnol- ogy* **2016**, *27*, 125704.

(48) Qi, X.; Zhou, T.; Deng, S.; Zong, G.; Yao, X.; Fu, Q. Size-specified graphene oxide sheets: Ultrasonication assisted preparation and characterization. *J. Mater. Sci.* **2014**, *49*, 1785–1793.
(49) Sierra, U.; Álvarez, P.; Santamaría, R.; Granda, M.; Blanco, C.; Menéndez, R. A multi-step exfoliation approach to maintain the lateral size of graphene oxide sheets. *Carbon* **2014**, *80*, 830–832.
(50) Wang, X.; Sun, Q.; Cui, C.; Li, J.; Wang, Y. Anti-HER2 functionalized graphene oxide as survivin-siRNA delivery carrier inhibits breast carcinoma growth in vitro and in vivo. *Drug Des. Devel. Ther.* **2018**, *12*, 2841–2855.
(51) Di Santo, R.; Digiacomo, L.; Palchetti, S.; Palmieri, V.; Perini, G.; Pozzi, D.; Papi, M.; Caracciolo, G. Microfluidic manufacturing of surface-functionalized graphene oxide nanoflakes for gene delivery. *Nanoscale* **2019**, *11*, 2733–2741.
(52) Mirzaie, V.; Ansari, M.; Nematollahi-Mahani, S.N.; Moballegh Nasery, M.; Karimi, B.; Eslaminejad, T.; Pourshojaei, Y. Nano- Graphene Oxide-supported APTES-Spermine, as Gene Delivery System, for Transfection of pEGFP-p53 into Breast Cancer Cell Lines. *Drug Des. Devel. Ther.* **2020**, *14*, 3087–3097.
(53) Wang, Y.; Sun, G.; Gong, Y.; Zhang, Y.; Liang, X.; Yang, L. Functionalized Folate-Modified Graphene Oxide/PEI siRNA Nanocomplexes for Targeted Ovarian Cancer Gene Therapy. *Nanoscale Res. Lett.* **2020**, *15*, 57.
(54) Li, J.; Ge, X.; Cui, C.; Zhang, Y.; Wang, Y.; Wang, X.; Sun, Q. Preparation and Characterization of Functionalized Graphene Oxide Carrier for siRNA Delivery. *Int. J. Mol. Sci.* **2018**, *19*, 3202.
(55) Huang, J.; Zong, C.; Shen, H.; Liu, M.; Chen, B.; Ren, B.; Zhang, Z. Mechanism of Cellular Uptake of Graphene Oxide Studied by Surface-Enhanced Raman Spectroscopy. *Small* **2012**, *8*, 2577–2584.
(56) Nejabat, M.; Charbgoo, F.; Ramezani, M. Graphene as multifunctional delivery platform in cancer therapy. *J. Biomed. Mater. Res. A* **2017**, *105*, 2355–2367.
(57) Coleman, B.R.; Knight, T.; Gies, V.; Jakubek, Z.J.; Zou, S. Manipulation and Quantification of Graphene Oxide Flake Size: Photoluminescence and Cytotoxicity. *ACS Appl. Mater. Interfaces* **2017**, *9*, 28911–28921.
(58) Bidram, E.; Sulistio, A.; Amini, A.; Fu, Q.; Qiao, G.G.; Stewart, A.; Dunstan, D.E. Fractionation of graphene oxide single nano-sheets in water-glycerol solutions using gradient centrifugation. *Carbon* **2016**, *103*, 363–371.
(59) Sun, X.; Liu, Z.; Welsher, K.; Robinson, J.T.; Goodwin, A.; Zaric, S.; Dai, H. Nano-Graphene Oxide for Cellular Imaging and Drug Delivery. *Nano Res.* **2008**, *1*, 203–212.
(60) Luo, Y.; Tang, Y.; Liu, T.; Chen, Q.; Zhou, X.; Wang, N.; Ma, M.; Cheng, Y.; Chen, H. Engineering graphene oxide with ultrasmall SPIONs and smart drug release for cancer theranostics. *Chem. Commun.* **2019**, *55*, 1963–1966.
(61) Assali, A.; Akhavan, O.; Adeli, M.; Razzazan, S.; Dinarvand, R.; Zanganeh, S.; Soleimani, M.; Dinarvand, M.; Atyabi, F. Multifunctional core-shell nanoplatforms (gold@graphene oxide) with mediated NIR thermal therapy to promote miRNA delivery. *Nanomedicine* **2018**, *14*, 1891–1903.
(62) Basu, A.; Upadhyay, P.; Ghosh, A.; Chattopadhyay, D.; Adhikary, A. Folic-Acid-Adorned PEGylated Graphene Oxide Interferes with the Cell Migration of Triple Negative Breast Cancer Cell Line, MDAMB-231 by Targeting miR-21/PTEN Axis through NFκB. *ACS Biomater. Sci. Eng.* **2019**, *5*, 373–389.
(63) Chen, S.; Zhang, S.; Wang, Y.; Yang, X.; Yang, H.; Cui, C. Anti-EpCAM functionalized graphene oxide vector for tumor targeted siRNA delivery and cancer therapy. *Asian J. Pharm. Sci.* **2021**, *16*, 598–611.
(64) Izadi, S.; Moslehi, A.; Kheiry, H.; Karoon Kiani, F.; Ahmadi, A.; Masjedi, A.; Ghani, S.; Rafiee, B.; Karpisheh, V.; Hajizadeh, F.; et al. Codelivery of HIF-1α siRNA and Dinaciclib by Carboxylated Graphene Oxide-Trimethyl Chitosan-Hyaluronate Nanoparticles Significantly Suppresses Cancer Cell Progression. *Pharm. Res.* **2020**, *37*, 196.
(65) Maheshwari, R.; Gadeval, A.; Raval, N.; Kalia, K.; Tekade, R.K. Laser activatable nanographene colloids for chemo-photothermal combined gene therapy of triple-negative breast cancer. *Mater. Sci. Eng. C Mater. Biol. Appl.* **2021**, *5*, 112605.
(66) Yang, Y.Y.; Zhang, W.; Liu, H.; Jiang, J.J.; Wang, W.J.; Jia, Z.Y. Cell-Penetrating Peptide-Modified Graphene Oxide Nanoparticles Loaded with Rictor siRNA for the Treatment of Triple-Negative Breast Cancer. *Drug Des. Devel. Ther.* **2021**, *15*, 4961–4972.
(67) Yang, Z.; Yang, D.; Zeng, K.; Li, D.; Qin, L.; Cai, Y.; Jin, J. Simultaneous Delivery of antimiR-21 and Doxorubicin by Graphene Oxide for Reducing Toxicity in Cancer Therapy. *ACS Omega* **2020**, *5*, 14437–14443.
(68) Zheng, J.; Meng, D.; Zheng, X.; Zhang, Y.; Chen, H. Graphene-based materials: A new tool to fight against breast cancer. *Int. J. Pharm.* **2021**, *603*, 120644.
(69) Imani, R.; Shao, W.; Taherkhani, S.; Emami, S.H.; Prakash, S.; Faghihi, S. Dual-functionalized graphene oxide for enhanced siRNA delivery to breast cancer cells. *Colloids Surf. B Biointerfaces* **2016**, *147*, 315–325.
(70) Hwang, D.W.; Kim, H.Y.; Li, F.; Park, J.Y.; Kim, D.; Park, J.H.; Han, H.S.; Byun, J.W.; Lee, Y.S.; Jeong, J.M.; et al. In vivo visualization of endogenous miR-21 using hyaluronic acid-coated graphene oxide for

targeted cancer therapy. *Biomaterials* **2017**, *121*, 144–154.
(71) Bahreyni, A.; Yazdian-Robati, R.; Hashemitabar, S.; Ramezani, M.; Ramezani, P.; Abnous, K.; Taghdisi, S.M. A new chemotherapy agent-free theranostic system composed of graphene oxide nano-complex and aptamers for treatment of cancer cells. *Int. J. Pharm.* **2017**, *526*, 391–399.
(72) Li, Q.; Xiu, Y.; Zhang, X.; Liu, R.; Du, Q.; Shun, X.; Chen, S.; Li, W. Preparation of 99mTc-C60(OH)x and its biodistribution studies. *Nucl. Med. Biol.* **2002**, *29*, 707–710.
(73) Ji, Z.Q.; Sun, H.; Wang, H.; Xie, Q.; Liu, Y.; Wang, Z. Biodistribution and tumor uptake of C60(OH)xin mice. *J. Nanopart. Res.* **2006**, *8*, 53–63.
(74) Yang, S.-T.; Guo, W.; Lin, Y.; Deng, X.-Y.; Wang, H.-F.; Sun, H.-F.; Liu, Y.-F.; Wang, X.; Wang, W.; Chen, M.; et al. Biodistribution of Pristine Single-Walled Carbon Nanotubes In Vivo. *J. Phys.Chem. C* **2007**, *111*, 17761–17764.
(75) Zhang, X.; Yin, J.; Peng, C.; Hu, W.; Zhu, Z.; Li, W.; Fan, C.; Huang, Q. Distribution and biocompatibility studies of graphene oxide in mice after intravenous administration. *Carbon* **2011**, *49*, 986–995.
(76) Pei, X.; Zhu, Z.; Gan, Z.; Chen, J.; Zhang, X.; Cheng, X.; Wan, Q.; Wang, J. PEGylated nano-graphene oxide as a nanocarrier for delivering mixed anticancer drugs to improve anticancer activity. *Sci. Rep.* **2020**, *10*, 2717.
(77) Trusek, A.; Kijak, E.; Granicka, L. Graphene oxide as a potential drug carrier—Chemical carrier activation, drug attachment and its enzymatic controlled release. *Mater. Sci. Eng. C Mater. Biol. Appl.* **2020**, *116*, 111240.
(78) Karki, N.; Tiwari, H.; Tewari, C.; Rana, A.; Pandey, N.; Basak, S.; Sahoo, N.G. Functionalized graphene oxide as a vehicle for targeted drug delivery and bioimaging applications. *J. Mater. Chem. B* **2020**, *8*, 8116–8148.
(79) Liu, J.; Cui, L.; Losic, D. Graphene and graphene oxide as new nanocarriers for drug delivery applications. *Acta Biomater.* **2013**, *9*, 9243–9257.
(80) Hu, X.; Yu, Y.; Hou, W.; Zhou, J.; Song, L. Effects of particle size and pH value on the hydrophilicity of graphene oxide. *Appl. Surf. Sci.* **2013**, *273*, 118–121.
(81) Shih, C.J.; Lin, S.; Sharma, R.; Strano, M.S.; Blankschtein, D. Understanding the pH-dependent behavior of graphene oxide aqueous solutions: A comparative experimental and molecular dynamics simulation study. *Langmuir* **2012**, *28*, 235–241.
(82) Karki, N.; Tiwari, H.; Pal, M.; Chaurasia, A.; Bal, R.; Joshi, P.; Sahoo, N.G. Functionalized graphene oxides for drug loading, release and delivery of poorly water soluble anticancer drug: A comparative study. *Colloids Surf. B Biointerfaces* **2018**, *169*, 265–272.
(83) Farjadian, F.; Abbaspour, S.; Sadatlu, M.A.A.; Mirkiani, S.; Ghasemi, A.; Hoseini-Ghahfarokhi, M.; Mozaffari, N.; Karimi, M.; Hamblin, M.R. Recent Developments in Graphene and Graphene Oxide: Properties, Synthesis, and Modifications: A Review. *ChemistrySelect* **2020**, *5*, 10200–10219.
(84) Wang, Y.; Li, S.; Yang, H.; Luo, J. Progress in the functional modification of graphene/graphene oxide: A review. *RSC Adv.* **2020**, *10*, 15328–15345.
(85) Zhang, J.; Yan, L.; Wei, P.; Zhou, R.; Hua, C.; Xiao, M.; Tu, Y.; Gu, Z.; Wei, T. PEG-GO@XN nanocomposite suppresses breast cancer metastasis via inhibition of mitochondrial oxidative phosphorylation and blockade of epithelial-to-mesenchymal transition. *Eur. J. Pharmacol.* **2021**, *895*, 173866.
(86) Gu, Y.; Guo, Y.; Wang, C.; Xu, J.; Wu, J.; Kirk, T.B.; Ma, D.; Xue, W. A polyamidoamne dendrimer functionalized graphene oxide for DOX and MMP-9 shRNA plasmid co-delivery. *Mater. Sci. Eng. C Mater. Biol. Appl.* **2017**, *70*, 572–585.
(87) Zeng, Y.; Yang, Z.; Li, H.; Hao, Y.; Liu, C.; Zhu, L.; Liu, J.; Lu, B.; Li, R. Multifunctional Nanographene Oxide for Targeted Gene-Mediated Thermochemotherapy of Drug-resistant Tumor. *Sci. Rep.* **2017**, *7*, 43506.
(88) Huang, Y.-P.; Hung, C.-M.; Hsu, Y.-C.; Zhong, C.-Y.; Wang, W.-R.; Chang, C.-C.; Lee, M.-J. Suppression of Breast Cancer Cell Migration by Small Interfering RNA Delivered by Polyethylenimine-Functionalized Graphene Oxide. *Nanoscale Res. Lett.* **2016**, *11*, 247.
(89) Alibolandi, M.; Mohammadi, M.; Taghdisi, S.M.; Ramezani, M.; Abnous, K. Fabrication of aptamer decorated dextran coated nano-graphene oxide for targeted drug delivery. *Carbohydr. Polym.* **2017**, *155*, 218–229.
(90) Charmi, J.; Nosrati, H.; Mostafavi Amjad, J.; Mohammadkhani, R.; Danafar, H. Polyethylene glycol (PEG) decorated graphene oxide nanosheets for controlled release curcumin delivery. *Heliyon* **2019**, *5*, e01466.
(91) Maleki, P.; Sadeghi, Z.; Shahryar Rahpeyma, S.; Taheri, M.; Raheb, J. MTT assay dataset of polyethylenimine coated graphenoxide nanosheets on breast cancer cell lines (MCF7, MDA-MB-231, MDA-MB-468). *Hum. Antibodies* **2020**, *28*, 197–202.
(92) Mirzaie, Z.; Reisi-Vanani, A.; Barati, M. Polyvinyl alcohol-sodium alginate blend, composited with 3D-graphene oxide as a controlled release system for curcumin. *J. Drug Deliv. Sci. Technol.* **2019**, *50*, 380–387.

(93) Lu, Y.J.; Yang, H.W.; Hung, S.C.; Huang, C.Y.; Li, S.M.; Ma, C.C.; Chen, P.Y.; Tsai, H.C.; Wei, K.C.; Chen, J.P. Improving thermal stability and efficacy of BCNU in treating glioma cells using PAA-functionalized graphene oxide. *Int. J. Nanomed.* **2012**, *7*, 1737–1747.
(94) Saravanabhavan, S.S.; Rethinasabapathy, M.; Zsolt, S.; Kalambettu, A.B.; Elumalai, S.; Janakiraman, M.; Huh, Y.S.; Natesan, B. Graphene oxide functionalized with chitosan based nanoparticles as a carrier of siRNA in regulating Bcl-2 expression on Saos-2 & MG-63 cancer cells and its inflammatory response on bone marrow derived cells from mice. *Mater. Sci. Eng. C Mater. Biol. Appl.* **2019**, *99*, 1459–1468.
(95) Bart, J.; Tiggelaar, R.; Yang, M.; Schlautmann, S.; Zuilhof, H.; Gardeniers, H. Room-temperature intermediate layer bonding for microfluidic devices. *Lab Chip* **2009**, *9*, 3481–3488.
(96) Bazban-Shotorbani, S.; Hasani-Sadrabadi, M.M.; Karkhaneh, A.; Serpooshan, V.; Jacob, K.I.; Moshaverinia, A.; Mahmoudi, M. Revisiting structure-property relationship of pH-responsive polymers for drug delivery applications. *J. Control. Release* **2017**, *253*, 46–63.
(97) Imani, R.; Prakash, S.; Vali, H.; Faghihi, S. Polyethylene glycol and octa-arginine dual-functionalized nanographene oxide: An optimization for efficient nucleic acid delivery. *Biomater. Sci.* **2018**, *6*, 1636–1650.
(98) Wang, B.; Su, X.; Liang, J.; Yang, L.; Hu, Q.; Shan, X.; Wan, J.; Hu, Z. Synthesis of polymer-functionalized nanoscale graphene oxide with different surface charge and its cellular uptake, biosafety and immune responses in Raw264.7 macrophages. *Mater. Sci. Eng. C Mater. Biol. Appl.* **2018**, *90*, 514–522.
(99) Abedi-Gaballu, F.; Dehghan, G.; Ghaffari, M.; Yekta, R.; Abbaspour-Ravasjani, S.; Baradaran, B.; Ezzati Nazhad Dolatabadi, J.; Hamblin, M.R. PAMAM dendrimers as efficient drug and gene delivery nanosystems for cancer therapy. *Appl. Mater. Today* **2018**, *12*, 177–190.
(100) Palmieri, V.; Di Pietro, L.; Perini, G.; Barba, M.; Parolini, O.; De Spirito, M.; Lattanzi, W.; Papi, M. Graphene Oxide Nano- Concentrators Selectively Modulate RNA Trapping According to Metal Cations in Solution. *Front. Bioeng. Biotechnol.* **2020**, *8*, 421.
(101) Fong, J.F.Y.; Ng, Y.H.; Ng, S.M. Chapter 7—Carbon dots as a new class of light emitters for biomedical diagnostics and therapeutic applications. In *Fullerens, Graphenes and Nanotubes*; Grumezescu, A.M., Ed.; William Andrew Publishing: Norwich, NY, USA, 2018; pp. 227–295.
(103) Patil, T.V.; Patel, D.K.; Dutta, S.D.; Ganguly, K.; Lim, K.T. Graphene Oxide-Based Stimuli-Responsive Platforms for Biomedical Applications. *Molecules* **2021**, *26*, 2797.
(104) Yang, L.; Kim, T.H.; Cho, H.Y.; Luo, J.; Lee, J.M.; Chueng, S.D.; Hou, Y.; Yin, P.T.; Han, J.; Kim, J.H.; et al. Hybrid Graphene-Gold Nanoparticle-based Nucleic Acid Conjugates for Cancer-Specific Multimodal Imaging and Combined Therapeutics. *Adv. Funct. Mater.* **2021**, *31*, 2006918.
(105) Nurunnabi, M.; Parvez, K.; Nafiujjaman, M.; Revuri, V.; Khan, H.A.; Feng, X.; Lee, Y.-K. Bioapplication of graphene oxide derivatives: Drug/gene delivery, imaging, polymeric modification, toxicology, therapeutics and challenges. *RSC Adv.* **2015**, *5*, 42141–42161.
(106) Hossen, S.; Hossain, M.K.; Basher, M.K.; Mia, M.N.H.; Rahman, M.T.; Uddin, M.J. Smart nanocarrier-based drug delivery systems for cancer therapy and toxicity studies: A review. *J. Adv. Res* **2019**, *15*, 1–18.
(107) Hsu, J.L.; Hung, M.-C. The role of HER2, EGFR, and other receptor tyrosine kinases in breast cancer. *Cancer Metastasis Rev.* **2016**, *35*, 575–588.
(108) Carvalho, J.; Paiva, A.; Cabral Campello, M.P.; Paulo, A.; Mergny, J.-L.; Salgado, G.F.; Queiroz, J.A.; Cruz, C. Aptamer-based Targeted Delivery of a G-quadruplex Ligand in Cervical Cancer Cells. *Sci. Rep.* **2019**, *9*, 7945.
(109) Antwi-Boasiako, A.A.; Dunn, D.; Dasary, S.S.R.; Jones, Y.K.; Barnes, S.L.; Singh, A.K. Bioconjugated graphene oxide-based Raman probe for selective identification of SKBR3 breast cancer cells. *J. Raman Spectrosc.* **2017**, *48*, 1056–1064.
(110) Saeed, A.A.; Sánchez, J.L.A.; O'Sullivan, C.K.; Abbas, M.N. DNA biosensors based on gold nanoparticles-modified graphene oxide for the detection of breast cancer biomarkers for early diagnosis. *Bioelectrochemistry* **2017**, *118*, 91–99.
(111) Ali, M.A.; Mondal, K.; Jiao, Y.; Oren, S.; Xu, Z.; Sharma, A.; Dong, L. Microfluidic Immuno-Biochip for Detection of Breast Cancer Biomarkers Using Hierarchical Composite of Porous Graphene and Titanium Dioxide Nanofibers. *ACS Appl. Mater. Interfaces* **2016**, *8*, 20570–20582.
(112) Akhavan, O.; Ghaderi, E.; Akhavan, A. Size-dependent genotoxicity of graphene nanoplatelets in human stem cells. *Biomaterials* **2012**, *33*, 8017–8025.
(113) Li, Y.; Wu, Q.; Zhao, Y.; Bai, Y.; Chen, P.; Xia, T.; Wang, D. Response of MicroRNAs to In Vitro Treatment with Graphene Oxide. *ACS Nano* **2014**, *8*, 2100–2110.
(114) Ribeiro, B.F.M.; Souza, M.M.; Fernandes, D.S.; do Carmo, D.R.; Machado-Santelli, G.M. Graphene oxide-based nanomaterial interaction with human breast cancer cells. *J. Biomed. Mater. Res. A* **2020**, *108*, 863–870.
(115) Liao, C.; Li, Y.; Tjong, S.C. Graphene Nanomaterials: Synthesis, Biocompatibility, and Cytotoxicity. *Int. J.*

Mol. Sci. **2018**, *19*, 3564.
(116) Li, J.; Zhang, X.; Jiang, J.; Wang, Y.; Jiang, H.; Zhang, J.; Nie, X.; Liu, B. Systematic Assessment of the Toxicity and Potential Mechanism of Graphene Derivatives In Vitro and In Vivo. *Toxicol. Sci.* **2019**, *167*, 269–281.
(117) Yue, H.; Wei, W.; Yue, Z.; Wang, B.; Luo, N.; Gao, Y.; Ma, D.; Ma, G.; Su, Z. The role of the lateral dimension of graphene oxide in the regulation of cellular responses. *Biomaterials* **2012**, *33*, 4013–4021.
(118) Kre˛towski, R.; Jabłońska-Trypuc´, A.; Cechowska-Pasko, M. The Preliminary Study on the Proapoptotic Effect of Reduced Graphene Oxide in Breast Cancer Cell Lines. *Int. J. Mol. Sci.* **2021**, *22*, 12593.
(119) Farell, M.; Self, A.; Guza, C.; Song, H.; Apollon, L.; Gomez, E.W.; Kumar, M. Lipid-Functionalized Graphene Loaded with hMnSOD for Selective Inhibition of Cancer Cells. *ACS Appl. Mater. Interfaces* **2020**, *12*, 12407–12416.
(120) Han, X.M.; Zheng, K.W.; Wang, R.L.; Yue, S.F.; Chen, J.; Zhao, Z.W.; Song, F.; Su, Y.; Ma, Q. Functionalization and optimization- strategy of graphene oxide-based nanomaterials for gene and drug delivery. *Am. J. Transl. Res.* **2020**, *12*, 1515–1534.
(121) Lalwani, G.; D'Agati, M.; Khan, A.M.; Sitharaman, B. Toxicology of graphene-based nanomaterials. *Adv. Drug Deliv. Rev.* **2016**, *105*, 109–144.
(122) Chowdhury, S.M.; Lalwani, G.; Zhang, K.; Yang, J.Y.; Neville, K.; Sitharaman, B. Cell specific cytotoxicity and uptake of graphene nanoribbons. *Biomaterials* **2013**, *34*, 283–293.
(123) Kim, H.; Kim, J.; Lee, M.; Choi, H.C.; Kim, W.J. Stimuli-Regulated Enzymatically Degradable Smart Graphene-Oxide-Polymer Nanocarrier Facilitating Photothermal Gene Delivery. *Adv. Healthc. Mater.* **2016**, *5*, 1918–1930.
(124) Gies, V.; Lopinski, G.; Augustine, J.; Cheung, T.; Kodra, O.; Zou, S. The impact of processing on the cytotoxicity of graphene oxide. *Nanoscale Adv.* **2019**, *1*, 817–826.
(125) Gies, V.; Zou, S. Systematic toxicity investigation of graphene oxide: Evaluation of assay selection, cell type, exposure period and flake size. *Toxicol. Res.* **2018**, *7*, 91–101.
(126) Chatterjee, N.; Eom, H.J.; Choi, J. A systems toxicology approach to the surface functionality control of graphene-cell interactions. *Biomaterials* **2014**, *35*, 110–1127.
(127) Akhavan, O. Graphene scaffolds in progressive nanotechnology/stem cell-based tissue engineering of the nervous system. *J. Mater. Chem. B* **2016**, *4*, 3169–3190.
(128) Zhang, Y.; Ali, S.F.; Dervishi, E.; Xu, Y.; Li, Z.; Casciano, D.; Biris, A.S. Cytotoxicity effects of graphene and single-wall carbon nanotubes in neural phaeochromocytoma-derived PC12 cells. *ACS Nano* **2010**, *4*, 3181–3186.
(129) Wang, K.; Ruan, J.; Song, H.; Zhang, J.; Wo, Y.; Guo, S.; Cui, D. Biocompatibility of Graphene Oxide. *Nanoscale Res. Lett.* **2011**, *6*, 8.
(130) Chang, Y.; Yang, S.T.; Liu, J.H.; Dong, E.; Wang, Y.; Cao, A.; Liu, Y.; Wang, H. In vitro toxicity evaluation of graphene oxide on A549 cells. *Toxicol. Lett.* **2011**, *200*, 201–210.
(131) Hu, W.; Peng, C.; Lv, M.; Li, X.; Zhang, Y.; Chen, N.; Fan, C.; Huang, Q. Protein corona-mediated mitigation of cytotoxicity of graphene oxide. *ACS Nano* **2011**, *5*, 3693–3700.
(132) Lammel, T.; Boisseaux, P.; Fernández-Cruz, M.L.; Navas, J.M. Internalization and cytotoxicity of graphene oxide and carboxyl graphene nanoplatelets in the human hepatocellular carcinoma cell line Hep G2. *Part. Fibre Toxicol.* **2013**, *10*, 27.
(133) Chen, B.; Liu, M.; Zhang, L.; Huang, J.; Yao, J.; Zhang, Z. Polyethylenimine-functionalized graphene oxide as an efficient gene delivery vector. *J. Mater. Chem.* **2011**, *21*, 7736–7741.
(134) Li, R.; Guiney, L.M.; Chang, C.H.; Mansukhani, N.D.; Ji, Z.; Wang, X.; Liao, Y.P.; Jiang, W.; Sun, B.; Hersam, M.C.; et al. Surface Oxidation of Graphene Oxide Determines Membrane Damage, Lipid Peroxidation, and Cytotoxicity in Macrophages in a Pulmonary Toxicity Model. *ACS Nano* **2018**, *12*, 1390–1402.
(135) Ghamkhari, A.; Abbaspour-Ravasjani, S.; Talebi, M.; Hamishehkar, H.; Hamblin, M.R. Development of a graphene oxide-poly lactide nanocomposite as a Smart Drug Delivery System. *Int. J. Biol. Macromol.* **2021**, *169*, 521–531.
(136) Roy, S.; Jaiswal, A. DNA binding and NIR triggered DNA release from quaternary ammonium modified poly(allylamine hydrochloride) functionalized and folic acid conjugated reduced graphene oxide nanocomposites. *Int. J. Biol. Macromol.* **2020**, *153*, 931–941.
(137) Behzadi, S.; Serpooshan, V.; Tao, W.; Hamaly, M.A.; Alkawareek, M.Y.; Dreaden, E.C.; Brown, D.; Alkilany, A.M.; Farokhzad, O.C.; Mahmoudi, M. Cellular uptake of nanoparticles: Journey inside the cell. *Chem. Soc. Rev.* **2017**, *46*, 4218–4244.

(138) Peruzynska, M.; Cendrowski, K.; Barylak, M.; Tkacz, M.; Piotrowska, K.; Kurzawski, M.; Mijowska, E.; Drozdzik, M. Comparative in vitro study of single and four layer graphene oxide nanoflakes—Cytotoxicity and cellular uptake. *Toxicol. In Vitro* **2017**, *41*, 205–213.
(139) Zhao, C.; Song, X.; Liu, Y.; Fu, Y.; Ye, L.; Wang, N.; Wang, F.; Li, L.; Mohammadniaei, M.; Zhang, M.; et al. Synthesis of graphene quantum dots and their applications in drug delivery. *J. Nanobiotechnol.* **2020**, *18*, 142.
(140) Sasidharan, A.; Panchakarla, L.S.; Chandran, P.; Menon, D.; Nair, S.; Rao, C.N.R.; Koyakutty, M. Differential nano-bio interactions and toxicity effects of pristine versus functionalized graphene. *Nanoscale* **2011**, *3*, 2461–2464.
(141) Wang, C.; Wu, C.; Zhou, X.; Han, T.; Xin, X.; Wu, J.; Zhang, J.; Guo, S. Enhancing Cell Nucleus Accumulation and DNA Cleavage Activity of Anti-Cancer Drug via Graphene Quantum Dots. *Sci. Rep.* **2013**, *3*, 2852.
(142) Akhavan, O.; Ghaderi, E.; Emamy, H.; Akhavan, F. Genotoxicity of graphene nanoribbons in human mesenchymal stem cells. *Carbon* **2013**, *54*, 419–431.
(143) Su, L.J.; Zhang, J.H.; Gomez, H.; Murugan, R.; Hong, X.; Xu, D.; Jiang, F.; Peng, Z.Y. Reactive Oxygen Species-Induced Lipid Peroxidation in Apoptosis, Autophagy, and Ferroptosis. *Oxid. Med. Cell. Longev.* **2019**, *2019*, 5080843.
(144) Ristic, B.; Harhaji-Trajkovic, L.; Bosnjak, M.; Dakic, I.; Mijatovic, S.; Trajkovic, V. Modulation of Cancer Cell Autophagic Responses by Graphene-Based Nanomaterials: Molecular Mechanisms and Therapeutic Implications. *Cancers* **2021**, *13*, 4145.
(145) Li, Y.; Liu, Y.; Fu, Y.; Wei, T.; Le Guyader, L.; Gao, G.; Liu, R.S.; Chang, Y.Z.; Chen, C. The triggering of apoptosis in macrophages by pristine graphene through the MAPK and TGF-beta signaling pathways. *Biomaterials* **2012**, *33*, 402–411.
(146) Zhang, W.; Wang, C.; Li, Z.; Lu, Z.; Li, Y.; Yin, J.-J.; Zhou, Y.-T.; Gao, X.; Fang, Y.; Nie, G.; et al. Unraveling Stress Induced Toxicity Properties of Graphene Oxide and the Underlying Mechanism. *Adv. Mater.* **2012**, *24*, 5391–5397.
(147) Gurunathan, S.; Han, J.W.; Eppakayala, V.; Kim, J.H. Green synthesis of graphene and its cytotoxic effects in human breast cancer cells. *Int. J. Nanomed.* **2013**, *8*, 1015–1027.
(148) Wang, L.; Yan, J. Superficial synthesis of photoactive copper sulfide quantum dots loaded nano-graphene oxide sheets combined with near infrared (NIR) laser for enhanced photothermal therapy on breast cancer in nursing care management. *J. Photochem. Photobiol. B* **2019**, *192*, 68–73.
(149) Allen, B.L.; Kichambare, P.D.; Gou, P.; Vlasova, I.I.; Kapralov, A.A.; Konduru, N.; Kagan, V.E.; Star, A. Biodegradation of single-walled carbon nanotubes through enzymatic catalysis. *Nano Lett.* **2008**, *8*, 3899–3903.
(150) Allen, B.L.; Kotchey, G.P.; Chen, Y.; Yanamala, N.V.; Klein-Seetharaman, J.; Kagan, V.E.; Star, A. Mechanistic investigations of horseradish peroxidase-catalyzed degradation of single-walled carbon nanotubes. *J. Am. Chem. Soc.* **2009**, *131*, 17194–17205.
(151) Andón, F.T.; Kapralov, A.A.; Yanamala, N.; Feng, W.; Baygan, A.; Chambers, B.J.; Hultenby, K.; Ye, F.; Toprak, M.S.; Brandner, B.D.; et al. Biodegradation of single-walled carbon nanotubes by eosinophil peroxidase. *Small* **2013**, *9*, 2721–2729.
(152) Kagan, V.E.; Konduru, N.V.; Feng, W.; Allen, B.L.; Conroy, J.; Volkov, Y.; Vlasova, I.I.; Belikova, N.A.; Yanamala, N.; Kapralov, A.; et al. Carbon nanotubes degraded by neutrophil myeloperoxidase induce less pulmonary inflammation. *Nat. Nanotechnol.* **2010**, *5*, 354–359.
(153) Kurapati, R.; Mukherjee, S.P.; Martín, C.; Bepete, G.; Vázquez, E.; Pénicaud, A.; Fadeel, B.; Bianco, A. Degradation of Single-Layer and Few-Layer Graphene by Neutrophil Myeloperoxidase. *Angew. Chem. Int. Ed. Engl.* **2018**, *57*, 11722–11727.
(154) Luan, X.; Martín, C.; Zhang, P.; Li, Q.; Vacchi, I.A.; Delogu, L.G.; Mai, Y.; Bianco, A. Degradation of Structurally Defined Graphene Nanoribbons by Myeloperoxidase and the Photo-Fenton Reaction. *Angew. Chem. Int. Ed. Engl.* **2020**, *59*, 18515–18521.
(155) Mukherjee, S.P.; Gliga, A.R.; Lazzaretto, B.; Brandner, B.; Fielden, M.; Vogt, C.; Newman, L.; Rodrigues, A.F.; Shao, W.; Fournier, P.M.; et al. Graphene oxide is degraded by neutrophils and the degradation products are non-genotoxic. *Nanoscale* **2018**, *10*, 1180–1188.
(156) Kurapati, R.; Martìn, C.; Palermo, V.; Nishina, Y.; Bianco, A. Biodegradation of graphene materials catalyzed by human eosinophil peroxidase. *Faraday Discuss.* **2021**, *227*, 189–203.
(157) Fadeel, B.; Bussy, C.; Merino, S.; Vázquez, E.; Flahaut, E.; Mouchet, F.; Evariste, L.; Gauthier, L.; Koivisto, A.J.; Vogel, U.; et al. Safety Assessment of Graphene-Based Materials: Focus on Human Health and the Environment.

ACS Nano **2018**, *12*, 10582–10620.
(158) Hsieh, H.-S.; Zepp, R.G. Reactivity of graphene oxide with reactive oxygen species (hydroxyl radical, singlet oxygen, and superoxide anion). *Environ. Sci. Nano* **2019**, *6*, 3734–3744.
(159) Campbell, E.; Hasan, M.T.; Pho, C.; Callaghan, K.; Akkaraju, G.R.; Naumov, A.V. Graphene Oxide as a Multifunctional Platform for Intracellular Delivery, Imaging, and Cancer Sensing. *Sci. Rep.* **2019**, *9*, 416.
(160) de Lázaro, I.; Vranic, S.; Marson, D.; Rodrigues, A.F.; Buggio, M.; Esteban-Arranz, A.; Mazza, M.; Posocco, P.; Kostarelos, K. Graphene oxide as a 2D platform for complexation and intracellular delivery of siRNA. *Nanoscale* **2019**, *11*, 13863–13877.
(161) Augustine, R.; Hasan, A.; Primavera, R.; Wilson, R.J.; Thakor, A.S.; Kevadiya, B.D. Cellular uptake and retention of nanoparticles: Insights on particle properties and interaction with cellular components. *Mater. Today Commun.* **2020**, *25*, 101692.
(162) Xu, J.; Liu, Y.; Li, Y.; Wang, H.; Stewart, S.; Van der Jeught, K.; Agarwal, P.; Zhang, Y.; Liu, S.; Zhao, G.; et al. Precise targeting of POLR2A as a therapeutic strategy for human triple negative breast cancer. *Nat. Nanotechnol.* **2019**, *14*, 388–397.
(163) Albanese, A.; Tang, P.S.; Chan, W.C. The effect of nanoparticle size, shape, and surface chemistry on biological systems. *Annu. Rev. Biomed. Eng.* **2012**, *14*, 1–16.
(164) Palmieri, V.; Perini, G.; De Spirito, M.; Papi, M. Graphene oxide touches blood: In vivo interactions of bio-coronated 2D materials. *Nanoscale Horiz.* **2019**, *4*, 273–290.
(165) Amrollahi-Sharifabadi, M.; Koohi, M.K.; Zayerzadeh, E.; Hablolvarid, M.H.; Hassan, J.; Seifalian, A.M. In vivo toxicological evaluation of graphene oxide nanoplatelets for clinical application. *Int. J. Nanomed.* **2018**, *13*, 4757–4769.
(166) Newman, L.; Jasim, D.A.; Prestat, E.; Lozano, N.; de Lazaro, I.; Nam, Y.; Assas, B.M.; Pennock, J.; Haigh, S.J.; Bussy, C.; et al. Splenic Capture and In Vivo Intracellular Biodegradation of Biological-Grade Graphene Oxide Sheets. *ACS Nano* **2020**, *14*, 10168–10186.
(167) Alsaedi, I.I.J.; Taqi, Z.J.; Abdul Hussien, A.M.; Sulaiman, G.M.; Jabir, M.S. Graphene nanoparticles induces apoptosis in MCF-7 cells through mitochondrial damage and NF-KB pathway. *Mater. Res. Express* **2019**, *6*, 095413.
(168) Hosseinzadeh, R.; Khorsandi, K.; Hosseinzadeh, G. Graphene oxide-methylene blue nanocomposite in photodynamic therapy of human breast cancer. *J. Biomol. Struct. Dyn.* **2018**, *36*, 2216–2223.
(169) Zhang, W.; Dai, J.; Zhang, G.; Zhang, Y.; Li, S.; Nie, D. Photothermal/pH Dual-Responsive Drug Delivery System of Amino- Terminated HBP-Modified rGO and the Chemo-Photothermal Therapy on Tumor Cells. *Nanoscale Res. Lett.* **2018**, *13*, 379.
(170) Lazarovits, J.; Chen, Y.Y.; Sykes, E.A.; Chan, W.C.W. Nanoparticle–blood interactions: The implications on solid tumor targeting. *Chem. Commun.* **2015**, *51*, 2756–2767.
(171) Pelaz, B.; del Pino, P.; Maffre, P.; Hartmann, R.; Gallego, M.; Rivera-Fernández, S.; de la Fuente, J.M.; Nienhaus, G.U.; Parak, W.J. Surface Functionalization of Nanoparticles with Polyethylene Glycol: Effects on Protein Adsorption and Cellular Uptake. *ACS Nano* **2015**, *9*, 6996–7008.
(172) Rhazouani, A.; Gamrani, H.; El Achaby, M.; Aziz, K.; Gebrati, L.; Uddin, M.S.; Aziz, F. Synthesis and Toxicity of Graphene Oxide Nanoparticles: A Literature Review of In Vitro and In Vivo Studies. *Biomed. Res. Int.* **2021**, *2021*, 5518999.
(173) Yang, K.; Gong, H.; Shi, X.; Wan, J.; Zhang, Y.; Liu, Z. In vivo biodistribution and toxicology of functionalized nano-graphene oxide in mice after oral and intraperitoneal administration. *Biomaterials* **2013**, *34*, 2787–2795.
(174) Cui, G.; Wu, J.; Lin, J.; Liu, W.; Chen, P.; Yu, M.; Zhou, D.; Yao, G. Graphene-based nanomaterials for breast cancer treatment: Promising therapeutic strategies. *J. Nanobiotechnol.* **2021**, *19*, 211.
(175) Liang, S.; Xu, S.; Zhang, D.; He, J.; Chu, M. Reproductive toxicity of nanoscale graphene oxide in male mice. *Nanotoxicology* **2015**, *9*, 92–105.
(176) Ema, M.; Hougaard, K.S.; Kishimoto, A.; Honda, K. Reproductive and developmental toxicity of carbon-based nanomaterials: A literature review. *Nanotoxicology* **2016**, *10*, 391–412.
(177) Li, J.; Liang, X.; Zhang, J.; Yin, Y.; Zuo, T.; Wang, Y.; Yang, X.; Shen, Q. Inhibiting pulmonary metastasis of breast cancer based on dual-targeting graphene oxide with high stability and drug loading capacity. *Nanomedicine* **2018**, *14*, 1237–1248.
(178) Yang, D.; Feng, L.; Dougherty, C.A.; Luker, K.E.; Chen, D.; Cauble, M.A.; Banaszak Holl, M.M.; Luker, G.D.; Ross, B.D.; Liu, Z.; et al. In vivo targeting of metastatic breast cancer via tumor vasculature-specific nano-graphene oxide. *Biomaterials* **2016**, *104*, 361–371.
(179) Hu, L.; Fu, Y.; Rong, L.; Yang, X.; Li, Y.; Wang, L.; Wu, W. Evaluating the cytotoxicity of graphene oxide using embryonic stem cells-derived cells. *J. Biomed. Mater. Res. A* **2020**, *108*, 1321–1328.

(180) Hashemi, M.S.; Gharbi, S.; Jafarinejad-Farsangi, S.; Ansari-Asl, Z.; Dezfuli, A.S. Secondary toxic effect of graphene oxide and graphene quantum dots alters the expression of miR-21 and miR-29a in human cell lines. *Toxicol. In Vitro* **2020**, *65*, 104796.
(181) Ma, J.; Liu, R.; Wang, X.; Liu, Q.; Chen, Y.; Valle, R.P.; Zuo, Y.Y.; Xia, T.; Liu, S. Crucial Role of Lateral Size for Graphene Oxide in Activating Macrophages and Stimulating Pro-inflammatory Responses in Cells and Animals. *ACS Nano* **2015**, *9*, 10498–10515.
(182) He, Y.; Zhang, L.; Chen, Z.; Liang, Y.; Zhang, Y.; Bai, Y.; Zhang, J.; Li, Y. Enhanced chemotherapy efficacy by co-delivery of shABCG2 and doxorubicin with a pH-responsive charge-reversible layered graphene oxide nanocomplex. *J. Mater. Chem. B* **2015**, *3*, 6462–6472.
(183) Wang, H.; Sun, D.; Zhao, N.; Yang, X.; Shi, Y.; Li, J.; Su, Z.; Wei, G. Thermo-sensitive graphene oxide–polymer nanoparticle hybrids: Synthesis, characterization, biocompatibility and drug delivery. *J. Mater. Chem. B* **2014**, *2*, 1362–1370.
(184) Lei, Y.; Zhang, G.; Li, H. Thermal-responsive nanocomposite hydrogel based on graphene oxide-polyvinyl alcohol/poly (N- isopropylacrylamide). *IOP Conf. Ser. Mater. Sci. Eng.* **2017**, *274*, 012115.
(185) Liu, H.; Sun, Y.; Lang, L.; Yang, T.; Zhao, X.; Cai, C.; Liu, Z.; Ding, P. Nuclear localization signal peptide enhances transfection efficiency and decreases cytotoxicity of poly(agmatine/N,N'-cystamine-bis-acrylamide)/pDNA complexes. *J. Cell. Biochem.* **2019**, *120*, 16967–16977.
(186) Wu, B.; Li, M.; Wang, L.; Iqbal, Z.; Zhu, K.; Yang, Y.; Li, Y. Size-transformable nanohybrids with pH/redox/enzymatic sensitivity for anticancer therapy. *J. Mater. Chem. B* **2021**, *9*, 4319–4328.
(187) Chen, R.J.; Zhang, Y. Controlled precipitation of solubilized carbon nanotubes by delamination of DNA. *J. Phys. Chem. B* **2006**, *110*, 54–57.
(188) Hsieh, C.J.; Chen, Y.C.; Hsieh, P.Y.; Liu, S.R.; Wu, S.P.; Hsieh, Y.Z.; Hsu, H.Y. Graphene Oxide Based Nanocarrier Combined with a pH-Sensitive Tracer: A Vehicle for Concurrent pH Sensing and pH-Responsive Oligonucleotide Delivery. *ACS Appl. Mater. Interfaces* **2015**, *7*, 11467–11475.
(189) de Oliveira, A.C.; Souza, P.R.; Vilsinski, B.H.; Winkler, M.E.G.; Bruschi, M.L.; Radovanovic, E.; Muniz, E.C.; Caetano, W.; Valente, A.J.M.; Martins, A.F. Thermo- and pH-Responsive Gelatin/Polyphenolic Tannin/Graphene Oxide Hydrogels for Efficient Methylene Blue Delivery. *Molecules* **2021**, *26*, 4529.
(190) Bina, A.; Raissi, H.; Hashemzadeh, H.; Farzad, F. Conjugation of a smart polymer to doxorubicin through a pH-responsive bond for targeted drug delivery and improving drug loading on graphene oxide. *RSC Adv.* **2021**, *11*, 18809–18817.
(191) Karimi, S.; Namazi, H. Fe3O4@PEG-coated dendrimer modified graphene oxide nanocomposite as a pH-sensitive drug carrier for targeted delivery of doxorubicin. *J. Alloys Compd.* **2021**, *879*, 160426.
(192) Shi, Z.; Li, Q.; Mei, L. pH-Sensitive nanoscale materials as robust drug delivery systems for cancer therapy. *Chin. Chem. Lett.* **2020**, *31*, 1345–1356.
(193) Yang, Z.; Li, Y.; Gao, J.; Cao, Z.; Jiang, Q.; Liu, J. pH and redox dual-responsive multifunctional gene delivery with enhanced capability of transporting DNA into the nucleus. *Colloids Surf. B Biointerfaces* **2017**, *153*, 111–122.
(194) An, J.; Gou, Y.; Yang, C.; Hu, F.; Wang, C. Synthesis of a biocompatible gelatin functionalized graphene nanosheets and its application for drug delivery. *Mater. Sci. Eng. C Mater. Biol. Appl.* **2013**, *33*, 2827–2837.
(195) Gadeval, A.; Maheshwari, R.; Raval, N.; Kalyane, D.; Kalia, K.; Tekade, R.K. Green graphene nanoplates for combined photo- chemo-thermal therapy of triple-negative breast cancer. *Nanomedicine* **2020**, *15*, 581–601.
(196) Gai, L.X.; Wang, W.Q.; Wu, X.; Su, X.J.; Yang, F.C. NIR absorbing reduced graphene oxide for photothermal radiotherapy for treatment of esophageal cancer. *J. Photochem. Photobiol. B* **2019**, *194*, 188–193.
(197) Lu, N.; Liu, J.; Li, J.; Zhang, Z.; Weng, Y.; Yuan, B.; Yang, K.; Ma, Y. Tunable dual-stimuli response of a microgel composite consisting of reduced graphene oxide nanoparticles and poly(N-isopropylacrylamide) hydrogel microspheres. *J. Mater. Chem. B* **2014**, *2*, 3791–3798.
(198) Fong, Y.T.; Chen, C.H.; Chen, J.P. Intratumoral Delivery of Doxorubicin on Folate-Conjugated Graphene Oxide by In-Situ Forming Thermo-Sensitive Hydrogel for Breast Cancer Therapy. *Nanomaterials* **2017**, *7*, 388.
(199) Chen, X.; Liu, L.; Jiang, C. Charge-reversal nanoparticles: Novel targeted drug delivery carriers. *Acta Pharm. Sin. B* **2016**, *6*, 261–267.
(200) Yang, X.; Zhang, X.; Liu, Z.; Ma, Y.; Huang, Y.; Chen, Y. High-Efficiency Loading and Controlled Release of Doxorubicin Hydrochloride on Graphene Oxide. *J. Phys. Chem. C* **2008**, *112*, 17554–17558.
(201) Bao, H.; Pan, Y.; Ping, Y.; Sahoo, N.G.; Wu, T.; Li, L.; Li, J.; Gan, L.H. Chitosan-functionalized graphene oxide as a nanocarrier for drug and gene delivery. *Small* **2011**, *7*, 1569–1578.
(202) Abbasian, M.; Roudi, M.M.; Mahmoodzadeh, F.; Eskandani, M.; Jaymand, M. Chitosan-grafted-poly(methacrylic acid)/graphene oxide nanocomposite as a pH-responsive de novo cancer chemotherapy nanosystem. *Int. J. Biol. Macromol.* **2018**, *118*, 1871–1879.

(203) Diaz-Diestra, D.; Thapa, B.; Badillo-Diaz, D.; Beltran-Huarac, J.; Morell, G.; Weiner, B.R. Graphene Oxide/ZnS:Mn Nanocomposite Functionalized with Folic Acid as a Nontoxic and Effective Theranostic Platform for Breast Cancer Treatment. *Nanomaterials* **2018**, *8*, 484.
(204) Mousavi, S.M.; Hashemi, S.A.; Ghasemi, Y.; Amani, A.M.; Babapoor, A.; Arjmand, O. Applications of graphene oxide in case of nanomedicines and nanocarriers for biomolecules: Review study. *Drug Metab. Rev.* **2019**, *51*, 12–41.
(205) Asantewaa, G.; Harris, I.S. Glutathione and its precursors in cancer. *Curr. Opin. Biotechnol.* **2021**, *68*, 292–299.
(206) Liu, C.-C.; Zhao, J.-J.; Zhang, R.; Li, H.; Chen, B.; Zhang, L.-L.; Yang, H. Multifunctionalization of graphene and graphene oxide for controlled release and targeted delivery of anticancer drugs. *Am. J. Transl. Res.* **2017**, *9*, 5197–5219.
(207) Qi, L.-Y.; Wang, Y.; Hu, L.-F.; Zhao, P.-S.; Yu, H.-Y.; Xing, L.; Gao, X.-D.; Cao, Q.-R.; Jiang, H.-L. Enhanced nuclear gene delivery via integrating and streamlining intracellular pathway. *J. Control. Release* **2022**, *341*, 511–523.
(208) Ma, N.; Song, A.; Li, Z.; Luan, Y. Redox-Sensitive Prodrug Molecules Meet Graphene Oxide: An Efficient Graphene Oxide-Based Nanovehicle toward Cancer Therapy. *ACS Biomater. Sci. Eng.* **2019**, *5*, 1384–1391.
(209) Davoodi, P.; Srinivasan, M.P.; Wang, C.H. Synthesis of intracellular reduction-sensitive amphiphilic polyethyleneimine and poly(ϵ-caprolactone) graft copolymer for on-demand release of doxorubicin and p53 plasmid DNA. *Acta Biomater.* **2016**, *39*, 79–93.
(210) Trusek, A.; Kijak, E. Drug Carriers Based on Graphene Oxide and Hydrogel: Opportunities and Challenges in Infection Control Tested by Amoxicillin Release. *Materials* **2021**, *14*, 3182.
(211) Lee, S.J.; Yhee, J.Y.; Kim, S.H.; Kwon, I.C.; Kim, K. Biocompatible gelatin nanoparticles for tumor-targeted delivery of polymerized siRNA in tumor-bearing mice. *J. Control. Release* **2013**, *172*, 358–366.
(212) Madkhali, O.; Mekhail, G.; Wettig, S.D. Modified gelatin nanoparticles for gene delivery. *Int. J. Pharm.* **2019**, *554*, 224–234.
(213) Monroe, J.D.; Belekov, E.; Er, A.O.; Smith, M.E. Anticancer Photodynamic Therapy Properties of Sulfur-Doped Graphene Quantum Dot and Methylene Blue Preparations in MCF-7 Breast Cancer Cell Culture. *Photochem. Photobiol.* **2019**, *95*, 1473–1481.
(214) Shaheen, F.; Hammad Aziz, M.; Fakhar-E-Alam, M.; Atif, M.; Fatima, M.; Ahmad, R.; Hanif, A.; Anwar, S.; Zafar, F.; Abbas, G.; et al. An In Vitro Study of the Photodynamic Effectiveness of GO-Ag Nanocomposites against Human Breast Cancer Cells. *Nanomaterials* **2017**, *7*, 401.
(215) Lin, C.H.; Chen, Y.C.; Huang, P.I. Preparation of Multifunctional Dopamine-Coated Zerovalent Iron/Reduced Graphene Oxide for Targeted Phototheragnosis in Breast Cancer. *Nanomaterials* **2020**, *10*, 1957.
(216) Lu, Y.J.; Lan, Y.H.; Chuang, C.C.; Lu, W.T.; Chan, L.Y.; Hsu, P.W.; Chen, J.P. Injectable Thermo-Sensitive Chitosan Hydrogel Containing CPT-11-Loaded EGFR-Targeted Graphene Oxide and SLP2 shRNA for Localized Drug/Gene Delivery in Glioblastoma Therapy. *Int. J. Mol. Sci.* **2020**, *21*, 7111.

Chapter 3: Harnessing graphene oxide nanocarriers for siRNA delivery in a 3D spheroid model of lung cancer

This chapter reports a published research article investigating GO-based nanocarriers for siRNA delivery in 3D lung cancer spheroid models. The study focuses on how GO size and surface functionalization influence cytotoxicity, cellular uptake, and gene silencing efficiency, and highlights the advantages of 3D models over conventional 2D cultures for evaluating gene delivery performance.

I had a primary role in the execution of this study, including all cell culture, transfection, imaging, data analysis, and interpretation of the results presented in this chapter. I prepared all figures and took a leading role in drafting and revising the manuscript.

Reference:

Grilli, F.; Hassan, E. M.; Variola, F.; Zou, S. Harnessing graphene oxide nanocarriers for siRNA delivery in a 3D spheroid model of lung cancer. Biomater. Sci. 2023, 11, 6635-6649.

Abstract

Gene therapy has been recently proposed as an effective strategy for cancer treatment. A significant body of literature proved the effectiveness of nanocarriers to deliver therapeutic agents to 2D tumor models, which are simple but not always representative of the *in vivo* reality. In this study, we analyze the efficiency of 3D spheroids in mimicking the tumor microenvironment, combined with a minimally modified graphene oxide (GO) based nanocarrier for siRNA delivery as a new system for cell transfection. Small interfering RNA (siRNA) targeting cluster of differentiation 47 (CD47; CD47_siRNA) was used as anti-tumor therapeutic agent to silence the genes expressing CD47. This is a surface marker able to send a "don't eat me" signal to macrophages to prevent their phagocytosis. Also, we report the analysis of different GO formulations, in terms of size (small: about 100 nm; large: > 650 nm) and functionalizations (unmodified or modified with polyethylene glycol, PEG; and the dendrimer PAMAM), aiming to establish the efficiency of unmodified GO as a nanocarrier for the transfection of A549 lung cancer spheroids. Small modified GO (smGO) showed the highest transfection efficiency values (> 90%) in 3D models. Interestingly, small unmodified GO (sGO) was found to be promising for transfection, with efficiency values > 80% using a higher siRNA ratio (i.e., 3:1). These results demonstrated the higher efficiency of spheroids compared to 2D models for transfection, and the high potential of unmodified GO to carry siRNA, providing a promising new *in vitro* model system for the analysis of anticancer gene therapies.

3.1 Introduction

Cancer is one of the primary causes of mortality worldwide [1], and the study of its biology and possible treatment is one of the main goals of biomedical research. To improve our understanding of its mechanisms towards more effective therapeutic solutions significant efforts have been applied to the development of physiologically accurate *in vitro* models in order to find a connection between two-dimensional (2D) cell cultures and animal models. Results from this work has yielded three-

dimensional (3D) models such as *in vitro* tumor spheroids2. Several studies have been carried out to compare the cytotoxicity, internalization, and cellular sensitivity to chemotherapeutic drugs or other anticancer therapies, such as radiotherapy or gene therapy, using both 2D and 3D models [2-5]. It was found that cell behavior is highly dependent on the model used, showing higher sensitivity for the therapeutic agent in 2D and 3D as a function of the cell line. However, the size of spheroids and cell packing density could play an important role in uptake tests using nanoparticles, introducing new parameters, such as the limitation of nutrient transport and the complexity of cell-cell interaction *in vitro* [6]. Therefore, cellular spheroids have become a complex heterogeneous model with cell-cell interactions and a gradient of oxygen, pH, and nanoparticle concentration between the outermost layers and the centre of mass, which is more representative of reality [2, 6, 7]. Moreover, cells in a spheroidal arrangement demonstrated to show a more realistic phenotype concerning 2D monolayers [8]. In the last decade, gene therapy has gained increasing interest due to its high potential for the effective treatment of cancer, cardiovascular diseases, rare infections and genetic diseases [9, 10]. In the case of cancer, transfection can be used to change the protein expression of the cells to make them less aggressive or more sensitive to therapeutic agents or even just to the patient's immune system. In this context, cluster of differentiation 47 (CD47) is a surface protein that is expressed by many normal cell lines, but overexpressed on almost all tumors and acts by regulating several signaling systems associated with tumor growth and invasion [11-13]. One of the main pathways of CD47 inhibits the action of the immune system. Upon binding of this protein to the inhibitory receptor (i.e., signal regulatory protein, SIRPα), present on the surface of macrophages, the CD47-receptor complex sends an antiphagocytic "don't eat me" signal to prevent phagocytosis [12, 13]. Suppression of CD47 overexpression on cancer cells can lead to inhibition of the resistance of the tumor itself by making it "visible" to the immune surveillance and thus being eliminated through phagocytosis [11]. In the field of gene therapy, RNA is a powerful therapeutic tool currently established for manipulating gene expression14. In particular, small interfering RNA (siRNA) can be employed as a promising anti-cancer technique to specifically and selectively down-regulate protein expression by targeting and

binding the specific mRNA present in the cytosol of cells thanks to the complementary base pairing [15]. We and others have tested the siRNA targeting CD47 (CD47_siRNA) to effectively knockdown CD47 protein expression in several cancer cell lines, inhibiting the anti-phagocytosis signal of such cancer cells and demonstrating their susceptibility to macrophages following treatment [11, 15-17]. In order to obtain the transfection, the siRNA must enter the body, pass through the circulation and reach the tumor site and penetrate the cell membrane to bind the mRNA inside the cancerous cells. During this journey, several difficulties and barriers can arise which limited the efficacy and use of siRNA. Within the blood, unprotected nucleic acid must avoid renal filtration, internalization by phagocytes, aggregation with serum proteins, and enzymatic degradation by endogenous nucleases [18]. The half-life of unmodified siRNA within blood has been estimated to range from several minutes to 1 hour [19]. Furthermore, the absence of tumor recognition factors makes targeting non-specific within the body. Therefore, a gene that shares a similarity with the target gene can be inadvertently silenced, with possible unwanted side effects. Finally, penetration through the cell membrane can be difficult as nucleic acids and the plasma membrane both have strong hydrophilicity and net negative charge [19, 20]. These effects result in a limited therapeutic efficiency of siRNA with a small percentage arriving to the target tumor cells, even after injecting large quantities of siRNA [15]. These considerations suggest that siRNA delivery need an effective carrier in order to obtain a successful and efficient tumor transfection.

Among the large arrays of available nanocarriers, graphene oxide (GO) has gained a lot of interest during the past two decades due to its unique characteristics, such as a two-dimensional single-layer structure, which provides it a high surface-to-volume ratio that is very important in interacting with cells [21]. In fact, a large surface area allows more interactions with cellular structures and likely achieves greater internalization, while a small volume limits its toxicity as less material will have to be removed from the body [21, 22]. In addition, the surface of GO flakes is rich in functional groups that can bind to different molecules, including payload in large quantities. GO is also able to respond to different stimuli, such as pH or near infrared radiation (NIR), which could enable the design of a

multifunctional substrate for tumor treatment [23, 24]. Finally, it is biocompatible and its toxicity is reduced due in part to the presence of negative charges on its surface, which limits its harmful interactions with cell membranes [25]. Nevertheless, GO is generally used after undergoing functionalization by the addition of polymer or dendrimer molecules that can increase its stability in the body fluids and make its surface more compatible for nucleic acid loading and cell internalization [24-26]. The GO surface has been modified with functional groups such as polyethyleneimine (PEI), polyethylene glycol (PEG), chitosan, and dendrimers to deliver anticancer drugs and genes *in vitro* and *in vivo* [14, 21]. However, the addition of polymers implies further processing of the material, and it can also increase the GO toxicity as a result of the positive charges from the addition of cationic polymers, inducing cytotoxicity for cells due to the strong physical interactions with the cell membrane, which can cause its damage and breakage [25, 27]. On the other hand, GO has a hydrophilic nature, suggesting that it possesses great potential to generate a uniform dispersion in aqueous solutions and to effectively penetrate cell membranes without the addition of other molecules [28].

In this study, spheroids of A549 cells were used as a 3D model of lung cancer. CD47_siRNA was used to knockdown the overexpressed CD47 protein in A549 cells. GO nanocarriers with two different size ranges (small: around 100 nm, and big: >650 nm), either unmodified or modified with PEG and PAMAM, were used to deliver CD47_siRNA in A549 spheroids. Silencing CD47 in cells grown in spheroids could be of a great benefit in the understanding of *in vivo* tumor response to gene therapies. Moreover, the use of different GO formulations can clarify the impact of modification and dimension on cell internalization and transfection. In particular, the possibility of combining 3D models with unmodified GO nanocarriers, simpler to prepare since no chemical functionalizations are involved, for the transfection of CD47_siRNAs could offer an excellent model system solution for the study of anti-cancer treatments.

3.2 Materials and methods

3.2.1 Materials and reagents

Dulbecco's Modified Eagle's Medium (DMEM), Phosphate Buffered Saline (PBS) 1X solution (pH 7.4), Fetal Bovine Serum (FBS), 0.5% trypsin EDTA (10X Trypsin), Opti-MEM transfection media and Nunclon™ Sphera™ 96-well U-bottom, 12-well flat bottom super low attachment plates, used to prepare single and multi-spheroids, respectively, and 96-well flat bottom plates for toxicity measurements were purchased from Thermo Fisher Scientific (Canada). Cell Counting Kit 8 (WST-8) was purchased from Cedarlane (Canada). PE anti human CD47 antibody was purchased from BioLegend (USA). PE-Annexin V Apoptosis Detection Kit was purchased from BD-Biosciences (Canada). DsiRNA CD47 (CD47_siRNA), negative control DsiRNA (ctrl N) and Nuclease Free Duplex Buffer used for transfection were purchased from Integrated DNA Technologies (IDT, USA). The CD47_siRNA duplex sequences used for transfection are: 5′-rGrCrArArCrArArCrCrUrUrUrCrCrArGrCrUrArCrUrUrUTG-3′ and 5′-rCrArArArArGrUrArGrCrUrGrGrArArArGrGrUrUrGrUrUrGrCrArG-3′. The negative control was provided as a "universal negative control", not a scrambled sequence of the above.

In house GO (hGO) was synthesized through the modified Hummer's method and filtered to produce big GO (bGO, > 650 nm). hGO underwent sonication process (probe sonicator, Cole Parmer, Canada) at 10 W for 9 intervals of 10 minutes on/off in a 0 °C water bath was used to create small GO (sGO, around 100 nm). Part of such bGO and sGO were subsequently chemically modified by the addition of 6-arm amine-terminated polyethylene glycol (PEG, 25 mg, Jenkem Technology, 15 kDa) and PAMAM dendrimers (10 μL, 4.0 generation, primary amine surface area, 10.1 w/w% in water, 10 kDa, Dendritech Inc.) as previously reported14. Modified GO flakes dispersions of large size (bmGO > 650 nm; 0.7 mg/mL) and small size (smGO ~100 nm; 1 mg/mL) were obtained. Commercial GO water dispersions (250 mL; concentration 0.5 mg/mL) was purchased from Grephenea, Cambridge, US.

3.2.2 Cell culturing of normal and cancerous cell lines

NIH 3T3 (mouse embryonic fibroblasts, normal cells), A549 (human lung cancer cell), HepG2 (human liver cancer cell), NB4 and THP-1 (acute myelocytic leukaemia cancer cells) were purchased from American Type Culture Collection (ATCC, USA) and were cultured in DMEM, supplemented with 10% FBS, at 37 °C in a humidified atmosphere containing 5% CO2.

3.2.3 3D spheroids realization with NIH 3T3, A549, HepG2, NB4 and THP-1 cells

All cultured cells were trypsinized and centrifuged at 1500 rpm for 5 min. The resulting pellet was resuspended and the cell viability was assessed through Trypan blue before plating. Successively, cells were suspended in fresh media and seeded at 5×10^3 cells/well in a non-adherent 96-well plate to grow spheroids. Every 3 days, 100 µL of media was changed in each well with fresh one paying attention to not disturb the cells at the bottom. Spheroids formation and growth was evaluated at 24, 48, 72, 96 h, 7 and 10 d after seeding. A549 and HepG2 cells were also seeded at 2.5×10^5 cells/well in a non-adherent 12-well plate for the formation of multi-spheroids for apoptosis and transfection experiments.

3.2.4 GO cytotoxicity and induced cell apoptosis in 2D cell models

The WST-8 assay was used to assess the viability of cells in 2D culture after exposure to hGO and a commercial GO (cGO), (n = 6). NIH 3T3 and A549 cells were seeded on 96-well flat-bottom plates at a density of 2.5-3.5 $\times 10^3$ cells/well and incubated in 100 µL of media for 24 h at 37 °C under 5% CO2 to allow them to adhere. The following day, these two cell lines, plus NB4 (seeding density of 7×10^3), were treated with different concentrations of hGO and cGO (1, 4, 16, 64 µg/mL) for a predetermined exposure period of either 24, 48 or 72 h. Cells without treatments were used as controls. At each time point, 10 µL of WST-8 was added to each well and the plates were incubated

at 37 °C for 2 h. The absorbance was measured at 450 nm by a microplate reader (FLUOstar Omega microplate reader, Mandel Scientific, Canada). To determine the viability percentage of the cells after GO treatments, the following equation was used:

$$\%\ viability = \frac{Ab_{sample} - Ab_{GO}}{Ab_{cells} - Ab_{blank}} \times 100\% \quad (3.1)$$

where Ab_{sample} is the absorbance of the cell containing sample treated with n µg/mL GO, Ab_{GO} is the absorbance of the same n µg/mL GO without cells, Ab_{cells} is the absorbance of the untreated cells and Ab_{blank} is the absorbance of the media alone.

3.2.5 Apoptosis and transfection efficiency evaluation by flow cytometric measurements

NIH 3T3, A549, and NB4 cultured in 2D were also analyzed to determine cell apoptosis after GO exposure using PE-Annexin V apoptosis detection kit by flow cytometry analysis (BD-FACS Canto model 640166, SN: V0099, USA). hGO and cGO concentrations and analyzed time points were kept the same as in WST-8 test. NIH 3T3 and A549 cells were seeded on 6-well plates at a density of 1 × 105 cells/well and incubated in 2 mL of media for 24 h at 37 °C under 5% CO2 to allow them to adhere. The following day, NIH 3T3, A549, and NB4 were treated with hGO and cGO. At each time point, cells were harvested and treated with trypsin for 5-10 minutes to obtain individual cell suspensions, followed by centrifugation at 1500 rpm for 5 min. The cell pellets were suspended in 100 µL of binding buffer and then 5 µL of PE-Annexin V was added to the cell suspension and incubated for 15 min. Finally, 400 µL of binding buffer was added and cell apoptosis was evaluated.

For the transfection analysis, A549 cells were seeded at 2.5×10^5 cells/well in non-adherent 12-well tissue culture plates and at 1×10^5 cells/well in 6-well adherent plates to form 3D spheroids and 2D monolayer, respectively. Cells were allowed to grow and reach 75% of confluence in 2D culture or form spheroids in 5 d in DMEM supplemented with 10% FBS. Then, the media was changed with

Opti-MEM media for transfection. For the preparation of the CD47_siRNA and GO complexes (CD47_siRNA-GOs) with the different formulations of GO, transfection-mixes (transfection media-CD47_siRNA-GO) were prepared by mixing CD47_siRNA (in 1:1 or 3:1 CD47_siRNA:GO wt:wt) in 200 µL of Opti-MEM transfection media with each of the GO formulations (i.e., smGO, bmGO, sGO, and bGO) and incubated for 1 h at room temperature (21 ± 2 °C). Then the different transfection mixes were added to the A549 cells at a concentration of 0.25 µg/mL and incubated at 37 °C under 5% CO2 for 48 h. To ensure that CD47_siRNA was delivered specifically to the target cells, a universal negative control (ctrl N) was used. CD47_siRNA alone (ctrl CD47) was also used to evaluate the uptake of the target siRNA by the cells without any delivery system. Finally, untreated cells were used as transfection controls (ctrl untr).

The transfection of CD47_siRNA was evaluated using standard antibody staining with PE anti-human CD47 antibodies to measure levels of CD47 markers expression. The efficiency of transfection was assessed by measuring the expression levels of the CD47 marker in the treated cells and the ctrl untr. After centrifugation, the pellet was washed twice, and suspended in cold PBS (4 °C) and then 5 µL of PE anti-human CD47 was added and incubated at room temperature for 30 min. The siRNA knockdown efficiency of CD47 markers was calculated according to the following formula:

$$\%\ knockdown\ efficiency = \frac{MFI_{ctrl\ untr} - MFI_{transf\ sample}}{MFI_{ctrl\ untr}} \times 100\% \quad (3.2)$$

where MFI_{untr} is the mean fluorescence intensity (MFI) of untransfected cells, MFI_{transf} sample is the mean fluorescence intensity of cells treated with CD47_siRNA-GOs.

Since three-dimensional conformations of spheroids can prevent adequate diffusion of media to the center of the cell mass, the percentage of cells undergoing apoptosis were also evaluated using PE Annexin V apoptosis detection kit followed by flow cytometry analysis at 24, 48, 72, 96h, 7 and 10

d after seeding. From the apoptosis percentages obtained through flow cytometry, cell viability was also calculated with the following formula:

$$\%\ cell\ viability = 100\ \% - \%\ apoptosis \quad (3.3)$$

3.2.6 Statistical analysis

All flow cytometry and cytotoxicity results are presented as mean ± standard deviation (SD). Experiments were repeated 3 times in duplicate (n = 3). All flow cytometric data was then analyzed using FlowJo software (10.6 version, 2019). All statistical analysis and bar/dots graphs were done with GraphPad Prism 8.02. Differences between more than three conditions were analyzed using one-way ANOVA test, while differences among two independent variables on a dependent variable were evaluated by two-way ANOVA. A value of $P < 0.05$ was considered statistically significant.

3.3 Results and Discussion

3.3.1 3D spheroids formation with normal and cancer cell lines

NIH 3T3, A549, HepG2, THP-1, and NB4 cells were grown into spheroids to mimic the *in vivo* microenvironment. Optical microscopy images show the formation of single spheroids (Figure 3.1A) and multi spheroids (Figure 3.1B). The morphology of the spheroids changes in shape, density and size, depending on the cell lines, despite the seeding density was kept consistent (5×10^3 cells/well), highlighting the differences among cell lines in terms of size and packing capacity [6]. A good spheroid is defined as a cell mass that grows in a spherical shape, has well-defined boundaries, and is characterized by a clear colour [29]. NIH 3T3 cells demonstrated a marked ability to rapidly form spheroids, satisfying the aforementioned criteria already at 24h. Similarly, A549 cells proved to be capable of forming such 3D structures after 5-7 days of incubation. HepG2 cells showed rapid aggregation ability but less

uniformity in size and shape. This is particularly evident from the images of the multi-spheroids in Figure 3.1B. Finally, both leukemia cell lines were found to be unable to form spheroids independently, highlighting a difference between adherent and suspension cell lines. After 48 h (Figure 3.1A), THP-1 cells began to aggregate to some extent but lost this feature in the following days, resulting only in a mass of accumulated cells at the bottom of the well. In contrast, NB4 cells never showed any tendency to aggregate and remained completely disaggregated even after 7 days of culture (Figure 3.1A). To the best of our knowledge, no studies have reported the formation of spheroids using NB4 cells, while THP-1 cells were observed to undergo disaggregation in a previous work, similar to our findings [30]. In this study, THP-1 cells differentiated into macrophages and formed compact spheroids, while the non-differentiated THP-1 cells were in a loose aggregate configuration after 3 d of incubation. Similar results were published with adherent cells, where NIH 3T3 formed a compact spheroid structure starting just 6 h after seeding, while A549 cells resulted in a loose aggregate during the first days of incubation6. Accordingly, liver spheroids took up to 3 weeks to reach a functionally mature conformation, starting with the same seeding density [31]. In addition, authors reported that the morphology of HepG2 spheroids were more compact and regular, most likely due to the different spheroid formation procedure, in which cells were seeded in microwells and subjected to centrifugation to ensure their accumulation in the centre of the well. In another study, irregular lung cancer spheroids shape was observed using the hanging-drop method for their formation [8]. Longer spheroid formation time limited the initial seeding density that can be used, as a low cell number should be seeded to avoid cell death in the centre of the 3D cell culture due to a lack of nutrients that struggle to penetrate within a large cell mass [32]. For these reasons, A549 lung cancer cells were chosen for our subsequent experiments reported below.

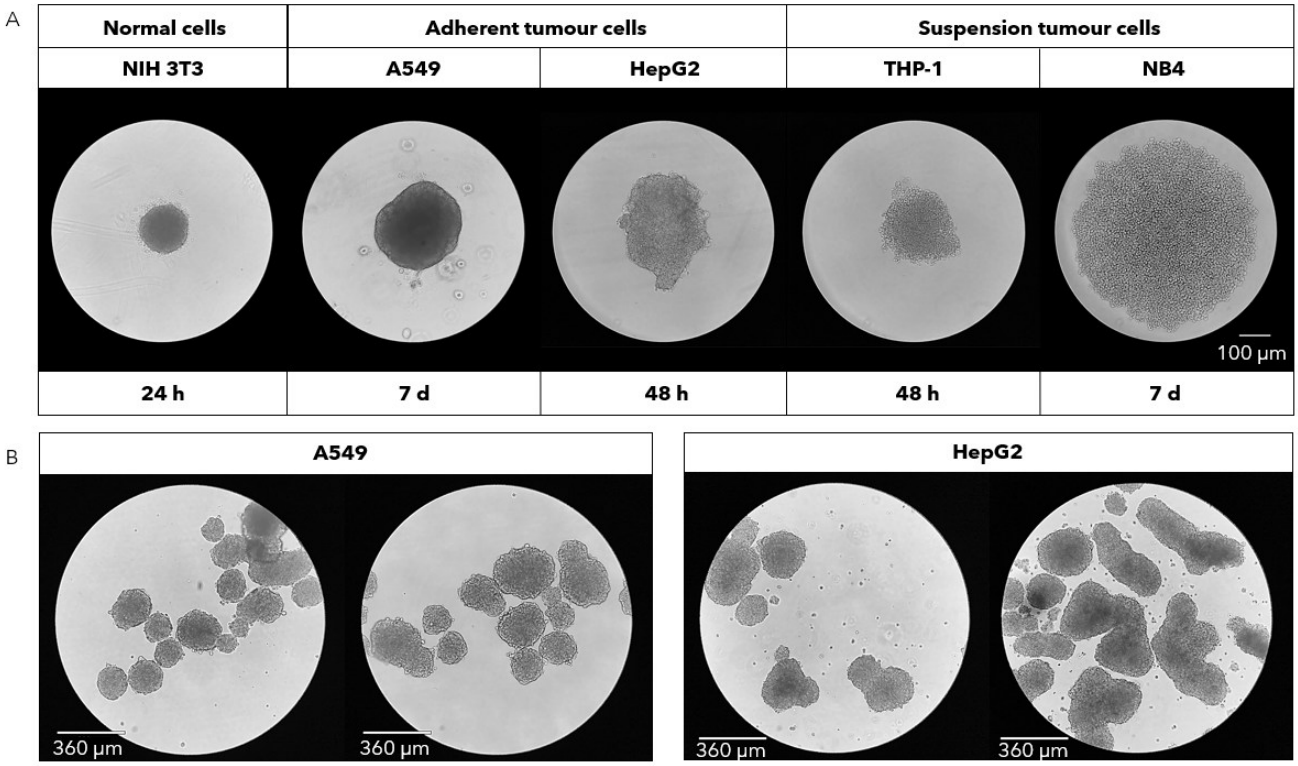

Figure 3.1. Spheroids of different cell lines formed at different time points after seeding of 5000 cells/well in 96-well U-bottom plates for the formation of single spheroids (A) and 12-well flat bottom plates for the formation of multi-spheroids (B). The spheroids were realized using ultra low cell attachment plates.

3.3.2 Lung cancer 2D cultures and spheroids realization and viability test

A549 lung cancer cells were thus selected and used for growing spheroids and comparing them to the respective 2D cultures in terms of viability and CD47 protein expression. The two cell models (Figure 3.2A) were created by seeding A549 cells in two different multi-wells, namely standard 6-well plates for 2D culture and 12-well super low cell attachment plates for the growth of multi-spheroids. A549 cells began to aggregate approximately 96 h after seeding and form spheroids within 7 d (Figure 3.2B). Apoptosis was monitored for up to 3 d starting with the same seeding concentration (2.5×10^5 cell/well), since by that time, 2D culture cells reached 70-80% confluence. Results of cell viability (Figure 3.2C) derived from apoptosis measurements indicated that both 2D and 3D cultures, are viable (cell viability $\geq 90\%$) at each time point, with no significant differences observed between the two cultures. Notably, cell

viability in 2D culture increased over time ($P < 0.05$), whereas in spheroids, it remained almost constant. This can be explained by the fact that A549 cells in 2D have a high division rate (about 28h) [33], while cells in spheroidal configuration present a lower proliferation, maybe due to the cell contact inhibition [34]. However, the time required for the spheroid formation before performing other tests could influence cell viability and thus cell response to different analysis [6]. The spheroids were maintained in culture for up to 10 d to check their behaviour and viability for longer cultures period to assess the maximum incubation time with high cell viability, before performing further experiments. Apoptosis tests were completed by low cytometry (Figure 3.2D) and the cell viability was derived (Figure 3.2E) considering the percentage of cells negative to the stain. From the results obtained at each time point (i.e., 24, 48, 72, 96 h and 7, 10 d), the cells within the spheroids are viable throughout all the culture period (cell viability ≥ 80%). However, although there was no significant reduction in viability until day 7, by day 10 the viability was significantly lower (80%) compared to every other time point (≥ 90%), possibly suggesting the cell stress due to a lack of nutrients which struggle to penetrate from the surrounding to the centre of the spheroid. These results suggest that cells can survive much longer as 3D spheroids than in 2D cultures, and the number of cells that can be seeded and supported in 3D is much greater than in 2D. Same observations can be found in a previous study [35]. In another study A549 cells were cultured in spheroids, and the viability at days 3 and 7 reached values of 86% and 65%, respectively [32]. However, the lower viability percentages obtained can be attributed to the higher cell seeding density used in that study. Specifically, A549 cells were seeded in a concentration of about 8×10^4 cells/cm^2 in 200 µL of media, while in our experiments the same cells were seeded at about 6.5×10^4 cells/cm^2 in 2 mL of media. It has been demonstrated, using different cell lines and dead cell staining (e.g., propidium iodide, caspase 3/7), that limiting the initial seeding cell number can prevent cell suffering and death in the core of the spheroid during its formation, resulting in spheroids composed mostly of viable cells [3, 36, 37].

We also evaluated CD47 surface marker expression in A549 cultured in both 2D and 3D configurations through flow cytometry and PE anti-human CD47 antibody. The results showed a significant reduction ($P < 0.05$) in CD47 expression in the spheroids (8741 ± 712) compared to the 2D culture (10270 ± 1162). This finding is consistent with previous studies that showed a decreased protein expression intensity in many cell lines, including A549, when cultured in 3D with respect to 2D [35, 38]. The reduced expression in 3D cultures might be closer to the *in vivo* situations, since 2D conditions generally promote abnormal cellular proliferation, metabolism and cell interactions, which are not similar to the *in vivo* cancer tissues behaviour [35]. In conclusion, spheroids demonstrated to be a potential powerful cell culture tool for further experiment.

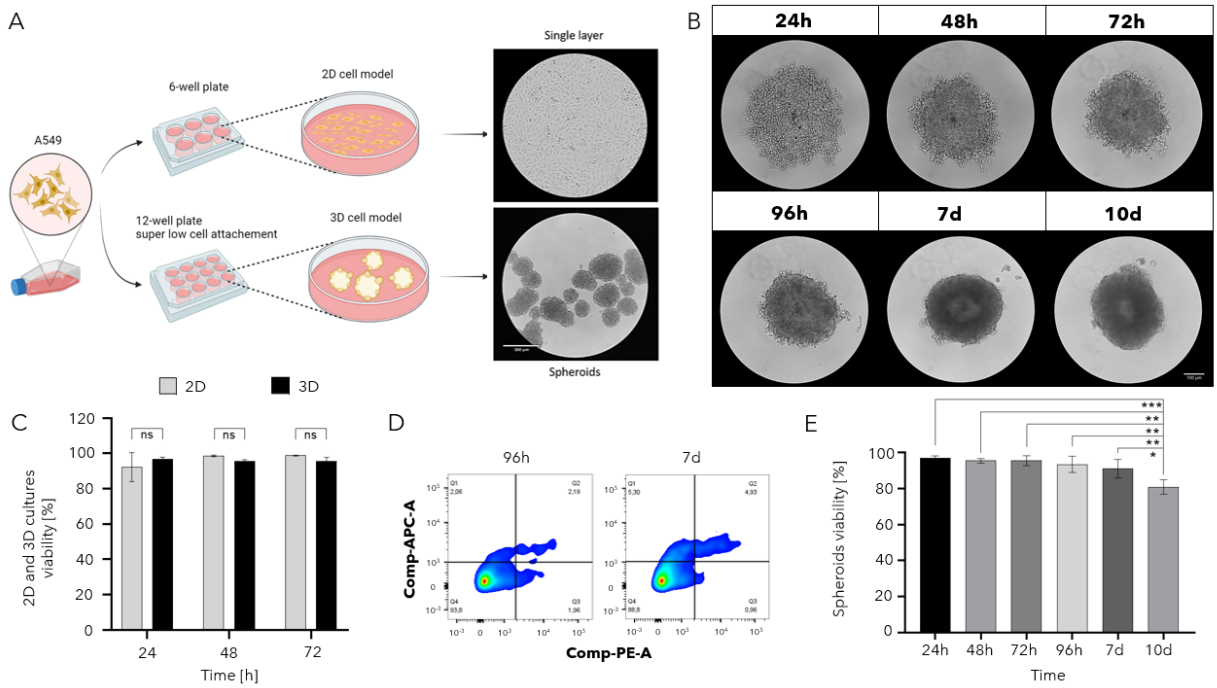

Figure 3.2. A549 spheroids formation (A-B), apoptosis (C) and viability (D) at different time points after seeding 2500 cells/well. (A) Schematic representation of the cell seeding procedure for the preparation of 2D and 3D cellular models. (B) Microscopy images showing the spheroid formation over 10 days. (C) Viability percentages of 2D and 3D cell cultures were obtained from apoptosis measurements at 24, 48, and 72 h. (D) Representative flow cytometry plots of apoptosis results after 96 h and 7 days, using PE Annexin V apoptosis detection kit. (E) Viability percentages obtained from the apoptosis results in (D) carried out at all the time points in (B). Values in (C) and (E) are shown as mean ± SD of three trials of duplicate samples (n = 3). The statistical significance between the two cell models in (C) was determined by two-way ANOVA, where $P < 0.05$ was considered significant and $P > 0.05$ is not significant (ns). One-way ANAOVA was used for statistical analysis in (E): $P < 0.05$ was considered significant (*$P < 0.05$; **$P < 0.01$; ***$P < 0.001$Results with $p > 0.05$ are not shown.

3.3.3 Cytotoxicity and cell apoptosis of GO in 2D cultures of normal and cancer cell lines

To assess the cytotoxicity of hGO, its interactions with cells were studied and compared with cGO. Four different concentrations (i.e., 1, 4, 16, and 64 μg/mL) were selected. The higher concentrations are generally not used for transfection but were chosen to have an indication of the maximum usable noncytotoxic limit (cell viability ≥ 80%). As for cells, three lines were considered, namely one normal line (i.e., NIH 3T3), and two tumor lines, of which one adherent (i.e., A549), and one in suspension (i.e., NB4).

Results of these toxicity tests (Fig 3A-C) demonstrate the presence of dependence with respect to concentration and cell line. Notably, as the dose of GO used increases, the cell viability of all three cell lines tested decreases. A549 showed high viability values, showing the lowest results of about 40% after 24 h of incubation with hGO and 21% after 48 h with cGO at a concentration of 64 μg/mL. Also, for 1 and 4 μg/mL of both hGO and cGO, A549 cells remained viable throughout all the culture period. Similarly, NB4 showed the same trend for the two lower concentrations (4 and 16 μg/mL) of GOs, while demonstrating a higher sensitivity to the material in terms of toxicity when used at concentrations ≥ 16 μg/mL. Already at 24 h, NB4 viability was 38% and 17% for hGO and cGO, respectively, at a concentration equal to 16 μg/mL, and 6% and 12% at 64 μg/mL. Similarly, NIH 3T3 did not show toxicity for both the GO formulations at a concentration of 1 μg/mL for all 3 d. However, different results were obtained for 4 μg/mL with a cell viability < 80% in the first two days and then increased to about 80% after 72 h, with a higher cell viability for the cells treated with hGO compared to cGO at each time point. For concentrations ≥ 16 μg/mL, NIH 3T3 showed cell viability values < 50% already at 24 h and < 10% at 48 h for both the GOs. Interestingly, all three cell lines do not show a time dependency. Especially for NB4, the cell viability increases during the time when incubated with both the GO formulations at each concentration. NIH 3T3 and A549, instead, show a different behaviour. NIH 3T3 viability increased in time when incubated with the two lower concentrations of GOs (≤ 4 μg/mL) and

decrease with the two higher (≥ 16 μg/mL), while A549 cells viability shows the opposite trend. For all the cell lines, concentrations and time points, hGO generally showed less toxicity than cGO. In agreement with our results, the concentration dependency has previously been reported for NIH 3T3 and A549, with much greater toxicity of GO for the normal cells, while discrepancies about time dependency are reported in the literature [39, 40]. Another parameter that might affect the results is the test used. MTT and WST-8 assays were used in previous work to study the cytotoxicity of GO flakes and it was observed that GO interfered with the reagents, giving inaccurate results [41].

To better study the toxicity of GO on the three cell lines, apoptosis tests were also completed through flow cytometry (Figure 3.3D-F). Similar to WST-8 tests, apoptosis evaluation presented a concentration and cell line dependency with respect to both hGO and cGO. A549 cells showed apoptosis values of < 20% for concentrations up to 4 μg/mL of both GO formulations during the entire culture period, and up to 48 h for 16 μg/mL. The highest concentration (64 μg/mL) of hGO resulted in higher apoptosis, with 36% of cells in an apoptotic state after 24 h, and increasing over time, reaching 83% at 72 h. At this concentration, cGO showed reduced apoptosis compared to hGO during the incubation period, with a peak of 45% after 3 d. NB4 cells showed almost no apoptosis for all concentrations of both in house and commercial GOs up to 4 μg/mL during 3 d of incubation. The highest apoptosis registered was 37% for cGO at a concentration of 64 μg/mL. These results for suspension cells are in agreement with the findings of a previous study [42]. Similarly, NIH 3T3 cells presented very low apoptosis percentages (< 6%) for both hGO and cGO at concentrations ≤ 4 μg/mL during the whole culture period, while for concentrations ≥ 16 μg/mL, apoptosis increased significantly over time, reaching values > 90% for hGO and cGO at 64 μg/mL after 48 h.

The cell viability results obtained through the WST-8 assay and apoptosis measurements are depicted in the heat map in Figure 3.3G and compared with each other. NIH 3T3 cells begin

to show very low viability values (< 30%) as early as 24 h for the highest concentration of hGO, with viability < 10% for GO concentrations ≥ 16 µg/mL at day 3.

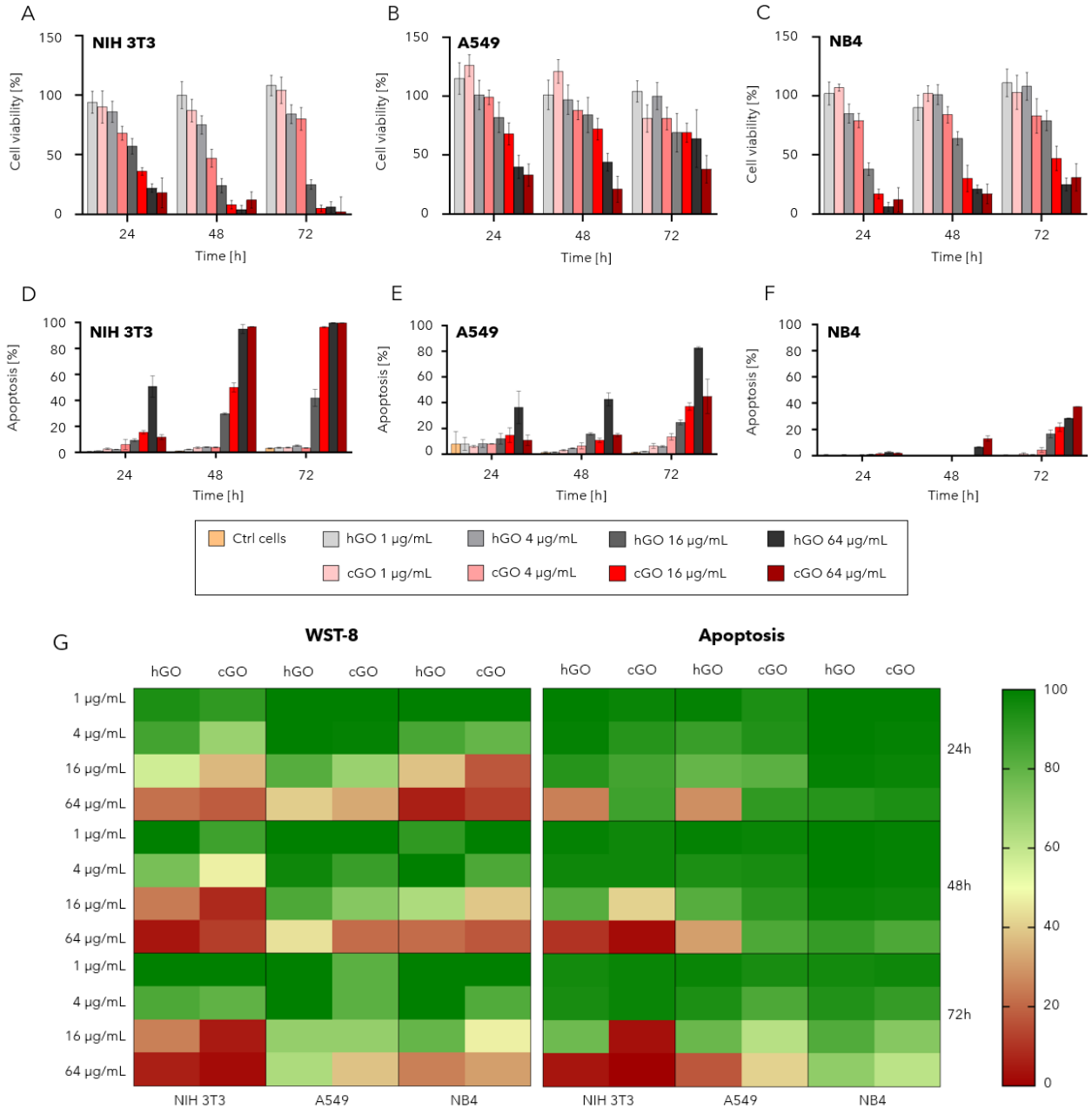

Figure 3.3. Cell viability and apoptosis assays of cancer and normal cells incubated with different GO concentrations (0, 1, 4, 16, and 64 µg/mL) for 24, 48 and 72 h. (A-C) Viability results obtained through WST-8 cytotoxicity assay and calculated relative to the control cells (GO concentration: 0 µg/mL) in (A) NIH 3T3 fibroblasts, (B) A549 lung cancer cells, and (C), NB4 leukemia cancer cells. (D-F) Apoptosis results of cancer and normal cells in (A-B) obtained through PE Annexin V apoptosis detection kit and flow cytometry measurements. (G) Heat map summarizing the viability results obtained through WST-8 in (A-C) and the ones derived from apoptosis measurements (D-F). Values on each graph (A-F) are shown as mean ± SD of three trials of duplicate samples (n = 3). Statistical significance was determined by one-way ANOVA, where $p < 0.05$ was considered significant and $P > 0.05$ is not significant (ns).

These results were different from what was observed with the WST-8, in which viability values < 50% were recorded for concentrations ≥ 16 μg/mL already at 24 h for both hGO and cGO. In contrast, the NB4 cells remained in the green spectrum of the heatmap for all concentrations at both 24 and 48 h, showing viability values between 60-80% only at 72 h and for the higher concentrations (≥ 16 μg/mL). These results are consistent with the WST-8 results, even though the cell viability derived from apoptosis test was higher. For example, at, the cell viability from the WST-8 test was > 40% 24 h with 64 μg/mL of both hGO and cGO, while the one derived from the apoptosis measurement was > 80%.

A549 cells show intermediate sensitivity to the material in comparison to the other cell lines. With 64 μg/mL of hGO at 24h, viability < 40% was determined, which decreases to a minimum of 10-19% at 72h. For such cells, cGO showed cytotoxicity only at 72 h for 16 and 64 μg/mL, with a minimum viability value of about 40-49%, demonstrating less toxicity than hGO on A549 cells. The viability values with WST-8 and apoptosis-derived calculations presented similar results, with some differences observed for the highest concentration of cGO. For instance, at 24 h and 16 μg/mL of hGO and cGO, WST-8 assay showed cell viabilities of around 80%, while the apoptosis analysis revealed viabilities of 80% and 70%, respectively. However, significant differences were observed for the highest concentration of cGO. Specifically, WST-8 assay showed that cell viability was < 40% already after 24 h, whereas with the apoptosis test, viability remained > 80% until 48 h. Furthermore, observing all three cell lines and the viability results derived from the apoptosis test, we found a time-dependent toxicity of GOs that was not evident with the WST-8 assay. The lower toxicity of GO on NB4 cells compared to A549 ones, could be explained by the lower probability of suspension cells to interact with GO flakes. When cells adhere to a substrate and cannot move to interact with nanocarriers, and their internalization become easier. Another factor could be that adherent cells have the extra cellular matrix receptors on their surface, which are crucial for increasing the interaction efficiency with GO flakes with respect to suspension cells, which

lack these receptors [43]. However, for all three cell lines, the cell viability of samples treated with hGO was consistently higher than that of samples treated with cGO at all concentrations and time points, in agreement with both the WST-8 and apoptosis analyses. In addition, hGO was not toxic at concentrations up to 4 ug/mL for all cell lines, as cell viability remained above 90% and 80% for the apoptosis and WST-8 assays, respectively, for up to 3 d of incubation, as previously reported [14]. These results confirm the possibility of using hGO safely at low concentrations (≤ 4 μg/mL) for transfection.

3.3.4 Transfection efficiency in 3D vs 2D lung cancer cell models

After validating the biocompatibility of GO, even when used at concentrations of 4 μg/mL, and optimizing spheroid growth, the following step was to test whether 3D models were different than 2D models for transfection. To this end, transfection experiments using CD47_siRNA with smGO, bmGO, sGO and bGO as delivery systems were carried out and the transfection efficiency was then evaluated in A549 2D cultures and 3D spheroids. A decrease in CD47 expression levels was represented by the shift of the peaks towards lower PE-CD47 intensities of the treated samples with respect to the controls (Figure 3.4A-H), which demonstrated the successful siRNA transfection through GO nanocarriers [44]. The carrier formulation of smGO demonstrated the highest knockdown of CD47 marker expression in both cell cultures over all other model systems, with an efficiency of 40% in 2D and 90% in 3D culture, respectively. The efficiency decreased when using sGO, resulting in approximately 7% and 61% knockdown in 2D and 3D cultures, respectively. Results using bmGO displayed values of 22% and 68% for 2D and 3D cultures, respectively, indicating a slightly higher knockdown efficiency compared to sGO. Interestingly, model systems using bGO evidenced a knockdown efficiency of only 2% and 7% in 2D and 3D cultures, respectively, which was similar to the control groups (6% and 13% for ctrl CD47 and 16% and 7% for ctrl N, in 2D and 3D cultures, respectively). Apoptosis tests were also performed

on all samples after transfection (Figure 3.4I), demonstrated the safety of all the complexes used for transfection, with cell viabilities of > 90%. These results thus revealed not only a strong dependence of CD47 knockdown efficiency on GO size and functionalization, but also a remarkable higher efficacy of such nanocarriers when used in combination with 3D over 2D cell cultures. Figure 3.4I displays the difference in transfection efficiency between the two cell cultures for each delivery system used. Significant higher knockdown percentage results are obtained for smGO, bmGO and sGO after the delivery of CD47_siRNA in spheroids in respect to 2D cell cultures, while comparable results are obtained for ctrl N, ctrl CD47 and bGO-CD47. This result is surprising since cells in a 3D configuration are closely packed to each other, and this aspect might limit the diffusion and penetration of nanocarriers in the centre of the spheroid, restricting the transfection only in the outer layer [4]. However, it has been demonstrated that the transfection efficiency in spheroids is highly dependent on the cell line. When cells form a less dense spheroid, the transfection efficiency can be high since the cell packing doesn't limit the penetration of nanocarriers to the centre of the spheroid[5]. In fact, as previously assessed, different cell lines show different abilities in packing in 3D configurations. Another factor that can affect transfection efficiency in the two different cell cultures is the cells' ability to divide. When cultured in 3D spheroids, cells have a limited proliferation capacity, which can reduce the transfectability of nucleic acid. As a result, RNAs has shown higher transfectability in non-dividing cells compared to DNA, making it more suitable for transfection in 3D cultures [34]. Another study has shown that the difference in transfection efficiency between 2D and 3D cultures can also be influenced by the delivery system used[3]. They observed that when using calcium phosphate based nanocarriers led to higher transfection efficiency in spheroids (3D) in contrast to 2D cultures. However, when using Lipofectamine (a different type of nanocarrier), the opposite result was observed (i.e., higher transfection efficiency in 2D cultures compared to spheroids). This observation is supported by studies demonstrating a higher internalization of nanocarriers in HeLa (human

cervical cancer cell line), MCF-7, and MDA-MB-231 (human breast cancer cell lines) cells grown as spheroids compared to 2D cultures [7].

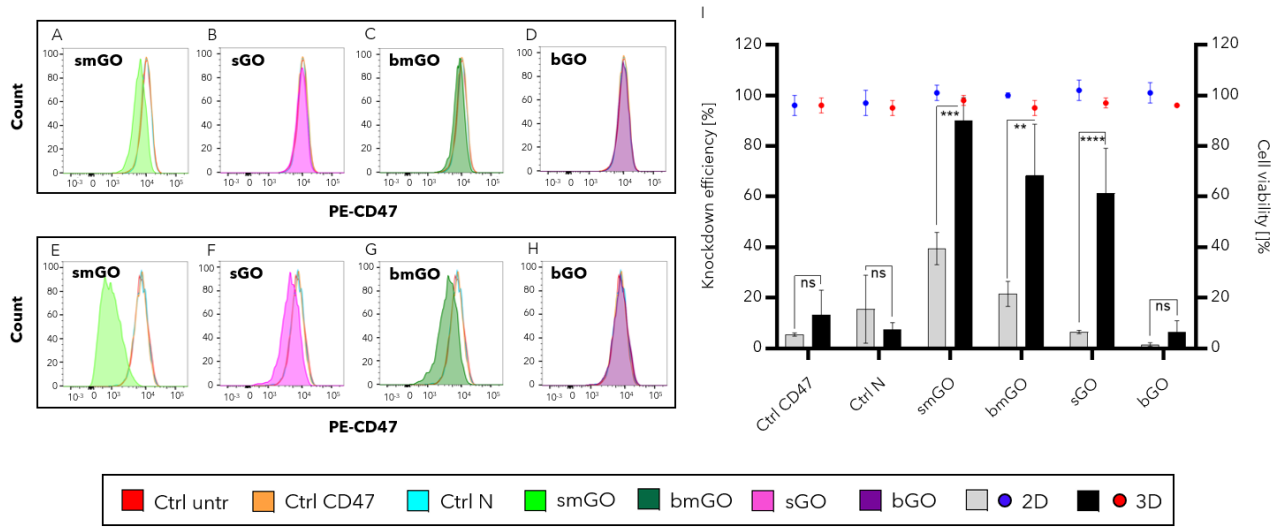

Figure 3.4. Flow cytometry histograms showing the MFI of PE-CD47 in A549 2D cell culture (A-D) and 3D spheroids (E-H) after transfection of CD47_siRNA with smGO (A, E), sGO (B, F), bmGO (C, G) and bGO (D, H). (I) Representative bar graph of the knockdown efficiency and dot plots of cell viability, both measured in respect to ctrl untr and highlighting the difference between 3D and 2D models. Values in the graphs are shown as mean ± SD of three trials of duplicate samples (n = 3). The statistical significance was determined by two-way ANOVA, where $P < 0.05$ was considered significant (*$P < 0.05$; **$P < 0.01$; ***$P < 0.001$; ****$P < 0.0001$) and $P > 0.05$ is not significant (ns).

3.3.5 Influence of GO flakes size and functionalization on transfection efficiency in 3D spheroids

The size and chemical modification of GO flakes have demonstrated to affect the CD47_siRNA transfection in A549 and other cell lines [13]. Adjusting the size of nanocarriers is an important parameter that can be altered to improve their ability to penetrate the plasma membrane [25]. In addition, chemical modification of the GO surface is another option that is often used to increase the cellular internalization of GO-based carriers [21]. Here, to assess the knockdown efficiency, we conducted an analysis comparing different GO-based nanocarrier formulations. Specifically, we compared the effectiveness of smGO, sGO, bmGO and bGO as delivery system for CD47_siRNA in A549 spheroids. In Figure 3.5A-D, the flow cytometry measurements are shown as histograms, where the shift in the curves for the cells

transfected through the different GO formulations can be compared with the three controls (ctrl untr, ctrl CD47 and ctrl N). smGO showed a narrow peak concentrated around low mean fluorescent intensity (MFI) values of PE-CD47, demonstrated an internalization of nanocarriers inside the cells and a uniform CD47 knockdown. Similarly, sGO showed a peak that was distributed at low PE fluorescent intensities, even though there were higher values as well. In contrast, bmGO exhibited a wide peak, indicating that CD47 expression was not uniform among cells after transfection. A narrow peak was displayed for the case of bGO, but no shift was observed with respect to the controls, suggesting that no transfection occurred. These results suggest the presence of a difference in the internalization and transfection processes related to the GO flake dimension. For a clear illustration, MFI values were also plotted in the dot plot in Figure 3.5E. The results showed that smGO, sGO and bmGO can be used efficiently to achieve CD47_siRNA transfection in spheroids, as the MFI of cells is significantly reduced (< 3900) after treatment compared to all three controls (> 7800; Figure 3.5E). As expected, the MFI of bGO-treated cells was not significantly lower (8620) than that of all the controls (7821-8729), demonstrating the inefficiency of such GO formulation to deliver CD47_siRNA into A549 spheroids. These results point out a size-dependent transfection efficiency that can be reconducted to the internalization of these nanocarriers by the cells, with a lower cellular uptake for the big sizes for both the modified and unmodified GO formulations. This result is also supported by other[45], whereas unmodified GO flakes with a lateral size of about 10-40 μm were observed to not be able to enter the plasma membrane. However, even if it was reported that the cell internalization of GO is size-dependent in different cell lines [46, 47], interestingly, the literature is not in total consensus [38, 48, 49]. Our results also show that smGO is the most efficient nanocarrier formulation, followed immediately by bmGO, with knockdown efficiencies of 90% and 69%, respectively (Figure 3.5F). The modification of GO flakes with PEG and PAMAM resulted in a higher transfection efficiency, demonstrating a high influence of the modification on the cellular internalization.

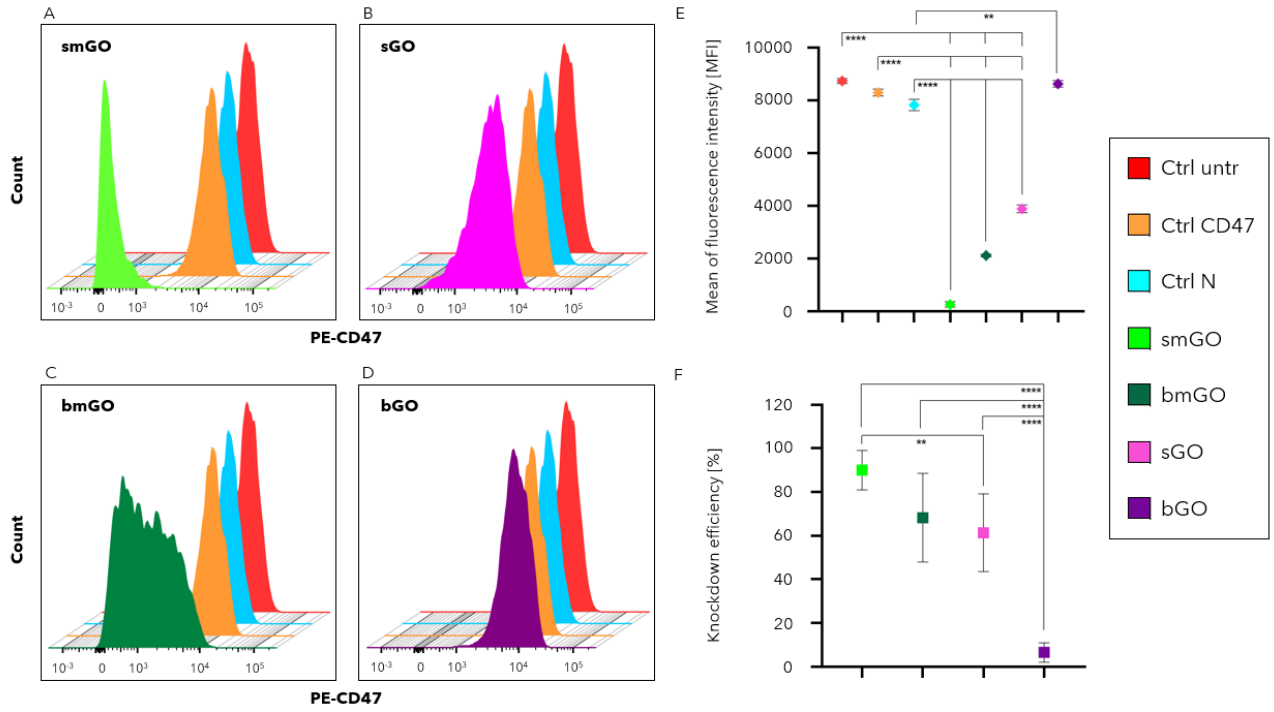

Figure 3.5. Flow cytometry measurements of PE-CD47 MFI in spheroids after transfection of CD47_siRNA complex with smGO (A), sGO (B), bmGO (C) and bGO (D). (E) Representative dot graph of MFI measured in (A-D). (F) CD47 knockdown efficiency in respect to ctrl untr of spheroids treated with the four GO formulations (smGO, sGO, bmGO and bGO). Values in the graphs are shown as mean ± SD of three trials of duplicate samples (n = 3). The statistical significance was determined by one-way ANOVA, where $P < 0.05$ was considered significant (*$P < 0.05$; **$P < 0.01$; ****$P < 0.0001$). Not significant results ($P > 0.05$) are not shown.

This result is in good agreement with the literature, since the addition of polymers (such as PEG, PEI, polyvinyl alcohol (PVA), and chitosan) on the GO flakes enhanced their stability in the body fluids, and thus increased the binding sites for the nucleic acids loading and the interactions with the plasma membranes, due to the positive charges of the polymer chains [23, 50, 51]. However, in our work the use of sGO for the transfection yields an efficiency of about 60%, significantly lower than that obtained with smGO, but comparable to the efficiency of bmGO. In contrast, bGO, as anticipated from the MFI values, exhibits significantly lower knockdown efficiency than all other GO formulations, demonstrating no transfection results. The reason why sGO showed an interestingly high transfection efficiency still needs to be better studied. Nonetheless, a possible explanation may be reconducted to the different interaction of the siRNA with the GO surface. When the GO is modified with the

addition of polymers, a higher number of binding sites are available for the nucleic acids. In addition, the positive charges of the polymers and the negative charges of the siRNA can lead to a stronger interaction [52-54]. These factors can be advantageous during the formation of siRNA-GO complexes, but detrimental for the release of the nucleic acid once the nanocarrier enter inside the cell. On the other hand, unmodified GO may be less efficient in terms of the number of nucleic acids bound to each flake, but their release in the cytosol may be easier. Modification of GO was also often used because it could avoid the clearance of the nanocarriers from the bloodstream when injected *in vivo*. However, carriers at the nanoscale can circulate in the body for longer time without being recognized by macrophages and can easier penetrate the tissues when < 200 nm [21, 55]. From these results, we observed that the modification of GO flakes might be the first parameter influencing the nanocarrier internalization by the cells, followed by their size. Nevertheless, sGO demonstrated a great potential in being used for further experiments.

3.3.6 Transfection with different ratios of anti-CD47 siRNA and GO flakes in 3D spheroids

To determine whether it was possible to increase the transfection efficiency using sGO as delivery system, we decided to determine if increasing the ratio of CD47_siRNA:GO to 3:1 would make a difference. The GO formulations used here were 1:1 and 3:1 sGO-to-bGO ratios. In Figure 6A-B the flow cytometry measurements of the treated samples were reported as peaks of PE-CD47 fluorescent intensities and compared with the ctrl untr and ctrl CD47. bGO-CD47_siRNA 1:1 showed a peak very similar in shape to the controls, with high intensity values, showing no transfection, as previously observed. Increasing the ratio to 3:1, bGO presented a little shift to the left and a wider peak, suggesting that with a higher number of siRNA bound to the GO flakes, even if a very low percentage of them are internalized by the cells, some transfection can be observed. Differently, sGO-CD47_siRNA 1:1 presents a wide peak slightly shifted in respect to the controls and spread in a range between 0 and 10^4

log fluorescent intensity. This indicated a behaviour similar to bGO-CD47_siRNA 3:1, but with a higher probability for the nanocarriers to be internalized since the peak is taller for lower intensity values. Interestingly, increasing the siRNA to delivery system ratio to 3:1, the peak distribution of fluorescent intensity remained spread over the same range, but the mean shifted to a lower fluorescent intensity. This indicates a higher average level of transfection. These observations were confirmed by the MFI values reported in Figure 6C.

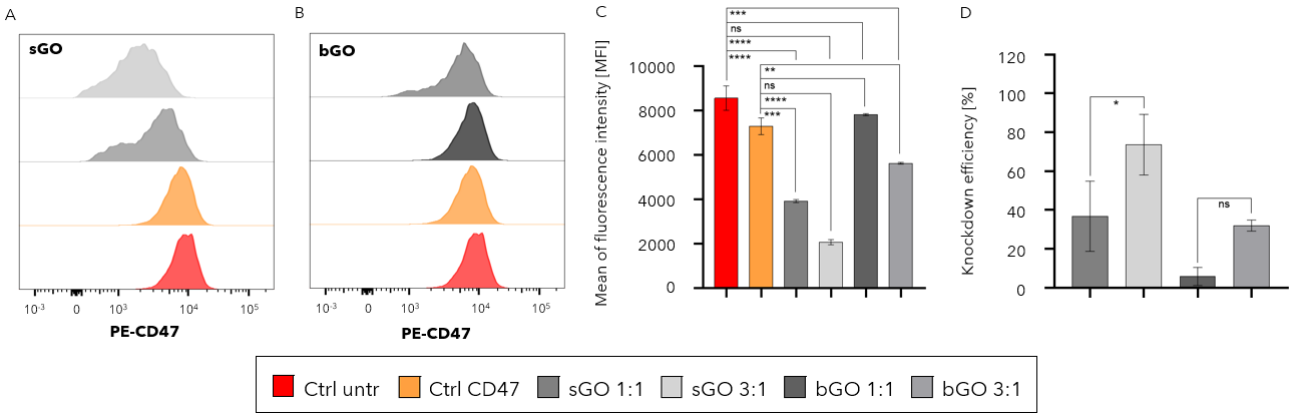

Figure 3.6. CD47 knockdown represented in flow cytometry measurement on spheroids treated with sGO (A) and bGO (B) with 1:1 and 3:1 ratio. (C) Representative bar graph of the MFI in (A-B). (D) Knockdown efficiency measured with respect to ctrl untr, and highlighting the difference between 1:1 and 3:1 ratios. Values in the graphs are shown as mean ± SD of three trials of duplicate samples (n = 3). The statistical significance was determined by one-way ANOVA, where $P < 0.05$ was considered significant (*$P < 0.05$; **$P < 0.01$; ***$P < 0.001$; ****$P < 0.0001$), and $P > 0.05$ is not significant

No significant difference in MFI was found between the CD47_siRNA:bGO 1:1 and the controls (8552 and 7289 for ctrl untr and ctrl CD47, respectively), which indicated that no transfection occurred. However, a significant decrease in MFI was reported for every other delivery system and ratio with respect to controls. This shows that these delivery systems were able to transfect CD47 in A549 spheroids, although with varying efficiency. A higher knockdown efficiency for both GO formulations when used in a 3:1 ratio was observed (Figure 6D). However, by employing bGO, the efficiency increased from about 6% to 32%, with 1:1 and 3:1 ratios, respectively, but it never exceeded 35-40% and was not significant. Therefore, bGO formulation remined the least efficient GO formulation for the experimental

conditions used in this study. On the other hand, when using sGO, the knockdown efficiency was shown to reach and exceed 80% when used in a 3:1 ratio. These results are significantly higher than those obtained with 1:1 ratio. This analysis demonstrated that increasing the CD47_siRNA:GO ratio it's possible to obtain higher transfection efficiency, as observed in other studies [14, 56]. GO thus proves to be potentially viable alternative to chemically modified GO. This alternative might be preferable in some cases because unmodified GO, such as sGO, is less processed and therefore less expensive and complex. Moreover, unmodified GO can be less toxic because it does not contain the dendrimer, which has many positive charges that are useful for binding nucleic acids but may be harmful to cells [27].

3.4 Conclusions

Tumor spheroids were successfully grown as *in vitro* cell models for CD47_siRNA transfection using GO-based vectors. Lung cancer spheroids were found to form and remain viable for up to 10 days of culture, demonstrating prolonged viability over traditional 2D cultures. Moreover, spheroids also exhibit metabolic and proliferative gradients more similar to those of *in vivo* tumors. Remarkably, our results indicate that A549 spheroids showed a higher ability to be transfected than 2D cultures, achieving silencing values of the gene responsible for CD47 marker expression around 90%. T result is very promising compared to other studies reported in the literature using different vectors and cell lines.

In addition, different hGO formulations were used and compared as vectors to deliver CD47_siRNA into A549 spheroids. First, it was shown that all four GO-based formulations did not exhibit cytotoxicity or apoptosis effects in tumor and normal cells even for concentrations much higher than that used for transfection, indicating their safety to be administered. Subsequently, it was observed that chemical modification and GO flake size are two parameters highly influencing the ability of nanocarriers to be internalized in both 2D and 3D cell cultures of A549, with modification having a greater influence than size. Interestingly,

sGO was able to achieve very similar transfection values to smGO simply by increasing the CD47_siRNA:GO ratio to 3:1, proving to be a promising alternative as a nucleic acid delivery system in cancer cells.

These results demonstrate the advantages of employing spheroid models in terms of similarity to the *in vivo* environment, ease of maintenance, and genetic manipulation using small GO-based vectors. These promising results pave the way for the use of this model system for further studies on different cell lines, vectors and therapeutic agents for the study of *in vitro* tumor gene therapies.

References

(1) Sung, H.; Ferlay, J.; Siegel, R. L.; Laversanne, M.; Soerjomataram, I.; Jemal, A.; Bray, F. Global Cancer Statistics 2020: GLOBOCAN Estimates of Incidence and Mortality Worldwide for 36 Cancers in 185 Countries. *CA Cancer J. Clin*., **2021**, *71*, 209-249.
(2) Rodrigues, T.; Kundu, B.; Silva-Correia, J.; Kundu, S. C.; Oliveira, J. M.; Reis, R. L.; Correlo, V. M. Emerging tumor spheroids technologies for 3D in vitro cancer modeling. *Pharmacol. Ther*., **2018**, *184*, 201-211.
(3) Sokolova, V.; Rojas-Sanchez, L.; Bialas, N.; Schulze, N.; Epple, M. Calcium phosphate nanoparticle-mediated transfection in 2D and 3D mono- and co-culture cell models. *Acta Biomater*., **2019**, *84*, 391-401.
(4) Monfared, Y. K.; Mahmoudian, M.; Cecone, C.; Caldera, F.; Haiaty, S.; Heidari, H. R.; Rahbarghazi, R.; Matencio, A.; Zakeri-Milani, P.; Trotta, F. Hyper-Branched Cationic Cyclodextrin Polymers for Improving Plasmid Transfection in 2D and 3D Spheroid Cells. *Pharmaceutics*, **2022**, *14*, 2690.
(5) Schäfer, M. E. A.; Keller, F.; Schumacher, J.; Haas, H.; Vascotto, F.; Sahin, U.; Hafner, M.; Rudolf, R. 3D Melanoma Cocultures as Improved Models for Nanoparticle-Mediated Delivery of RNA to Tumors. *Cells*, **2022**, *11*, 1026.
(6) Sambale, F.; Lavrentieva, A.; Stahl, F.; Blume, C.; Stiesch, M.; Kasper, C.; Bahnemann, D.; Scheper, T. Three dimensional spheroid cell culture for nanoparticle safety testing. *J. Biotechnol*., **2015**, *205*, 120-129.
(7) Juarez-Moreno, K.; Chavez-Garcia, D.; Hirata, G.; Vazquez-Duhalt, R. Monolayer (2D) or spheroids (3D) cell cultures for nanotoxicological studies? Comparison of cytotoxicity and cell internalization of nanoparticles. *Toxicol. In Vitro*, **2022**, *85*, 105461.
(8) Hurrell, T.; Lilley, K. S.; Cromarty, A. D. Proteomic responses of HepG2 cell monolayers and 3D spheroids to selected hepatotoxins. *Toxicol. Lett*., **2019**, *300*, 40-50.
(9) Huang, Z.; Yu, P.; Tang, J. Characterization of Triple-Negative Breast Cancer MDA-MB-231 Cell Spheroid Model. *Onco Targets Ther*., **2020**, *13*, 5395-5405.
(10) Rolver, M. G.; Elingaard-Larsen, L. O.; Pedersen, S. F. Assessing Cell Viability and Death in 3D Spheroid Cultures of Cancer Cells. *J. Vis. Exp*., **2019**, *148*.
(11) Feng, M.; Marjon, K. D.; Zhu, F.; Weissman-Tsukamoto, R.; Levett, A.; Sullivan, K.; Kao, K. S.; Markovic, M.; Bump, P. A.; Jackson, H. M.; Choi, T. S.; Chen, J.; Banuelos, A. M.; Liu, J.; Gip, P.; Cheng, L.; Wang, D.; Weissman, I. L. Programmed cell removal by calreticulin in tissue homeostasis and cancer. *Nat. Commun*., **2018**, *9*, 3194.
(12) Kaczmarek, J. C.; Kowalski, P. S.; Anderson, D. G. Advances in the delivery of RNA therapeutics: from concept to clinical reality. *Genome Med*., **2017**, *9*, 60.
(13) Love, K. T.; Mahon, K. P.; Levins, C. G.; Whitehead, K. A.; Querbes, W.; Dorkin, J. R.; Qin, J.; Cantley, W.; Qin, L. L.; Racie, T.; Frank-Kamenetsky, M.; Yip, K. N.; Alvarez, R.; Sah, D. W.; de Fougerolles, A.; Fitzgerald, K.; Koteliansky, V.; Akinc, A.; Langer, R.; Anderson, D. G. Lipid-like materials for low-dose, in vivo gene silencing. *Proc. Natl. Acad. Sci. USA*, **2010**, *107*, 1864-1869.
(14) Hassan, E. M.; Zou, S. Novel nanocarriers for silencing anti-phagocytosis CD47 marker in acute myeloid leukemia cells. *Colloids Surf B Biointerfaces*, **2022**, *217*, 112609.
(15) Singh, A.; Trivedi, P.; Jain, N. K. Advances in siRNA delivery in cancer therapy. *Artif. Cells Nanomed. Biotechnol*., **2018**, *46*, 274-283.
(16) Hayat, S. M. G.; Bianconi, V.; Pirro, M.; Jaafari, M. R.; Hatamipour, M.; Sahebkar, A. CD47: role in the immune system and application to cancer therapy. *Cell. Oncol*., **2020**, *43*, 19-30.
(17) Hassan, E. M.; McWhirter, S.; Walker, G. C.; Martinez-Rubi, Y.; Zou, S. Elimination of Cancer Cells in Co-Culture: Role of Different Nanocarriers in Regulation of CD47 and Calreticulin-Induced Phagocytosis. *ACS Appl. Mater. Interfaces*, **2023**, *15*, 3791-3803.
(18) Alexis, F.; Pridgen, E.; Molnar, L. K.; Farokhzad, O. C. Factors Affecting the Clearance and Biodistribution of Polymeric Nanoparticles. *Mol. Pharm*., **2008**, *5*, 505-515.
(19) Layzer, J. M.; McCaffrey, A. P.; Tanner, A. K.; Huang, Z.; Kay, M. A.; Sullenger, B. A. In vivo activity of nuclease-resistant siRNAs. *RNA*, **2004**, *10*, 766-771.
(20) Whitehead, K. A.; Langer, R.; Anderson, D. G. Knocking down barriers: advances in siRNA delivery. *Nat. Rev. Drug Discov*., **2009**, *8*, 129-138.
(21) Itoo, A. M.; Vemula, S. L.; Gupta, M. T.; Giram, M. V.; Kumar, S. A.; Ghosh, B.; Biswas, S. Multifunctional graphene oxide nanoparticles for drug delivery in cancer. *J. Control Release*, **2022**, *350*, 26-59.
(22) Morgan, R. G.; Chambers, A. C.; Legge, D. N.; Coles, S. J.; Greenhough, A.; Williams, A. C. Optimized delivery of siRNA into 3D tumor spheroid cultures in situ. *Sci. Rep*., **2018**, *8*, 7952.
(23) Saravanabhavan, S. S.; Rethinasabapathy, M.; Zsolt, S.; Kalambettu, A. B.; Elumalai, S.; Janakiraman, M.; Huh, Y. S.; Natesan, B. Graphene oxide functionalized with chitosan based nanoparticles as a carrier of siRNA in regulating Bcl-2 expression on Saos-2 & MG-63 cancer cells and its inflammatory response on bone marrow derived cells from mice. *Mater. Sci. Eng. C Mater. Biol. Appl*., **2019**, *99*, 1459-1468.

(24) Wang, L.; Yan, J. Superficial synthesis of photoactive copper sulfide quantum dots loaded nano-graphene oxide sheets combined with near infrared (NIR) laser for enhanced photothermal therapy on breast cancer in nursing care management. *J. Photochem. Photobiol. B*, **2019**, *192*, 68-73.
(25) Grilli, F.; Hajimohammadi, P. G.; Zou, S. Characteristics of Graphene Oxide for Gene Transfection and Controlled Release in Breast Cancer Cells. *Int. J. Mol. Sci*., **2022**, *23*.
(26) Karki, N.; Tiwari, H.; Pal, M.; Chaurasia, A.; Bal, R.; Joshi, P.; Sahoo, N. G. Functionalized graphene oxides for drug loading, release and delivery of poorly water soluble anticancer drug: A comparative study. *Colloids Surf. B Biointerfaces*, **2018**, *169*, 265-272.
(27) Chen, S.; Zhang, S.; Wang, Y.; Yang, X.; Yang, H.; Cui, C. Anti-EpCAM functionalized graphene oxide vector for tumor targeted siRNA delivery and cancer therapy. *Asian J. Pharm. Sci*., **2021**, *16*, 598-611.
(28) Kiew, S. F.; Kiew, L. V.; Lee, H. B.; Imae, T.; Chung, L. Y. Assessing biocompatibility of graphene oxide-based nanocarriers: A review. *J. Control Release*, **2016**, *226*, 217-228.
(29) Ishiguro, T.; Ohata, H.; Sato, A.; Yamawaki, K.; Enomoto, T.; Okamoto, K. Tumor-derived spheroids: Relevance to cancer stem cells and clinical applications. *Cancer Sci*., **2017**, *108*, 283-289.
(30) Mukundan, S.; Singh, P.; Shah, A.; Kumar, R.; O'Neill, K. C.; Carter, C. L.; Russell, D. G.; Subbian, S.; Parekkadan, B. In Vitro Miniaturized Tuberculosis Spheroid Model. *Biomedicines*, **2021**, *9*, 1209.
(31) Stransky, S.; Cutler, R.; Aguilan, J.; Nieves, E.; Sidoli, S. Investigation of reversible histone acetylation and dynamics in gene expression regulation using 3D liver spheroid model. *Epigenetics Chromatin*, **2022**, *15*, 35.
(32) Saleh, F.; Harb, A.; Soudani, N.; Zaraket, H. A three-dimensional A549 cell culture model to study respiratory syncytial virus infections. *J. Infect. Public Health*, **2020**, *13*, 1142-1147.
(33) Limame, R.; Wouters, A.; Pauwels, B.; Fransen, E.; Peeters, M.; Lardon, F.; De Wever, O.; Pauwels, P. Comparative analysis of dynamic cell viability, migration and invasion assessments by novel real-time technology and classic endpoint assays. *PLoS One*, **2012**, *7*, e46536.
(34) Uchida, S.; Yanagihara, K.; Matsui, A.; Kataoka, K.; Itaka, K. mRNA as a Tool for Gene Transfection in 3D Cell Culture for Future Regenerative Therapy. *Micromachines*, **2020**, *11*, 426.
(35) Ravi, M.; Kaviya, S. R.; Paramesh, V. Culture phases, cytotoxicity and protein expressions of agarose hydrogel induced Sp2/0, A549, MCF-7 cell line 3D cultures. *Cytotechnology*, **2016**, *68*, 429-441.
(36) Kessel, S.; Cribbes, S.; Bonasu, S.; Rice, W.; Qiu, J.; Chan, L. L. Real-time viability and apoptosis kinetic detection method of 3D multicellular tumor spheroids using the Celigo Image Cytometer. *Cytometry A*, **2017**, *91*, 883-892.
(37) Singh, M.; Close, D. A.; Mukundan, S.; Johnston, P. A.; Sant, S. Production of Uniform 3D Microtumors in Hydrogel Microwell Arrays for Measurement of Viability, Morphology, and Signaling Pathway Activation. *Assay Drug Dev. Technol*., **2015**, *13*, 570-583.
(38) Ito, A.; Nasako, H.; Akizuki, R.; Takashina, Y.; Eguchi, H.; Matsunaga, T.; Yoshino, Y.; Endo, S.; Ikari, A. Elevation of Chemosensitivity of Lung Adenocarcinoma A549 Spheroid Cells by Claudin-2 Knockdown through Activation of Glucose Transport and Inhibition of Nrf2 Signal. *Int. J. Mol. Sci*., **2021**, *22*, 6582.
(39) Coleman, B. R.; Knight, T.; Gies, V.; Jakubek, Z. J.; Zou, S. Cytotoxicity Assessment of Ti–Al–C Based MAX Phases and Ti3C2Tx MXenes on Human Fibroblasts and Cervical Cancer Cells. *ACS Appl. Mater. Interfaces*, **2017**, *9*, 28911-28921.
(40) Liao, Y.; Wang, W.; Li, Z.; Wang, Y.; Zhang, L.; Huang, X.; Cai, P. Comparative proteomic analysis reveals cytotoxicity induced by graphene oxide exposure in A549 cells. *J. Appl. Toxicol*., **2021**, *41*, 1103-1114.
(41) Liao, K. H.; Lin, Y. S.; Macosko, C. W.; Haynes, C. L. Cytotoxicity of graphene oxide and graphene in human erythrocytes and skin fibroblasts. *ACS Appl. Mater. Interfaces*, **2011**, *3*, 2607-2615.
(42) Gurunathan, S.; Kang, M. H.; Jeyaraj, M.; Kim, J. H. Mitochondrial Peptide Humanin Protects Silver Nanoparticles-Induced Neurotoxicity in Human Neuroblastoma Cancer Cells (SH-SY5Y). *Int. J. Mol. Sci*., **2019**, *20*, 4439.
(43) Montier, T.; Delepine, P.; Le Ny, K.; Fichou, Y.; Le Bris, M.; Hardy, E.; Picquet, E.; Clement, J. C.; Yaouanc, J. J.; Ferec, C. KLN-5: a safe monocationic lipophosphoramide to transfect efficiently haematopoietic cell lines and human $CD34^+$ cells. *Biochim. Biophys. Acta*, **2004**, *1665*, 118-133.
(44) Liu, J.; Wang, L.; Zhao, F.; Tseng, S.; Narayanan, C.; Shura, L.; Willingham, S.; Howard, M.; Prohaska, S.; Volkmer, J.; Chao, M.; Weissman, I. L.; Majeti, R. Pre-Clinical Development of a Humanized Anti-CD47 Antibody with Anti-Cancer Therapeutic Potential. *PLoS One*, **2015**, *10*, e0137345.
(45) Zhou, M.; Lozano, N.; Wychowaniec, J. K.; Hodgkinson, T.; Richardson, S. M.; Kostarelos, K.; Hoyland, J. A. Graphene oxide: A growth factor delivery carrier to enhance chondrogenic differentiation of human mesenchymal stem cells in 3D hydrogels. *Acta Biomater*., **2019**, *96*, 271-280.
(46) Di Santo, R.; Digiacomo, L.; Palchetti, S.; Palmieri, V.; Perini, G.; Pozzi, D.; Papi, M.; Caracciolo, G. Microfluidic manufacturing of surface-functionalized graphene oxide nanoflakes for gene delivery. *Nanoscale*, **2019**, *11*, 2733-2741.
(47) Mirzaie, V.; Ansari, M.; Nematollahi-Mahani, S. N.; Nasery, M. M.; Karimi, B.; Eslaminejad, T.; Pourshojaei, Y. Nano-Graphene Oxide-supported APTES-Spermine, as Gene Delivery System, for Transfection of pEGFP-p53 into Breast Cancer Cell Lines. *Drug. Des. Devel. Ther*., **2020**, *14*, 3087-3097.

(48) Contreras-Torres, F. F.; Rodriguez-Galvan, A.; Guerrero-Beltran, C. E.; Martinez-Loran, E.; Vazquez-Garza, E.; Ornelas-Soto, N.; Garcia-Rivas, G. Differential cytotoxicity and internalization of graphene family nanomaterials in myocardial cells. *Mater. Sci. Eng. C Mater. Biol. Appl*., **2017**, *73*, 633-642.
(49) Mendes, R. G.; Koch, B.; Bachmatiuk, A.; Ma, X.; Sanchez, S.; Damm, C.; Schmidt, O. G.; Gemming, T.; Eckert, J.; Rummeli, M. H. A size dependent evaluation of the cytotoxicity and uptake of nanographene oxide. *J. Mater. Chem. B*, **2015**, *3*, 2522-2529.
(50) Mirzaie, Z.; Reisi-Vanani, A.; Barati, M. Polyvinyl alcohol-sodium alginate blend, composited with 3D-graphene oxide as a controlled release system for curcumin. *J. Drug Deliv. Sci. Technol*., **2019**, *50*, 380-387.
(51) Zhang, J.; Yan, L.; Wei, P.; Zhou, R.; Hua, C.; Xiao, M.; Tu, Y.; Gu, Z.; Wei, T. PEG-GO@XN nanocomposite suppresses breast cancer metastasis via inhibition of mitochondrial oxidative phosphorylation and blockade of epithelial-to-mesenchymal transition. *Eur. J. Pharmacol*., **2021**, *895*, 173866.
(52) Bao, H.; Pan, Y.; Ping, Y.; Sahoo, N. G.; Wu, T.; Li, L.; Li, J.; Gan, L. H. Biodegradation of graphene oxide-polymer nanocomposite films in wastewater. *Small*, **2011**, *7*, 1569-1578.
(53) He, Y.; Zhang, L.; Chen, Z.; Liang, Y.; Zhang, Y.; Bai, Y.; Zhang, J.; Li, Y. Enhanced chemotherapy efficacy by co-delivery of shABCG2 and doxorubicin with a pH-responsive charge-reversible layered graphene oxide nanocomplex. *J. Mater. Chem. B*, **2015**, *3*, 6462-6472.
(54) Yadav, N.; Kumar, N.; Prasad, P.; Shirbhate, S.; Sehrawat, S.; Lochab, B. Stable Dispersions of Covalently Tethered Polymer Improved Graphene Oxide Nanoconjugates as an Effective Vector for siRNA Delivery. *ACS Appl. Mater. Interfaces*, **2018**, *10*, 14577-14593.
(55) Zhi, F.; Dong, H.; Jia, X.; Guo, W.; Lu, H.; Yang, Y.; Ju, H.; Zhang, X. ; Hu, Y. Functionalized Graphene Oxide Mediated Adriamycin Delivery and miR-21 Gene Silencing to Overcome Tumor Multidrug Resistance In Vitro. *PLoS One*, **2013**, *8*, e60034.
(56) Yazdani, S.; Mozaffarian, M.; Pazuki, G.; Hadidi, N.; Gallego, I.; Puras, G.; Pedraz, J. L. Design of double functionalized carbon nanotube for amphotericin B and genetic material delivery. *Sci. Rep*., **2022**, *12*, 21114.

Chapter 4: Graphene Oxide-Based Gene Modulation in Preferential Elimination of Lung Cancer Cells in a 3D Tumor Microenvironment Model

This chapter reports a research article centered on the development and application of a multicellular 3D tumor microenvironment model to evaluate gene therapy strategies for preferential cancer cell elimination. The model integrates lung cancer cells, stromal fibroblasts, and macrophages within an extracellular matrix to capture key biological and structural features that regulate therapeutic specificity in complex tumor settings. The Supplementary Information associated with this published article is included in the Appendix of this thesis for completeness.

I had a primary role in the conceptualization and execution of this study. I performed most of the experimental work, including cell culture, flow cytometry, immunohistochemistry, cell viability and apoptosis assays, as well as the majority of imaging and quantitative PCR analyses. I prepared all figures and led the drafting of the manuscript. Assistance was limited to the preparation and sectioning of the 3D models; all other data analysis, interpretation, and experimental work were conducted by me.

Reference:

Grilli, F.; Sakib, S.; Variola, F.; Zou, S. Graphene Oxide-Based Gene Modulation in Preferential Elimination of Lung Cancer Cells in a 3D Tumor Microenvironment Model. Adv. Nanobiomed. Res. 2025, 5, 2500028.

Abstract

Lung cancer remains the leading cause of cancer-related mortality worldwide, owing to its aggressive nature, late-stage diagnosis, and resistance to conventional therapies. Gene therapy offers a promising alternative by modulating specific genetic pathways to target cancer cells while sparing healthy cells. This study investigates the potential of chemically functionalized nanoscale graphene oxide (GO) as carriers for delivering therapeutic genes in a three-dimensional tumor microenvironment (TME) model, incorporating lung cancer cells, human lung fibroblasts, and macrophages in a Matrigel-collagen matrix to mimic the structural properties and immune functions. These therapeutic genes, including small interfering RNAs (siRNA) and plasmid DNAs (pDNA), regulate immune evasion markers (CD47 and CD24) and apoptosis-inducing proteins (ANT1). GO nanocarriers demonstrate preferential uptake in cancer cells, achieving transfection and gene modulation within the TME model. The individual delivery of genes downregulates cancer markers and induces ANT1 expression, resulting in lung cancer cell elimination. Co-delivery of CD47_siRNA and ANT1_pDNA produces synergistic efficacy, enhancing cancer cell elimination. These findings highlight the potential of GO-based gene therapies as a targeted and effective approach for lung cancer treatment, setting the stage for *in vivo* validation and clinical translation.

4.1 Introduction

Globally, lung cancer ranks as the highest contributor to cancer-related mortality [1]. driven by its rapid progression, frequent late-stage detection, and the limited efficacy of conventional treatments, including chemotherapy and radiotherapy. Additionally, these therapies are inherently non-specific and often cause significant damage to healthy, non-malignant tissues. For instance, chemotherapeutic agents and radiation therapies can adversely affect high-turnover tissues, leading to side effects such as myelosuppression, mucositis, anemia, alopecia, and pneumonitis [2-4].

These challenges have accelerated the development of innovative, targeted therapeutic approaches, with nanocarrier-based nucleic acid delivery emerging as a promising alternative [5]. This strategy leverages nanocarriers modified with different functional groups or targeting ligands to ensure precise and effective delivery of gene molecules such as messenger RNA (mRNA), small interfering RNA (siRNA), and microRNA (miRNA) to the target cell populations [5]. By selectively modulating gene expression in cancer cells, gene therapy offers a more focused approach to suppress tumor growth and enhance immune-mediated cancer cell destruction while minimizing effects on healthy tissues [6].

Graphene oxide (GO) has gained considerable attention as a nanocarrier platform for gene therapy due to its exceptional physical and chemical properties [7-10]. Its large surface area and abundance of oxygen-containing functional groups enable efficient loading of diverse therapeutic nucleic acids, including siRNA and plasmid DNA (pDNA) [11]. Functionalization with polyethylene glycol (PEG) and polyamidoamine (PAMAM) enhances GO's stability, biocompatibility, and cellular internalization [12]. GO materials have shown distinct advantages for gene delivery over other nanocarriers. While viral vectors and lipid-based nanoparticles are among the most established gene delivery systems, they pose notable limitations. Viral vectors offer high transfection efficiency but raise concerns regarding immunogenicity, insertional mutagenesis, and limited cargo capacity [13]. Lipid nanoparticles (LNPs), such as those used in mRNA vaccine formulations, have shown promise for systemic delivery but often face challenges, including variable biodistribution, poor solid tumor penetration, and inflammatory responses [14]. Physical methods like electroporation can facilitate non-viral transfection but are typically invasive, poorly reproducible, and less suitable for *in vivo* applications due to cell damage and low viability [15]. In our previous work [16, 17], we demonstrated that GO nanocarriers achieve comparable or improved delivery outcomes relative to these platforms, with reduced immunogenicity and enhanced stability under physiological conditions. These attributes position GO as a promising alternative for gene delivery, particularly in complex environments such as the AFT 3D lung cancer model. Another example is polyethyleneimine (PEI),

a cationic polymer, that has demonstrated a strong binding affinity to nucleic acids, allowing for high drug loading capacity, which is then efficiently taken up by cells and subsequently released. However, poor bioavailability and high cytotoxicity limit the use of PEI as a carrier. Modifying PEI with GO can minimize this cytotoxicity and result in high transfection efficiency [18, 19]. GO-based carriers also exhibit considerably higher drug-loading capacity, enabled by their large surface area, π-π stacking and electrostatic interactions, compared to lipid nanocarriers and liposomes, which have limited loading capacity due to the constraints posed by a lipid bilayer and the aqueous core [20, 21]. One study demonstrated higher transfection efficiency of pluripotent stem cells using GO-PEI carriers compared to a commercially available lipid nanocarrier kit (Lipofectamine) [22]. The same study also reported that GO carriers exhibited lower immunogenicity, likely contributing to improved bioavailability through reduced immune clearance [22]. Additionally, stimuli-responsive GO systems have emerged as promising innovations. These systems are engineered to respond to specific tumor-associated triggers such as acidic pH, elevated glutathione (GSH), or overexpressed enzymes like matrix metalloproteinases, enabling localized and controlled gene or drug release [23-28]. This strategy reduces systemic toxicity and enhances delivery precision within the tumor microenvironment. In our previous work [29-30], we analyzed various GO formulations differing in size—small (~100 nm) and large (>650 nm)—and surface functionalization (unmodified, PEGylated, and/or conjugated with the dendrimer PAMAM) for siRNA transfection in A549 lung cancer spheroids. Among these, the small modified GO (smGO) nanocarrier demonstrated the highest transfection efficiency, achieving over 90% siRNA delivery in 3D lung cancer spheroid models [31]. Building on this foundation, we now aim to explore the versatility of this platform for delivering multiple nucleic acids targeting various genes, potentially enhancing therapeutic specificity.

CD47 is an immune checkpoint protein that inhibits macrophage-mediated phagocytosis by engaging the signal regulatory protein alpha (SIRPα) receptor on macrophages, allowing cancer cells to evade immune surveillance [32], CD24 similarly functions as an immune-evasion marker by binding to sialic acid, binding Ig like lectin 10 (SIGLEC-10) on macrophages, suppressing the immune response

[33, 34]. In contrast, ANT1, a mitochondrial protein, promotes apoptosis by disrupting mitochondrial function, exploiting the metabolic vulnerabilities of cancer cells [35]. In our earlier work, we demonstrated the efficacy of CD47_siRNA delivery in silencing the CD47 gene, paving the way for immune-mediated cancer cell clearance [16, 36]. Expanding this approach to CD24_siRNA and ANT1_pDNA offers a multi-faceted strategy for inducing cancer cell death through complementary mechanisms.

The tumor microenvironment (TME) consists of complex interactions between cancer cells, stromal cells, immune cells, and the extracellular matrix (ECM), all of which play significant roles in tumor progression and response to therapies [37]. Among these, macrophages are critical in immune surveillance and cancer cell elimination [38]. However, cancer cells often utilize immune evasion strategies to escape detection, such as the modulation of immune checkpoints [39]. Immune checkpoint molecules, like CD47 and CD24, disrupt macrophage-mediated responses, while reduced expression of proteins such as ANT1 helps cancer cells resist apoptosis [33, 40, 41]. Overcoming these evasion mechanisms remains a critical challenge for effective cancer therapy.

This paper explores the potential of smGO nanocarriers as a versatile platform for the delivery of multiple genes aimed at the specific elimination of lung cancer. A major challenge in translating gene therapies to clinical applications is the lack of preclinical models that capture the complexity of interactions between cancer cells, stromal cells, immune cells, and the ECM [42-44]. Here, we created a 3D multi-cell model that incorporates key components of the TME, providing a functional system for studying cancer elimination therapies. This 3D lung cancer model, referred to as the AFT model, incorporates A549 lung cancer cells, human lung fibroblasts (HLF), and THP-1-derived macrophages embedded in a Matrigel-collagen matrix. This multi-cellular model is designed to reflect key cellular and non-cellular structural and immune components of the TME, offering a more comprehensive valuation of gene therapy specificity and efficacy. The Matrigel-collagen ECM mimics the structural and biochemical factors present in TME and provides factors such as laminin, collagen, nidogen, and

proteoglycans to promote migration, cell-cell interactions, and immune cell infiltration [45, 46]. Additionally, the AFT model also recapitulates the interplay between cancer cells, immune cells, and stromal cells that drive tumor growth and facilitate immune evasion in the TME, representing a more physiologically relevant model to study cancer-stromal crosstalk, ECM-mediated signaling, and macrophage-mediated phagocytic elimination of cancer [47]. THP-1-derived macrophages have widely been used as a suitable *in vitro* model to study M1/M2 polarization and tumor–immune interactions due to their tumor-associated macrophage (TAM)-like behaviour [48]. When cultured with cancer cells or cancer cell-conditioned media, THP-1 macrophages upregulate TAM markers and acquire phenotypic traits associated with the tumor microenvironment [49, 51]. While the AFT model may not fully represent the entirety of TME interactions, it nonetheless provides valuable insights into the immune functions within the TME, which are critical for determining therapeutic potential. Using this system, we assessed the internalization and gene modulation capabilities of smGO nanocarriers, followed by demonstrating their high efficiency in regulating target proteins, specifically the cancer cell markers CD47 and CD24, as well as ANT1, which are associated with apoptosis and cancer progression. Notably, macrophages help enhance cancer cell elimination by mediating immune responses, which are disrupted in cancer cells through CD47 and CD24 siRNA therapies. In addition, we also exploit the large surface area and functional groups on smGO nanocarriers to achieve co-delivery of multiple gene cargos and harness their synergistic effects to achieve enhanced cancer-specific elimination.

4.2. Materials and methods

4.2.1 Chemicals and Reagents

A549 (human lung cancer cell) and THP-1 (acute myelocytic leukemia cancer cells) were purchased from the American Type Culture Collection (ATCC, USA). HLF (human lung fibroblasts) and FGM™-2 Fibroblast Growth Medium-2 BulletKit™ (Fibroblast Growth Basal medium (FBM-2),

insulin, human fibroblastic growth factor (hFGF-B) and gentamicin sulfate-amphotericin (GA-1000)) were purchased from Lonza (Canada). 6-arm amine-terminated polyethylene glycol (PEG, 25 mg, 15 kDa) was purchased from Jenkem Technology (USA), and PAMAM dendrimers (10 μL, 4.0 generation, primary amine, 10.1 w/w% in water, 10 kDa) from Dendritech Inc. (USA). Dulbecco's Modified Eagle's Medium (DMEM), Phosphate Buffered Saline (PBS) 1X solution (pH 7.4), Fetal Bovine Serum (FBS), bovine serum albumin (BSA), 0.5% trypsin EDTA (10X Trypsin), Matrigel® Matrix Basement Membrane Growth factor reduced, Opti-MEM transfection media, Nunclon™ Sphera™ 96-well U-bottom, 12-well flat bottom super low attachment plates, 96-well flat bottom plates, Power SYBR Green RNA-to-CT 1-Step Kit, Fisher Healthcare Tissue-Plus™ O.C.T. Compound, Caspase 9, CD14, CD68, CD24, CD47 monoclonal antibodies, goat anti-rabbit IgG secondary antibody Alexa Fluor 488 and 555, goat anti-mouse IgG secondary antibody Alexa Fluor 555, Hoechst 33342, Prolong Gold Antifade Mountant and Normal Goat Serum 10% were purchased from Thermo Fisher Scientific (Canada). Glass-bottom dishes (0.17 mm/#1.5) were purchased from Willco Wells B.V. Collagen Type I Rat Tail from Corning (USA). Cell Titer-Glo® 3D Cell Viability Assay and Caspase-Glo® 3/7 Assay were purchased from Promega (Canada). CD24 Silencer Select (CD24_siRNA) and Silencer Select Negative Control (NC 24) were purchased from Ambion (Canada). SLC25A4 lenti-ORF (ANT1_pDNA) was purchased from Origene (Canada). DsiRNA CD47 (CD47_siRNA), negative control DsiRNA (NC 47) and Nuclease Free Duplex Buffer used for transfection were purchased from Integrated DNA Technologies (IDT, USA). BD Pharmingen™ PE Annexin V Apoptosis Detection Kit I was purchased from BD Biosciences (USA). PE-anti-human CD47 and CD24 antibodies for flow cytometry were purchased from BioLegend (USA). RNeasy UCP Micro Kit for RNA extraction analysis and Quantitect Primer assays for GAPDH, CD47, CD24 and SLC25A4 (ANT1) used for reverse transcription polymerase chain reaction (RT-qPCR) analysis were purchased from QIAGEN (USA). Anti-Cytokeratin 7 (CK7) antibody and Alexa Fluor®488 Lightning-Link antibody conjugation kit for GO labeling were purchased from Abcam (Canada).

4.2.2 Preparation of GO-based nanocarrier

GO was synthesized through the modified Hummer's method and filtered to produce GO flakes (with most flake sizes > 650 nm). GO underwent a sonication process (probe sonicator, Cole Parmer, Canada) at 10 W for nine intervals of 10 minutes on/off in a 0 °C water bath used to create small flakes of GO (with lateral dimension around 100 nm). Subsequently, GO was chemically modified by adding PEG and PAMAM, as previously reported [15].

4.2.3 Atomic force microscopy

Atomic force microscopy topography imaging was carried out via a MultiMode AFM with a NanoScope V controller (Bruker Nano Surfaces Division, Santa Barbara, CA, USA) in the Peak Force QNM mode. The peak force to tap the sample surface with the tip was kept at the lowest stable imaging level of 200–400 pN. Silicon nitride ScanAsyst-Air AFM probes (Bruker AFM Probes, Camarillo, CA, USA) were used in peak force feedback measurements. Their manufacturer specified that typical tip diameter and spring constants are 2 nm and 0.4 N/m, respectively. While images of sizes of up to 20 μm × 20 μm were acquired to ensure good homogeneity without overlapping of flakes of GO and modified GO, all the images used to measure the size of the flakes were 0.5–2 and 2.5–5 μm in scan size, for small-GO (or GO-conjugates) and big-GO (or GO-conjugates), respectively, acquired with 512 × 512 pixels or 1024 × 1024 resolution. The AFM probe cantilever was vertically oscillated at 2 kHz at a lateral scan rate of 0.8–1.4 Hz.

4.2.4 Fourier transform infrared (FTIR)

The chemical properties of smGO and GO were characterized using an FTIR spectrometer (Nicolet 6700, ThermoFisher) equipped with a substrate sample holder accessory. This allowed measurements

of GO and smGO on thin films on silicon substrates in the range of 400 to 4000 cm^{-1} with a resolution of 4 cm^{-1}.

Conjugation of Alexa Flour 488 to smGO: smGO was labeled with Alexa Fluor 488 dye following the manufactory protocol. Briefly, the modifier was added to 10 μg of smGO (1 mg mL-1), mixed with the lyophilized Alexa Fluor 488 conjugation mix and incubated for 15 mins. Finally, the quencher was added and incubated for 5 mins. The conjugated smGO was stored at 4°C in darkness.

4.2.5 Nucleic acid loading of smGO

For the preparation of the CD47_siRNA, CD24_siRNA, ANT1_pDNA and smGO complexes (smGO-CD47_siRNA; smGO-CD24_siRNA; smGO-ANT1_pDNA), transfection-mixes were prepared by mixing the different nucleic acids (in 3:1 nucleic acid:smGO wt:wt) in 200 μL of Opti-MEM transfection media with smGO, and incubated for 1 h at room temperature (21 ± 2 °C). Universal negative controls (NC 47; NC 24) were used to form smGO-NC47 and smGO-NC24 complexes. For co-delivery purposes, transfection mixes were prepared following the same procedure by mixing two different nucleic acids (in 1.5:1.5:1 nucleic acid 1:nucleic acid 2:smGO wt:wt:wt) in 200 μL of Opti-MEM transfection media with smGO to obtain smGO-CD47_siRNA-CD24_siRNA, smGO-CD47_siRNA-ANT1_pDNA and smGO-CD24_siRNA-CD47_siRNA complexes.

4.2.6 Cell culture

A549 were cultured in DMEM, supplemented with 10% FBS. THP-1 was cultured in RPMI-1640 supplemented with 10% FBS and 2-mercaptoethanol to a final concentration of 0.05 mM, respectively. HLF were cultured in Fibroblast Growth Basal medium (FBM-2) supplemented with 5% Insulin, 5% of human fibroblastic growth factor (hFGF-B), and 5% gentamicin sulfate-

amphotericin (GA-1000). All the cells were cultured at 37 °C in a humidified atmosphere containing 5% CO2.

4.2.7 Generation of 3D AFT model with A549, HLF, and THP-1 Cells

All cell lines were cultured in 2D, trypsinized and centrifuged at 1500 rpm for 5 min. Successively, 5×10^3 cells per sphere of each cell line (i.e., A549, THP-1, and HLF) were counted and suspended in a 1:1 mixture of Matrigel and collagen and seeded in 5 µL droplets onto a non-adherent 6 or 12-well plate to form spheroids. The three-cell model in matrice containing A549, HLF, and THP-1 cells, labeled as AFT model, was incubated at 37 °C for 40 minutes to allow the matrix to polymerize. Subsequently, 1 mL of DMEM + 10% FBS was added and changed every 2 days for 6 days to allow the cells to grow and form the 3D structures inside the matrix.

Single-cell or two-cell models in different combinations were realized, following the same procedure as explained above, and used as control models: A549 alone (A model), HLF alone (F model), THP-1 alone (T model), A549 and HLF alone (AF model), A549 and THP-1 (AT model), HLF and THP-1 (FT model).

4.2.8 Transfections

AFT models were placed in 12-well low attachment plates with Opti-MEM media for transfection. A549, HLF and THP-1 single cells were seeded on adherent 6-well plates at a density of 1.25×10^5 cells per well and incubated in DMEM for 24 h at 37 °C under 5% CO2 to allow them to adhere. The following day, the media was removed and replaced with Opti-MEM media for transfection. The different transfection mixes (smGO-CD47; smGO-CD24; smGO-ANT1, smGO-CD47-CD24; smGO-CD47-ANT1, smGO-CD24-ANT1) were added to the cells and AFT models at a concentration of 1 µg mL^{-1} and incubated at 37 °C under 5% CO2 for 24, 48, and 72 h. For the groups

treated with CD47_siRNA and CD24_siRNA, universal negative controls (NC 47; NC 24) were used as controls. CD47_siRNA, CD24_siRNA, and ANT1_pDNA alone were also used to evaluate the uptake of the target siRNAs and pDNA by the cells without any delivery system. smGO alone (with lower concentration) was also tested to confirm no effects from the carrier nanomaterial. Finally, untreated cells were used as transfection controls (untrans). For smGO uptake analysis, smGO-Alexa Fluor 488 without nucleic acid was used and incubated for 24 and 48 h with the 2D monocultures and 72h with the AFT model.

4.2.9 Immunohistochemistry (IHC) and immunocytochemistry (ICC)

For IHC, the AFT models were harvested, washed, and freshly frozen in the OCT compound to generate tissue blocks. The frozen blocks were used to prepare frozen sections (10 μm) placed on glass slides (Figure S4.1C in the SI). For ICC, dissociated A549, HLFs, and THP-1 monocytes were fixed with 4% PFA, suspended at a concentration of 1x106 cells mL^{-1}, and placed on slides using Shandon Cytospin 4 Cytocentrifuge. The slides were washed with PBS and blocked with 10% goat serum for 1h at RT. The sections were then incubated with the primary antibodies (at a 1:100 dilution) overnight at 4 °C. Fluorescence labeling was performed using secondary antibodies conjugated with Alexa Fluor 488 and 555 (at a 1:500 dilution) for 1 h at RT. Hoechst was used for labeling the nuclei. Coverslips were mounted using mounting media and cured overnight before visualization. Three sections (three technical replicates) at different depths within the center of the AFT model were used for quantifications.

4.2.10 Fluorescent microscopy

Immune-stained cells were visualized on an Echo Revolve R4 (Discover Echo, USA) fluorescent microscope equipped with 10× magnification objective (Olympus Life Science), and DAPI (ex:

380/30; em: 450/50), FITC (ex: 470/40; em: 525/50) and TRTC (ex: 530/40; em: 605/70) filters from the manufacturer. The images (895 × 750 μm^2 and 2448 × 2048 $pixel^2$) were analyzed using ImageJ software. Details about the quantification of protein expression using fluorescent intensity and cell count are included in the SI.

4.2.11 RT-qPCR

RT-qPCR was employed to assess transfection efficiency by measuring CD47, CD24, and ANT1 mRNA expression. The AFT model was harvested, and RNA extraction was performed using the RNeasy Micro Kit following the manufacturer's instructions, followed by RT-qPCR analysis. RT-qPCR was performed on an Applied Biosystems™ 7500 Fast Real-Time PCR System using Power SYBR Green RNA-to-CT 1-Step Kit. The amplification conditions of qPCR were as follows: 48°C for 30 min, 95 °C for 10 min, followed by 40 cycles at 95 °C for 15 sec and 60 °C for 1 min. The qPCR primers used in this study are listed in the Chemicals and Reagents. CD47, CD24, and ANT1 gene expression was normalized against the housekeeping gene GAPDH to obtain the ΔCq value, which was then converted to the ΔCq expression value using exponential transformation (ΔCq expression = $2^{-\Delta Cq}$). The mean ΔCq expression was normalized to the negative controls (NC 47 and NC 24 for CD47 and CD24, respectively), and the percentage knockdown was calculated by subtracting the ΔΔCq from 1 (defined by the expression levels of the untreated sample) and multiplying by 100. To determine the ANT1 expression fold increase, the mean ΔCq expression was normalized to the untransfected control.

4.2.12 Microplate reader

ATP levels and caspases 3/7 levels were measured by Cell Titer-Glo® and Caspases-Glo® 3/7, respectively, according to the manufacturer's instructions. Briefly, AFT models were transferred in

white 96-well plates with flat bottoms with an equal volume of media and reagent. For ATP analysis, each sphere was completely lysed through pipetting to allow an effective extraction of the ATP. Subsequently, the plates were incubated at room temperature for 60 min on a microplate shaker at 500 rpm. Luminescence was measured using the FLUOstar Omega microplate reader (Mandel Scientific, Canada). Cell viability and apoptosis after transfection were calculated using the treated AFT models compared to the untransfected control.

4.2.13 Flow cytometry

For flow cytometry, A549, HLF, and THP-1 cells were grown in 2D monocultures, harvested post-transfection, and prepared at a concentration of 1 million cells per 100 µL in cold PBS (4°C) supplemented with 0.5% BSA. These cells underwent labeling procedures using fluorophore-conjugated antibodies, including PE-CD47 or PE-CD24 (at a 1:20 dilution). Labeling was conducted on ice for 30 minutes, and the mixture was washed twice. Additionally, to evaluate the apoptotic effects of smGO-CD47_siRNA, smGO-CD24_siRNA and smGO-ANT1_pDNA transfections, PE-Annexin V, a marker of early apoptosis [52], and 7AAD (at a 1:20 dilution), a marker for late stage apoptotic or necrotic cells [53], were added to the cells and incubated on ice for 15 minutes prior to analysis using a BD Accuri™ C6 Plus Flow Cytometer (BD Biosciences, USA). A total of 30,000 cells per sample were analyzed. Data analysis was conducted using FlowJo software 10.8.1. Debris and doublets were excluded based on side scatter and forward scatter parameters. The transfection efficiency was assessed by measuring the expression levels of the target marker in the treated cells compared to the control untransfected and multiplied by 100.

4.2.14 Statistical Analysis

All data are presented as mean ± standard deviation (SD). RT-qPCR results are obtained from 3 biological repetitions (n = 3). For immunohistochemistry images' quantifications, three separate models with treatments (n = 3) were analyzed, and the results were averaged to obtain the final values and SD. Microplate reader results are given by 3 biological repetitions (n = 3) of 6 technical replicates. Flow cytometry experiments were repeated 3 times in triplicates (n = 3, three wells per plate and three plates were tested). All statistical analyses were performed with GraphPad Prism 8.02. Variations across more than three conditions were analyzed using a one-way ANOVA, while the effects of two independent variables on a dependent variable were assessed using a two-way ANOVA. A value of $P < 0.05$ was considered statistically significant.

4.3 Results and Discussion

4.3.1 smGO-mediated gene transfection regulates target protein expression in the AFT model

Building on our previous work demonstrating the high transfection efficiency of smGO nanocarriers for siRNA delivery in co-culture and 3D lung cancer spheroid models [16, 30, 31], the current study expands their application to the delivery of multiple nucleic acids and their role in modulating target proteins within the tumor microenvironment.

4.3.1.1 Role of smGO nanocarrier internalization in gene transfection

Using a previously reported procedure [29], which employed a modified Hummer's method and thorough cleaning processes, GO was synthesized from oxidized graphite, yielding single-layer GO with lateral sizes exceeding 10 microns (Figure 4.1A). The smGO, obtained by precisely reducing GO sizes and functionalizing them with PEG and PAMAM, exhibited increased roughness compared to unmodified GO flakes (Figure 4.1A). The presence of amide groups (amide I at 1645 cm^{-1}, amide

II at 1555 cm^{-1}), N–H at 3400 cm^{-1}, and decreased intensity of carbonyl (C=O, 1720 cm^{-1}), hydroxyl (O–H, 3200–3500 cm^{-1}), and C–OH (1415 cm^{-1}) groups in smGO indicated nucleophilic reaction between the epoxide and ketone groups of GO with the amine groups of PEG and PAMAM to form covalent bonds (Figure 4.1B and 1C). These modifications provide multiple binding sites for nucleic acids, facilitating enhanced internalization, cargo delivery, and transfection efficiency [54]. Our earlier studies confirmed that smGO-mediated nucleic acid delivery efficiently modulated target gene expression in both 2D cultures and 3D spheroid models [16, 30, 31, 36].

Critical steps were undertaken to establish a reliable and reproducible methodology to construct and optimize the 3D lung cancer microenvironment AFT model (Figure S4.1A-D). Initially, the focus was on identifying the optimal ECM compositions to support 3D cell structures, ensuring the viability and functionality of immune and cancer cells. To optimize the extracellular matrix composition for the AFT model, we evaluated different formulations of Matrigel, collagen, and their mixtures based on cellular morphology and proliferation. A 1:1 ratio of Matrigel to collagen was selected, as it provided the best balance of structural support and physiological relevance, promoting stable 3D architecture and intercellular interactions. Matrigel, collagen, and 1:1 mixtures were compared with cell morphology and proliferation analyses to determine the composition best suited for maintaining physiological relevance and promoting cellular interactions. Building on ECM optimization, matrix deposition on multiwell plates was refined to enhance reproducibility and ease of handling. Methods included direct droplet deposition in pre-warmed media for immediate polymerization and placement of droplets in either adherent or low-attachment multiwell plates. Each was evaluated for its effects on AFT morphology, consistency, and practicality (more details are provided in SI).

With the AFT model established, smGO nanocarrier internalization was assessed to confirm its suitability for nucleic acid delivery within the 3D microenvironment. The internalization of smGO nanocarriers in the AFT model was first examined by incubating AFTs with Alexa Fluor 488 conjugated smGO without nucleic acid, where the fluorophore is covalently bound to the smGO via

carboxyl groups (Figure 4.1C). Microscopic evaluations showed green fluorescence predominantly within the cells in the AFT (Figure 4.1D, the samples were 10 μm sections of frozen sections of AFT samples; the preparation of sections was illustrated in Figure S4.1E-G). Very few instances of fluorescently labelled smGO adhered non-specifically to the ECM were observed (Figure 4.1D, white arrows). This is likely due to the extensive washes performed during the preparation of frozen blocks and after the sections have been prepared prior to nuclei staining and mounting, which removed most of the non-internalized particles. Overall, this indicated successful penetration through the matrix and cellular internalization of smGO throughout the entire 3D structure. However, non-uniform fluorescence intensity distributions were observed, suggesting variations in nanocarrier uptake among different cell types in the AFT model, potentially influencing subsequent gene modulation outcomes [55, 56].

Gene expression was evaluated by performing transfections of the AFT models with smGO-CD47_siRNA, smGO-CD24_siRNA, and smGO-ANT1_pDNA. Treatment with smGO-CD47_siRNA led to a significant 58% downregulation of the CD47 gene expression in AFT when total cells were considered (Figure 4.1E). This reduction was calculated by comparing CD47 gene level after transfection to universal negative control (NC 47), which aligns with our previous findings of substantial knockdown in both 2D cultures and 3D spheroid models of A549 cancer cells (note, the 58% downregulation reported here is not the CD47 protein expression, which was found previously to be as high as 90% downregulated after transfection in 3D spheroids) [30, 31]. Conversely, a modest 20% reduction in CD24 gene level (Figure 4.1F) was observed upon treatment with smGO-CD24_siRNA. This difference in knockdown efficiency likely arises from variations in target gene abundance and baseline expression levels [55-59]. CD47, widely expressed on A549 and THP-1 cells [16, 30, 60, 61], allows for more uniform knockdown due to higher target abundance, which enhances siRNA efficacy [58]. Similar downregulation results have been obtained in other studies involving lung cancer cells [62, 63]. In contrast, CD24 expression varies significantly across cell types, higher in A549 cells but comparatively lower in HLF and THP-1 cells [64, 65].

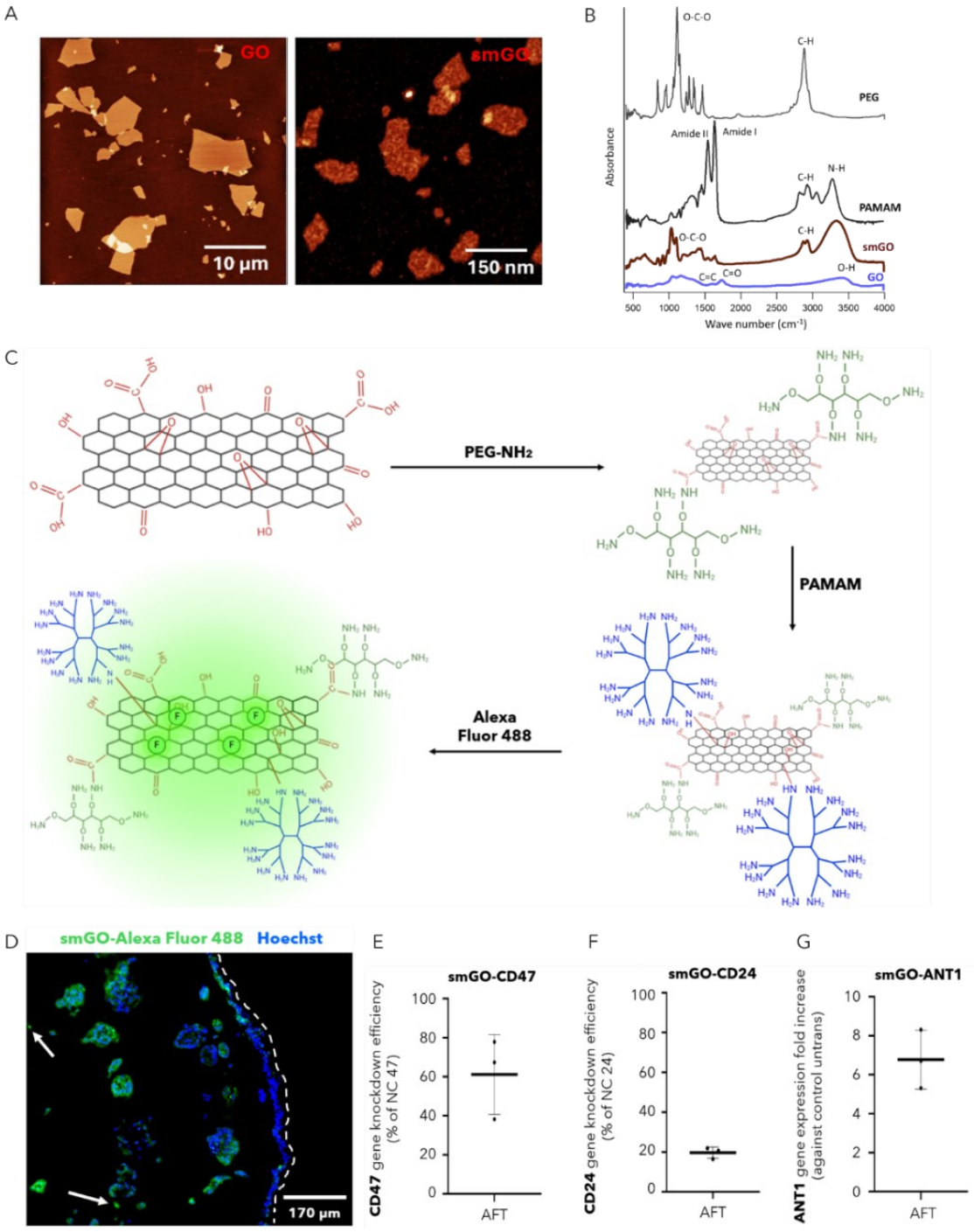

Figure 4.1. Uptake and gene regulation of smGO nanocarriers in the AFT model. (A) AFM topographic images of GO (left panel, scale bar = 10 µm) and smGO flakes (right panel, scale bar = 150 nm), highlighting the morphological differences after functionalization. Z-range: 0-5 nm. (B) FTIR spectra of GO, smGO (GO functionalized with PEG and PAMAM), PEG, and PAMAM, illustrating the chemical modifications. (C) Schematic representation of smGO, showing its functionalization with PEG and PAMAM and conjugation with Alexa Fluor 488 dye. (D) Fluorescent image of smGO-Alexa Fluor 488 treated AFT sample, showing a central section (~10 µm thick) of the AFT model. Blue: nuclei stained with Hoechst; green: smGO-Alexa Fluor-488; white dashed line: 3D model section border. Scale bar = 170 µm. (E-G) Changes in gene levels post-transfection of the AFT model for (E) CD47, (F) CD24, and (G) ANT1 genes, demonstrating the effectiveness of smGO-mediated delivery.

Furthermore, smGO-ANT1_pDNA treatment induced a seven-fold increase in ANT1 gene expression (Figure 4.1G). While ANT1 protein is highly expressed in terminally differentiated tissues, its expression is typically low in proliferating lung and breast cancer cells [66]. Upregulated ANT1 protein overexpression promoted mitochondrial dysfunction in cancer cells, triggering apoptosis and cell death [41, 66]. This highlights the therapeutic potential of smGO for selectively inducing cancer cell elimination by leveraging mitochondrial stress pathways.

4.3.1.2 Protein knockdown specificity in cancer cells within the AFT model

The discrepancy in knockdown efficiencies necessitated the evaluation of cancer cell-specific gene silencing. To assess selective silencing in cancer cells versus other cell types, cytokeratin 7 (CK7), a well-established marker for lung adenocarcinoma [67], was used to identify A549 cells within the AFT model [68]. Immunocytochemistry for CK7 on dissociated single cell suspensions of A549, HLF and THP-1 monocytes (Figure S4.2) confirmed that CK7 was predominantly expressed in A549 cells [69], with minimal expression in THP-1 monocytes and none in HLF cells, validating its use for cancer cell identification. This distinction allowed for the separate quantification of gene silencing in cancer cells compared to non-cancerous cell types, such as THP-1 macrophages and HLF, providing a clearer understanding of the targeting specificity of smGO nanocarriers.

Figure 4.2 represented the downregulation of CD47 and CD24 marker expression in the AFT model following transfection. It illustrated immunohistochemistry images of sections from the central region of AFT model samples. Quantification of CK7+ve (cancer) and CK7-ve (non-cancer) cells (Figure S4.3) revealed that 58% of the total cells in the AFT model were CK7+ve, and 42% were CK7-ve (Table S4.1; intensity and number-based cell count analyses are included in the SI). Fluorescence intensity analysis of the red staining representing CD47 and CD24 marker expression levels showed reduced intensity in the post transfection samples compared to the untransfected controls, indicating

successful downregulation of these markers. The images from each section (3-10 per section, covering the entire section) were used to quantify the intensity, with SD values reported.

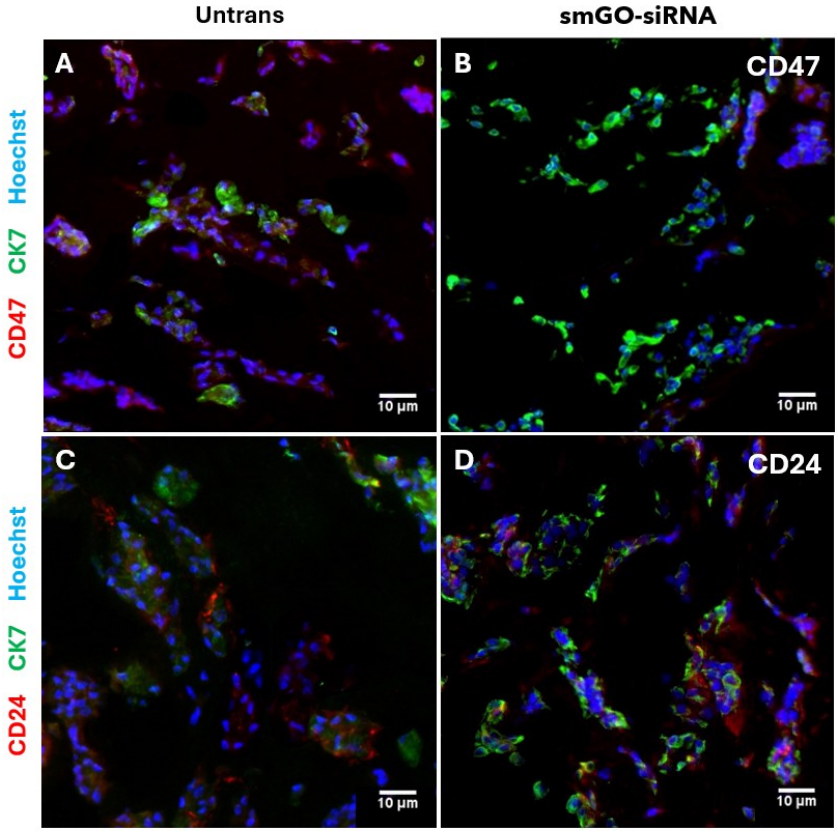

Figure 4.2. Downregulation of CD47 and CD24 marker expression in the AFT model following transfection. Immunohistochemistry images of 10 µm thick sections (from the central portion) of the AFT model: (A) Untransfected control (untrans) and (B) smGO-CD47_siRNA transfected AFT model; (C) Untransfected control (untrans) and (D) smGO-CD24_siRNA transfected AFT model. (Blue: nuclei (Hoechst); red: CD47 and CD24 markers (both with Alexa Fluor 555 labelled antibodies, respectively); green: CK7+ve cancer cells (Alexa Fluor 488)). Scale bars = 10 µm.

A 97% reduction in CD47 and a 49% reduction in CD24 protein expression was observed within the CK7+ve cancer cell population in the transfected samples (i.e., smGO-siRNAs) compared to the untransfected controls, while reductions of 26% and 11%, respectively, were obtained in CK7-ve non-cancer cells (Figure 4.2, Table 4.1). This apparent non-linearity between mRNA and protein levels (Figure 4.1E, F; Table 4.1) is well documented and may reflect several biological and regulatory mechanisms [70, 71]. Both CD47 and CD24 are glycosylphosphatidylinositol (GPI)-anchored cell surface glycoproteins known for rapid membrane turnover and post-transcriptional regulation, particularly under immune surveillance conditions [72, 73]. Moderate reductions at the

mRNA level may result in substantial loss of surface protein due to internalization and degradation, as protein abundance is not always directly correlated with transcript levels [70, 71, 74] Additionally, the downregulation of these markers and the activation of phagocytosis may initiate intracellular cascades that further suppress protein expression post-translationally or promote cleavage/internalization, reinforcing protein loss. Prior studies have shown that phagocytosis-enhancing signalling events can also influence CD47 expression or localization, potentially creating a positive feedback loop that amplifies target cell removal [75, 76]. Moreover, GO has been shown to interfere with ribosomal activity and translational processes, possibly contributing to the discrepancy between mRNA and protein levels [77].

Table 4.1. Knockdown efficiency of CD47 and CD24 in CK7+ve (cancer) and CK7-ve (non-cancer) cells, calculated from fluorescent images of the AFT model in Figure 4.2 using Equation S1 and S2. Values are reported as mean ± SD of three sections (about 10 μm each) from the central region of three untransfected AFT samples.

Type of cells	% CD47 marker knockdown		% CD24 marker knockdown	
	on CK7+ve population	on total AFT population	on CK7+ve population	on total AFT population
CK7+ve (58%±5% of the total)	97%±2%	56%±5%	49%±7%	28%±5%
CK7-ve (42%±5% of the total)	26%±5%	11%±2%	11%±4%	5%±2%

The specificity of CD47 and CD24 downregulation was further supported by knockdown distribution: 56% of the total cells were CD47-downregulated cancer cells (CK7+ve), while only 11% were CK7-ve non-tumor cells (Table 4.1). For CD24, 28% of the total cells were CD24- downregulated cancer cells, compared to just 5% of non-cancerous origin (Table 4.1). These results are consistent with previous studies, confirming the effectiveness of CD47_siRNA transfection in specifically targeting lung cancer cells [16, 30, 62]. Overall, the results demonstrate the ability of smGO nanocarriers to selectively deliver siRNA to cancer cells while minimizing off-target effects in non-cancerous cell types.

4.3.1.3 Specific uptake of smGO in cancer cells in the AFT model

The observed silencing of CD47 and CD24 in A549 cancer cells likely results from the preferential uptake of smGO. Factors influencing this uptake include cell type-specific surface markers and the physicochemical properties of smGO, such as size, shape, and surface modifications [12, 31, 55]. Cancer cells, such as A549, exhibit higher endocytosis rates and increased surface receptor expression (e.g., scavenger receptors) compared to normal cells, facilitating nanocarrier internalization [56, 78-80]. Furthermore, functionalized GOs have been shown to enter A549 cells and localize in the cytoplasm and nucleus without causing damage [81, 82]. At the same time, fibroblast-produced extracellular matrix may act as a physical barrier, delaying nanocarrier penetration [7, 83-86].

In our study, the PEG and PAMAM modifications likely enhance cellular uptake and intracellular delivery by leveraging the increased endocytosis rates observed in cancer cells [7, 87]. In addition, as shown in Figure S4.4, smGO appeared to be selectively taken up by the cancer cell population, as evidenced by the colocalization of Alexa Fluor 555 labeled CK7 antibody (specific to A549 cancer cells) with Alexa Fluor 488 labeled smGO. Only a small number of non-cancer cells showed smGO (green in Figure S4.4). These findings align with previous reports highlighting the potential of modified GOs as an effective, selective delivery platform for targeting cancer cells in heterogeneous cellular environments [8, 15].

To confirm the cancer cell-specific uptake of the smGO, 2D monocultures of A549 cells, HLFs, and THP-1-derived macrophages were treated with Alexa Fluor 488-conjugated smGO. The internalization of smGO-Alexa Fluor 488 was observed as bright green, fluorescent dots near the cell membrane, adjacent to the Hoechst-stained nuclei (blue) (Figure 4.3A), showing the highest accumulation of smGO in A549 cells compared to HLF and THP-1 cells. Additionally, representative flow cytometry histograms (Figure 4.3B) showed the analysis results of Alexa Fluor 488 positive and negative cells, where 30, 000 cells were evaluated per cell line. The mean fluorescence intensity (MFI), measured by flow cytometry, revealed that A549 cells had the most remarkable propensity for

smGO internalization, with 85%±4% of the cells showing positive Alexa Fluor 488 staining. In contrast, HLF and THP-1 cells exhibited lower internalization rates, with 11%±7% and 30%±2% of the respective populations positive for Alexa Fluor 488 after 48 h smGO treatments (Figure 4.3B and 3C). Although a higher degree of GO uptake has been previously reported in immortalized fibroblast cells [90, 91], primary fibroblasts such as the HLFs used in this study are anticipated to have significantly lower uptake levels than immortalized cells [91, 92]. Immortalized fibroblasts (e.g., NIH3T3) have been shown to behave similarly to cancer cells by employing multiple pathways for nanomaterial internalization [92], whereas primary fibroblasts are non-phagocytic and are expected to exhibit limited GO uptake relative to their immortalized counterparts.

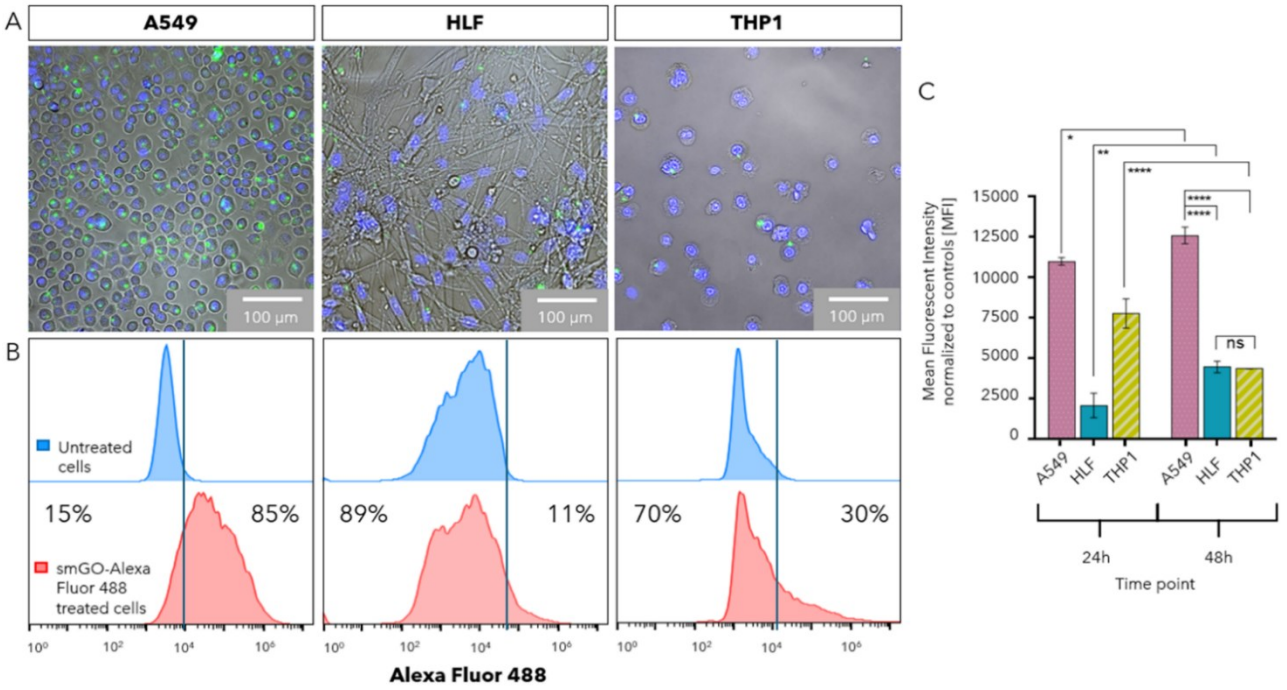

Figure 4.3. Uptake of smGO in A549, HLF, and THP-1 cells in 2D monocultures. (A) Representative fluorescence images of Alexa Fluor 488-labeled smGO-treated cells in the three individual 2D-cultured cell lines at 48 h post-treatment, with nuclei stained blue (Hoechst). The uptake of labeled smGO is shown by green fluorescence signals. Scale bars = 100 µm. (B) Mean fluorescence intensity (MFI) of Alexa Fluor 488 in smGO-treated and untreated cells (48 h) was measured by flow cytometry to quantify internalization across each cell type. Experiments were conducted with three independent biological replicates, each with triplicate wells (n = 3), and a minimum of 30,000 cells were analyzed per condition. (C) Bar graph showing the MFI values from labelled smGO treatments at 24 and 48 h. Statistical significance was determined using one-way ANOVA, with *P < 0.05; **P < 0.01; ***P < 0.001; ****P < 0.0001 considered significant. P > 0.05 was considered not significant (ns).

One surprising result was the relatively low internalization capacity of THP-1 macrophages. As phagocytic cells, macrophages, including THP-1-derived macrophages (confirmed through immunohistochemistry for CD14, a surface marker of THP-1 monocytes in Figure S4.5A and S5B [93], and CD68, a surface marker of THP-1 macrophages [94], in Figure S4.5C and S5D), typically internalize foreign particles as part of immune surveillance [95]. Consequently, these THP-1-derived macrophages are generally presumed to demonstrate high uptake efficiency for nanocarriers. However, the uptake efficiency of smGO by THP-1 cells likely depends on various factors, including particle size, surface modifications, and the activation state of the macrophages [12, 96, 97]. Materials smaller than 200 nm, such as smGO, are less likely to be recognized by the immune cells, reducing the likelihood of phagocytosis [98, 99]. Additionally, PEG modification on smGO decreases opsonization, minimizing macrophage recognition and uptake [12, 100]. A previous study demonstrated that GO flakes, ranging from nanometers to micrometers, were predominantly found outside THP-1 macrophages or adhered to their membranes after 24 h of exposure [96].

These results demonstrate that A549 lung cancer cells exhibit significantly higher internalization rates of smGO nanocarriers compared to HLF and THP-1 cells. This leads to A549-specific downregulation of target genes and proteins, highlighting the potential of smGO for cancer-targeted delivery of therapeutic cargo in a heterogeneous cellular environment. Moreover, these findings emphasize the need for further investigation into the mechanisms underlying the differential uptake across cell types, as this could provide insights into optimizing nanocarrier designs for more effective cancer treatment.

4.3.2 smGO mediated gene therapy leads macrophage driven cancer cell elimination

Gene therapies targeting cancer cells require precise assessment of cell death mechanisms, as these directly influence therapeutic specificity and efficacy. To evaluate the potential of smGO-based nanocarriers for gene therapies, apoptosis was analyzed using Caspase 9 immunohistochemistry and

Caspase 3/7 assays, while cell viability was determined through ATP quantification (Cell Titer assay) alongside image-based cell counting [101, 102].

4.3.2.1 Macrophage-cancer cell interactions

Figure 4.4 presented the analysis of cell viability and apoptosis in the AFT model following transfection with smGO-CD47_siRNA, smGO-CD24_siRNA, and smGO-ANT1_pDNA. Cell apoptosis (Caspases 3/7 Glo assay, red dashed lines in Figure 4.4A) and viability (Cell Titer Glo, blue lines) were monitored over time, using luminescence-based assays (six AFT samples per transfection experiment, with three repetitions from different batches of AFT). In untreated controls or those treated with smGO alone (without siRNA or pDNA), viability remained above 90% over 72 h, confirming that the AFT model remained viable in the absence of targeted gene therapy (Figure 4.4A) and that smGO is safe to use as a delivery system at the used concentration, as confirmed in our previous study [31].

In contrast, AFT models treated with smGO-CD47_siRNA exhibited nearly 100% cell viability at 24 h, even though apoptotic protein expression increased nearly eightfold compared to untreated controls, suggesting the initiation of irreversible apoptosis [103]. This was confirmed at 72 h when cell viability declined to approximately 71%. Similarly, CD24_siRNA treatment resulted in a 73% decrease in viability at 72 h, while ANT1-pDNA induced a more rapid response, with apoptotic protein expression rising five-fold by 6 h. This was followed by a rapid decline in viability to 67% at 24 h and 61% at 72 h, reflecting a faster onset of cell death (Figure 4.4A). CD47 and CD24 knockdown significantly elevated cancer cell apoptosis (Figure 4.4A), corroborating findings in previous studies on the effectiveness of these therapies [33, 104].

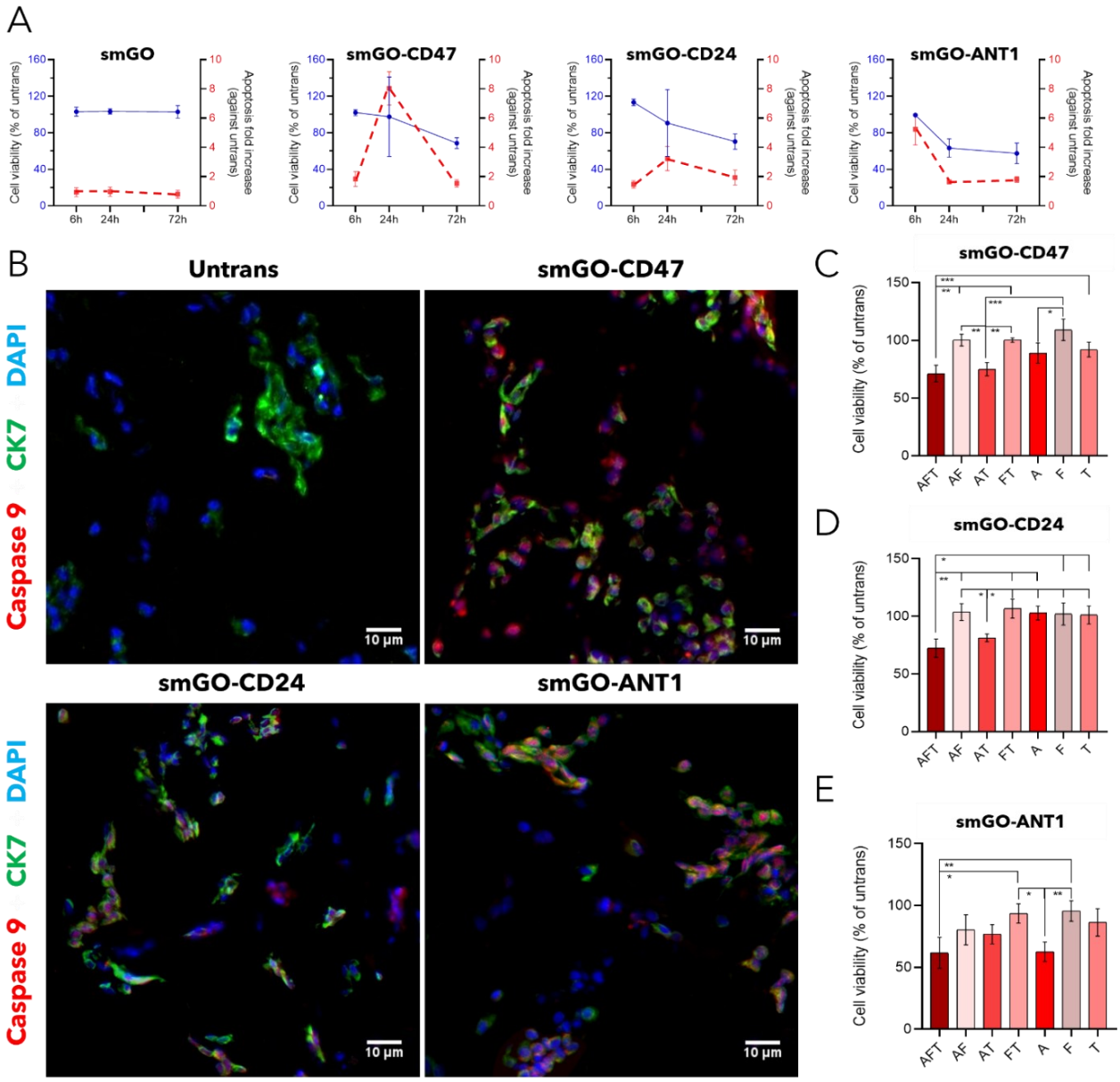

Figure 4.4. Apoptosis and cell viability assessment of AFT models following transfection with CD47_siRNA, CD24_siRNA, and ANT1_pDNA. (A) Cell viability (Cell Titer Glo assay) and apoptosis (Caspases 3/7 Glo assay) rates of total cells in AFT models at 6, 24, and 72 h post-transfection. (B) Immunohistochemistry images of AFT sections from untransfected control (untrans) and smGO-CD47_siRNA, smGO-CD24_siRNA, and smGO-ANT1_pDNA transfected samples. (Blue: Hoechst-stained nuclei, red: Alexa Fluor 555-labeled anti-Caspase 9 antibody, green: Alexa Fluor 488-labeled anti-CK7 antibody for cancer cells (CK7+ve)). Sections were 10 µm thick, derived from the central region of each AFT sample. Scale bars = 10 µm. (C-E) Bar graphs depicting cell viability in AFT and 3D control models (AF, AT, FT, A, F, T) at 72 h after transfection. Statistical significance was determined by one-way ANOVA, with *P < 0.05, **P < 0.01, ***P < 0.001 considered significant. No significant results (P > 0.05) are not shown.

The role of macrophages in enhancing therapeutic outcomes was previously demonstrated in co-culture systems [16, 36], where CD47_siRNA downregulation identified macrophages as critical mediators of phagocytosis. To investigate the phagocytic effects on cancer cell death, CK7+ve and Caspase 9+ve cells were quantified using immunohistochemistry imaging and cell counting. Figure 4.4B showed fluorescence images of AFT model sections stained for CK7 (green with Alexa Fluro 488 labeled anti-CK7 antibody, identifying cancer cells) and Caspase 9 (red with Alexa Fluro 555 labeled anti-Caspase 9) in untransfected and transfected AFT samples (with smGO-CD47_siRNA, smGO-CD24_siRNA, and smGO-ANT1_pDNA). The analysis was based on the red-colored cell count, where increased Caspase 9 staining indicates higher apoptosis protein expression. Cell apoptosis was quantified as the ratio between Caspase 9-positive cells and the total cells for each cell line, considering both CK7+ve and CK7-ve areas (Table 4.2). Cancer cell apoptosis specificity, namely the specificity factor, was determined as the ratio between the apoptotic CK7+ve and CK7-ve cells (Table 4.2).

Table 4.2. Apoptosis percentages of CK7+ve (cancer) and CK7-ve (non-cancer) cells in the AFT model (after 72 h transfections), along with total apoptosis rates and cancer cell apoptosis specificity factor values, derived from Figure 4.4B using Equation S3 (mean ± SD).

Treatment	CK7+ve cells apoptosis %	CK7-ve cells apoptosis %	Total cell apoptosis %	Specificity factor
Untrans	3±1	6±2	9±2	n/a
smGO-CD47	37±5	24±5	61±7	1.5
smGO-CD24	29±4	22±4	51±6	1.3
smGO-ANT1	40±6	13±5	53±8	3.1

Results revealed that CD47_siRNA treatment resulted in 61% of apoptotic cells (Caspase 9+ve), with 37% from cancer cells (Caspase 9+ve and CK7+ve) and 24% from non-cancer cells (Caspase 9+ve and CK7-ve cells), yielding a specificity factor of 1.5 (Table 4.2). CD24_siRNA transfection showed a comparable but slightly lower specificity factor (1.3) with 51% total apoptosis, while ANT1 therapy demonstrated the highest specificity (3.1), with 53% total apoptosis (40% from CK7+ve cancer cells and 13% from CK7-ve non-cancer cells) (Table 4.2 and Figure 4.4B). These results align with the

findings in Section 2.1.3, which highlighted smGO's preferential uptake by cancer cells and its role in enhancing therapy specificity (Figure 4.3). This was particularly evident in ANT1_pDNA therapy, where heightened metabolic activity and exogenous gene expression susceptibility in cancer cells contribute to selective apoptosis [53, 54, 105].

4.3.2.2. Role of 3D models and ECM in therapy efficacy

The tumor microenvironment, particularly the extracellular matrix within 3D models, plays a pivotal role in therapy outcomes. The 3D Matrigel-collagen matrix facilitates spatial interactions and adhesion among cancer cells, macrophages, and fibroblasts, closely mimicking *in vivo* conditions [106, 107]. This contrasts with traditional 2D cultures, where such cellular cross-talk is limited. To further explore the TME's influence, cell viability values in 3D single and dual-cell samples after transfections were compared to those in AFT samples.

Figure 4.4C-E provided quantitative data on apoptosis levels across different transfection conditions. The samples include one-cell (A, F, T) and two-cell (AF, FT, AT) 3D models transfected with smGO-CD47_siRNA (Figure 4.4C), smGO-CD24_siRNA (Figure 4.4D), and smGO-ANT1_pDNA (Figure 4.4E). Cell viability was measured using Cell Titer Glo after 72 h of transfection. In AFT models, smGO-CD47_siRNA and smGO-CD24_siRNA therapies reduced viability to 71% and 73%, respectively, consistent with macrophage-driven phagocytosis (Figure 4.4C and 4D). ANT1_DNA therapy reduced viability further, with AFT models showing 61% viability at 72 h, comparable to the single-cell A model (63%, Figure 4.4E). This finding reinforces the notion that ANT1's effects are largely macrophage independent. Interestingly, fibroblast-containing models (e.g., FT) showed minimal changes in viability (>90%), highlighting the cell-specific nature of these therapies [42, 51, 108]. This is further supported by immunohistochemistry for CD14 and CD68 in AFT model (Figure S4.5) [93, 94]. The presence of CD68, a pan-macrophage marker commonly associated with TAM, in the untransfected AFTs [109, 110], indicated macrophage integration and activation in the AFT

model (Figure S4.5C). The increased co-localization of THP-1 cells with CK7+ve cancer cells after transfection with CD47_siRNA, compared to untransfected control (Figure S4.5). This co-localization indicates phagocytic clearance via macrophages, which likely accounts for increased apoptosis and viability loss of cancer cells (Figure 4.4A-B, Table 4.2). Silencing of CD47 in the cancer cells downregulates its interaction with SIRPα on macrophages, reducing phagocytosis inhibitory signal and making A549 cancer cells more susceptible to recognition and engagement by macrophages [111], 2D monoculture analyses of the direct effects of individual therapies further support this. In monocultures, (i.e., A, A549; F, HLF; or T, THP-1 cells), transfection with CD47 or CD24 siRNAs significantly reduced marker expression (e.g., CD47 knockdown: A549, 96%; HLF, 18%; THP-1, 42%, Figure S4.6A, S6B and Table S4.2), but induced minimal apoptosis (<7%) (Figure S4.6C and Table S4.2). Notably, cell apoptosis remained below 10% across all three cell lines following transfections (Table S4.2), suggesting that these transfections of siRNAs alone do not directly induce cell death. In contrast, ANT1_pDNA treatment markedly increased A549 apoptosis (31%), while HLF and THP-1 cells maintained lower apoptosis (8% and 17%, respectively). This demonstrates the selective vulnerability of A549 cancer cells to ANT1-driven apoptosis, which was not observed in the non-cancerous cell types [112].

Unlike 2D cultures, the 3D Matrigel-collagen matrix better mimics the complexity of the TME by facilitating spatial proximity, adhesion, migration, and signaling among cancer cells, macrophages, and fibroblasts. Fibroblasts can play a key role in the TME by secreting cytokines, chemokines, and growth factors and remodeling ECM proteins to dictate immune cell behavior [47]. In the AFT model, HLFs may influence the differentiation of THP-1 monocytes into macrophages and enhance their recruitment to the proximity of A549 cells by producing chemo attractants. Fibroblasts can remodel the Matrigel ECM to create structural pathways that facilitate the physical interactions between macrophages and cancer cells [47]. This environment enhances the efficacy of CD47 and CD24 therapies by promoting localized macrophage-cancer cell interactions, which are critical for triggering phagocytosis. This increased crosstalk in the AFT model also amplifies the effect of ANT1

transfection on cancer cell elimination. Following apoptosis induction, the presence of macrophages intensifies the effect on transfected cells, explaining the higher apoptosis rates observed in the AFT model (Table 4.2) compared to the results in 2D monocultures (Table S4.2). The reduced apoptosis observed in monocultures underscores the importance of cellular crosstalk within the 3D model, aligning with findings in macrophage-cancer co-culture systems [47].

4.3.2.3 Broader insights for TME

Our previously published data also showed that monoculture spheroids of A549 lung cancer cells did not exhibit significant viability changes after CD47_siRNA treatment alone, but marked apoptosis was observed when co-cultured with macrophages [16, 31]. Our current results also align with reported studies demonstrating that CD47 and CD24 therapies enhance macrophage-driven cancer cell elimination by disrupting the "don't eat me" signal mediated by SIRPα interactions [51]. These therapies capitalize on macrophages' innate phagocytic activity, particularly in 3D models that mimic the complexity of the TME. By comparison, ANT1 gene therapy acts independently, directly inducing apoptosis through mitochondrial pathways [41, 66, 113, 114]. Furthermore, *in vivo* studies have demonstrated that ANT1 gene therapy can effectively suppress tumor growth, as seen in breast cancer xenografts models with a 50% reduction in tumor size over 40 days [66]. The distinct mechanisms of these therapies emphasize their complementary roles. CD47/CD24 knockdowns rely on cellular cross-talk and macrophage activation, while ANT1 bypasses these pathways to directly target cancer cell vulnerabilities. This multi-faceted approach offers significant potential for tailored combination cancer therapies that leverage both macrophage-driven and direct apoptotic mechanisms.

The CD47_siRNA therapy in our study demonstrated significant efficacy, corroborating prior studies where co-culturing cancer cells (e.g., A549, THP-1, HL60, NB4, HepG2) with macrophages led to high rates of cancer cell apoptosis, ranging between 89-93% [16, 36]. Although apoptosis rates in our current study were lower, this variation can be attributed to differences in culture systems (3D multi-

cell matrix models versus 2D co-cultures), as well as variations in analytical methods employed [115]. In addition, our findings align with studies demonstrating that overexpression of ANT1 in cancer cells induces apoptosis through mitochondrial dysfunction [66]. ANT1 plays a critical role in the inner mitochondrial membrane by facilitating the exchange of ADP and ATP between the mitochondria and cytoplasm. When overexpressed, ANT1 disrupts this exchange, destabilizing mitochondrial homeostasis and leading to apoptosis [35]. ANT1 overexpression has been shown to upregulate pro-apoptotic proteins (e.g., Bax) and downregulate anti-apoptotic proteins (e.g., Bcl-xL), activating caspases and triggering cell death. This mechanism was consistent with our findings, where ANT1_pDNA transfection resulted in substantial cancer cell apoptosis, further supporting its potential as an apoptosis-inducing therapeutic agent [41, 66].

4.3.3. Co-delivery of multiple nucleic acid cargo leads to enhanced cancer cell elimination

The unique properties of GO—such as its large surface area and oxygen-rich functional groups (hydroxyl, carboxyl, and epoxy)—enable the adsorption of negatively charged nucleic acids via electrostatic interactions and π-π stacking [11]. This allows for GO to be used for synergistic combination therapies using multiple therapeutic agents [20]. Combined delivery of anticancer drugs doxorubicin (DOX) and camptothecin (CPT) using folic acid modified GOs have shown higher cytotoxicity against breast cancer cells compared to when treated with DOX and CPT alone; highlighting the utility of GO as a multifunctional drug delivery platform [116]. The versatility of GO based co-delivery system is further illustrated by development of GO platform loaded with chemotherapeutic DOX and gene therapy Bcl2 siRNA to target multiple pathways to improve anticancer efficacy [18].

4.3.3.1. Synergistic effects of co-delivered gene therapies

Functionalization with PEG and PAMAM, as in smGO, enhances stability, bioavailability, and binding capacity by reducing steric hindrance and introducing additional amine groups. These modifications allow smGO to bind and deliver multiple nucleic acids for efficient gene transfection [7, 11, 117-119]. As a result, smGO emerges as a flexible and adaptable platform, capable of co-delivering different genes to achieve synergistic or additive effects, advancing the prospects of effective cancer therapies. Gene modulation following co-delivery was assessed by quantitative PCR and is reported in Table S4.3. Notably, co-delivery resulted in more pronounced gene regulation than single-gene treatments (e.g., CD47 downregulation reached 64% with co-delivery versus 30% with CD47_siRNA alone), highlighting the benefit of simultaneous targeting of multiple pathways in our 3D tumor model.

The impact of this co-delivery capability was assessed using the AFT model, focusing on apoptosis induction and changes in cell viability. Figure 4.5A presents immunohistochemistry images of untransfected AFT sections and those transfected with smGO-CD47_siRNA-ANT1_pDNA, smGO-CD24_siRNA-ANT1_pDNA, and smGO-CD47_siRNA-CD24_siRNA. CK7 staining (green) highlighted cancer cells, while Caspase 9 (red) marked apoptotic cells. The analysis quantified apoptotic cells as percentages of CK7+ve and CK7-ve cells (Table 4.3), providing insights into the selective impact of therapy on CK7+ve cancer cells versus surrounding regions.

After these visual observations, Figure 4.5B summarizes quantitative results of luminescence-based cell viability and apoptosis assays for AFT models transfected with combinations of smGO-CD47_siRNA-ANT1_pDNA, smGO-CD24_siRNA-ANT1_pDNA, and smGO-CD47_siRNA-CD24_siRNA. Cell viability (blue lines in Figure 4.5B) was assessed using CellTiter-Glo, and apoptosis (red dashed lines) was evaluated with Caspase-Glo 3/7. Data represent the mean ± SD of at least six technical replicates across three independent biological experiments (n = 3). All co-delivery combinations effectively reduced cancer cell viability to below 60% within 24 h. Among

these, smGO-CD47_siRNA-ANT1_pDNA achieved the most significant cancer-specific apoptosis (Table 4.3) and reduced the total cell viability to 47% at 24 h (Figure 4.5B). Similarly, smGO-CD47_siRNA-CD24_siRNA reduced cell viability to 45% by 72 h, underscoring the potential of multi-target approaches to amplify therapeutic outcomes (Table S4.3).

The effectiveness of these co-delivery approaches lies in their ability to target complementary mechanisms. For instance, CD47_siRNA promotes macrophage-mediated clearance, while ANT1_pDNA directly induces apoptosis in cancer cells resistant to phagocytosis. This multi-pronged strategy mirrors earlier successes, such as the co-delivery of tumor necrosis factor-related apoptosis-inducing ligand expressing plasmid (pTRAIL) with siRNAs targeting anti-apoptotic genes Bcl2-like 12 and superoxide dismutase 1 using PEI nanocarriers [120]. By inducing apoptosis through pTRAIL and sensitizing cancer cells via anti-apoptotic gene silencing, these approaches achieved enhanced cancer removal in breast cancer models. Similarly, the pairing of CD47_siRNA and CD24_siRNA broadened the immune blockade, addressing immune evasion while providing a comprehensive defense against tumor heterogeneity—a critical challenge in cancer therapy [120, 121].

Beyond their biological synergy, co-delivery approaches offer practical benefits over sequential treatments. Simultaneous delivery of nucleic acids using smGO reduces the time window for cancer cells to develop resistance mechanisms, a common limitation of stepwise approaches [121, 122]. Moreover, this streamlined approach simplifies therapeutic regimens, reducing patient burden and improving compliance [123]. The modular design of smGO further enhances its versatility, allowing precise control over the ratio of siRNA to pDNA to tailor treatments to specific cancer subtypes or stages. For instance, ANT1-centric therapies may be particularly effective for rapidly proliferating tumors, while CD47-CD24 co-delivery could better address tumors with immunosuppressive microenvironments.

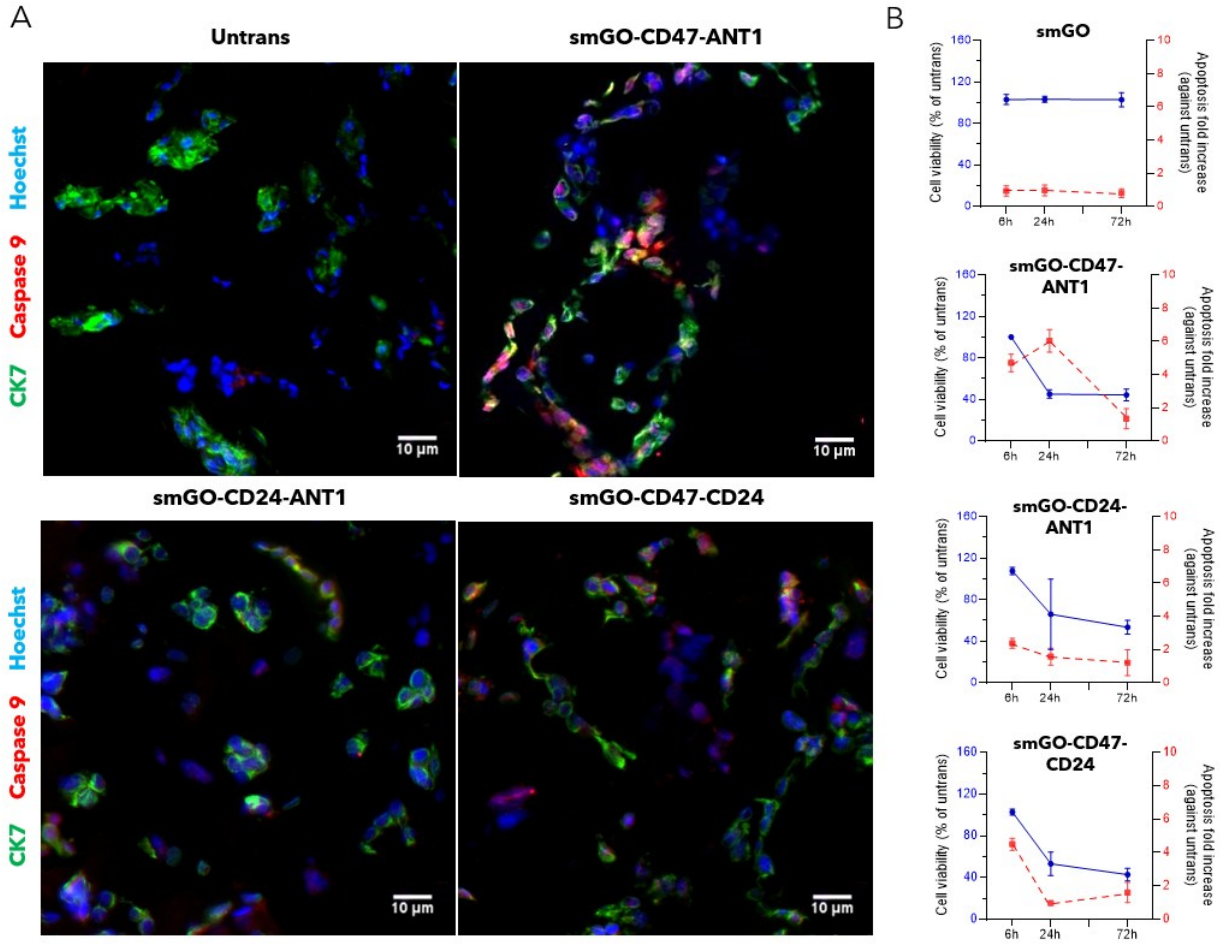

Figure 4.5. Apoptosis and cell viability of AFT models following transfection with combined co-delivery of CD47_siRNA, CD24_siRNA, and ANT1_pDNA in various combinations. (A) Immunohistochemistry images of AFT sections (10 µm thick, central portion of the sample) for untransfected controls (untrans) and samples transfected with smGO-CD47_siRNA-ANT1_pDNA, smGO-CD24_siRNA-ANT1_pDNA, and smGO-CD47_siRNA-CD24_siRNA (blue: Hoechst-stained nuclei; red: Alexa Fluor 555-labeled anti-Caspase 9 antibody; green: Alexa Fluor 488-labeled anti-CK7 antibody). CK7+ve cells represent cancer cells. Scale bars = 10 µm. (B) Quantitative analysis of cell viability and apoptosis rates in AFT models at 6 h, 24 h, and 72 h post-transfection. Statistical significance was evaluated using two-way ANOVA. Results are reported as *P < 0.05, **P < 0.01; non-significant comparisons (P > 0.05) are not shown.

Table 4.3. Co-delivery treatments with smGO-CD47-ANT1, smGO-CD24-ANT1, and smGO-CD47-CD24: Percentages of apoptotic cancer cells (CK7+ve) and non-cancer cells (CK7-ve) in the AFT model, along with total cell apoptosis and cancer-cell-specificity factor values, derived from Figure 4.5A using Equation S3 (mean ± SD).

	% CK7+ve cells apoptosis	% CK7-ve cells apoptosis	% Total cell apoptosis	Specificity factor
Untrans	3±1	6±2	9±2	n/a
smGO-CD47-ANT1	44±4	15±5	59±6	2.9
smGO-CD24-ANT1	29±6	22±3	51±7	1.3
smGO-CD47-CD24	32±5	24±3	56±6	1.3

4.3.3.2. Comparisons with conventional chemotherapy and implications for therapy design

The results from the co-delivery approach significantly outperformed conventional chemotherapy treatments like paclitaxel and cisplatin. In similar 3D tumor models, these agents yielded cell viabilities of approximately 75% (paclitaxel) and 50% (cisplatin) [51]. Furthermore, they caused substantial cytotoxicity to fibroblasts and monocytes (e.g., viability reductions to 55% and 25% for paclitaxel, and 10% and 20% for cisplatin, respectively). In contrast, smGO-mediated gene therapy not only reduced cancer cell viability more effectively but also spared non-cancerous cells.

The selective uptake of smGO by cancer cells is a key factor in this improved outcome (discussed in Section 2.1.3), as the higher metabolic activity and endocytosis rates of cancer cells enable selective intracellular delivery of nucleic acids. Additionally, the modular nature of smGO allows for fine-tuning of nucleic acid ratios to optimize therapeutic outcomes while minimizing off-target effects, flexibility not typically afforded by conventional chemotherapeutics.

The success of co-delivery approaches using smGO emphasizes the potential for designing customized gene therapies that leverage distinct, complementary nucleic acid mechanisms. The rapid apoptosis achieved with the CD47-ANT1 co-delivery suggests it is particularly suited for aggressive cancers that require immediate treatment. On the other hand, the CD47-CD24 combination may be ideal for the long-term management of cancer cell growth, particularly in tumors with immune suppression.

Importantly, smGO's compatibility with a wide range of nucleic acids paves the way for incorporating next-generation therapies, such as CRISPR-based gene editing and regulatory RNA co-delivery [124, 125]. This adaptability could allow for even more precise interventions, enabling not only gene silencing but also genome editing and immune modulation [126]. By building on smGO's modular design, future cancer therapies can be tailored to address the complexities of cancer heterogeneity and resistance, offering a promising path forward for more personalized and effective treatments.

4.4. Conclusion

This study highlights the promise of smGO nanocarriers as a flexible and efficient platform for gene therapy in lung cancer. With their large surface area, adaptable design, and ability to deliver a variety of nucleic acids, smGO enabled effective modulation of key therapeutic targets such as CD47, CD24, and ANT1. These genetic interventions translated into meaningful outcomes, including significant protein regulation and selective cancer cell elimination, all achieved within a complex and physiologically relevant 3D tumor model. One of the standout features of smGO was its ability to target cancer cells specifically, minimizing harm to healthy cells. This precision addresses a major limitation of traditional treatments and underscores the potential of nanocarrier-based gene therapies. Further refinements for specific targeting of cancer cells may be achieved through peptide-based functionalization. For instance, decorating smGO with RGD (arginine–glycine–aspartic acid) peptides [27], which bind to integrin αvβ3 overexpressed in many tumors, could enhance cellular uptake and targeted elimination of cancer cells [24]. Similarly, functionalization with the GE11 peptide may enable delivery to EGFR-overexpressing breast and colorectal cancer cells [127]. These approaches have the potential to improve tumor-specific delivery, minimize off-target effects, and facilitate controlled release in response to cues from the tumor microenvironment. The co-delivery of multiple nucleic acids proved particularly effective, with combinations like CD47 and ANT1 amplifying therapeutic results by simultaneously targeting complementary mechanisms. This approach not only enhanced cancer cell elimination but also demonstrated the value of tackling tumor complexity through multi-faceted strategies. The inclusion of multi-cell 3D models provided a deeper understanding of the tumor microenvironment, revealing the critical role of macrophages in boosting immune-mediated clearance of cancer cells. These insights emphasize the importance of replicating real-world tumor dynamics in research to design therapies that can perform robustly in clinical settings.

While the results are encouraging, further studies are needed to bring these findings closer to clinical application. Future efforts should focus on validating the approach in animal models, refining co-delivery strategies, and ensuring the long-term safety of smGO-based therapies. With its precision, versatility, and ability to overcome some of the most challenging aspects of cancer treatment, smGO holds significant potential to pave the way for more effective and less toxic therapies in lung cancer care.

References

(1) Siegel, R. L.; Giaquinto, A. N.; Jemal, A. Cancer statistics, 2024, *CA Cancer J. Clin*. **2024**, *74*, 12−49.
(2) Hart, L.; Ogbonnaya, A.; Boykin, K.; Deyoung, K.; Bailey, R.; Heritage, T.; Lopez-Gonzalez, L.; Huang, H.; Gordan, L. Burden of chemotherapy-induced myelosuppression among patients with extensive-stage small cell lung cancer: A retrospective study from community oncology practices, *Cancer Med*. **2023**, *12*, 10020−10030.
(3) Rahi, M. S.; Parekh, J.; Pednekar, P.; Parmar, G.; Abraham, S.; Nasir, S.; Subramaniyam, R.; Jeyashanmugaraja, G. P.; Gunasekaran, K. Radiation-Induced Lung Injury-Current Perspectives and Management, *Clin. Pract.* **2021**, *11*, 410−429.
(4) Zoń, A.; Bednarek, I. Cisplatin in Ovarian Cancer Treatment-Known Limitations in Therapy Force New Solutions, *Int. J. Mol. Sci*. **2023**, *24*, 7585.
(5) Lee, H. Y.; Mohammed, K. A.; Nasreen, N. Nanoparticle-based targeted gene therapy for lung cancer, *Am. J. Cancer Res.* **2016**, *6*, 1118−1134.
(6) Cesur-Ergün, B.; Demir-Dora, D. Gene therapy in cancer, *J. Gene Med*. **2023**, *25*, e3550.
(7) Campbell, E.; Hasan, M. T.; Pho, C.; Callaghan, K.; Akkaraju, G. R.; Naumov, A. V. Graphene Oxide as a Multifunctional Platform for Intracellular Delivery, Imaging, and Cancer Sensing, *Sci. Rep.* **2019**, *9*, 416.
(8) Chen, G. Y.; Chen, C. L.; Tuan, H. Y.; Yuan, P. X.; Li, K. C.; Yang, H. J.; Hu, Y. C. Graphene Oxide Triggers Toll-Like Receptors/Autophagy Responses In Vitro and Inhibits Tumor Growth In Vivo, *Adv. Healthc. Mater*. **2014**, *3*, 1486−1495.
(9) Feng, L.; Li, K.; Shi, X.; Gao, M.; Liu, J.; Liu, Z. Smart pH-Responsive Nanocarriers Based on Nano-Graphene Oxide for Combined Chemo- and Photothermal Therapy Overcoming Drug Resistance, *Adv. Healthc. Mater*. **2014**, *3*, 1261−1271.
(10) Gonçalves, G.; Vila, M.; Portolés, M. T.; Vallet-Regi, M.; Gracio, J.; Marques, P. A. A. P. Nano-Graphene Oxide: A Potential Multifunctional Platform for Cancer Therapy, *Adv. Healthc. Mater*. **2013**, *2*, 1072−1090.
(11) Grilli, F.; Gohari, P. H.; Zou, S. Characteristics of Graphene Oxide for Gene Transfection and Controlled Release in Breast Cancer Cells, *Int. J. Mol. Sci*. **2022**, *23*, 6802.
(12) Kim, H.; Kim, J.; Lee, M.; Choi, H. C.; Kim, W. J. Stimuli-Regulated Enzymatically Degradable Smart Graphene-Oxide-Polymer Nanocarrier Facilitating Photothermal Gene Delivery, *Adv. Healthc. Mater*. **2016**, *5*, 1918−1930.
(13) Bulcha, J. T.; Wang, Y.; Ma, H.; Tai, P. W. L.; Gao, G. Viral vector platforms within the gene therapy landscape, *Signal Transduct. Target. Ther.* **2021**, *6*, 53.
(14) Wang, H. L.; Wang, Z. G.; Liu, S. L. Lipid Nanoparticles for mRNA Delivery to Enhance Cancer Immunotherapy, *Molecules* **2022**, *27*, 5607.
(15) Rakoczy, K.; Kisielewska, M.; Sędzik, M.; Jonderko, L.; Celińska, J.; Sauer, N.; Szlasa, W.; Saczko, J.; Novickij, V.; Kulbacka, J. Electroporation in Clinical Applications—The Potential of Gene Electrotransfer and Electrochemotherapy, *Appl. Sci*. **2022**, *12*, 10821.
(16) Hassan, E. M.; McWhirter, S.; Walker, G. C.; Martinez-Rubi, Y.; Zou, S. Elimination of Cancer Cells in Co-Culture: Role of Different Nanocarriers in Regulation of CD47 and Calreticulin-Induced Phagocytosis, *ACS Appl. Mater. Interfaces* **2023**, *15*, 3791−3803,
(17) Sakib, S.; Zou, S. Attenuation of Chronic Inflammation in Intestinal Organoids with Graphene Oxide-Mediated Tumor Necrosis Factor-α_Small Interfering RNA Delivery. *Langmuir* **2024**, *40*, 3402-3413.
(18) Zhang, L.; Lu, Z.; Zhao, Q.; Huang, J.; Shen, H.; Zhang, Z. Enhanced Chemotherapy Efficacy by Sequential Delivery of siRNA and Anticancer Drugs Using PEI-Grafted Graphene Oxide. *Small* **2011**, *7*, 460.
(19) Feng, L.; Zhang, S.; Liu, Z. Graphene based gene transfection, *Nanoscale* **2011**, *3*, 1252.
(20) J. Liu, L. Cui, D. Losic, Graphene and graphene oxide as new nanocarriers for drug delivery applications, *Acta Biomater.* **2013**, *9*, 9243−9257.
(21) Ghasemiyeh, P.; Mohammadi-Samani, S. Solid lipid nanoparticles and nanostructured lipid carriers as novel drug delivery systems: applications, advantages and disadvantages, *Res. Pharm. Sci*. **2018**, *13*, 288−303.
(22) Choi, H. Y.; Lee, T.-J.; Yang, G.-M.; Oh, J.; Won, J; Han, J.; Jeong, G.-J.; Kim, J.; Kim, J.-H.; Kim, B.-S.; Cho, S.-G. Efficient mRNA delivery with graphene oxide-polyethylenimine for generation of footprint-free human induced pluripotent stem cells, *J. Control. Release* **2016**, *235*, 222−235.
(23) Yadav, S. K.; Das, S.; Lincon, A; Saha, S.; BoseDasgupta, S.; Ray, S. K.; Das, S. Gelatin-decorated Graphene oxide: A nanocarrier for delivering pH-responsive drug for improving therapeutic efficacy against atherosclerotic plaque, *Int. J. Pharm*. **2024**, *651*, 123737.
(24) Wei, M.; Lu, T.; Nong, Z.; Li, G.; Pan, X.; Wei, Y.; Yang, Y.; Wu, N.; Huang, J.; Pan, M.; Li, X.; Meng, F. Reductive response and RGD targeting nano-graphene oxide drug delivery system, *J. Drug Deliv. Sci. Technol*. **2019**, *53*, 101202.
(25) Wu, B.; Li, M.; Wang, L.; Iqbal, Z.; Zhu, K.; Yang, Y.; Li, Y. Size-transformable nanohybrids with pH/redox/enzymatic sensitivity for anticancer therapy, *J. Mater. Chem. B* **2021**, *9*, 4319−4328.
(26) Wang, H.; Sun, D.; Zhao, N.; Yang, X.; Shi, Y.; Li, J.; Su, Z.; Wei, G. Thermo-sensitive graphene oxide–polymer nanoparticle hybrids: synthesis, characterization, biocompatibility and drug delivery, *J. Mater. Chem. B* **2014**, *2*, 1362−1370.

(27) Yu, Q.; Zhang, B.; Li, J.; Li, M. The design of peptide-grafted graphene oxide targeting the actin cytoskeleton for efficient cancer therapy, *Chem. Commun*. **2017**, *53*, 11433−11436.
(28) Tian, J.; Luo, Y.; Huang, L.; Feng, Y.; Ju, H.; Yu, B. Y. Pegylated folate and peptide-decorated graphene oxide nanovehicle for in vivo targeted delivery of anticancer drugs and therapeutic self-monitoring, *Biosens. Bioelectron*. **2016**, *80*, 519−524.
(29) Gies, V.; Lopinski, G.; Augustine, J.; Cheung, T.; Kodra, O.; Zou, S. The impact of processing on the cytotoxicity of graphene oxide, *Nanoscale Adv.* **2019**, *1*, 817−826.
(30) Hassan, E. M.; Zou, S. Novel nanocarriers for silencing anti-phagocytosis CD47 marker in acute myeloid leukemia cells, *Colloids Surf. B: Biointerfaces* **2022**, *217*, 112609.
(31) Grilli, F.; Hassan, E. M.; Variola, F.; Zou, S. Harnessing graphene oxide nanocarriers for siRNA delivery in a 3D spheroid model of lung cancer, *Biomater. Sci.* **2023**, *11*, 6635.
(32) Lau, A. P. Y.; Khavkine-Binstock, S. S.; Thu, K. L. CD47: The Next Frontier in Immune Checkpoint Blockade for Non-Small Cell Lung Cancer, *Cancers* **2023**, *15*, 5229.
(33) Barkal, A. A.; Brewer, R. E.; Markovic, M.; Kowarsky, M.; Barkal, S. A.; Zaro, B. W.; Krishnan, V.; Hatakeyama, J.; Dorigo, O.; Barkal, L. J.; Weissman, I. L. CD24 signalling through macrophage Siglec-10 is a target for cancer immunotherapy, *Nature* **2019**, *572*, 392−396.
(34) Bradley, C. A. CD24 — a novel 'don't eat me' signal, *Nat. Rev. Drug Discov*. **2019**, *18*, 747−747.
(35) Chevrollier, A.; Loiseau, D.; Reynier, P.; Stepien, G. Adenine nucleotide translocase 2 is a key mitochondrial protein in cancer metabolism, *Biochim. Biophys. Acta Bioenerg*. **2011**, *1807*, 562−567.
(36) E. M. Hassan, G. C. Walker, C. Wang, S. Zou, Anti-leukemia effect associated with down-regulated CD47 and up-regulated calreticulin by stimulated macrophages in co-culture, *Cancer Immunol. Immun*. **2021**, *70*, 787−801.
(37) De Visser, K. E.; Joyce, J. A. The evolving tumor microenvironment: From cancer initiation to metastatic outgrowth, *Cancer Cell* **2023**, *41*, 374−403.
(38) Yang, L.; Zhang, Y. Tumor-associated macrophages: from basic research to clinical application, *J. Hematol. Oncol*. **2017**, *10*, 58.
(39) Yu, Z.; Zou, J.; Xu, F. Tumor-associated macrophages affect the treatment of lung cancer, *Heliyon* **2024**, *10*, e29332.
(40) Veillette, A.; Chen, J. SIRPα-CD47 Immune Checkpoint Blockade in Anticancer Therapy, *Trends Immunol.* **2018**, *39*, 173−184.
(41) Vial, J.; Huchedé, P.; Fagault, S.; Basset, F.; Rossi, M.; Geoffray, J.; Soldati, H.; Bisaccia, J.; Elsensohn, M- H.; Creveaux, M.; Neves, D.; Blay, J. Y.; Fauvelle, F.; Bouquet, F.; Streichenberger, N.; Corradini, N.; Bergeron, C.; Maucort-Boulch, D.; Castets, P.; Carré, M.; Weber, K.; Castets, M. Low expression of ANT1 confers oncogenic properties to rhabdomyosarcoma tumor cells by modulating metabolism and death pathways, *Cell Death Discov*. **2020**, *6*, 64.
(42) Balážová, K.; Clevers, H.; Dost, A. F. The role of macrophages in non-small cell lung cancer and advancements in 3D co-cultures, *eLife* **2023**, *12*, e82998.
(43) Chen, S.; Giannakou, A.; Golas, J.; Geles, K. G. Multidimensional Coculture System to Model Lung Squamous Carcinoma Progression, *J. Vis. Exp*. **2020**, *157*, e60644.
(44) Nyga, A.; Neves, J.; Stamati, K.; Loizidou, M.; Emberton, M.; Cheema, U. The next level of 3D tumor models: immunocompetence, *Drug Discov. Today* **2016**, *21*, 1421−1428.
(45) Kleinman, H. K.; Martin, G. R. Matrigel: basement membrane matrix with biological activity, *Semin. Cancer Biol.* **2005**, *15*, 378−386.
(46) Lu, P.; Weaver, V. M.; Werb, Z. The extracellular matrix: a dynamic niche in cancer progression, *J. Cell Biol*. **2012**, *196*, 395−406.
(47) Hanahan, D.; Coussens, L. M. Accessories to the crime: functions of cells recruited to the tumor microenvironment, *Cancer Cell* **2012**, *21*, 309−322.
(48) Chanput, W.; Mes, J. J.; Wichers, H. J. THP-1 cell line: An in vitro cell model for immune modulation approach, *Int. Immunopharmacol*. **2014**, *23*, 37−45.
(49) Genin, M.; Clement, F.; Fattaccioli, A.; Raes, M.; Michiels, C. M1 and M2 macrophages derived from THP-1 cells differentially modulate the response of cancer cells to etoposide, *BMC Cancer* **2015**, *15*, 577.
(50) Mantovani, A.; Sica, A.; Sozzani, S.; Allavena, P.; Vecchi, A.; Locati, M. The chemokine system in diverse forms of macrophage activation and polarization, *Trends Immunol*. **2004**, *25*, 677−686.
(51) Rebelo, S. P.; Pinto, C.; Martins, T. R.; Harrer, N.; Estrada, M. F.; Loza-Alvarez, P.; Cabeçadas, J.; Alves, P. M.; Gualda, E. J.; Sommergruber, W.; Brito, C. 3D-3-culture: A tool to unveil macrophage plasticity in the tumor microenvironment, *Biomaterials* **2018**, *163*, 185−197.
(52) Vermes, I.; Haanen, C.; Steffens-Nakken, H.; Reutellingsperger, C. A novel assay for apoptosis Flow cytometric detection of phosphatidylserine expression on early apoptotic cells using fluorescein labelled Annexin V, *J. Immunol. Methods* **1995**, *184*, 39−51.
(53) Philpott, N. J.; Turner, A. J. C.; Scopes, J.; Westby, M.; Marsh, J. C. W.; Gordon-Smith, E. C.; Dalgleish, A. G.; Gibson, F. M. The Use of 7-Amino Actinomycin D in Identifying Apoptosis: Simplicity of Use and Broad Spectrum of Application Compared With Other Techniques, *Blood* **1996**, *87*, 2244−2251.
(54) Kim, H.; Namgung, R.; Singha, K.; Oh, I. K.; Kim, W. J. Graphene Oxide–Polyethylenimine Nanoconstruct as a Gene Delivery Vector and Bioimaging Tool, *Bioconjugate Chem*. **2011**, *22*, 2558−2567.

(55) Mitchell, M. J.; Billingsley, M. M.; Haley, R. M.; Wechsler, M. E.; Peppas, N. A.; Langer, R. Engineering precision nanoparticles for drug delivery, *Nat. Rev. Drug Discov*. **2021**, *20*, 101−124.
(56) Susnik, E.; Bazzoni, A.; Taladriz-Blanco, P.; Balog, S.; Moreno-Echeverri, A. M.; Glaubitz, C.; Oliveira, B. B.; Ferreira, D.; Viana Baptista, P.; Petri-Fink, A.; Rothen-Rutishauser, B. Epidermal growth factor alters silica nanoparticle uptake and improves gold-nanoparticle-mediated gene silencing in A549 cells, *Front. Nanotechnol*. **2023**, *5*, 1220514.
(57) Han, H. In Disease Gene Identification: Methods and Protocols, *Springer*, New York, **2018**, pp. 293−302.
(58) Hong, S. W.; Jiang, Y.; Kim, S.; Li, C. J.; Lee, D. K. Target Gene Abundance Contributes to the Efficiency of siRNA-Mediated Gene Silencing, *Nucleic Acid Ther*. **2014**, *24*, 192−198.
(59) Lu, Z. J.; Mathews, H. D. Fundamental differences in the equilibrium considerations for siRNA and antisense oligodeoxynucleotide design, *Nucleic Acids Res.* **2008**, *36*, 3738−3745.
(60) Chen, X.-J.; Guo, C. H.; Wang, Z. C.; Yang, Y.; Pan, Y. H.; Liang, J. Y.; Sun, M. G.; Fan, L. S.; Liang, L.; Wang, W. Hypoxia-induced ZEB1 promotes cervical cancer immune evasion by strengthening the CD47-SIRPα axis, *Cell Commun. Signal*. **2024**, *22*, 15.
(61) Kaur, S.; Isenberg, J. S.; Roberts, D. D. CD47 (Cluster of Differentiation 47), *Atlas Genet. Cytogenet. Oncol. Haematol*. **2021**, *25*, 83−102.
(62) Wang, Y.; Xu, Z.; Guo, S.; Zhang, L.; Sharma, A.; Robertson, G. P.; Huang, L. Intravenous Delivery of siRNA Targeting CD47 Effectively Inhibits Melanoma Tumor Growth and Lung Metastasis, *Mol. Ther.* **2013**, *21*, 1919−1929.
(63) Wu, J.; Li, Z.; Yang, Z.; Guo, L.; Zhang, Y.; Deng, H.; Wang, C.; Feng, M. A Glutamine-Rich Carrier Efficiently Delivers Anti-CD47 siRNA Driven by a "Glutamine Trap" To Inhibit Lung Cancer Cell Growth, *Mol. Pharmaceutics* **2018**, *15*, 3032−3045.
(64) Roudi, R.; Madjd, Z.M; Ebrahimi, M.; Samani, F; Samadikuchaksaraei, A. CD44 and CD24 cannot act as cancer stem cell markers in human lung adenocarcinoma cell line A549, *Cell. Mol. Biol. Lett*. **2014**, *19*, 23−36.
(65) Zhang, X.; Yu, C.; Liu, J. Q.;. Bai, X. F. Dendritic cell expression of CD24 contributes to optimal priming of T lymphocytes in lymph nodes, *Front. Immunol*. **2023**, *14*, 1116749.
(66) Jang, J.-Y.; Choi, Y.; Jeon, Y. K.; Aung, K. C. Y.; Kim, C. W. Over-expression of Adenine Nucleotide Translocase 1 (ANT1) Induces Apoptosis and Tumor Regression in vivo, *BMC Cancer* **2008**, *8*, 160.
(67) Whithaus, K.; Fukuoka, J.; Prihoda, T. J.; Jagirdar, J. Evaluation of napsin A, cytokeratin 5/6, p63, and thyroid transcription factor 1 in adenocarcinoma versus squamous cell carcinoma of the lung, *Arch. Pathol. Lab. Med*. **2012**, *136*, 155−162.
(68) Luo, H. T.; Liang, C- X.; Luo, R. C.; Gu, W. G. Identification of relevant prognostic values of cytokeratin 20 and cytokeratin 7 expressions in lung cancer, *Biosci. Rep*. **2017**, **37**, BSR20171086.
(69) Mishra, D. K.; Creighton, C. J.; Zhang, Y; Gibbons, D. L.; Kurie, J. M.; Kim, M. P. Gene expression profile of A549 cells from tissue of 4D model predicts poor prognosis in lung cancer patients, *Int. J. Cancer* **2014**, *134*, 789−798.
(70) Vogel, C.; Marcotte, E. M. Insights into the regulation of protein abundance from proteomic and transcriptomic analyzes, *Nat. Rev. Genet*. **2012**, *13*, 227−232.
(71) Franks, A.; Airoldi, E.; Slavov, N. Post-transcriptional regulation across human tissues, *PLoS Comput. Biol*. **2017**, *13*, e1005535.
(72) Poncet, C.; Frances, V.; Gristina, R.; Scheiner, C.; Pellissier, J. F.; Figarella-Branger, D. CD24, a glycosylphosphatidylinositol-anchored molecules is transiently expressed during the development of human central nervous system and is a marker of human neural cell lineage tumors*, Acta Neuropathol*. **1996**, *91*, 400.
(73) Oldenborg, P.-A. CD47: A Cell Surface Glycoprotein Which Regulates Multiple Functions of Hematopoietic Cells in Health and Disease, *Int. Sch. Res. Notices* **2013**, *2013*, 614619.
(74) Schwanhäusser, B.; Busse, D.; Li, N.; Dittmar, G.; Schuchhardt, J.; Wolf, J.; Chen, W.; Selbach, M. Global quantification of mammalian gene expression control, *Nature* **2011**, *473*, 337.
(75) Kojima, Y.; Volkmer, J. P.; McKenna, K.; Civelek, M.; Lusis, A. J.; Miller, C. L.; Direnzo, D.; Nanda, V.; Ye, J.; Connolly, A. J.; Schadt, E. E.; Quertermous, T.; Betancur, P.; Maegdefessel, L.; Matic, L. P.; Hedin, U.; Weissman, I. L.; Leeper, N. J. CD47-blocking antibodies restore phagocytosis and prevent atherosclerosis, *Nature* **2016**, *536*, 86.
(76) Mezzapelle, R.; De Marchis, F.; Passera, C.; Leo, M.; Brambilla, F.; Colombo, F.; Casalgrandi, M.; Preti, A.; Zambrano, S.; Castellani, P.; Ertassi, R.; Silingardi, M.; Caprioglio, F.; Basso, V.; Boldorini, R.; Carretta, A.; Sanvito, F.; Rena, O.; Rubartelli, A.; Sabatino, L.; Mondino, A.; Crippa, M. P.; Colantuoni, V.; Bianchi, M. E. CXCR4 engagement triggers CD47 internalization and antitumor immunization in a mouse model of mesothelioma, *EMBO Mol. Med*. **2021**, *13*, e12344.
(77) Laguna-Teno, F.; Suarez-Diez, M.; Tamayo-Ramos, J. A. Commonalities and Differences in the Transcriptional Response of the Model Fungus Saccharomyces cerevisiae to Different Commercial Graphene Oxide Materials, *Front. Microbiol*. **2020**, *11*, 1943.
(78) Alnasser, F.; Castagnola, V.; Boselli, L.; Esquivel-Gaon, M.; Efeoglu, E.; McIntyre, J.; Byrne, H. J.; Dawson, K. A. Graphene Nanoflake Uptake Mediated by Scavenger Receptors, *Nano Lett.* **2019**, *19*, 1260−1268.
(79) Baid, K.; Nellimarla, S.; Huynh, A.; Boulton, S.; Guarné, A.; Melacini, G.; Collins, S. E.; Mossman, K. L. Direct binding and internalization of diverse extracellular nucleic acid species through the collagenous domain of class A scavenger receptors, *Immunol. Cell Biol.* **2018**, *96*, 922−934.

(80) Nakano, N.; Fukuhara-Takaki, K.; Jono, T.; Nakajou, K.; Eto, N.; Horiuchi, S.; Takeya, M.; Nagai, R. Association of Advanced Glycation End Products with A549 Cells, a Human Pulmonary Epithelial Cell Line, Is Mediated by a Receptor Distinct from the Scavenger Receptor Family and RAGE, *J. Biochem*. **2006**, *139*, 821−829.
(81) Elshoky, H. A.; El-Sayed, N. M.; Hassouna, Y. H.; Salaheldin, T. A.; Gaber, M. H.; Ali, M. H. A. Improved in vitro biocompatibility and cytoplasmic localization of gold nanoparticles and graphene oxide nanosheets assessed using confocal microscopy, *J. Drug Deliv. Technol*. **2023**, *86*, 104678.
(82) Huang, J.; Zong, C.; Shen, H.; Liu, M.; Chen, B.; Ren, B.; Zhang, Z. Mechanism of Cellular Uptake of Graphene Oxide Studied by Surface-Enhanced Raman Spectroscopy, *Small* **2012**, *8*, 2577−2584.
(83) Dabrowski, B.; Zuchowska, A.; Kasprzak, A.; Zukowska, G. Z.; Brzozka, Z. Cellular uptake of biotransformed graphene oxide into lung cells, *Chem. Biol. Interact.* **2023**, *376*, 110444.
(84) Engelberg, S.; Modrejewski, J.; Walter, J. G.; Livney, Y. D.; Assaraf, Y. G. Cancer cell-selective, clathrin-mediated endocytosis of aptamer decorated nanoparticles, *Oncotarget* **2018**, *9*, 20993−21006.
(85) Giamas, G. Cancer Gene Therapy: vision and strategy for the new decade, *Cancer Gene Ther*. **2020**, *27*, 115−115.
(86) Jin, C.; Wang, F.; Tang, Y.; Zhang, X.; Wang, J.; Yang, Y. Distribution of Graphene Oxide and TiO2-Graphene Oxide Composite in A549 Cells, *Biol. Trace Elem. Res.* **2014**, *159*, 393−398.
(87) Li, R.; Wang, Y.; Du, J.; Wang, X.; Duan, A.; Gao, R.; Liu, J.; Li, B. Graphene oxide loaded with tumor-targeted peptide and anti-cancer drugs for cancer target therapy, *Sci. Rep*. **2021**, *11*, 1725.
(88) Zhou, T.; Zhang, B.; Wei, P.; Du, Y.; Zhou, H.; Yu, M.; Yan, L.; Zhang, W.; Nie, G.; Chen, C.; Tu, Y.; Wei, T. Energy metabolism analysis reveals the mechanism of inhibition of breast cancer cell metastasis by PEG-modified graphene oxide nanosheets, *Biomaterials* **2014**, *35*, 9833.
(89) Fiorillo, M.; Verre, A. F.; Iliut, M.; Peiris-Pagés, M.; Ozsvari, B.; Gandara, R.; Cappello, A. R.; Sotgia, F.; Vijayaraghavan, A.; Lisanti, M. P. Graphene oxide selectively targets cancer stem cells, across multiple tumor types: Implications for non-toxic cancer treatment, via "differentiation-based nano-therapy", *Oncotarget* **2015**, *6*, 3553−3562.
(90) Chen, Y.; Taufiq, T.; Zeng, N.; Lozano, N.; Karakasidi, A.; Church, H.; Jovanovic, A.; Jones, S. A.; Panigrahi, A.; Larrosa, I.; Kostarelos, K.; Casiraghi, C.; Vranic, S. Defect-free graphene enhances enzyme delivery to fibroblasts derived from patients with lysosomal storage disorders, *Nanoscale* **2023**, *15*, 9348.
(91) Chen, Y.; Rivers-Auty, J.; Crică, L. E.; Barr, K.; Rosano, V.; Arranz, A. E.; Loret, T.; Spiller, D.; Bussy, K. Kostarelos, C.; Vranic, S. Dynamic interactions and intracellular fate of label-free, thin graphene oxide sheets within mammalian cells: role of lateral sheet size, *Nanoscale Adv*. **2021**, *3*, 4166−4185.
(92) Xiao, Y.; Xu, W.; Komohara, Y.; Fujiwara, Y.; Hirose, H.; Futaki, S.; Niidome, T. Effect of Surface Modifications on Cellular Uptake of Gold Nanorods in Human Primary Cells and Established Cell Lines, *ACS Omega* **2020**, *5*, 32744−32752.
(93) Bosshart, H.; Heinzelmann, M. THP-1 cells as a model for human monocytes, *Ann. Transl. Med*. **2016**, *4*, 21.
(94) Tremble, L. F.; McCabe, M.; Walker, S. P.; McCarthy, P.; Tynan, R. F.; Beecher, S.; Werner, R.; Clover, A. J. P.; Power, X. D. G.; Forde, P. F.; Heffron, C. C. B. B. Differential association of CD68+ and CD163+ macrophages with macrophage enzymes, whole tumor gene expression and overall survival in advanced melanoma, *Br. J. Cancer* **2020**, *123*, 1553−1561.
(95) Xia, Y.; Rao, L.; Yao, H.; Wang, Z.; Ning, X. P. Chen, Engineering Macrophages for Cancer Immunotherapy and Drug Delivery, *Adv. Mater*. **2020**, *32*, 2002054.
(96) Luo, Y.; Peng, J.; Huang, C.; Cao, Y. Graphene oxide size-dependently altered lipid profiles in THP-1 macrophages, *Ecotoxicol. Environ. Saf*. **2020**, *199*, 110714.
(97) Wu, Y.; Wan, S.; Yang, S.; Hu, H.; Zhang, C.: Lai, J.; Zhou, J.; Chen, W.; Tang, X.; Luo, J.; Zhou, X.; Yu, L.; Wang, L.; Wu, A.; Fan, Q.; Wu, J. Macrophage cell membrane-based nanoparticles: a new promising biomimetic platform for targeted delivery and treatment, *J. Nanobiotechnol*. **2022**, *20*, 542.
(98) R. Hosseinzadeh, K. Khorsandi, G. Hosseinzadeh, Graphene oxide-methylene blue nanocomposite in photodynamic therapy of human breast cancer, *J. Biomol. Struct. Dyn*. **2018**, *36*, 2216−2223.
(99) Zhang, W.; Dai, J.; Zhang, G.; Zhang, Y.; Li, S.; Nie, D. Photothermal/pH Dual-Responsive Drug Delivery System of Amino-Terminated HBP-Modified rGO and the Chemo-Photothermal Therapy on Tumor Cells, *Nanoscale Res. Lett*. **2018**, *13*, 379.
(100) Lazarovits, J.; Chen, Y. Y.; Sykes, E. A.; Chan, W. C. W. Nanoparticle–blood interactions: the implications on solid tumor targeting, *Chem. Commun*. **2015**, *51*, 2756−2767.
(101) Lakhani, S. A.; Masud, A.; Kuida, K.; Porter, G. A.; Booth, C. J.; Mehal, W. Z.; Inayat, I.; Flavell, R. A. Caspases 3 and 7: Key Mediators of Mitochondrial Events of Apoptosis, *Science* **2006**, *311*, 847.
(102) Li, P.; Zhou, L.; Zhao, T.; Liu, X.; Zhang, P.; Liu, Y.; Zheng, X.; Li, Q. Caspase-9: structure, mechanisms and clinical application, *Oncotarget* **2017**, *8*, 23996−24008.
(103) Liu, X.; He, Y.; Li, F.; Huang, Q.; Kato, T. A.; Hall, R. P.; Li, C.-Y. Caspase-3 Promotes Genetic Instability and Carcinogenesis, *Mol. Cell* **2015**, *58*, 284−296.
(104) Chen, Q.; Guo, X.; Ma, W. Opportunities and challenges of CD47-targeted therapy in cancer immunotherapy, *Oncol. Res*. **2024**, *32*, 49−60.
(105) Gimondi, S.; Vieira De Castro, J.; Reis, R. L.; Ferreira, H.; Neves, N. M. On the size-dependent internalization of sub-hundred polymeric nanoparticles, *Colloids Surf. B: Biointerfaces* **2023**, *225*, 113245.

(106) Lee, S.; Hong, J. H.; Kim, J. S.; Yoon, J. S.; Chun, S. H.; Hong, S. A.; Kim, E. J.; Kang, K.; Lee Kang, J.; Ko, Y. H.; Ahn, Y.-H. Cancer-associated fibroblasts activated by miR-196a promote the migration and invasion of lung cancer cells, *Cancer Lett.* **2021**, *508*, 92−103.
(107) Mu, P.; Zhou, S.; Lv, T.; Xia, F.; Shen, L.; Wan, J.; Wang, Y.; Zhang, H.; Cai, S.; Peng, J.; Hua, G.; Zhang, Z. Newly developed 3D in vitro models to study tumor–immune interaction, *J. Exp. Clin. Cancer Res*. **2023**, *42*, 81.
(108) Raveendran, N.; Vaswani, K.; Han, P.; Basu, S.; Moran, C. S.; Ivanovski, S. Modeling inflammatory response using 3D bioprinting of polarized macrophages, *Int. J. Bioprinting* **2024**, *10*, 398-412
(109) Komohara, Y.; Jinushi, M.; Takeya, M. Clinical significance of macrophage heterogeneity in human malignant tumors, *Cancer. Sci.* **2014**, *105*, 1−8.
(110) Zhang, J.; Li, S.; Liu, F.; Yang, K. Role of CD68 in tumor immunity and prognosis prediction in pan-cancer, *Sci. Rep*. **2022**, *12*, 7844.
(111) Willingham, S. B.; Volkmer, J. P.; Gentles, A. J.; Sahoo, D.; Dalerba, P.; Mitra, S. S.; Wang, J.; Contreras-Trujillo, H.; Martin, R.; Cohen, J. D.; Lovelace, P.; Scheeren, F. A.; Chao, M. P.; Weiskopf, K.; Tang, C.; Volkmer, A. K.; Naik, T. J.; Storm, T. A.; Mosley, A. R.; Edris, B.; Schmid, S. M.; Sun, C. K.; Chua, M. S.; Murillo, O.; Rajendran, P.; Cha, A. C.; Chin, R. K.; Kim, D.; Adorno, M.; Raveh, T.; Tseng, D.; Jaiswal, S.; Enger, P.; Steinberg, G. K.; Li, G.; So, S. K.; Majeti, R.; Harsh, G. R.; Van de Rijn, M.; Teng, N. N.; Sunwoo, J. B.; Alizadeh, A. A.; Clarke, M. F.; Weissman, I. L. The CD47-signal regulatory protein alpha (SIRPa) interaction is a therapeutic target for human solid tumors, *Proc. Natl. Acad. Sci. U. S. A*. **2012**, *109*, 6662−6667.
(112) Miyazaki, K.; Oyanagi, J.; Hoshino, D.; Togo, S.; Kumagai, H.; Miyagi, Y. Cancer cell migration on elongate protrusions of fibroblasts in collagen matrix, *Sci. Rep*. **2019**, *9*, 292.
(113) Lena, A.; Rechichi, M.; Salvetti, A.; Vecchio, D.; Evangelista, M.; Rainaldi, G.; Gremigni, V.; Rossi, L. The silencing of adenine nucleotide translocase isoform 1 induces oxidative stress and programmed cell death in ADF human glioblastoma cells, *FEBS J*. **2010**, *277*, 2853−2867.
(114) Ulchenko, D.; Miloykovich, L.; Zemlyanaya, O.; Shimanovsky, N.; Fedotcheva, T. Possible Participation of Adenine Nucleotide Translocase ANT1 in the Cytotoxic Action of Progestins, Glucocorticoids, and Diclofenac on Tumor Cells, *Pharmaceutics* **2023**, *15*, 2787.
(115) Del Bufalo, F.; Manzo, T.; Hoyos, V.; Yagyu, S.; Caruana, I.; Jacot, J.; Benavides, O.; Rosen, D.; Brenner, M. K. 3D modeling of human cancer: A PEG-fibrin hydrogel system to study the role of tumor microenvironment and recapitulate the in vivo effect of oncolytic adenovirus, *Biomaterials* **2016**, *84*, 76−85.
(116) Zhang, L.; Xia, J.; Zhao, Q.; Liu, L.; Zhang, Z. Functional Graphene Oxide as a Nanocarrier for Controlled Loading and Targeted Delivery of Mixed Anticancer Drugs, *Small* **2010**, *6*, 537.
(117) Abedi-Gaballu, F.; Dehghan, G.; Ghaffari, M.; Yekta, R.; Abbaspour-Ravasjani, S.; Baradaran, B.; Ezzati Nazhad Dolatabadi, J.; Hamblin, M. R. PAMAM dendrimers as efficient drug and gene delivery nanosystems for cancer therapy, Appl. Mater. *Today* **2018**, *12*, 177−190.
(118) Mirzaie, V.; Ansari, M.; Nematollahi-Mahania, S. N.; Nasery, M. M.; Karimi, B.; Eslaminejad, T.; Pourshojaei, Y. Nano-Graphene Oxide-supported APTES-Spermine, as Gene Delivery System, for Transfection of pEGFP-p53 into Breast Cancer Cell Lines, *Drug Des. Devel. Ther*. **2020**, *14*, 3087−3097.
(119) Pei, X.; Zhu, Z.; Gan, Z.; Chen, J.; Zhang, X.; Cheng, X.; Wan, Q.; Wang, J. PEGylated nano-graphene oxide as a nanocarrier for delivering mixed anticancer drugs to improve anticancer activity, *Sci. Rep.* **2020**, *10*, 2717.
(120) Thapa, B.; Remant, K. C.; Bahniuk, M.; Schmitke, J.; Hitt, M.; Lavasanifar, A.; Kutsch, O.; Seol, D.-W.; Uludag, H. Breathing New Life into TRAIL for Breast Cancer Therapy: Co-Delivery of pTRAIL and Complementary siRNAs Using Lipopolymers, *Hum. Gene Ther*. **2019**, *30*, 1531−1546.
(121) He, C.; Tang, Z.; Tian, H.; Chen, X. Co-delivery of chemotherapeutics and proteins for synergistic therapy, *Adv. Drug Deliv. Rev*. **2016**, *98*, 64−76.
(122) Tomek, S.; Horak, P.; Pribill, I.; Haller, G.; Rössler, M.; Zielinski, C. C.; Pils, D.; Krainer, M. Resistance to TRAIL-induced apoptosis in ovarian cancer cell lines is overcome by co-treatment with cytotoxic drugs, *Gynecol. Oncol*. **2004**, *94*, 107−114.
(123) Li, X.; Peng, X.; Zoulikha, M.; Boafo, G. F.; Magar, K. T.; Ju, Y.; He, W. Multifunctional nanoparticle-mediated combining therapy for human diseases, Signal Transduct. *Target. Ther.* **2024**, *9*, 1.
(124) Li, S.; Sun, Y.; Du, M.; Shangguan, A.; Liu, Z.; Li, W.; Lina, L.; Liu, W.; Zhang, S.; Han, H. Graphene Oxide Nanoparticles Combined with CRISPR/Cas9 System Enable Efficient Inhibition of Pseudorabies Virus, *Bioconjugate Chem.* **2023**, *34*, 326−332.
(125) Yue, H.; Zhou, X.; Cheng, M.; Xing, D. Graphene oxide-mediated Cas9/sgRNA delivery for efficient genome editing, *Nanoscale* **2018**, *10*, 1063.
(126) Lee, B.; Gries, K.; Valimukhametova, A. R.; McKinney, R. L.; Gonzalez-Rodriguez, R.; Topkiran, U. C.; Coffer, J.; Akkaraju, G. R.; Naumov, A. V. In Vitro Prostate Cancer Treatment via CRISPR-Cas9 Gene Editing Facilitated by Polyethyleneimine-Derived Graphene Quantum Dots, *Adv. Funct. Mater*. **2023**, *33*, 2305506.
(127) Qiu, Z.; Hu, J.; Li, Z.; Yang, X.; Hu, J.; You, Q.; Bai, S.; Mao, Y.; Hua, D.; Yin, J. Graphene oxide-based nanocomposite enabled highly efficient targeted synergistic therapy for colorectal cancer, *Colloids Surf. A: Physicochem. Eng. Asp.* **2020**, *593*, 124585.

Chapter 5: Dual Graphene Oxide-Based Multi-Gene Delivery for Cancer Elimination via Stromal and Immune Reprogramming

This chapter reports a submitted research article describing a gene-therapy strategy evaluated in a 3D tumor model, with a specific focus on enhancing cancer cell specificity. The study integrates targeted gene delivery with a multicellular 3D cancer model to investigate how microenvironmental complexity influences therapeutic selectivity and treatment response. The Supplementary Information associated with this submitted article is included in the Appendix of this thesis for completeness.

I conceived the experimental design and performed all cell cultures, biological experiments, data analysis, and interpretation of results presented in this chapter. I prepared all figures and wrote the manuscript. Assistance was limited to the sectioning of the 3D models.

Abstract

Cancer therapies are often limited by poor cellular specificity and tumor microenvironment-mediated immunosuppression. We developed a dual-function graphene oxide (GO)-based gene delivery platform combining direct cancer cell elimination with stromal and immune reprogramming. CD47-targeting siRNA and ANT1-encoding plasmid DNA selectively induced apoptosis in tumor cells, while TGFβ-targeting siRNA altered cancer-associated fibroblasts (CAFs) phenotype and was associated with a shift in macrophage polarization toward a pro-inflammatory, tumor-restraining phenotype. We evaluated this approach in a 3D multicellular lung cancer model consisting of A549 cells, human lung fibroblasts, and THP-1-derived macrophages. TGFβ silencing alone modulated stromal and immune features without direct cytotoxicity, whereas CD47/ANT1 modulation reduced overall cell viability to ~51%. When both therapeutic functions were applied together, overall cell viability was further reduced to ~29%. EGFR-targeted GO-CD47-ANT1 (GE11 peptide modified formulation) enhanced tumor-cell uptake and selective apoptosis in $CK7^+$ cancer cells to 91%, while sparing $CK7^-$ non-malignant populations (16%). Mechanistically, combined therapy suppressed immunosuppressive macrophage markers (CD163, IL10, TGFβ), restored epithelial integrity (E-cadherin 3.5-fold), and attenuated CAF activation (αSMA 0.3-fold; vimentin 0.6-fold). GE11 functionalization shifted nanocarrier internalization toward EGFR-mediated cancer cell uptake, minimizing off-target delivery to fibroblasts and macrophages. These findings demonstrate that synergistic modulation of cancer cells and the tumor microenvironment is essential for robust and selective tumor elimination. Our study establishes a modular, mechanism-informed GO platform integrating dual therapeutic functions, targeted cancer cell killing and microenvironmental reprogramming, highlighting its translational potential in physiologically relevant tumor models.

5.1 Introduction

Despite advances in chemotherapy, radiotherapy, and immunotherapy for the treatment of cancer, many clinical interventions remain limited by systemic toxicity, incomplete tumor specificity, and the emergence of therapy resistance [1, 2]. Gene therapy is gaining attention due to its potential for high tumor specificity and reduced off-target effects [3-8]. Contemporary gene delivery strategies exploit the precision to eradicate malignant cells while sparing healthy tissues selectively. However, the efficacy and durability of these approaches are inextricably shaped by the stromal and immune context surrounding the cancer, where tumor cells coexist with cancer-associated fibroblasts (CAFs), endothelial cells, immune cells, extracellular matrix (ECM) components, and a diverse array of soluble mediators [3, 9-12]. Cell-cell and cell-matrix interactions within this ecosystem govern nearly all steps of tumor development, from proliferation and invasion to immune evasion and metastatic dissemination. Cell-cell communication via adhesion molecules and secreted factors between cancer cells and immune cells, such as tumor-associated macrophages (TAMs), influences tumor growth and metastatic potential. Malignant cells reprogram macrophages via cytokines, leading to the generation of TAMs that support angiogenesis, degrade the ECM via proteases, and suppress cytotoxic T cell activity, facilitating immune evasion and metastasis [13].

CAFs are generated when resident fibroblasts become activated within the tumor milieu, acquiring a contractile and secretory phenotype that fuels tumor growth, invasion, metastasis, and therapy resistance. Dysregulated ECM remodeling by CAFs can alter ECM stiffness and composition, promote metastasis and inhibit immune cell infiltration. Matrix proteins like tenascin-C and osteonectin have been shown to induce matrix remodeling that inhibits $CD8^+$ T cell infiltration and supports macrophage polarization toward immunosuppressive phenotypes in breast and colorectal cancers [14].

3D co-cultures of lung cancer spheroids with CAFs demonstrated a significant increase in cancer spheroid growth and a rise in invasive protrusions compared to monocultures, linked to fibroblast-cancer interactions and fibroblast-mediated ECM remodelling [12, 15, 16]. Moreover, *in vitro* co-

culture experiments of cancer and immune cells and *in vivo* tumor models elucidate how tumor-derived signals regulate immune responses, modulating them to favor cancer proliferation and invasion [9, 17, 18]. Therefore, increasing evidence now highlights the profound impact of these interactions on patient prognosis and therapeutic response [12, 18-21], underscoring the need for therapeutic strategies that not only target cancer cells directly but also account for the microenvironmental constraints imposed by their surrounding cues.

Lung cancer, one of the deadliest malignancies, is heavily infiltrated by myeloid cells (*i.e.*, granulocytes, monocytes, macrophages, and dendritic cells) [22, 23], which regulate immune suppression, angiogenesis, metastasis, and therapy resistance. In solid tumors, macrophages often represent the largest myeloid population, comprising up to 50% of the tumor mass in lung cancer [9, 23]. Recruited monocytes can differentiate into macrophages spanning a functional spectrum, ranging from pro-inflammatory, tumor-restraining M1 states to immunosuppressive, tumor-promoting M2 phenotypes. It has been shown that macrophages in the presence of cancer cells closely align with the M2-like phenotype and strongly promote tumor progression via proliferation, angiogenesis, ECM remodeling, and immunosuppression [22-24]. M2-like macrophages correlate with poor response to standard therapies and, for this reason, have emerged as a promising therapeutic target [25-28], with controlled tumor progression in murine models and patients, resulting in prolonged survival [27, 29]. These findings highlight the substantial potential of harnessing macrophage biology to achieve specific cancer elimination.

Among the many regulators of tumor survival, cluster of differentiation 47 (CD47) is a key immune checkpoint that engages SIRPα on macrophages to suppress phagocytosis [30, 31]. Overexpression of CD47 in cancer cells constitutes a fundamental mechanism of immune evasion, and its inhibition restores macrophage recognition and phagocytic clearance of tumor cells. Conversely, adenine nucleotide translocator 1 (ANT1), a mitochondrial protein involved in metabolic regulation, is frequently downregulated in cancer cells. Its re-expression disrupts mitochondrial function and promotes apoptosis, exploiting cancer-specific metabolic vulnerabilities [32].

In our previous work [25, 33, 34], we established a graphene oxide (GO) nanocarrier system (~100 nm lateral size, 1 nm thickness; modified with polyethylene glycol (PEG) and PAMAM dendrimer) capable of efficiently loading and delivering multiple genetic payloads. Due to its large surface area, abundant oxygen-containing groups, and strong π-π and electrostatic interactions, GO carriers protect nucleic acids while achieving high transfection efficiency and cancer-selective activity [35-38]. This platform enabled co-delivery of CD47_siRNA and ANT1_pDNA to selectively reduce cancer cell survival in 3D lung cancer-stromal-immune models comprising lung cancer cells, fibroblasts, and monocyte-derived macrophages. This dual-targeted approach induced substantial apoptosis in cancer cells (up to 75%) while exhibiting minimal toxicity toward healthy cells (~35% apoptosis), demonstrating selective elimination driven by coordinated immune and metabolic reprogramming.

Building on this foundation, we now aim to enhance cancer cell elimination further while minimizing collateral effects on stromal and immune populations by incorporating an additional therapeutic target deeply intertwined with cancer regulation. Transforming growth factor-β (TGFβ) is a multifunctional cytokine produced by tumor cells, immune cells, and CAFs. It drives the activation of fibroblasts into CAFs and stimulates ECM deposition. It also promotes the proliferation and migration of cancer cells while impairing immune cell activity, including that of macrophages [19, 39-41]. Elevated TGFβ levels correlate strongly with poor prognosis, metastatic progression, and resistance to chemo- and immunotherapies. Accordingly, therapeutic inhibition of TGFβ signaling has been shown to suppress CAFs activation, normalize the ECM, and sensitize tumors to otherwise ineffective treatments by dismantling pro-survival and immunosuppressive signals [42-45].

Building on our previously established GO-based delivery platform [37], we now incorporate an active-targeting component by functionalizing GO-PEG-PAMAM with GE11, a 12-amino-acid peptide that selectively binds the epidermal growth factor receptor (EGFR), which is overexpressed in lung adenocarcinoma cells [46-48]. GE11 conjugation has been shown to enhance tumor-specific internalization and gene expression in EGFR-overexpressing tumors while maintaining low mitogenicity. Similar targeting strategies in other carriers improve tumor accumulation, uptake, and

therapeutic efficacy while reducing off-target effects [49, 50]. Integrating GE11 with GO-based multi-gene carriers provides a rational strategy for selective and potent reprogramming of the tumor microenvironment, maximizing cancer cell elimination while minimizing unintended effects on healthy tissues.

5.2 Materials and Methods

5.2.1 Cell Culture

Human lung carcinoma A549 cells (ATCC, USA) were maintained in Dulbecco's Modified Eagle Medium (DMEM, Gibco, USA) supplemented with 10 % fetal bovine serum (FBS, Gibco). Human lung fibroblasts (HLF; Lonza, Canada) were cultured in Fibroblast Growth Basal medium (FBM-2) supplemented with 5% Insulin, 5% human fibroblast growth factor (hFGF-B), and 5% gentamicin sulfate-amphotericin (GA-1000; FGM™-2 Fibroblast Growth Medium-2 BulletKit™, Lonza, Canada). THP-1 monocytes (ATCC, USA) were maintained in RPMI-1640 medium (Gibco) containing 10 % FBS and 2-mercaptoethanol to a final concentration of 0.05 mM. Dendritic cells (DC; ABM, Canada) were maintained in PriGrow X Series Medium for T0525 (ABM, Canada) supplemented with 10% FBS. All cells were incubated at 37 °C in a humidified atmosphere with 5 % CO_2.

5.2.2 Establishment of the 3D Lung Cancer Model

A 3D lung cancer model containing A549 cancer cells (A), HLF fibroblasts (F), and THP-1 (T) was developed following the same procedure as described in our previous work (referred to as the AFT model) [37]. Briefly, to prepare the extracellular matrix, Matrigel® Matrix Basement Membrane Growth factor reduced (Corning, USA) was mixed with collagen type I (3 mg/mL, Corning) in a 1:1 ratio on ice. The cell mixture (A:F:T, 1:1:1, 15 × 10^3 cells/model) was resuspended in the Matrigel-collagen solution and deposited as droplets (5 μL) into Nunclon™ Sphera™ low-attachment well

plates (Thermo Fisher Scientific, Canada). After polymerization at 37 °C for 1 h, pre-warmed culture medium (DMEM with 10% FBS) was added gently to each well. The constructs were maintained for 6 d to allow complete cellular organization within the 3D matrix before any treatment. AFTs treated with 50ng/mL of Phorbol 12-myristate 13-acetate (PMA, Sigma-Aldrich, Canada) for THP-1 macrophage activation. After 24h of PMA treatment, the medium was replaced with fresh medium, and the cells were allowed to recover for 24h prior to further treatments.

Control models containing two cell lines (A549 and HLF: AF model; A549 and THP-1: AT model; HLF and THP-1: FT model) were realized following the same procedure. For immune-specific control experiments, additional models incorporating DCs were prepared. AF-DC constructs (A:F:DC, 1:1:1; 15×10^3 cells per model) and AFT-DC constructs (A:F:T:DC, 1:1:0.5:0.5; 15×10^3 cells per model) were generated using the same matrix preparation and culture protocol.

5.2.3 Functionalization of Graphene Oxide Nanocarriers

Graphene oxide (GO) sheets were produced from natural graphite powder following a modified Hummers' oxidation method, as previously reported.[33, 34] The oxidized product was repeatedly washed and filtered to obtain a single-layer GO with lateral dimensions exceeding 650 nm. The resulting dispersion was thoroughly rinsed with deionized water and stored at 1 mg/mL. To generate the small-sized formulation, GO sheets were subjected to controlled intermittent probe sonication (probe sonicator, Cole Parmer, Canada) at low power (10 W) and 0 °C to obtain nanosheets with an average lateral size of approximately 100 nm [51, 52].

GO was functionalized with six-arm amine-terminated polyethylene glycol (PEG, 15 kDa; Jenkem Technology, USA) and fourth-generation, primary amine polyamidoamine (PAMAM, 10 kDa; 10.1 w/w% in water, Dendritech Inc., USA) using carbodiimide coupling chemistry, as previously described [33].

For experiments involving targeted nanocarriers, the GO-PEG-PAMAM material was biofunctionalized by further conjugation with the GE11 peptide (amino acid sequence

YHWYGYTPQNVI, MW ≈ 1757 Da; GenScript, USA) via carbodiimide-mediated coupling. GE11 solution (1 mg/mL) was mixed with 0.1 M MES buffer (pH 5.5) and activated with freshly prepared 1-ethyl-3-(3-dimethylaminopropyl)carbodiimide hydrochloride (EDC, Sigma-Aldrich, USA; 0.546 mg, 2.846 μmol) and N-hydroxysuccinimide (NHS, Sigma-Aldrich; 0.328 mg, 2.846 μmol) for 20 min at room temperature to form reactive NHS esters. The activated GE11 solution was then added dropwise to the GO-PEG-PAMAM dispersion under gentle stirring, and the mixture was incubated at room temperature for 4 h. The resulting GE11-functionalized nanocarrier was washed repeatedly with water using Amicon Ultra centrifugal filters (30 kDa; MilliporeSigma, USA) to remove unreacted reagents. The final dispersion was stored at 4 °C for further use in selected experiments. For simplicity, the untargeted formulation, GO-PEG-PAMAM, will be referred to as GO, and the GO-PEG-PAMAM-GE11 formulation as GE11/GO.

For uptake analysis, GO and GE11/GO were labeled with Alexa Fluor 488 or 568 dyes (Conjugation Kit (Fast) Lightning-Link®, Abcam, USA) following the manufacturer's protocol [37]. Briefly, the modifier was added to 10 μg of GO or GE11/GO (1 mg/mL), mixed with the lyophilized Alexa Fluor conjugation mix, and incubated for 15 min. Finally, the quencher was added, and the mixture was incubated for 5 min. The conjugated material was stored at 4 °C in darkness.

5.2.4 Gene Loading and Transfection Procedures

siRNA duplexes targeting CD47 and TGFβ (CD47_siRNA and TGFβ_siRNA; IDT, USA), and plasmid DNA encoding ANT1 (ANT1_pDNA; Origene, USA) were complexed with GO to form transfection mixes. GO, CD47_siRNA, and ANT1_pDNA were mixed at a 3:1 w/w nucleic acid-to-carrier ratio (CD47:ANT1 1:1 w/w) [31], in Opti-MEM Reduced-Serum Medium (Gibco) to form the transfection mix GO-CD47-ANT1. Similarly, GO and TGFβ_siRNA were mixed at a 1.5:1 w/w nucleic acid-to-carrier ratio to form the transfection mix GO-TGFβ. Mixtures were incubated for 60 min at room temperature to enable electrostatic adsorption of nucleic acids onto the nanocarrier.

For transfection experiments, the resulting GO-gene complexes were added to AFT constructs at a final nanocarrier concentration of 0.5 μg/mL and incubated under standard culture conditions for 72 h. Combinatorial transfection of CD47_siRNA, ANT1_pDNA, and TGFβ_siRNA was performed by adding the transfection mixes GO-CD47-ANT1 and GO-TGFβ at a final nanocarrier concentration of 1 μg/mL (1:1 w/w of GO-CD47-ANT1 and GO-TGFβ transfection mixes). Control samples included untreated AFT models (untransfected control), AFT models treated with naked nucleic acids (*i.e.*, CD47_siRNA, ANT1_pDNA, TGFβ_siRNA) and GO flakes without genes. Transfection efficiency and gene modulation were analyzed at 72 h post-treatment. Gene loading and transfection procedures using GE11/GO were performed following the same methods.

5.2.5 Immunohistochemistry (IHC)

For IHC, AFT were washed with phosphate buffered saline (PBS) (Thermo Fisher Scientific, Canada) and fresh frozen in Optimal Cutting Temperature (OCT) compound (Fisher Healthcare Tissue-Plus™, Thermo Fisher Scientific, Canada) to generate tissue blocks. The frozen blocks were used to prepare frozen sections (10 μm thick), which were placed on glass slides. The sections were then washed with PBS, permeabilized using 0.1% Triton X-100 (Sigma-Aldrich, USA), and blocked in 5% normal goat serum (Thermo Fisher Scientific, Canada) for 1h at RT. Primary antibodies against Caspase 9, cluster of differentiation 68 (CD68), E-cadherin (Thermo Fisher Scientific, Canada), alpha-smooth muscle actin (αSMA), vimentin and cytokeratin 7 (CK7; Abcam) were applied overnight at 4 °C. After washing, Alexa Fluor 488- or 555-conjugated goat anti-rabbit or anti-mouse secondary antibodies (Thermo Fisher Scientific, Canada) were added for 1 h at room temperature. Nuclei were counterstained with Hoechst 33342 (Thermo Fisher Scientific, Canada), and samples were mounted for imaging using Prolong Gold Antifade Mountant (Thermo Fisher Scientific, Canada) and cured overnight before visualization.

Fluorescence images were acquired with an Echo Revolve R4 (Discover Echo, USA) microscope equipped with 10× magnification objective (Olympus Life Science, Japan), and DAPI (ex: 380/30;

em: 450/50), FITC (ex: 470/40; em: 525/50) and TRITC (ex: 530/40; em: 605/70) filters. The images (895 × 750 μm^2 and 2448 × 2048 $pixel^2$) were analyzed using ImageJ.[53]

For image intensity quantifications, background-subtracted integrated fluorescence intensity of the target protein was measured for each section and divided by the corresponding nuclei count to account for differences in cell number. Protein expression levels were then normalized to the untransfected control and expressed as relative fold change.

For quantification of co-localization events, individual cells were identified by nuclear staining, and co-localization of the target signal with CK7 staining was assessed on a per-cell basis. The number of double-positive, single-positive, and double-negative cells was expressed as a percentage of the total number of cells within each population ($CK7^+$ or $CK7^-$).

Three sections of three different spheres (three technical replicates) from three separate experiments (three biological repeats) to varying depths within the center of the AFT model were used for quantifications.

5.2.6 RT-qPCR

Total RNA was extracted from the 3D AFT constructs using the RNeasy Micro Kit (Qiagen, USA) following the manufacturer's protocol. RNA purity and concentration were measured with a NanoDrop 2000 spectrophotometer (Thermo Fisher). RT-qPCR was performed on an Applied Biosystems™ 7500 Fast Real-Time PCR System and reverse transcription and amplification were performed with the Power SYBR Green RNA-to-CT 1-Step Kit (Thermo Fisher) using gene-specific primers for the housekeeping gene GAPDH and the targets CD47, ANT1, TGFβ, CD68, IL1β, TNFα, IL6, CD163, and IL10 (Quantitect Primer assays, Qiagen, Canada). qPCR reactions were conducted in 96-well optical plates (Applied Biosystems, USA) in triplicate. Relative expression levels were determined using the $2^{-\Delta\Delta Ct}$ method. Briefly, gene expression was normalized to the housekeeping gene GAPDH to obtain the ΔCq value for each target, which was then averaged across triplicates and normalized to the untransfected control to obtain the ΔΔCq. An exponential transformation (ΔΔCq

expression = $2^{-\Delta\Delta Cq}$) was used to obtain the fold change for each target relative to the untransfected control.

5.2.7 Cell Viability Evaluation

Cell viability was determined using the Cell Titer-Glo® Luminescent Cell Viability Assay (Promega, USA) and cell damage was assessed using the Lactate Dehydrogenase (LDH) Assay kit (Abcam, Canada) according to the manufacturer's instructions. For viability analysis, AFT constructs were transferred into opaque white 96-well plates (Corning) and equilibrated to room temperature before reagent addition (1:1 w/w reagent-to-medium). For ATP extraction, plates were shaken at 800 rpm for 10 min to ensure effective ATP extraction from the cells, then incubated at room temperature for 30 min at 500 rpm. Luminescence was recorded with a FLUOstar Omega microplate reader (Mandel Scientific, Canada). For LDH assessment, 100 µL of the LDH reaction mix was added to 10 µL of media in a transparent 96-well plate, and the mixture was incubated for 30 mins at RT before absorbance was measured at 490 nm. Data were normalized to untransfected controls to determine percentage viability and apoptotic activity.

5.2.8 Statistical Analysis

All data are presented as mean ± standard deviation (SD). RT-qPCR results are obtained from 3 biological repetitions (n = 3). For immunohistochemical image quantification, three sections per model (at different depths from the central region of the model), three technical replicates, and three separate biological repeats (n = 3) were analyzed. The results were averaged to obtain the final values and SD. Microplate reader results are given by 3 biological repetitions (n = 3) of a minimum of 3 technical replicates. All statistical analyses were performed with GraphPad Prism 8.02 (GraphPad Software, USA). Variations across more than three conditions were analyzed using a one-way ANOVA. At the same time, the effects of two independent variables on a dependent variable were assessed using a two-way ANOVA. A value of $P < 0.05$ was considered statistically significant.

5.3 Results and Discussion

5.3.1 3D Multicellular Cancer Model Recapitulates Tumor-Immune-Stroma Interactions

To enable mechanistic analysis of macrophage differentiation, polarization and therapeutic response within a lung tumor microenvironment, we established 3D constructs composed of A549 lung cancer cells, lung fibroblasts, and THP-1 monocytes, as previously described by our group.[37] Single-cell suspensions of A549, fibroblasts and THP-1 cells (AFT model) were encapsulated within Matrigel-collagen microdroplets to support 3D growth and spontaneous cell-cell and cell-matrix interactions (Figure 5.1A). The encapsulated cells self-assembled into integrated tumor-stroma-immune spheroids with a spherical morphology and an average diameter of 1972 ± 80 μm (Figure 5.1B). This value was calculated from measurements of 30 spheroids obtained across three independent biological replicates (10 spheroids per replicate) and falls within a size range that enables the development of spatially heterogeneous microenvironments and immune-stromal interactions within the spheroid. By day 11, $CK7^+$ lung adenocarcinoma [11, 54] cancer cells constituted 77 ± 2% of the total population (Figure S5.1) and organized into cohesive, spheroid-like epithelial structures (Figure 5.1C, orange arrows), a characteristic feature of epithelial tumor dominance in 3D matrices that reflects strong cell-cell adhesion and coordinated tissue organization [11, 21, 55]. THP-1 monocyte differentiation into macrophages was confirmed by dense $CD68^+$ multicellular clusters [24, 56], accounting for 16 ± 2% of the population (Figure 5.1C and Figure S5.1) [9, 18]. Lung fibroblasts ($CK7^-/CD68^-$) represented 7 ± 0.2% of the population and exhibited slower proliferation and a dispersed spatial distribution (Figure 5.1C and Figure S5.1), consistent with their supportive yet regulatory role in 3D tumor architecture rather than direct tissue dominance [9, 16, 21]. After 6 d of maturation, AFT constructs were treated with GO-CD47-ANT1 nanocarriers, a gene-delivery system previously validated by our group for efficient modulation of immune evasion and apoptotic signaling in cancer cells [37]. Transcriptional profiles of macrophage-associated cytokines and polarization markers associated with pro-inflammatory (M1-like) or immunosuppressive, tissue-remodeling (M2-like) phenotypes were then analyzed. The panel included M1-associated cytokine genes (IL1β, TNFα, and IL6) and

M2-associated markers (CD163, IL10, and TGFβ), which are commonly linked to inflammatory versus immunosuppressive, extracellular-matrix-remodeling macrophage states [9, 24, 56].

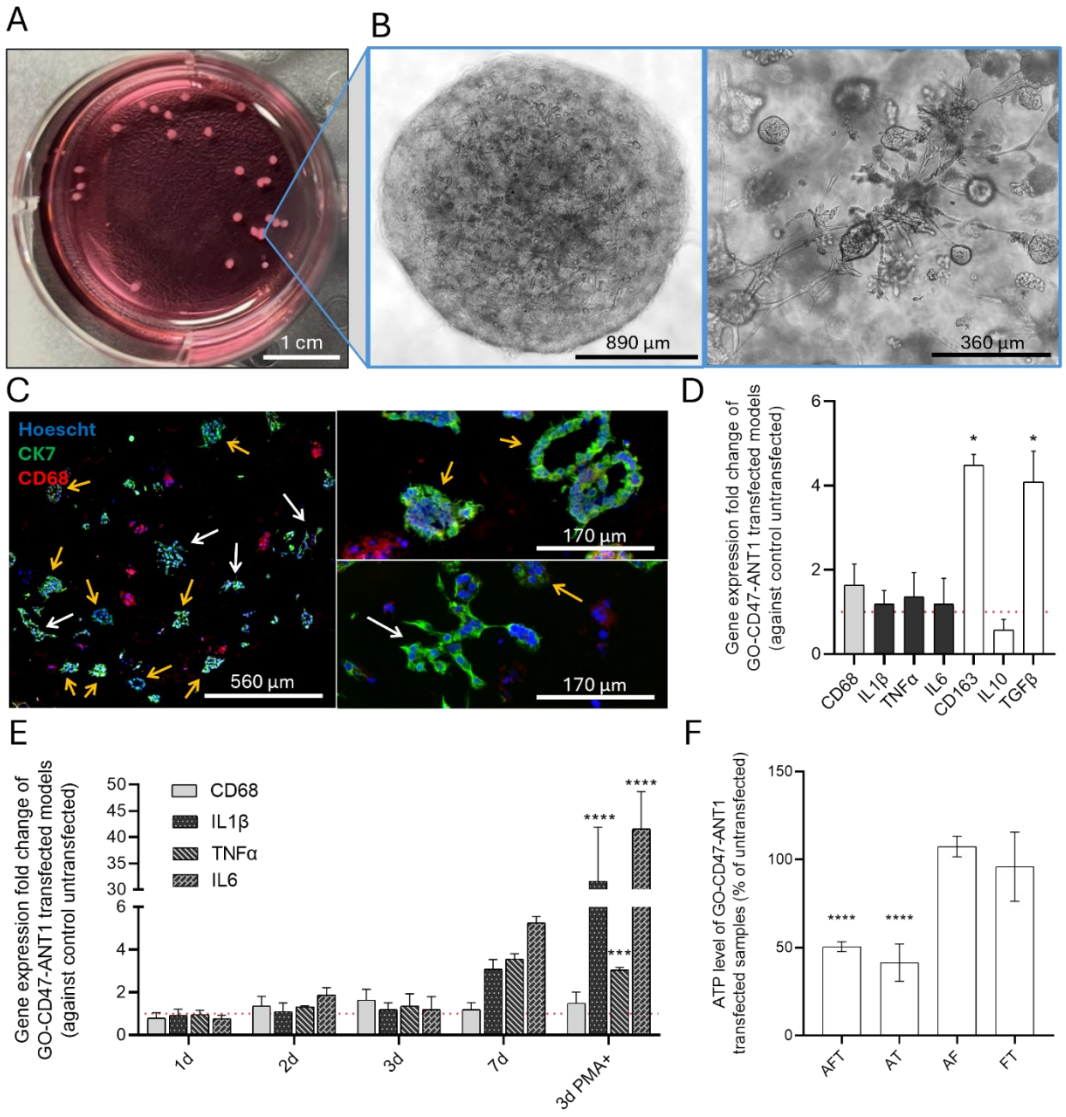

Figure 5.1. Characterization of the AFT 3D lung cancer model and macrophage polarization dynamics. A) AFT model in a multiwell after 6 d of incubation. Scale bar = 1 cm. B) Brightfield image showing the entire structure (left panel) and internal 3D cellular organization (right panel). Scale bars = 890 and 360 µm. C) IHC images of 10 µm thick sections from the central region of the AFT model. A low-magnification overview is shown on the left panel, while the right panel shows higher-magnification views. Blue: Hoechst nuclei; green: $CK7^+$ cancer cells; red: $CD68^+$ THP-1-derived macrophages. $CK7^+$ cells form spheroidal-like constructs (orange arrows) and disorganized structures (white arrows). Scale bars = 560 and 170 µm. D) qPCR of macrophage polarization cytokines and markers after 72 h GO-CD47-ANT1 transfection. Bar graph displays M0 (CD68), M1 (IL1β, TNFα, IL6) and M2 (CD163, IL10, TGFβ) gene expression. E) qPCR analysis over different transfection times and comparison with 3-day-transfected PMA-stimulated AFT constructs. F) Cell-viability (ATP quantification) in AFT and control co-culture models (AT: A549&THP-1, AF: A549&fibroblasts, FT: fibroblasts&THP-1) after GO-CD47-ANT1 transfection, highlighting PMA effects. Statistical significance was determined against the untransfected AFT model using one-way and two-way ANOVA (*P<0.05; **P<0.01; ***P<0.001; and ****P<0.0001; and P>0.05, not significant, not shown).

Gene-expression analysis in Figure 5.1D showed that macrophages adopted a predominantly immunosuppressive transcriptional profile following GO-CD47-ANT1 transfection, with mRNA levels of CD163 and TGFβ increasing 4.5-fold and 4.1-fold, respectively, and only minimal transcript induction of IL1β, TNFα, and IL6 (~1.2–1.4-fold). Although IL10 transcripts were reduced (~0.6-fold), the overall transcriptional profile, characterized by increased CD163 and TGFβ, indicates a shift toward M2-like tissue-remodeling and tumor-supportive macrophage states, reflecting transcriptional activity rather than absolute cytokine abundance [25]. This discrepancy suggests that 3D tumor microenvironment actively dampens macrophage inflammatory activation, even in the presence of gene-delivery interventions, likely through sustained cancer-fibroblast-macrophage crosstalk that reinforces M2-like polarization cues. These results are in line with the 3D tumor-immune-fibroblast models, which show that concurrent cancer-fibroblast interactions are required to promote $CD163^+$ M2-like macrophages and that THP-1 cell polarization depends on interactions with other cell types [9].

We next monitored IL1β, TNFα and IL6 transcript levels from 1 d to 7 d after transfection (Figure 5.1E). The gradual increase of M1 cytokine transcripts over seven days indicates delayed immune activation, consistent with progressive relief of tumor-mediated immune suppression rather than immediate inflammatory reprogramming. Exposure to PMA, a common treatment for differentiating THP-1 cells into macrophages [56, 57], prior to transfection, led to a rapid and robust increase in M1 cytokines mRNA levels within 72 h of transfection (Figure 5.1E), with IL1β, TNFα, and IL6 transcript levels increasing by 31.6-fold, 3-fold, and 41.5-fold, respectively. Consistent with known PMA effects on THP-1 differentiation, these results demonstrate that macrophage inflammatory activation is intrinsically suppressed within the 3D tumor microenvironment and requires strong exogenous pro-inflammatory cues for rapid induction [57].

A pro-inflammatory macrophage phenotype is usually associated with boosted cytotoxic immune functions, increased phagocytosis of malignant cells, and restriction of cancer cell growth and invasion [56]. Consequently, given the enhanced pro-inflammatory environment induced by pre-

treating AFT models with PMA, we then analyzed the cell viability after transfection. Figure 5.1F shows that AFT viability dropped to around 51%. AF models lacking immune cells exhibited no measurable reduction in viability, highlighting the contribution of macrophages to cancer cell elimination.

In contrast, the FT model, which contained no cancer cells, maintained high viability, indicating that the gene-therapy effects were primarily directed toward cancer cells rather than stromal components. Notably, AT models containing cancer and immune cells but lacking the fibroblasts exhibited higher sensitivity, with a reduced cell viability to 41%. These findings demonstrate that fibroblasts exert a dominant protective effect against gene-therapy-induced cytotoxicity, substantially reducing overall treatment sensitivity. This reduced response aligns with extensive evidence implicating fibroblasts in therapy resistance through ECM deposition, immune exclusion, and impaired therapeutic penetration [58-60]. The observed delayed M1 cytokine induction highlights the intrinsic immunosuppressive nature of the 3D tumor microenvironment, consistent with *in vivo* observations where macrophage activation is constrained by tumor and stromal signaling. Fibroblasts, representing only ~7% of the population, exerted a disproportionately strong protective effect, reflecting their known roles in ECM deposition, immune exclusion, and physical barrier formation that limit therapeutic penetration [58-60]. These results highlight the importance of incorporating stromal components in preclinical models, as their absence may overestimate treatment efficacy. Furthermore, the gradual increase in IL1β, TNFα, and IL6 over 7 d suggests that the timing of gene delivery and therapeutic readouts should account for the progressive relief of tumor-mediated immune suppression, which may be critical for optimizing combination interventions. Altogether, these results establish that although pro-inflammatory macrophage activation enhances therapeutic efficacy, stromal components—particularly fibroblasts—remain dominant regulators of treatment resistance. This interplay motivates strategies that combine immune activation with targeted stromal reprogramming, as described in subsequent sections.

5.3.2 TGFβ Targeting Reprograms Stromal and Immune Features

5.3.2.1 Optimization of Multi-Gene Delivery in the AFT Model

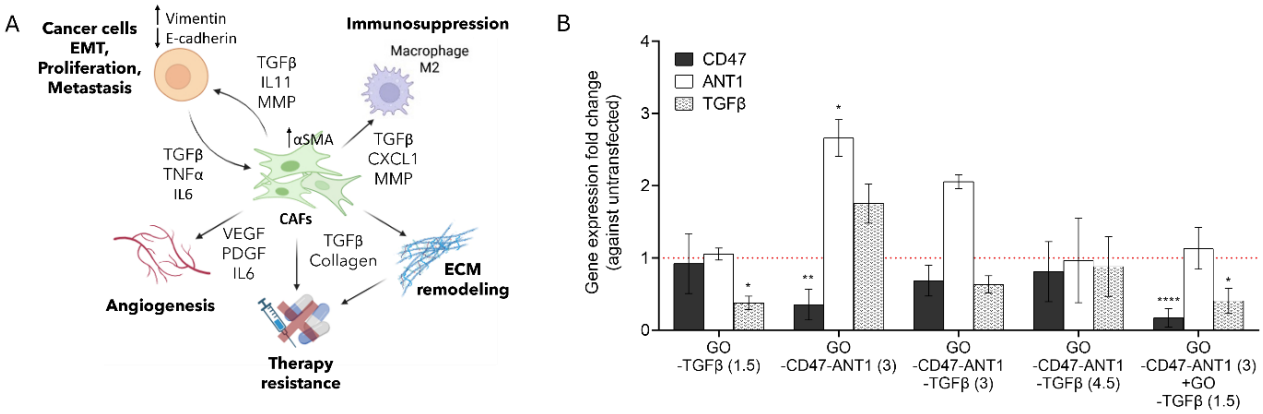

Figure 5.2. GO-based nanocarriers enable multi-gene regulation of TGFβ, CD47, and ANT1. A) Schematic representation of the interactions among cancer cells, fibroblasts, and macrophages mediated by TGFβ within the tumor microenvironment. The diagram summarizes known pathways involved in stromal activation and cancer-supportive functions mediated by CAFs. B) qPCR measurements of CD47, ANT1 and TGFβ gene expression regulation following transfection with different formulations of GO-based delivery systems. Statistical significance was determined against the untransfected AFT model using two-way ANOVA, with *P<0.05; **P<0.01; ****P<0.0001 considered significant, and P> 0.05 was considered not significant.

In tumor contexts, fibroblasts readily transition into CAFs, adopting a contractile and highly secretory phenotype that amplifies multiple tumor-supportive processes. As schematically illustrated in Figure 5.2A, activated CAFs enhance cancer cell aggressiveness by promoting epithelial-mesenchymal transition (EMT) through the secretion of cytokines, chemokines, and matrix-modifying enzymes [12, 16, 20, 21]. At the immune level, CAFs secrete mediators such as TGFβ that recruit and polarize macrophages toward an immunosuppressive, M2-like phenotype, thereby weakening local antitumor immunity [9, 39].

CAFs further drive extensive ECM remodeling through collagen-rich matrix deposition, facilitating cancer cell migration while creating physical barriers to therapeutic penetration [12]. Disrupting this CAF-centered signaling loop can attenuate reciprocal crosstalk between stromal, immune, and cancer cells, thereby constraining tumor progression.

Central to all these interconnected stromal and immune functions is TGFβ, which acts as a dominant upstream regulator of CAF activation, immune suppression, and therapy resistance [43]. Selective inhibition of TGFβ1 has been shown to alleviate resistance to immune checkpoint blockade by reshaping the tumor immune microenvironment [61]. Given its pivotal role in cancer support, we sought to incorporate TGFβ_siRNA into our therapeutic strategy to enable TGFβ silencing.

To identify an effective co-delivery strategy for simultaneous modulation of CD47, ANT1, and TGFβ expression, multiple loading configurations and GO:siRNA:pDNA ratios were evaluated based on mRNA fold-change outcomes (Figure 5.2B). Treatment with GO-TGFβ_1.5, corresponding to a GO:siRNA ratio of 1:1.5 (w/w), produced a substantial and specific reduction of TGFβ mRNA levels (0.4-fold) without altering CD47 or ANT1 gene expression. In contrast, the GO-CD47-ANT1_3 formulation (1:3, GO:nucleic acid, w/w, with 1:1 siRNA:pDNA, w/w) efficiently downregulated CD47 transcripts (0.4-fold) while inducing ANT1 expression (2.7-fold), but concomitantly increased TGFβ mRNA levels (1.8-fold). When all three nucleic acids were co-loaded onto a single nanocarrier, the GO-CD47-ANT1-TGFβ_3 formulation (1:3, GO:nucleic acids, with 1:1:1 siRNA:pDNA:siRNA, w/w/w) produced only partial and non-significant modulation of each target gene (CD47: 0.7-fold; ANT1: 2.1-fold; TGF-β: 0.6-fold). The reduced transcriptional modulation compared to the GO-TGFβ and GO-CD47-ANT1 formulations suggests a lower overall transfection efficiency, likely arising from partial competition among the three nucleic acids for GO binding sites.

Notably, in our previous work [33], systematic GO-CD47_siRNA binding studies revealed a progressive increase in absorbance with increasing siRNA loading until saturation between ~1:3 and 1:5 (GO:siRNA, w/w). This saturation behaviour reflects the nanocarrier's finite loading capacity; additional nucleic acid beyond this threshold results in steric crowding and reduced adsorption efficiency [36, 62]. This is particularly relevant for multi-gene loading, because siRNAs and pDNAs differ markedly in size, steric hindrance, charge distribution, and structural flexibility. siRNAs are short and rigid, whereas pDNA is much larger and requires substantially more surface area for condensation [63]. Once the GO surface approaches saturation, competition among cargos becomes

pronounced, destabilizing the complex and reducing reproducibility, consistent with the attenuated gene modulation observed for the tri-loaded formulation. This interpretation is further supported by the GO-CD47-ANT1-TGFβ_4.5 formulation (1:4.5, GO:nucleic acids, with 1:1:1 siRNA:pDNA:siRNA, w/w/w), which exhibited weaker and more variable transcriptional modulation across all three targets, consistent with excessive payload competition (CD47: 0.8-fold; ANT1: 1.0-fold; TGFβ: 0.9-fold).

To overcome payload competition and surface saturation observed in tri-loaded GO systems, a two-system co-delivery strategy was evaluated by combining the GO-CD47-ANT1_3 formulation (1:3, GO:nucleic acids, with 1:1 siRNA:pDNA, w/w) with the GO-TGFβ_1.5 system (1:1.5; GO:siRNA, w/w). This two-GO carrier strategy produced robust CD47 knockdown (0.2-fold) and efficient TGFβ silencing (0.4-fold); however, ANT1 induction was reduced relative to that observed with the single GO-CD47-ANT1 system. The reduced ANT1 induction is likely influenced by early cancer cell loss induced by simultaneous CD47 and TGFβ suppression, which decreases the number of viable cancer cells contributing to bulk transcript measurements at the selected time point. This interpretation is further supported by the overall reduction in CD47 and TGFβ transcript abundance relative to single-system transfections, consistent with a decreased population of viable, transcriptionally active cancer cells rather than reduced delivery efficiency. Overall, these results suggest that the optimal time point for capturing ANT1 overexpression following combined GO-CD47-ANT1_GO-TGFβ treatment likely occurs earlier, prior to the onset of extensive apoptosis. This emphasizes the necessity of temporal profiling in multi-gene strategies to capture transient expression dynamics that may otherwise underestimate therapeutic impact.

5.3.2.2 TGFβ Silencing Modulates CAF Phenotypes and Stromal Signaling

Having established a delivery strategy that balances loading efficiency with biological timing, we next evaluated how concurrent TGFβ silencing alters CAF activation, ECM organization, and macrophage polarization within the 3D AFT model. TGFβ silencing is expected to reprogram CAFs

from a contractile, ECM-producing, and immunosuppressive state toward a quiescent, less tumor-supportive phenotype, an effect that we next confirmed in the AFT model. Immunofluorescence of untransfected AFT constructs (Figure 5.3A) confirmed robust αSMA and vimentin expression, indicating fibroblast transition into CAFs and an activated stromal compartment capable of ECM remodeling and promoting cancer cell motility [20, 21]. Concurrently, low E-cadherin expression in cancer cells confirmed ongoing EMT, consistent with TGFβ-driven stromal signaling and acquisition of a more invasive phenotype [42]. Only the combined GO-CD47-ANT1_GO-TGFβ treatment significantly modulated these markers, reducing αSMA and vimentin to 0.2-fold and 0.6-fold, respectively, and restoring E-cadherin 3.4-fold (Figure 5.3B), consistent with CAF deactivation and partial reversal of EMT in cancer cells. No such changes were observed with GO-CD47-ANT1 alone, indicating that CD47/ANT1 modulation does not affect CAF activation or epithelial integrity. In contrast, TGFβ silencing reduces CAF and mesenchymal features, confirming that TGFβ is a critical regulator of stromal-driven tumor support. These results are consistent with previous reports showing that TGFβ inhibition in stroma-rich models reduces αSMA expression and ECM deposition, facilitating improved therapeutic penetration.[42, 43, 45] In the AFT model, TGFβ silencing reduced αSMA and vimentin expression while partially restoring E-cadherin expression, consistent with attenuation of CAF-associated features and partial EMT reversal, and coincided with enhanced sensitivity to CD47/ANT1-mediated cytotoxicity achieved with the GO-based tri-delivery system. Collectively, these stromal and epithelial changes correlate with reduced cancer cell invasion and enhanced therapeutic sensitivity, emphasizing the central role of TGFβ in maintaining a tumor-supportive microenvironment.

In alignment with previous studies showing that stroma-targeted interventions promote immune-cell infiltration and drug delivery [34, 35, 37], these findings support a dual-modulation paradigm in which stromal normalization primes the microenvironment for targeted cancer cell elimination. In addition to remodeling the stroma, TGFβ inhibition shifts macrophage polarization toward an M1-

dominant, pro-inflammatory state. It acts synergistically with CD47 silencing and ANT1 expression to augment macrophage activation and tumor-cell recognition.

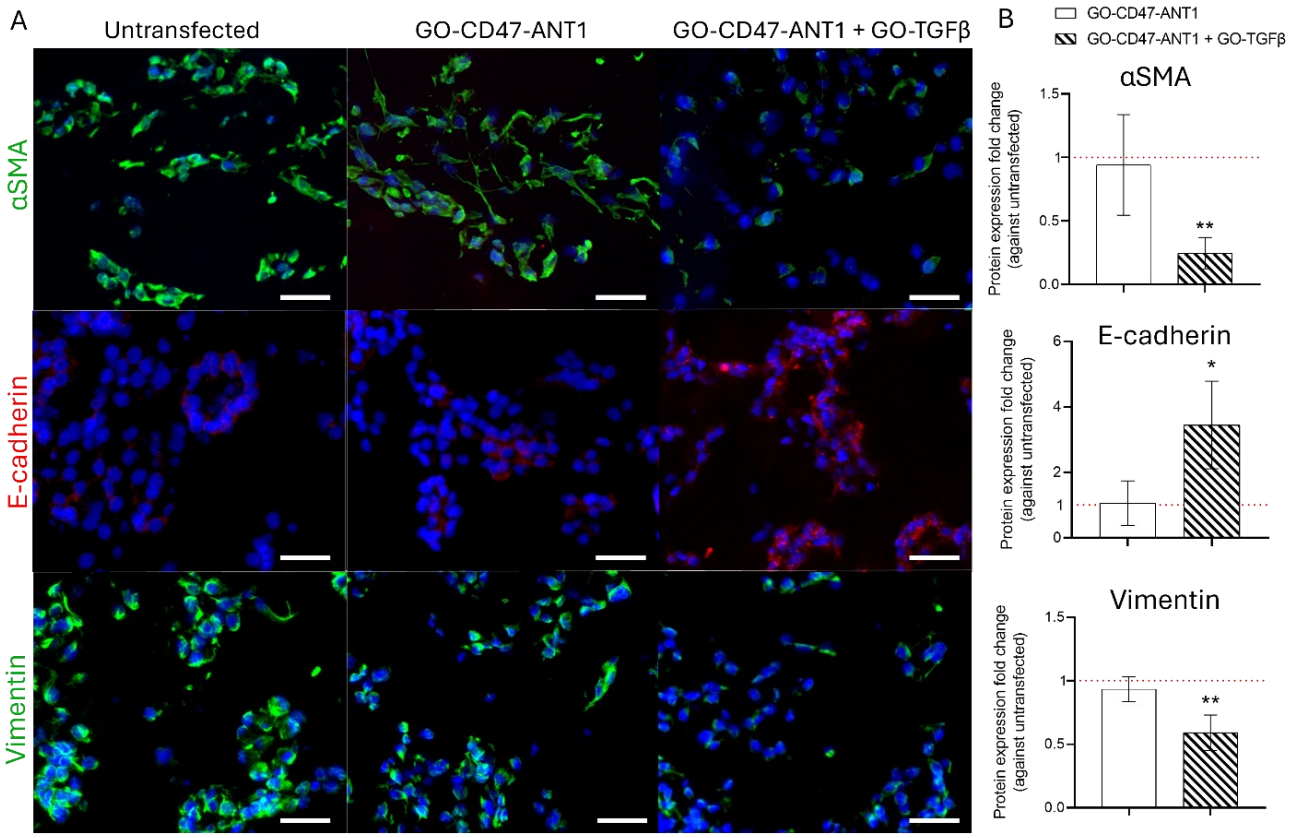

Figure 5.3. TGFβ implication on fibroblast activation in the AFT model. A) IHC images of AFT model sections (10 µm thick) showing expression of αSMA (green), vimentin (green), and E-cadherin (red) in untransfected, GO-CD47-ANT1-transfected, and GO-CD47-ANT1_GO-TGFβ-transfected constructs. Nuclei are identified by Hoescht staining (blue). Scale bar: 50 µm. B) Quantification of fluorescence intensity for αSMA, vimentin, and E-cadherin across treatment conditions relative to the untransfected control. Statistical significance was determined against the untransfected AFT model using one-way ANOVA, with *P<0.05; **P<0.01 considered significant, and P>0.05 was considered not significant.

5.3.2.3 TGFβ silencing biased monocyte polarization toward a pro-inflammatory, M1-like phenotype

Having demonstrated that TGFβ signaling regulates CAF-associated features and epithelial–mesenchymal plasticity in cancer cells, we next investigated its impact on macrophage phenotype. As an initial step, cell viability and LDH release were assessed to establish baseline cytotoxic effects across the different co-delivery strategies. Figures 4A and 4B summarize the impacts of GO-CD47-

ANT1_GO-TGFβ on cell viability and cell death relative to individual GO-CD47-ANT1 or GO-TGFβ treatments.

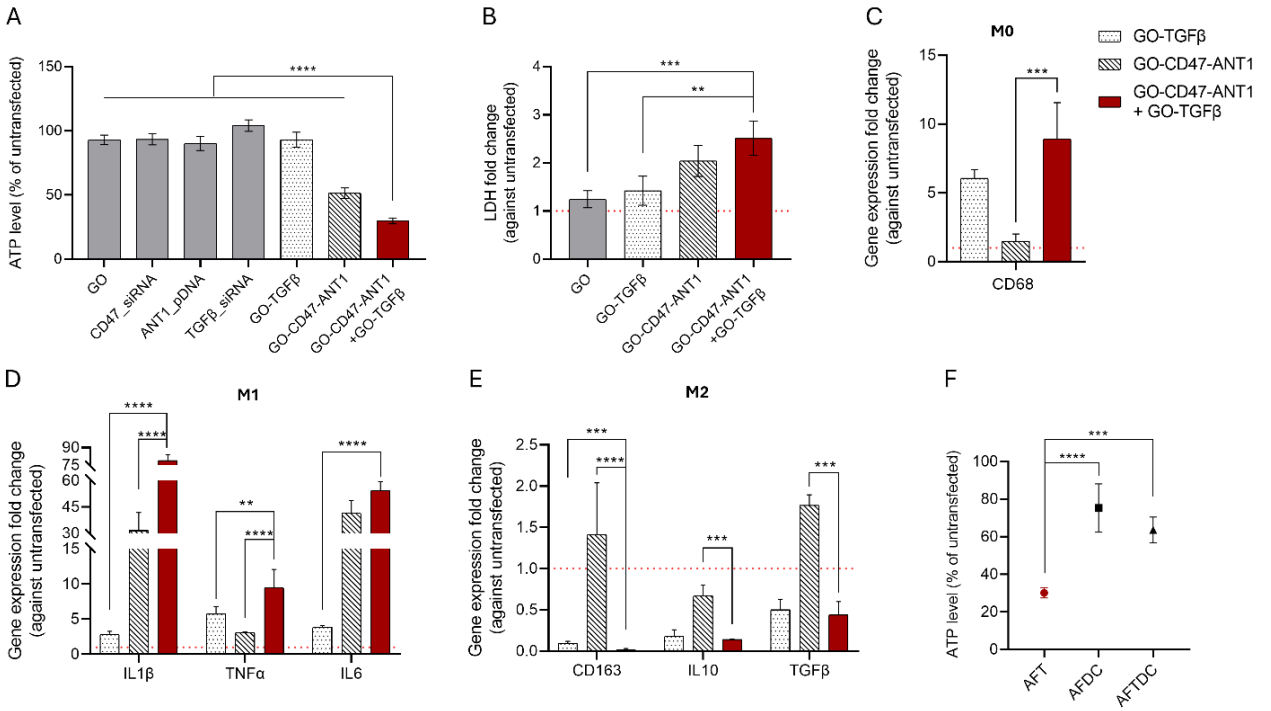

Figure 5.4. TGFβ involvement in macrophage activation and cancer cell elimination. A) Cell viability (ATP quantification) and B) cell death (LDH release) in AFT models treated with GO-TGFβ, GO-CD47-ANT1, or the combined GO-CD47-ANT1_GO-TGFβ therapy. qPCR measurements of genes expressing for C) CD68, D) M1-associated (IL1β, TNFα, IL6), and E) M2-associated proteins (CD163, IL10, TGFβ) following transfection with different GO-based gene-delivery formulations. F) Cell viability (ATP quantification) in AFT and control models containing THP-1 and/or DC following treatment with the combined GO-CD47-ANT1_GO-TGFβ system. Statistical significance was assessed relative to the AFT model treated with GO-CD47-ANT1_GO-TGFβ using one or two-way ANOVA, with *P<0.05; **P<0.01; ***P<0.001; ****P<0.0001 considered significant, and P>0.05 was considered not significant (not shown).

In untransfected controls and constructs treated with GO alone (without nucleic acids) or with free siRNA/pDNA (without GO), cell viability remained above 90% over 72 h (Figure 5.4A), confirming baseline biocompatibility [38]. Treatment with GO-TGFβ alone did not reduce overall viability, indicating that TGFβ silencing primarily modulates the microenvironment rather than directly inducing cancer cell death. In contrast, GO-CD47-ANT1 reduced viability to ~51%, consistent with cancer cell elimination via CD47 blockade-mediated phagocytosis and ANT1-driven apoptotic signaling [37]. Importantly, combining GO-CD47-ANT1 with GO-TGFβ further decreased viability

to ~29%, demonstrating that TGFβ silencing sensitizes tumor cells to immune- and apoptosis-mediated killing (Figure 5.4A).

LDH release (Figure 5.4B) confirmed these effects: GO-TGFβ induced minimal LDH release, GO-CD47-ANT1 increased LDH 2-fold, and the combined treatment further elevated it to ~2.5-fold. Together, these data indicate that TGFβ silencing enhances the cytotoxic effects of GO-CD47-ANT1, consistent with enhanced membrane damage and increased cancer cell susceptibility within the remodeled tumor microenvironment.

Consistent with prior studies, TGFβ silencing alone exerts minimal direct cytotoxicity while sensitizing tumors to immune-mediated and cytotoxic interventions [40]. In breast and pancreatic cancer models, it deactivates CAFs and normalizes stroma without directly affecting tumor-cell viability, yet enhances therapeutic responses when combined with cytotoxic or immunomodulatory strategies [43, 64, 65]. These observations align with evidence that endogenous TGFβ signaling protects tumor cells from therapy-induced stress. In contrast, its inhibition potentiates apoptosis and limits tumor progression when paired with additional anti-tumor modalities [45]. In a breast cancer model, a bifunctional therapeutic strategy of combining TGFβ inhibition with immune checkpoint blockade (*i.e.*, anti-PD-L1) effectively relieved TGFβ-driven immune suppression, enabling robust immune-cell-dependent tumor regression and prolonged survival [43]. Similarly, in our work, CD47 downregulation has been shown to facilitate cancer cell recognition by macrophages, potentially promoting phagocytic clearance, as previously demonstrated in 2D co-culture systems [25].

Given the established immunomodulatory role of TGFβ, macrophage-associated gene expression was next examined to determine whether the observed cytotoxic effects reflected changes in macrophage activation state. CD68 transcripts (Figure 5.4C and Figure S5.2) increased 6.1-fold with GO-TGFβ and 8.9-fold with combined GO-CD47-ANT1_GO-TGFβ, whereas GO-CD47-ANT1 alone induced a modest 1.5-fold increase, indicating TGFβ silencing promotes macrophage differentiation, amplified when combined with CD47 blockade, which is amplified when combined with CD47 blockade.

Analysis of macrophage polarization markers revealed treatment-dependent polarization profiles (Figure 5.4D and 4E and Figure S5.2). GO-TGFβ alone moderately upregulated IL1β, TNFα, and IL6 (2.8-fold, 5.7-fold, and 3.9-fold, respectively), reflecting partial macrophage activation upon relief of TGFβ-mediated immunosuppression (Figure 5.4D). GO-CD47-ANT1 treatment strongly induced IL1β (31.6-fold), TNFα (3-fold), and IL6 (41.5-fold), consistent with M1-like polarization driven by macrophage engagement with cancer cells. Notably, the combined treatment produced the most pronounced pro-inflammatory response (IL1β 79-fold, TNFα 9.5-fold, IL6 54.4-fold), indicating synergistic enhancement of M1-like macrophage activation through concurrent TGFβ inhibition and CD47 blockade. Concomitantly, expression of M2-associated markers CD163, IL10, and TGFβ was markedly reduced (0.02-, 0.1-, 0.4-fold, respectively; Figure 5.4E and Figure S5.2), reflecting suppression of immunosuppressive macrophage phenotypes. GO-CD47-ANT1 alone moderately upregulated CD163 and TGFβ, indicating partial M2-like signaling, which was fully counteracted by GO-TGFβ inclusion.

To directly assess the functional contribution of macrophages, AFT constructs containing THP-1 macrophages were compared with models incorporating dendritic cells (DCs), a myeloid cell population primarily involved in antigen presentation rather than direct phagocytic killing. In DC-containing constructs (AF-DC), the combined GO-CD47-ANT1_GO-TGFβ treatment produced a reduced cytotoxic response (Figure 5.4F). AF-DC constructs retained high ATP levels (~75%), whereas mixed AFT-DC constructs with fewer THP-1 cells showed intermediate viability (~64%). Importantly, qPCR analysis of gene modulation confirmed that transfection efficiency and target gene regulation were not compromised in DC-containing models (Table S5.1), indicating that the reduced cytotoxic outcome is not attributable to impaired delivery or gene silencing. Rather, these findings confirm that macrophage-specific effector functions are essential for cancer cell elimination, underscoring their central role in the efficacy of GO-CD47-ANT1_GO-TGFβ therapy.

Collectively, these results demonstrate that the therapeutic efficacy of the GO-CD47-ANT1_GO-TGFβ strategy arises from coordinated stromal and immune modulation. TGFβ silencing alleviates

CAF-derived immunosuppressive cues, thereby priming the tumor microenvironment for macrophage activation, while CD47 blockade and ANT1 expression promote tumor-cell recognition and cytotoxic engagement. Notably, our 3D AFT model demonstrates that robust cytotoxicity requires the presence of THP-1 macrophages, confirming that macrophage-specific effector functions are essential mediators of therapeutic efficacy. This dual modulation paradigm parallels *in vivo* strategies combining TGFβ pathway inhibition with immune checkpoint blockade, which have consistently shown improved tumor regression compared to single-agent therapies [35]. Collectively, these results highlight the importance of simultaneously targeting stromal normalization and immune activation to enable effective cancer cell elimination in complex, clinically relevant tumor microenvironments.

5.3.3 EGFR Targeted GO-Genes Delivery Enhances Cancer Cell Specificity

Conventional chemotherapeutic agents often lack cellular specificity, resulting in cytotoxic effects on both malignant and non-malignant cells within complex tissue models. In 3D co-culture systems similar to ours, such treatments reduce tumor viability to ~75% while simultaneously decreasing fibroblast and immune-cell viability to ~55% and ~25%, respectively, underscoring substantial off-target toxicity [9]. In contrast, targeted therapies have reshaped cancer treatment by improving therapeutic selectivity and limiting collateral damage to healthy tissues [4-8, 66]. In nanomedicine, these benefits arise from preferential cancer cell internalization and stimulus-responsive payload release. GO is a particularly efficient nanocarrier due to its large surface area and oxygen-rich functional groups (hydroxyl, carboxyl, and epoxy), which allow extensive surface functionalization and support stimuli-responsive release mechanisms, including pH- and near-infrared (NIR)-triggered delivery [35, 36, 62]. Together, these features support high drug loading and targeted therapeutic delivery in cancer models.

In our system, while GO-TGFβ acts broadly within the AFT model to reduce TGFβ-driven immunosuppressive signalling across stromal and immune compartments, the GO-CD47-ANT1

component offers an opportunity for additional refinement toward cancer cell-selective elimination. To this end, the GO-CD47-ANT1 nanocarrier was functionalized with the EGFR-targeting peptide GE11, enabling preferential delivery of phagocytosis- and apoptosis-regulating genes to EGFR-expressing cancer cells, while preserving the global microenvironmental modulation mediated by GO-TGFβ. The impact of this targeting strategy was therefore evaluated by assessing nanocarrier uptake, overall viability, and cancer-cell-specific apoptosis within the AFT model.

5.3.3.1 GE11 Functionalization Improves Uptake

A549 lung adenocarcinoma cells overexpress EGFR, which is widely exploited for targeted delivery. EGFR-directed ligands enhance nanocarrier uptake in malignant cells while limiting interactions with non-malignant stromal and immune cells [48, 50]. Figure 5.5A shows representative IHC sections of AFT constructs following treatment with Alexa Fluor-labelled GO-CD47-ANT1 and GE11/GO-CD47-ANT1 (used to track the CD47-ANT1 nanocarrier component; green), together with CK7 staining (red) to identify cancer cells. Both GO-CD47-ANT1_GO-TGFβ and GE11/GO-CD47-ANT1_GO-TGFβ formulations were efficiently internalized, with high uptake observed in $CK7^+$ cancer cells. However, qualitative inspection of the sections indicated that nanocarrier internalization by non-cancer cells occurred more frequently with the non-functionalized formulation (Figure 5.5A; white arrows), whereas GE11 functionalization visibly reduced off-target uptake. Image quantification (Figure 5.5B and Table S5.2) confirmed these observations. GO-CD47-ANT1_GO-TGFβ was internalized by 82% of $CK7^+$ cells and 35% of $CK7^-$ cells. GE11/GO-CD47-ANT1_GO-TGFβ increased $CK7^+$ uptake to 90% while reducing $CK7^-$ uptake to 14%, demonstrating improved cancer cell selectivity primarily through suppression of non-cancer-cell internalization.

To determine whether uptake differences were mediated by EGFR-dependent targeting, blocking experiments were performed by pre-incubating GE11 prior to transfection. In the absence of GE11 functionalization, blocking did not alter uptake ($CK7^+$: 80%; $CK7^-$: 36%; Figure 5.5B and Table S5.2), consistent with receptor-independent internalization. In contrast, GE11 blocking strongly

reduced uptake of the GE11-functionalized nanocarrier in CK7⁺ cells (from 90% to 23%; Figure 5.5B and Table S5.2), while CK7⁻ uptake remained low and unchanged (~14%; Figure 5.5B and Table S5.2).

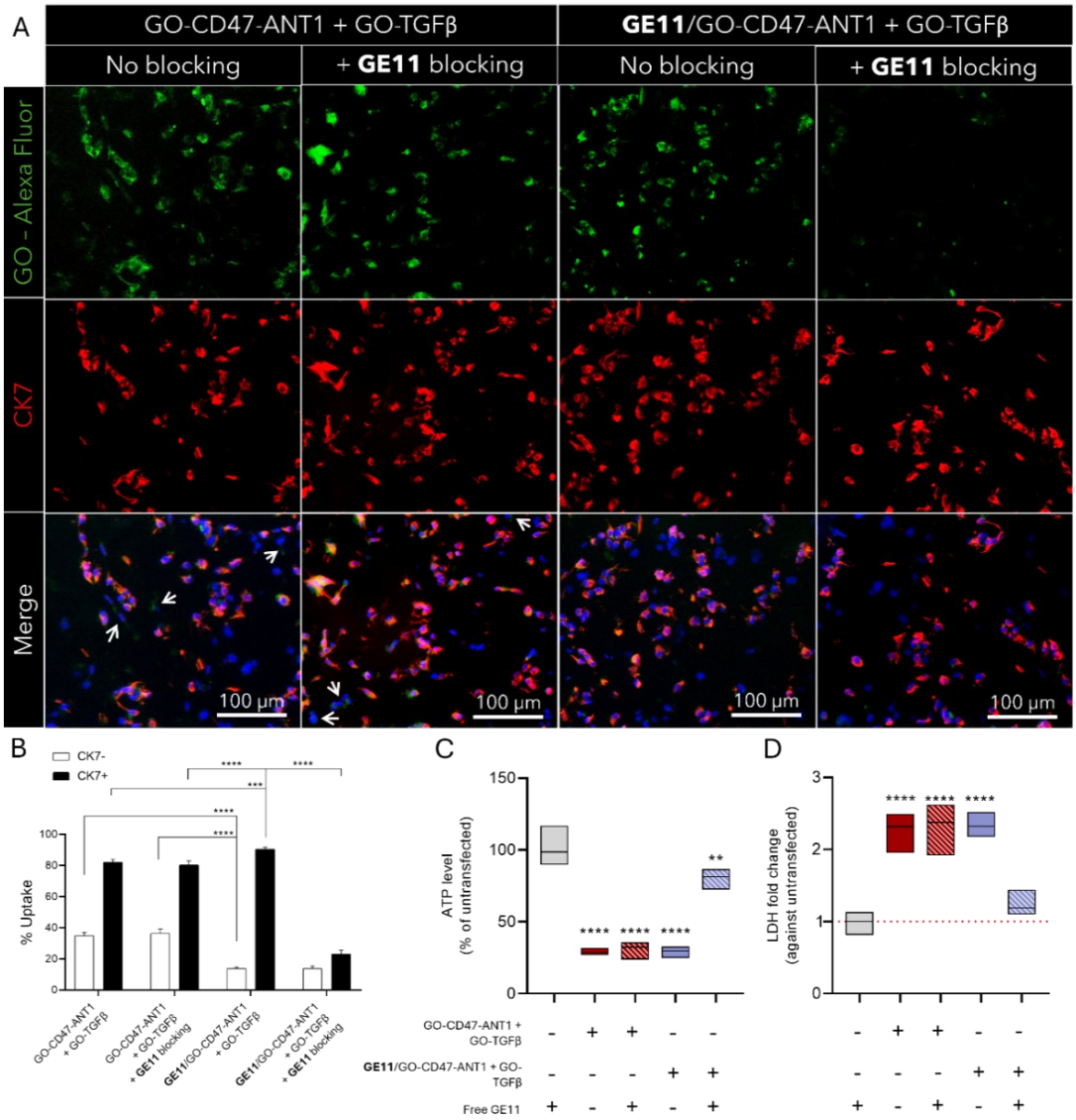

Figure 5.5. GE11 functionalization enhances cancer-cell–specific uptake while preserving therapeutic efficacy. A) Representative IHC images of AFT sections (10 µm thick) following treatment with Alexa Fluor-labelled (green) GO-CD47-ANT1_GO-TGFβ or GE11/GO-CD47-ANT1_GO-TGFβ. CK7 staining (red) identifies cancer cells, and nuclei by Hoescht staining (blue). Controls include unfunctionalized GO-CD47-ANT1_GO-TGFβ and corresponding EGFR-blocking. White arrows indicate nanocarrier uptake in CK7⁻ cells. Scale bars: 100 µm. B) Nanocarrier uptake quantified as the percentage of CK7⁺ (cancer) or CK7⁻ (non-cancer) cells exhibiting Alexa Fluor signal, normalized to the total number of cells within each population. C) Cell viability (ATP quantification) of AFT models following treatment with GO-CD47-ANT1_GO-TGFβ and GE11/GO-CD47-ANT1_GO-TGFβ, with and without GE11 blocking. D) Cell death assessed by LDH release. Statistical significance was determined using one- or two-way ANOVA, with comparisons made relative to the corresponding cell populations in the GE11/GO-CD47-ANT1_ GO-TGFβ treated model in panel B), and to the untransfected control in panels C) and D). **P<0.01; ***P<0.001; ****P<0.0001 considered significant, and P>0.05 was considered not significant (not shown).

These results indicate that GE11 functionalization shifts the cancer cell uptake mechanism toward a receptor-mediated process [46, 49, 50], improving selectivity predominantly by limiting off-target delivery rather than further increasing absolute cancer cell internalization. Consistent with these uptake trends, viability (ATP) and cytotoxicity (LDH) measurements confirmed that GE11 functionalization preserves therapeutic efficacy while introducing EGFR-dependent specificity (Figure 5.5C and D). Controls treated with GE11 alone and free genes maintained ~100% viability with no increase in LDH, confirming their lack of intrinsic toxicity under these conditions. GO-CD47-ANT1_GO-TGFβ reduced viability to ~29% and increased LDH release to ~2.3-fold, and this effect was unchanged by GE11 blocking (31% viability; ~2.3-fold LDH), supporting a receptor-independent mechanism for the non-functionalized formulation. Similarly, GE11/GO-CD47-ANT1_GO-TGFβ produced cytotoxicity comparable to that of the non-functionalized system (29% viability; ~2.3-fold LDH), indicating that targeting did not alter therapeutic potency. EGFR blocking nearly abolished the efficacy of the GE11-functionalized formulation, increasing viability to ~81% and reducing LDH release to ~1.2-fold, confirming that GE11-EGFR interactions mediated internalization and gene delivery.The relatively high cancer cell uptake observed even with the non-functionalized GO formulation is consistent with our previous 2D monoculture observations [37]. A549 cells exhibit elevated nanocarrier internalization, attributable to high basal endocytic activity and increased expression of surface receptors involved in nanoparticle uptake, rendering them particularly permissive to GO internalization [67, 68]. THP-1-derived macrophages typically exhibit high nanoparticle uptake via phagocytosis; however, in this system, the small GO flake size (<200 nm) combined with PEGylation likely reduced immune recognition and opsonization, thereby limiting macrophage uptake despite their phagocytic potential [36, 62, 69, 70]. Fibroblasts in a 2D study exhibited lower GO uptake, likely reflecting reduced basal endocytic activity and ECM barriers that hinder nanoparticle internalization [35]. CAFs have been shown to internalize substantially more nanoparticles than normal fibroblasts. Studies on gold nanoparticles reported up to 10-fold higher uptake in CAFs, approaching levels observed in cancer cells [71]. Similarly, pancreatic cancer models

exhibited ~50% higher uptake in CAFs with prolonged intracellular retention [72]. These results indicate that CAFs can internalize nanoparticles efficiently in tumor-like environments. In the AFT model, the lower abundance of fibroblasts (approximately ten-fold fewer than cancer cells) likely accounts for the detectable yet reduced non-cancer cell uptake. Together, these factors explain why non-targeted GO-CD47-ANT1 already exhibits partial cancer cell selectivity, allowing residual uptake by non-malignant cell internalization. Importantly, this underscores the value of incorporating a targeting ligand to restrict delivery of phagocytosis- and apoptosis-inducing genes to cancer cells, while preserving the non-selective GO–TGFβ component for broad microenvironmental modulation. Although AFT viability and LDH responses were similar for functionalized and non-functionalized formulations under non-blocked conditions, uptake and blocking experiments revealed distinct cellular targets underlying the observed cytotoxicity. This distinction highlights the importance of cell-type-resolved analysis in complex 3D tumor models, where comparable bulk efficacy can mask fundamentally different mechanisms of action. Reducing off-target delivery to stromal and immune compartments is particularly relevant in such systems, as unintended gene modulation in these populations may alter microenvironmental behavior and confound therapeutic interpretation. Thus, GE11 functionalization does not generate cytotoxic efficacy de novo but refines therapeutic selectivity by restricting gene delivery to malignant cells, an effect that may be especially advantageous *in vivo*, where minimizing unintended immunomodulation is critical for translational safety and efficacy.

5.3.3.2 GE11 functionalization enhanced cancer cell apoptosis

The impact of GE11-mediated targeting on apoptotic selectivity was evaluated in the AFT model by comparing apoptosis in cancer versus non-malignant cells. Figure 5.6A presents representative IHC sections of untransfected AFT constructs and those transfected with GO-CD47-ANT1, GO-CD47-

ANT1_GO-TGFβ, and GE11/GO-CD47-ANT1_GO-TGFβ. CK7 staining (green) highlighted cancer cells, while Caspase 9 (red) marked apoptotic cells.

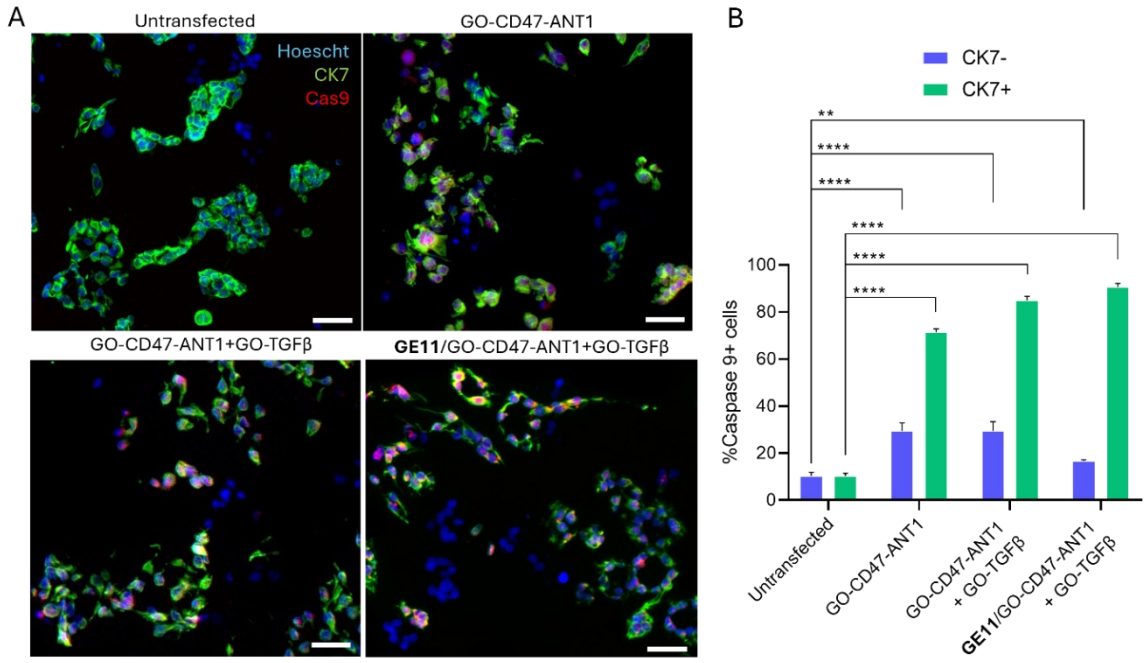

Figure 5.6. GE11-mediated targeting enhances cancer-cell-selective apoptosis in the AFT model. A) Representative IHC images of AFT sections (10 μm thick) showing CK7 (green) to identify cancer cells and caspase 9 (red) as a marker of apoptosis following treatment with GO-CD47-ANT1, GO-CD47-ANT1_GO-TGFβ, and GE11/GO-CD47-ANT1_GO-TGFβ, compared with untransfected controls. Nuclei are identified by Hoescht staining (blue). Scale bars: 50 μm. B) Apoptotic cells quantified as the percentage of $CK7^+$ (cancer) or $CK7^-$ (non-cancer) cells relative to the total number of cells within each population. Statistical significance was assessed using two-way ANOVA with comparisons made relative to the corresponding cell populations in the untransfected control. **P<0.01; ****P<0.0001 considered significant, and P>0.05 was considered not significant (not shown).

Quantitative image analysis (Figure 5.6B) assessed apoptosis in the $CK7^+$ and $CK7^-$ populations, enabling evaluation of therapeutic selectivity toward cancer cells. In untransfected constructs, apoptotic cells were evenly distributed between the $CK7^+$ and $CK7^-$ populations (10% each), reflecting low background apoptosis and confirming the model's baseline viability. GO-CD47-ANT1 markedly increased apoptosis, with 71% of $CK7^+$ cells and 29% of $CK7^-$ cells affected, indicating preferential cancer cell elimination accompanied by measurable off-target effects. The addition of GO-TGFβ further increased cancer cell apoptosis to 85%, while apoptosis in $CK7^-$ cells remained at 29%, consistent with enhanced tumor-cell susceptibility via immune and stromal modulation.

Notably, the GE11/GO-CD47-ANT1_GO-TGFβ formulation produced the highest degree of cancer-cell-selective apoptosis, with 91% of apoptotic $CK7^+$ cells and only 16% of the total $CK7^-$ cells in apoptosis (Figure 5.6B). This shift demonstrates that GE11-mediated targeting substantially reduces apoptosis in non-malignant cells while enriching apoptotic responses in cancer cells. Importantly, these findings indicate that GE11 functionalization refines cell-type specificity rather than increasing overall cytotoxic potency. This effect is particularly relevant in multicellular tumor models where off-target gene delivery may perturb stromal or immune function. These findings are consistent with prior studies showing that GO-based nanoplatforms enhance cancer cell specificity via preferential uptake and stimulus-responsive release [35, 62, 68]. For example, folate-functionalized reduced GO loaded with quercetin showed higher drug release under acidic conditions (35% at pH 5.5 vs 20% at pH 7.4 over 48 h), which further increased upon NIR irradiation (up to 70%), resulting in efficient killing of triple-negative breast cancer cells while sparing normal cells [36]. Similarly, targeted GO platforms with NIR stimulation reduced cancer cell viability to below 20% while sparing normal fibroblasts, demonstrating improved specificity relative to non-targeted systems [73].

Beyond physicochemical targeting, immune-mediated mechanisms further contribute to cancer cell specificity. In a previous work from our group, in AML co-cultured with human macrophages, immune activation led to downregulation of CD47 and upregulation of pro-phagocytic signals on leukemia cells, resulting in selective elimination of malignant cells while sparing normal hematopoietic populations [31].

Collectively, the selectivity obtained in this current study reflects the convergence of multiple mechanisms: receptor-mediated uptake via GE11, immune recognition and clearance driven by CD47 downregulation and ANT1 expression, and microenvironmental sensitization through TGFβ silencing. In the AFT model, these complementary mechanisms act in concert to concentrate apoptotic responses within the malignant compartment while minimizing unintended cytotoxicity in non-malignant cells, providing a mechanistic rationale for combining targeted nanocarrier delivery with microenvironmental reprogramming in complex tumor systems.

5.4 Conclusions

We report the development and validation of a GO-based dual gene-delivery platform designed to address two major barriers in cancer therapy: limited cancer cell specificity and an immunosuppressive, tumor-supportive microenvironment. Using a multicellular 3D lung cancer model incorporating cancer cells, fibroblasts, and macrophages, we demonstrate that TGFβ silencing alone reprograms stromal and immune components, reducing CAF activation and partially shifting macrophages toward a pro-inflammatory state, without directly inducing cancer cell cytotoxicity. In contrast, modulation of CD47 and ANT1 promotes macrophage-mediated cancer cell elimination, and combining these strategies produces a synergistic therapeutic response characterized by enhanced M1-like macrophage activation, suppression of immunosuppressive cues, and markedly reduced tumor viability.

Further refinement of the platform through GE11 peptide functionalization of the GO-CD47-ANT1 nanocarrier enabled EGFR-mediated targeting of lung cancer cells, significantly reducing off-target uptake and apoptosis in non-malignant populations. Although overall cytotoxicity remained comparable between targeted and non-targeted formulations, cell-type-resolved analyses revealed a pronounced shift toward selective apoptosis of cancer cells, underscoring the added value of ligand-directed delivery in complex multicellular systems.

Collectively, this work establishes a gene-delivery strategy that integrates direct targeting of malignant cells with concurrent microenvironmental modulation, demonstrating that effective cancer elimination in complex 3D models requires coordinated intervention at both tumor cell and stromal-immune levels. By leveraging the physicochemical versatility of graphene oxide and exploiting the complementary immune and stromal mechanisms, this platform provides a mechanistically grounded and precision-oriented framework for optimizing cancer-specific gene therapies in physiologically relevant 3D tumor models.

References

(1) Hart, L.; Ogbonnaya, A.; Boykin, K.; Deyoung, K.; Bailey, R.; Heritage, T.; Lopez-Gonzalez, L.; Huang, H.; Gordan, L. Burden of chemotherapy-induced myelosuppression among patients with extensive-stage small cell lung cancer: A retrospective study from community oncology practices. *Cancer Med* **2023**, *12*, 10020-10030.
(2) Rahi, M. S.; Parekh, J.; Pednekar, P.; Parmar, G.; Abraham, S.; Nasir, S.; Subramaniyam, R.; Jeyashanmugaraja, G. P.; Gunasekaran, K. Radiation-Induced Lung Injury-Current Perspectives and Management. *Clinics Pract* **2021**, *11*, 410-429.
(3) Ziolkowska-Suchanek, I.; Rozwadowska, N. Advancements in Gene Therapy for Non-Small Cell Lung Cancer: Current Approaches and Future Prospects. *Genes* **2025**, *16*, 569.
(4) Chen, S.; Zhang, S.; Wang, Y. F.; Yang, X.; Yang, H.; Cui, C. Y. Anti-EpCAM functionalized graphene oxide vector for tumor targeted siRNA delivery and cancer therapy. *Asian J Pharm Sci* **2021**, *16*, 598-611.
(5) Lu, Y. J.; Lan, Y. H.; Chuang, C. C.; Lu, W. T.; Chan, L. Y.; Hsu, P. W.; Chen, J. P. Injectable Thermo-Sensitive Chitosan Hydrogel Containing CPT-11-Loaded EGFR-Targeted Graphene Oxide and SLP2 shRNA for Localized Drug/Gene Delivery in Glioblastoma Therapy. *Int J Mol Sci* **2020**, *21*, 7111.
(6) Qu, Y.; Sun, F. F.; He, F.; Yu, C. G.; Lv, J. H.; Zhang, Q. Q.; Liang, D.; Yu, C.; Wang, J.; Zhang, X. N.; Xu, A. N.; Wu, J. D. Glycyrrhetinic acid-modified graphene oxide mediated siRNA delivery for enhanced liver-cancer targeting therapy. *Eur J Pharm Sci* **2019**, *139*, 105036.
(7) Wang, Y. F.; Sun, G. P.; Gong, Y. Y.; Zhang, Y. Y.; Liang, X. F.; Yang, L. Q. Functionalized Folate-Modified Graphene Oxide/PEI siRNA Nanocomplexes for Targeted Ovarian Cancer Gene Therapy. *Nanoscale Res Lett* **2020**, *15*, 57.
(8) Yang, L.; Kim, T. H.; Cho, H. Y.; Luo, J.; Lee, J. M.; Chueng, S. T. D.; Hou, Y. N.; Yin, P. T. T.; Han, J. Y.; Kim, J. H.; Chung, B. G.; Choi, J. W.; Lee, K. B. Hybrid Graphene-Gold Nanoparticle-Based Nucleic Acid Conjugates for Cancer-Specific Multimodal Imaging and Combined Therapeutics. *Adv Funct Mater* **2021**, *31*, 2006918.
(9) Rebelo, S. P.; Pinto, C.; Martins, T. R.; Harrer, N.; Estrada, M. F.; Loza-Alvarez, P.; Cabeçadas, J.; Alves, P. M.; Gualda, E. J.; Sommergruber, W.; Brito, C. 3D-3-culture: A tool to unveil macrophage plasticity in the tumor microenvironment. *Biomaterials* **2018**, *163*, 185-197.
(10) Domenici, G.; Lopes, N. F.; Trindade, G.; Gal, I. R.; Minard, J. M.; Rebelo, S. P.; Freitas, C.; Duarte, N.; Brito, C. Assessing Novel Antibody-Based Therapies in Reconstructive 3D Cell Models of the Tumor Microenvironment. *Adv Biol* **2024**, *8*, e2400431.
(11) Del Bufalo, F.; Manzo, T.; Hoyos, V.; Yagyu, S.; Caruana, I.; Jacot, J.; Benavides, O.; Rosen, D.; Brenner, M. K. 3D modeling of human cancer: A PEG-fibrin hydrogel system to study the role of tumor microenvironment and recapitulate the effect of oncolytic adenovirus. *Biomaterials* **2016**, *84*, 76-85.
(12) Pan, H. J.; Lee, C. W.; Wu, L. Y.; Hsu, H. H.; Tung, Y. C.; Liao, W. Y.; Lee, C. H. A 3D culture system for evaluating the combined effects of cisplatin and anti-fibrotic drugs on the growth and invasion of lung cancer cells co-cultured with fibroblasts. *Apl Bioeng* **2023**, *7*, 016117.
(13) Grant, G.; Ferrer, C. M. The role of the immune tumor microenvironment in shaping metastatic dissemination, dormancy, and outgrowth. *Trends Cell Biol* **2025**, *in press*.
(14) Hu, Q.; Zhu, Y. F.; Mei, J.; Liu, Y.; Zhou, G. R. Extracellular matrix dynamics in tumor immunoregulation: from tumor microenvironment to immunotherapy. *J Hematol Oncol* **2025**, *18*, 65.
(15) Takahashi, H. K., Y. 3D co-culture disc for spatiotemporal image analysis of cancer-stromal cell interaction. *Biomater Sci* **2021**, *9*, 4448-4458.
(16) Miyazaki, K.; Oyanagi, J.; Hoshino, D.; Togo, S.; Kumagai, H.; Miyagi, Y. Cancer cell migration on elongate protrusions of fibroblasts in collagen matrix. *Sci Rep* **2019**, *9*, 292.
(17) Zhang, X. H.; Zhang, S. S.; Han, Y. Y. FGF4 drives tumor progression in triple-negative breast cancer via IL6/STAT3-mediated macrophage M2 polarization and immune suppression. *Cell Div* **2025**, *20*, 22.
(18) Linde, N.; Casanova-Acebes, M.; Sosa, M. S.; Mortha, A.; Rahman, A.; Farias, E.; Harper, K.; Tardio, E.; Torres, I. R.; Jones, J.; Condeelis, J.; Merad, M.; Aguirre-Ghiso, J. A. Macrophages orchestrate breast cancer early dissemination and metastasis. *Nat Commun* **2018**, *9*, 21.
(19) He, J.; Tao, J.; Zhou, Y.; Li, H. J.; Feng, W. Q.; Xu, Y. Q. TGF-β-driven T-cell exclusion in ovarian cancer: single-cell and spatial transcriptomic views of immune low-response states. *Front Immunol* **2025**, *16*, 1698088.
(20) Cords, L.; Engler, S.; Haberecker, M.; Rüschoff, J. H.; Moch, H.; de Souza, N.; Bodenmiller, B. Cancer-associated fibroblast phenotypes are associated with patient outcome in non-small cell lung cancer. *Cancer Cell* **2024**, *42*, 396-412.
(21) Lee, S.; Hong, J. H.; Kim, J. S.; Yoon, J. S.; Chun, S. H.; Hong, S. A.; Kim, E. J.; Kang, K.; Kang, J. L.; Ko, Y. H.; Ahn, Y. H. Cancer-associated fibroblasts activated by miR-196a promote the migration and invasion of lung cancer cells. *Cancer Lett* **2021**, *508*, 92-103.
(22) Domagala-Kulawik, J. The role of the immune system in non-small cell lung carcinoma and potential for therapeutic intervention. *Transl Lung Cancer Res* **2015**, *4*, 177-190.
(23) Bied, M.; Ho, W. W.; Ginhoux, F.; Blériot, C. Roles of macrophages in tumor development: a spatiotemporal perspective. *Cell Mol Immunol* **2023**, *20*, 983-992.

(24) Genin, M.; Clement, F.; Fattaccioli, A.; Raes, M.; Michiels, C. M1 and M2 macrophages derived from THP-1 cells differentially modulate the response of cancer cells to etoposide. *BMC Cancer* **2015**, *15*, 577.
(25) Hassan, E. M.; McWhirter, S.; Walker, G. C.; Martinez-Rubi, Y.; Zou, S. Elimination of Cancer Cells in Co-Culture: Role of Different Nanocarriers in Regulation of CD47 and Calreticulin-Induced Phagocytosis. *ACS Appl Mater Interfaces* **2023**, *15*, 3791-3803.
(26) Ye, Z. F.; Chen, J. J.; Zhao, X. W.; Li, Y. M.; Harmon, J.; Huang, C. F.; Chen, J. Z.; Xu, Q. B. In Vitro Engineering Chimeric Antigen Receptor Macrophages and T Cells by Lipid Nanoparticle-Mediated mRNA Delivery. *ACS Biomater Sci Eng* **2022**, *8*, 722-733.
(27) Zhang, H.; Huo, Y.; Zheng, W. J.; Li, P.; Li, H.; Zhang, L. L.; Sa, L.; He, Y.; Zhao, Z. H.; Shi, C. H.; Shan, L. Q.; Yang, A. A.; Wang, T. Silencing of SIRPα enhances the antitumor efficacy of CAR-M in solid tumors. *Cell Mol Immunol* **2024**, *21*, 1335-1349.
(28) Luo, J. H.; Guo, M.; Huang, M. Y.; Liu, Y. F.; Qian, Y. P.; Liu, Q. Y.; Cao, X. T. Neoleukin-2/15-armored CAR-NK cells sustain superior therapeutic efficacy in solid tumors via c-Myc/NRF1 activation. *Signal Transduct Target Ther* **2025**, *10*, 78.
(29) Mao, Y. M.; Eissler, N.; Le Blanc, K.; Johnsen, J. I.; Kogner, P.; Kiessling, R. Targeting Suppressive Myeloid Cells Potentiates Checkpoint Inhibitors to Control Spontaneous Neuroblastoma. *Clin Cancer Res* **2016**, *22*, 3849-3859.
(30) Lau, A. P. Y.; Binstock, S. S. K.; Thu, K. L. CD47: The Next Frontier in Immune Checkpoint Blockade for Non-Small Cell Lung Cancer. *Cancers* **2023**, *15*, 5229.
(31) Hassan, E. M.; Walker, G. C.; Wang, C.; Zou, S. Anti-leukemia effect associated with down-regulated CD47 and up-regulated calreticulin by stimulated macrophages in co-culture. *Cancer Immunol Immunother* **2021**, *70*, 787-801.
(32) Chevrollier, A.; Loiseau, D.; Reynier, P.; Stepien, G. Adenine nucleotide translocase 2 is a key mitochondrial protein in cancer metabolism. *Biochim Biophys Acta* **2011**, *1807*, 562-567.
(33) Hassan, E. M.; Zou, S. Novel nanocarriers for silencing anti-phagocytosis CD47 marker in acute myeloid leukemia cells. *Colloid Surface B* **2022**, *217*, 112609.
(34) Gies, V.; Lopinski, G.; Augustine, J.; Cheung, T.; Kodra, O.; Zou, S. The impact of processing on the cytotoxicity of graphene oxide. *Nanoscale Adv* **2019**, *1*, 817-826.
(35) Campbell, E.; Hasan, M. T.; Pho, C.; Callaghan, K.; Akkaraju, G. R.; Naumov, A. V. Graphene Oxide as a Multifunctional Platform for Intracellular Delivery, Imaging, and Cancer Sensing. *Sci Rep* **2019**, *9*, 416.
(36) Grilli, F.; Gohari, P. H.; Zou, S. Characteristics of Graphene Oxide for Gene Transfection and Controlled Release in Breast Cancer Cells. *Int J Mol Sci* **2022**, *23*, 6802.
(37) Grilli, F.; Sakib, S.; Variola, F.; Zou, S. Graphene Oxide-Based Gene Modulation in Preferential Elimination of Lung Cancer Cells in a 3D Tumor Microenvironment Model. *Adv Nanobiomed Res* **2025**, *5*, 2500028.
(38) Grilli, F.; Hassan, E. M.; Variola, F.; Zou, S. Harnessing graphene oxide nanocarriers for siRNA delivery in a 3D spheroid model of lung cancer. *Biomater Sci* **2023**, *11*, 6635-6649.
(39) Zhang, F.; Wang, H. S.; Wang, X. F.; Jiang, G. M.; Liu, H.; Zhang, G.; Wang, H.; Fang, R.; Bu, X. Z.; Cai, S. H.; Du, J. TGF-β induces M2-like macrophage polarization via SNAIL-mediated suppression of a pro-inflammatory phenotype. *Oncotarget* **2016**, *7*, 52294-52306.
(40) Derynck, R.; Turley, S. J.; Akhurst, R. J. TGFβ biology in cancer progression and immunotherapy. *Nat Rev Clin Oncol* **2021**, *18*, 9-34.
(41) Tung, N. T. C.; Nogami, M.; Iwasaki, M.; Yahara, Y.; Seki, S.; Makino, H.; Kamei, K.; He, Z. Y.; Kawaguchi, Y. M2-like macrophages derived from THP-1 cells promote myofibroblast differentiation of synovial fibroblasts in association with the TGF-β1/SMAD2/3 signaling pathway. *Sci Rep* **2025**, *15*, 25505.
(42) Niu, M. K.; Yi, M.; Wu, Y. Z.; Lyu, L.; He, Q.; Yang, R.; Zeng, L.; Shi, J.; Zhang, J.; Zhou, P. F.; Zhang, T. T.; Mei, Q.; Chu, Q.; Wu, K. M. Synergistic efficacy of simultaneous anti-TGF-β/VEGF bispecific antibody and PD-1 blockade in cancer therapy. *J Hematol Oncol* **2023**, *16*, 94.
(43) Yang, M.; Qin, C.; Tao, L.; Cheng, G.; Li, J.; Lv, F.; Yang, N.; Xing, Z.; Chu, X.; Han, X.; Huo, M.; Yin, L. Synchronous targeted delivery of TGF-beta siRNA to stromal and tumor cells elicits robust antitumor immunity against triple-negative breast cancer by comprehensively remodeling the tumor microenvironment. *Biomaterials* **2023**, *301*, 122253.
(44) Han, Z. Z.; Kang, D. X.; Joo, Y.; Lee, J.; Oh, G. H.; Choi, S.; Ko, S.; Je, S.; Choi, H. J.; Song, J. J. TGF-β downregulation-induced cancer cell death is finely regulated by the SAPK signaling cascade. *Exp Mol Med* **2018**, *50*, 1-19.
(45) Kim, W.; Ye, Z.; Simonenko, V.; Shahi, A.; Malikzay, A.; Long, S. Z.; Xu, J. J.; Lu, A.; Horng, J. H.; Wu, C. R.; Chen, P. J.; Lu, P. Y.; Evans, D. M. Codelivery of TGFβ and Cox2 siRNA inhibits HCC by promoting T-cell penetration into the tumor and improves response to Immune Checkpoint Inhibitors. *Nar Cancer* **2024**, *6*, zcad059.
(46) Li, Z. H.; Zhao, R. J.; Wu, X. H.; Sun, Y.; Yao, M.; Li, J. J.; Xu, Y. H.; Gu, J. R. Identification and characterization of a novel peptide ligand of epidermal growth factor receptor for targeted delivery of therapeutics. *FASEB J* **2005**, *19*, 1978-1985.
(47) Hallaji, M.; Allahyari, M.; Teimoori-Toolabi, L.; Yasami-Khiabani, S.; Golkar, M.; Fard-Esfahani, P. Targeted cancer treatment using a novel EGFR-specific Fc-fusion peptide based on GE11 peptide. *Sci Rep* **2025**, *15*, 5107.

(48) Judmann, B.; Braun, D.; Schirrmacher, R.; Wangler, B.; Wangler, C.; Fricker, G. Toward the Development of GE11-Based Radioligands for Imaging of Epidermal Growth Factor Receptor-Positive Tumors. *ACS Omega* **2022**, *7*, 27690-27702.
(49) Guo, Z. H.; Sui, J. H.; Li, Y. M.; Wei, Q. C.; Wei, C. L.; Xiu, L. Y.; Zhu, R. H.; Sun, Y.; Hu, J. S.; Li, J. L. GE11 peptide-decorated acidity-responsive micelles for improved drug delivery and enhanced combination therapy of metastatic breast cancer. *J Mater Chem B* **2022**, *10*, 9266-9279.
(50) Huang, X. Q.; Chen, L. Z.; Zhang, Y. P.; Zhou, S. Y.; Cai, H. H.; Li, T.; Jin, H.; Cai, J. Y.; Zhou, H. B.; Pi, J. GE11 Peptide Conjugated Liposomes for EGFR-Targeted and Chemophotothermal Combined Anticancer Therapy. *Bioinorg Chem Appl* **2021**, *2021*, 5534870.
(51) Gies, V.; Zou, S. Systematic toxicity investigation of graphene oxide: evaluation of assay selection, cell type, exposure period and flake size. *Toxicol Res* **2018**, *7*, 93-101.
(52) Coleman, B. R.; Knight, T.; Gies, V.; Jakubek, Z. J.; Zou, S. Manipulation and Quantification of Graphene Oxide Flake Size: Photoluminescence and Cytotoxicity. *ACS Appl Mater Interfaces* **2017**, *9*, 28911-28921.
(53) Schneider, C. A.; Rasband, W. S.; Eliceiri, K. W. NIH Image to ImageJ: 25 years of image analysis. *Nat Methods* **2012**, *9*, 671-675.
(54) Luo, H. T.; Liang, C. X.; Luo, R. C.; Gu, W. G. Identification of relevant prognostic values of cytokeratin 20 and cytokeratin 7 expressions in lung cancer. *Biosci Rep* **2017**, *37*, Bsr20171086.
(55) Chen, S.; Giannakou, A.; Wyman, S.; Gruzas, J.; Golas, J.; Zhong, W. Y.; Loreth, C.; Sridharan, L.; Yamin, T. T.; Damelin, M.; Geles, K. G. Cancer-associated fibroblasts suppress SOX2-induced dysplasia in a lung squamous cancer coculture. *Proc Natl Acad Sci USA* **2018**, *115*, E11671-E11680.
(56) Jo, H.; Lee, E. Y.; Cho, H. S.; Rayhan, M. A.; Cho, A.; Chae, C. S.; You, H. J. THP-1 Monocytic Cells Are Polarized to More Antitumorigenic Macrophages by Serial Treatment with Phorbol-12-Myristate-13-Acetate and PD98059. *Medicina* **2024**, *60*, 1009.
(57) Lund, M. E.; To, J.; O'Brien, B. A.; Donnelly, S. The choice of phorbol 12-myristate 13-acetate differentiation protocol influences the response of THP-1 macrophages to a pro-inflammatory stimulus. *J Immunol Methods* **2016**, *430*, 64-70.
(58) Broz, M. T.; Ko, E. Y.; Ishaya, K.; Xiao, J. F.; De Simone, M.; Hoi, X. P.; Piras, R.; Gala, B.; Tessaro, F. H. G.; Karlstaedt, A.; Orsulic, S.; Lund, A. W.; Chan, K. S.; Guarnerio, J. Metabolic targeting of cancer associated fibroblasts overcomes T-cell exclusion and chemoresistance in soft-tissue sarcomas. *Nat Commun* **2024**, *15*, 2498.
(59) Song, D. Q.; Wu, Y. S.; Li, J.; Liu, J. Z.; Yi, Z. Y.; Wang, X. Y.; Sun, J. Z.; Li, L. Y.; Wu, Q. X.; Chen, Y. R.; Fang, H. Y.; Luan, T. K.; Du, H. M.; Huang, J.; Peng, W. Y.; Wei, Y. X.; Li, F.; Li, Q.; Zhang, L.; Zhu, Y.; Wan, J. Y.; Ren, G. S.; Li, H. Z. Insulin-like growth factor 2 drives fibroblast-mediated tumor immunoevasion and confers resistance to immunotherapy. *J Clin Invest* **2024**, *134*, e183366.
(60) Wei, J. R.; Dong, J.; Li, L. Cancer-associated fibroblasts-derived gamma-glutamyltransferase 5 promotes tumor growth and drug resistance in lung adenocarcinoma. *Aging* **2020**, *12*, 13220-13233.
(61) Liu, S. J.; Ren, J.; ten Dijke, P. Targeting TGFβ signal transduction for cancer therapy. *Signal Transduct Target Ther* **2021**, *6*, 8.
(62) Sadeghi, M. S.; Sangrizeh, F. H.; Jahani, N.; Abedin, M. S.; Chaleshgari, S.; Ardakan, A. K.; Baeelashaki, R.; Ranjbarpazuki, G.; Rahmanian, P.; Zandieh, M. A.; Nabavi, N.; Aref, A. R.; Salimimoghadam, S.; Rashidi, M.; Rezaee, A.; Hushmandi, K. Graphene oxide nanoarchitectures in cancer therapy: Drug and gene delivery, phototherapy, immunotherapy, and vaccine development. *Environ Res* **2023**, *237*, 117027.
(63) Scholz, C.; Wagner, E. Therapeutic plasmid DNA versus siRNA delivery: Common and different tasks for synthetic carriers. *J Control Release* **2012**, *161*, 554-565.
(64) Ellermeier, J.; Wei, J. W.; Duewell, P.; Hoves, S.; Stieg, M. R.; Adunka, T.; Noerenberg, D.; Anders, H. J.; Mayr, D.; Poeck, H.; Hartmann, G.; Endres, S.; Schnurr, M. Therapeutic Efficacy of Bifunctional siRNA Combining TGF-β1 Silencing with RIG-I Activation in Pancreatic Cancer. *Cancer Res* **2013**, *73*, 1709-1720.
(65) Moore, L. D.; Isayeva, T.; Siegal, G. P.; Ponnazhagan, S. Silencing of transforming growth factor-β1 by RNA interference for breast cancer: Implications for proliferation and migration and metastasis. *Clin Cancer Res* **2008**, *14*, 4961-4970.
(66) Liu, C. H.; Chen, Y. J.; Wu, W. C.; Lin, Y. H. Magnetic graphene oxide nanoflakes for dual RNA interfering delivery and gene knockdown in prostate and liver cancers. *Int J Biol Macromol* **2023**, *253*, 127357.
(67) Alnasser, F.; Castagnola, V.; Boselli, L.; Esquivel-Gaon, M.; Efeoglu, E.; McIntyre, J.; Byrne, H. J.; Dawson, K. A. Graphene Nanoflake Uptake Mediated by Scavenger Receptors. *Nano Lett* **2019**, *19*, 1260-1268.
(68) Dabrowski, B.; Zuchowska, A.; Kasprzak, A.; Zukowska, G. Z.; Brzozka, Z. Cellular uptake of biotransformed graphene oxide into lung cells. *Chem-Biol Interact* **2023**, *376*, 110444.
(69) Asoudeh, M.; Nguyen, N.; Raith, M.; Denman, D. S.; Anozie, U. C.; Mokhtarnejad, M.; Khomami, B.; Skotty, K. M.; Isaac, S.; Gebhart, T.; Vaigneur, L.; Gelgie, A.; Dego, O. K.; Freeman, T.; Beever, J.; Dalhaimer, P. PEGylated nanoparticles interact with macrophages independently of immune response factors and trigger a non-phagocytic, low-inflammatory response. *J Control Release* **2024**, *366*, 282-296.
(70) Luo, Y. M.; Peng, J. F.; Huang, C. B.; Cao, Y. Graphene oxide size-dependently altered lipid profiles in THP-1 macrophages. *Ecotox Environ Safe* **2020**, *199*, 110714.

(71) Bromma, K.; Bannister, A.; Kowalewski, A.; Cicon, L.; Chithrani, D. B. Elucidating the fate of nanoparticles among key cell components of the tumor microenvironment for promoting cancer nanotechnology. *Cancer Nanotechnol* **2020**, *11*, 8.
(72) Alhussan, A.; Bromma, K.; Bozdogan, E. P. D.; Metcalfe, A.; Karasinska, J.; Beckham, W.; Alexander, A. S.; Renouf, D. J.; Schaeffer, D. F.; Chithrani, D. B. Investigation of Nano-Bio Interactions within a Pancreatic Tumor Microenvironment for the Advancement of Nanomedicine in Cancer Treatment. *Curr Oncol* **2021**, *28*, 1962-1979.
(73) Assali, A.; Akhavan, O.; Adeli, M.; Razzazan, S.; Dinarvand, R.; Zanganeh, S.; Soleimani, M.; Dinarvand, M.; Atyabi, F. Multifunctional core-shell nanoplatforms (gold@graphene oxide) with mediated NIR thermal therapy to promote miRNA delivery. *Nanomedicine* **2018**, *14*, 1891-1903.

Chapter 6: Conclusions and Future Directions

This chapter summarizes the main findings of the thesis and integrates the conclusions from all experimental chapters to highlight their collective impact on cancer-specific gene therapy. The chapter concludes by outlining the broader implications of this work and proposing future directions for the translation and expansion of the approaches developed in this thesis.

6.1 Thesis Conclusions

This thesis demonstrates that chemically modified GO nanocarriers provide a safe, modular, and highly efficient non-viral platform for cancer gene therapy, while revealing that true therapeutic advancement arises from the progressive integration of microenvironmental modulation and active targeting. Optimized small PEG-PAMAM-functionalized GO achieved >90% transfection efficiency in 3D systems with no detectable cytotoxicity to tumor or normal cells, establishing a strong materials foundation for non-viral delivery. In multicellular 3D lung cancer-stromal-immune models, delivery of CD47_siRNA reduced CD47 mRNA by ~58%, while achieving ~97% CD47 protein silencing in $CK7^+$ cancer cells with minimal effect on $CK7^-$ populations (~26%), whereas ANT1_pDNA induced a ~7-fold increase in expression, activating mitochondrial apoptosis pathways. Co-delivery of CD47 and ANT1 produced synergistic effects, inducing ~75% cancer-cell apoptosis within 72 hours and reducing overall model viability to ~47% (Chapter 4), confirming that simultaneous targeting of immune evasion and metabolic vulnerability substantially enhances therapeutic efficacy compared to single-gene modulation. However, fibroblast-mediated protection and persistent immunosuppressive signaling limited complete tumor elimination, demonstrating that targeting cancer-intrinsic pathways alone is insufficient in complex microenvironments.

The integration of TGFβ silencing marked a mechanistic shift from tumor cell-focused therapy to coordinated reprogramming of the tumor microenvironment. In Chapter 5, the addition of TGFβ_siRNA further reduced overall survival to ~29%, while inducing ~85% cancer-cell apoptosis and minimal off-target effects (~29% apoptosis of normal cells) driven by stromal and immune normalization. TGFβ modulation attenuated CAF activation, reduced EMT-associated resistance features, and suppressed immunosuppressive macrophage gene expression, thereby dismantling protective signaling loops that previously limited gene therapy efficacy. This demonstrates that microenvironmental targeting transforms partial elimination into substantially deeper tumor control. Moreover, the subsequent incorporation of GE11-mediated EGFR targeting not only increases

cytotoxicity but also refines therapeutic precision: selective apoptosis in $CK7^+$ cancer cells reached ~91%, while off-target apoptosis in $CK7^-$ cells remained low (~16%). Thus, the stepwise integration of dual cancer marker modulation, stromal and immune reprogramming, and active nanocarrier targeting progressively enhanced both magnitude and selectivity of cancer elimination, shifting the platform from effective to precision-oriented therapy.

Within the broader landscape of non-viral gene therapy, these findings carry important translational implications. Compared to viral vectors, which offer high transduction efficiency but face immunogenicity, cargo limitation, and regulatory complexity, and lipid-based systems, which often struggle with solid tumor penetration and loading capacity, the GO-based platform developed here combines high surface area for multi-gene loading, tunable surface chemistry, and ligand functionalization within a single nanoscale carrier. Importantly, this work demonstrates that GO systems can achieve cancer cell-specific apoptosis levels of ~90% in multicellular 3D models while maintaining low off-target toxicity, positioning it as a strong alternative in the evolving non-viral gene therapy landscape. Furthermore, validation in physiologically relevant 3D tumor models strengthens translational relevance by accounting for stromal barriers and immune dynamics that are often overlooked in preclinical development, thereby reducing the risk of efficacy overestimation.

By integrating tunable non-viral nanocarriers with physiologically relevant 3D tumor models, this work demonstrates how the interplay among material design, biological targets, and multicellular crosstalk shapes therapeutic performance and specificity, thereby advancing the field of cancer gene therapy by establishing a materials-informed, microenvironment-aware strategy for tumor-selective genetic intervention.

6.2 Future Directions

The findings presented in this thesis open several promising avenues for future research to advance non-viral gene therapy toward clinically relevant cancer treatments. A first critical direction is to translate the developed GO-based gene delivery platforms into *in vivo* models, where additional biological barriers, such as vascular transport, immune clearance, and biodistribution, will further shape therapeutic performance. Systematic evaluation of dosing, administration routes, and temporal control of gene expression will be essential to determine how material properties optimized *in vitro* translate to complex physiological environments. In parallel, long-term biocompatibility and clearance studies will be required to fully assess the safety profile of repeated or combination gene delivery strategies. However, this work highlights the importance of advanced *in vitro* models as predictive tools rather than mere screening platforms. Future efforts should then focus on standardizing multicellular 3D tumor models and integrating quantitative readouts that link *in vitro* responses to *in vivo* outcomes. Such developments would strengthen the role of physiologically relevant models in reducing reliance on animal studies while accelerating rational therapeutic design. Future work should then develop 3D models incorporating additional cellular and extracellular components, such as endothelial cells, pericytes, and multiple immune cell lineages. These additions would enable the study of vascular-tumor interactions, hypoxia-driven signaling, immune cell infiltration dynamics, and treatment-induced changes in extracellular matrix remodeling and tumor stiffness, all of which are known to influence therapeutic response. More broadly, adapting the platform to patient-derived cells and organoid systems would increase biological relevance and facilitate personalized evaluation of gene therapy strategies based on tumor-specific genetic and microenvironmental profiles.

On the therapeutic side, the modular nature of GO nanocarriers enables exploration of multigene and multimodal interventions. Future studies could integrate gene delivery with additional therapeutic modalities, such as small-molecule inhibitors, immune agonists, or stimuli-responsive payloads, to

further enhance selectivity and efficacy. Refinement of targeting strategies, through optimized ligand density, dual-targeting approaches, or environment-responsive activation, may enable more precise spatial and cell-type-specific gene modulation within heterogeneous tumors. In this context, temporal sequencing of gene delivery, rather than simultaneous administration, represents an additional strategy to better control immune activation and stromal reprogramming before cancer targeting.

Collectively, these future directions position the strategies developed in this thesis as a flexible and scalable foundation for the continued evolution of cancer-specific, non-viral gene therapies.

Appendix

The appendices include supporting information associated with the research articles presented in Chapters 4 and 5. This section provides additional experimental details, supplementary figures, extended datasets, and methodological clarifications that support the main findings of these chapters but are not included in the main text to maintain clarity and continuity.

Chapter 4 Supportive Information

3D model formation

To optimize the construction of the three-dimensional lung cancer microenvironment model (Figure S4.1A-S1D), a series of critical steps were performed with the goal of determining a solid, reliable, and reproducible methodology. Several selections of extracellular matrix (ECM) materials were examined, followed by refining the plating technique in multiwell plates.

Matrix

Different ECM materials were evaluated, including Matrigel, collagen, and 1:1 mixture of the two. Matrigel alone promoted the formation of well-structured hollow acini and interconnected clusters, providing essential structural and biochemical support that facilitated cell migration and proliferation. However, its softness posed significant handling problems, as the structures were prone to break down during handling and experimental analysis, resulting in potential cell loss and variability in results. In addition, the soft nature of Matrigel hampered some analyses, such as morphological examination, as the structures collapsed when removed from the liquid, making it challenging to obtain accurate structural data. In contrast, collagen alone produced solid AFT models that allowed cell growth and proliferation but caused significant shrinkage, with diameters reduced to around one-third to one-quarter of the original size within three days. This shrinkage is likely due to the contractile activity of fibroblasts, which remodel the ECM, increasing stiffness and density [1], which in turn leads to high cell density and lack of organization, similar to the problems observed with spheroids, like the higher rates of cell death in the center of the structure [2]. The 1:1 mixture of Matrigel and collagen provided an optimal balance, offering a reasonable degree of stiffness that allowed easier handling of the structures while providing adequate space for cells to grow and form well-organized interconnected 3D structures (Figure S4.1B-S1D). This combination facilitated structural integrity and reproducibility, making it the matrix of choice for the construction of the 3D lung TME model.

Plating strategy

To optimize the plating strategy for constructing the three-dimensional lung cancer microenvironment model, three different approaches were evaluated to ensure homogeneity, structural integrity and ease of handling. The first method involved resuspending the cells in Matrigel and adding 10 µL of this suspension directly onto preheated culture media. This approach allowed rapid polymerization by heat, rapidly incorporating the cells into 3D structures. However, the polymerization process was not fast enough to maintain the shape of the droplets, resulting in structures that were heterogeneous, fragile, and prone to collapse during handling, thus increasing the risk of cell loss and variability in experimental results.

The second approach involved depositing the droplets on the surface of the multiwell plate and incubating them in the incubator for 1 hour before adding the hot medium. During the curing period, the cells tended to settle to the bottom of the droplet due to gravity, causing the cells to spread to the surface of the multiwell rather than colonizing the matrix resulting in a predominantly 2D culture.

The final approach, which proved to be the most effective, involved plating the cell-matrix mixture on the surface of a low-attachment multiwell plate (Figure S4.1A). This hydrophobic surface allowed the droplets to maintain a spherical-like shape, promoting the formation of uniform 3D spherical structures (Figure S4.1B and C). In addition, because the cells could not adhere to the surface of the well during and after polymerization, they remained within the matrix. After the incubation period of 1 hour, the addition of warm medium caused the spheres to detach from the bottom and remain suspended in the medium throughout the culture period. This method not only facilitated the collection of 3D models but also ensured that the original number of cells was maintained, reducing variability and improving the reproducibility of experimental results.

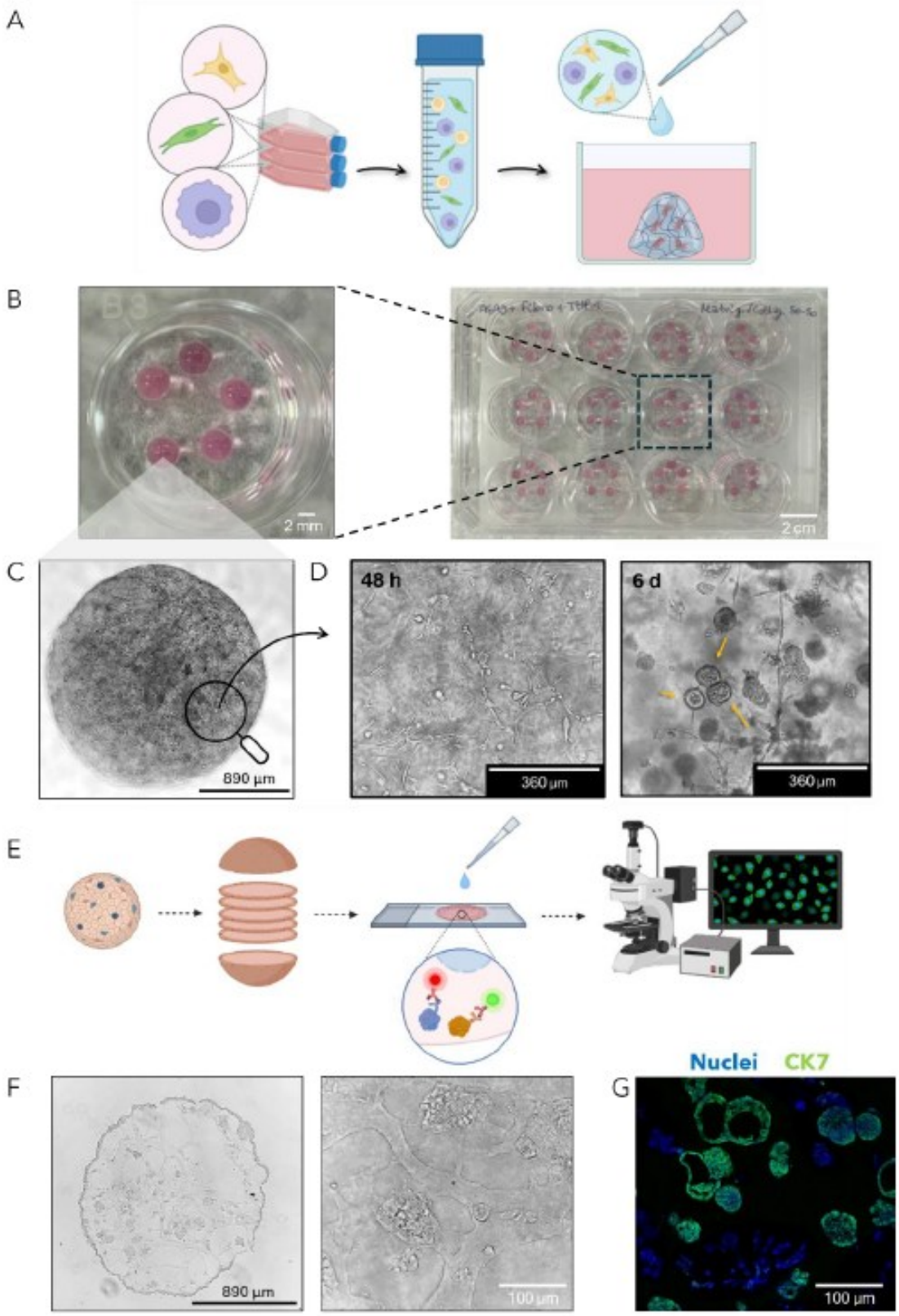

Figure S4.1. AFT model preparation and formation. (A) Schematic representation of the procedure followed for the preparation of the AFT model. (B) AFT model in multiwell after polymerization. Scale bars = 2 mm and 2 cm. (C) Brightfield image of the AFT model after 4 days of incubation. Scale bar = 890 µm. (D) Brightfield image showing the internal structure of the models after 48 h and 6 days of incubation. Yellow arrows: hollow spheroid-like structures. Scale bars = 360 µm. (E) Schematic representation of the procedure followed to prepare the frozen sections of the AFT model. For immunohistochemical analysis, three sections (spaced apart) from the central region of the model were utilized. (F) Brightfield image of an AFT section from the central region of the model (10 µm thick). Scale bars = 890 and 100 µm. (G) Fluorescent image of an AFT model section showing the internal structure of the model. Blue: Hoechst-stained nuclei, green: Alexa Fluor 488-labeled anti-CK7 antibody. Scale bar = 100 µm.

Cancer cells staining

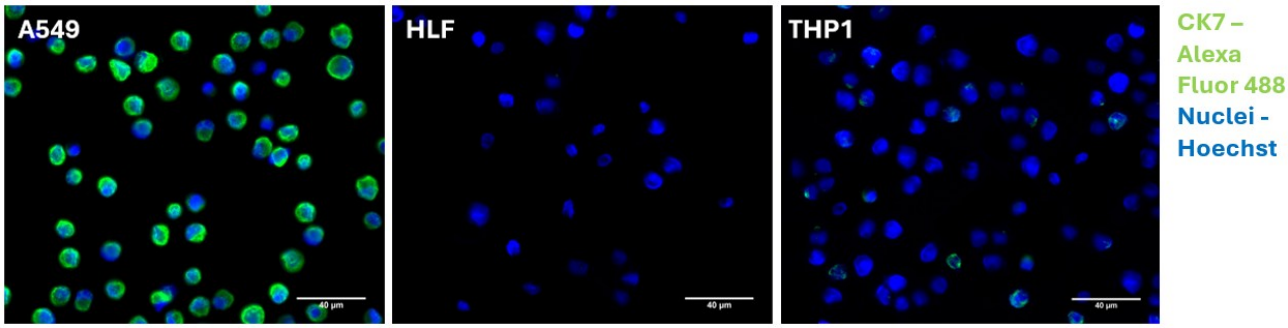

Figure S4.2. CK7 antibody binding validation. Immunocytochemistry images of dissociated single cell suspensions of A549, HLF and THP-1 monocytes. (Green: Alexa Fluor 488-labeled anti-CK7 antibody, blue: Hoechst-stained nuclei). Scale bars = 40 µm.

Quantification from IHC: Fluorescent intensity analysis

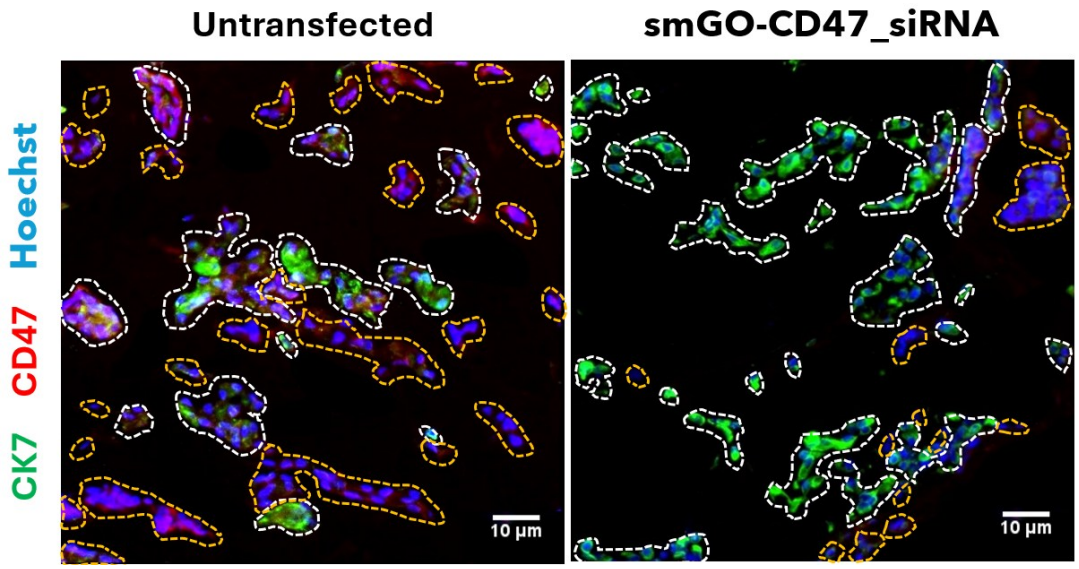

Figure S4.3. Immunohistochemistry analysis of AFT model sections. IHC images of the AFT model: Untransfected control (untrans) and smGO-CD47_siRNA transfected AFT model. (Blue: nuclei (Hoechst); red: CD47 marker (Alexa Fluor 555); green: CK7+ve cancer cells (Alexa Fluor 488); white dashed-lines: CK7+ve cells area; orange dashed-lines: CK7-ve area). Scale bars = 10 µm.

To quantify the downregulation of CD47 and CD24 protein expression, sections were analyzed with ImageJ software to determine the fluorescence intensity. The analysis was performed by segmenting CK7+ve and CK7-ve areas in each section (Figure S4.3), and the intensity of the protein

downregulation in the transfected samples was calculated by quantifying the CD47 or CD24 intensities in each sample using the following formulas:

$$Intensity = \frac{I_{target\ area} - I_{background}}{A_{target}} \quad \text{S(1)}$$

$$\%\ downregulation = \frac{I_{untrans} - I_{transf\ sample}}{I_{untrans}} \times 100\% \quad \text{S(2)}$$

Where $I_{target\ area}$ is the CD47 or CD24 intensity for the CK7+ve or CK7-ve areas in the different samples' sections, $I_{background}$ is the background intensity and A_{target} is the total CK7+ve or CK7-ve areas in the section. $I_{untrans}$ is the intensity of the target protein expression in the untransfected sample and $I_{trans\ sample}$ is the intensity of the target protein expression in the transfected samples.

Cell count-based analysis: To quantify the cells expressing the target proteins, sections were analyzed with ImageJ to determine the cell counts. The percentage of the target protein expression was calculated using the following formula:

$$\%\ Expression = \frac{n_{Target\ protein^+\ Hoechst^+}}{n_{Hoechst^+}} \times 100\% \quad \text{S(3)}$$

Where $n_{Target\ protein^+\ Hoechst^+}$ is the number of cells expressing the target protein and $n_{\ Hoechst^+}$ is the total number of cells in the samples' sections.

Table S4.1. Comparison of CK7+ve and CK7−ve cell populations in the untransfected AFT model using intensity-based and cell counting-based quantifications (Equation S1 and S3). Values are reported as mean±SD.

Type of Cell	Intensity-based	Cell counting-based
CK7 +	58%±5%	54%±6%
CK7 −	42%±5%	46%±6%

smGO internalization in the 3D model

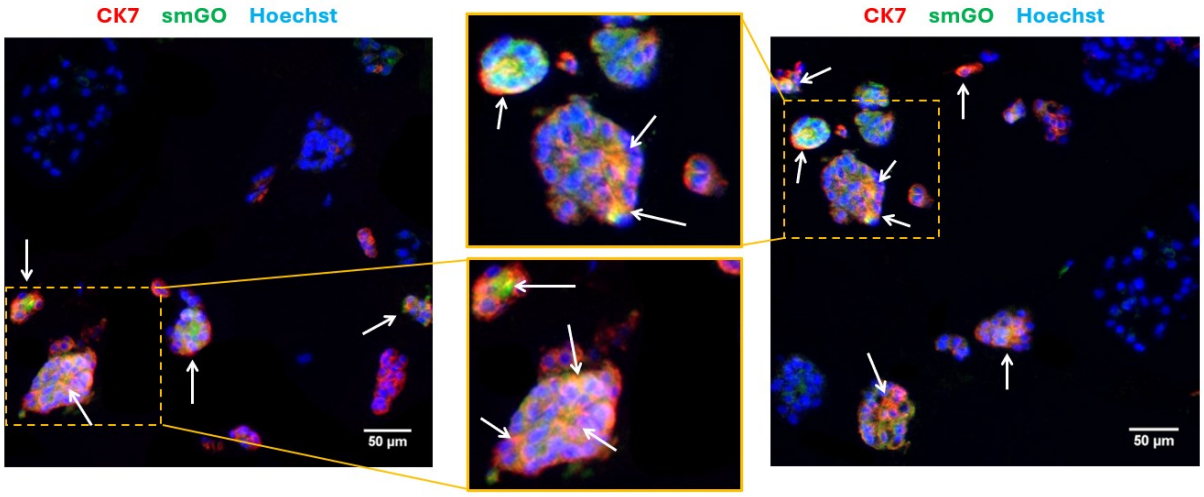

Figure S4.4. smGO uptake in the AFT model assessment. Immunohistochemistry images of sections of AFT models treated with Alexa Fluor 488-labeled smGO (no nucleic acids). (Blue: Hoechst-stained nuclei, green: Alexa Fluor 488-labeled smGO, red: Alexa Fluor 555-labeled anti-CK7 antibody for cancer cells (CK7+ve)). Scale bars = 50 µm.

THP-1 macrophage differentiation and immune surveillance activity

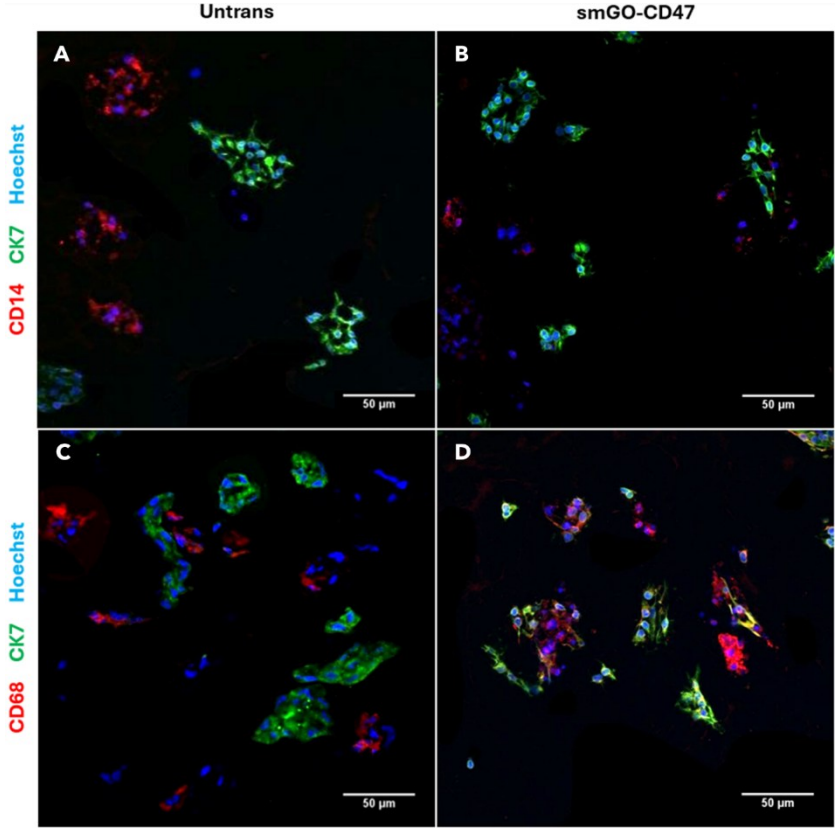

Figure S4.5. THP-1 macrophage differentiation assessment. Immunohistochemistry images of the AFT model: (A) Untransfected control (untrans) and (B) smGO-CD47_siRNA transfected AFT model, labeled with Alexa Fluor 555 anti-CD14 antibody; (C) untransfected control (untrans) and (D) smGO-CD47_siRNA transfected AFT model, labeled with Alexa Fluor 555 anti-CD68 antibody. (Blue: nuclei (Hoechst); red: CD14 (Alexa Fluor 555) and CD68(Alexa Fluor 555) markers; green: CK7+ve cancer cells (Alexa Fluor 488)). Scale bars = 50 µm.

Individual therapies' effect on A549, HLF and THP-1 2D monocultures

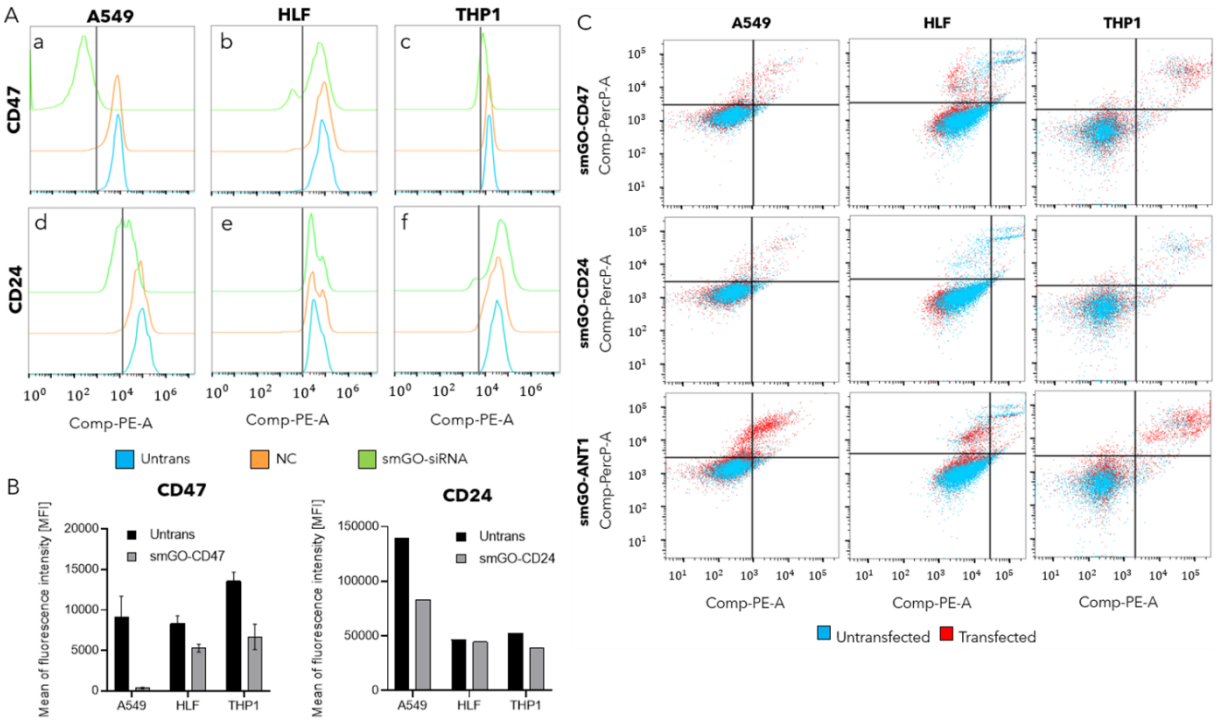

Figure S4.6. CD47 and CD24 markers downregulation and smGO-CD47, smGO-CD24 and smGO-ANT1 transfection induced apoptosis in A549, HLF, and THP-1 2D monocultures. (A) MFI of (a-c) PE-anti CD47 antibody and (d-f) PE-anti CD24 antibody in smGO-treated and untreated cells (48 h) measured by flow cytometry, quantifying marker downregulation in each cell type. (B) Bar graph showing the MFI values obtained from smGO-siRNA treatments in the three cell lines. (C) Scatter plots showing the MFI of PE-Annexin V and 7AAD staining in A549, HLF, and THP-1 untransfected and after transfection with smGO-CD47_siRNA, smGO-CD24_siRNA and smGO-ANT1_siRNA. Statistical significance was determined using one-way ANOVA, with *P < 0.05; **P < 0.01; ***P < 0.001; ****P < 0.0001 considered significant. P > 0.05 was considered not significant (ns).

Table S4.2. Gene knockdown efficiencies and apoptosis percentages in 2D monocultures of A549, HLF, and THP-1 cells, following smGO-mediated delivery of CD47_siRNA, CD24_siRNA, and ANT1_pDNA. The effect of CD47 and CD24 transfections was evaluated for both knockdown and apoptosis, whereas only the apoptotic effect was evaluated for ANT1 transfection. Apoptosis levels corresponding to each treatment group highlight the therapeutic impact of ANT1 upregulation on cancer cells.

	A549			HLF			THP-1		
%	**CD47**	**CD24**	**ANT1**	**CD47**	**CD24**	**ANT1**	**CD47**	**CD24**	**ANT1**
Knockdown	96±3%	37±8%	n/a	18±5%	4±2%	n/a	42±12%	19±6%	n/a
Apoptosis	5±2%	2±1%	31±6%	5±3%	3±1%	8±2%	5±2%	3±1%	17±4%

Co-delivery therapies' gene regulation in the AFT model

Table S4.3. Knockdown efficiencies of CD47 and CD24 and fold changes in ANT1 expression following co-delivery treatments with smGO-CD47, smGO-CD24, smGO-ANT1, smGO-CD47-CD24, smGO-CD47-ANT1, and smGO-CD24-ANT1.

	smGO-CD47	**smGO-CD24**	**smGO-ANT1**	**smGO-CD47-CD24**	**smGO-CD47-ANT1**	**smGO-CD24-ANT1**
% CD47 knockdown	30%	n/a	-	64%	61%	n/a
% CD24 knockdown	-	16%	-	30%	-	47%
Fold change of ANT1 expression	-	-	1.4	-	0.8	1.8

Chapter 5 Supportive Information

Cells quantification

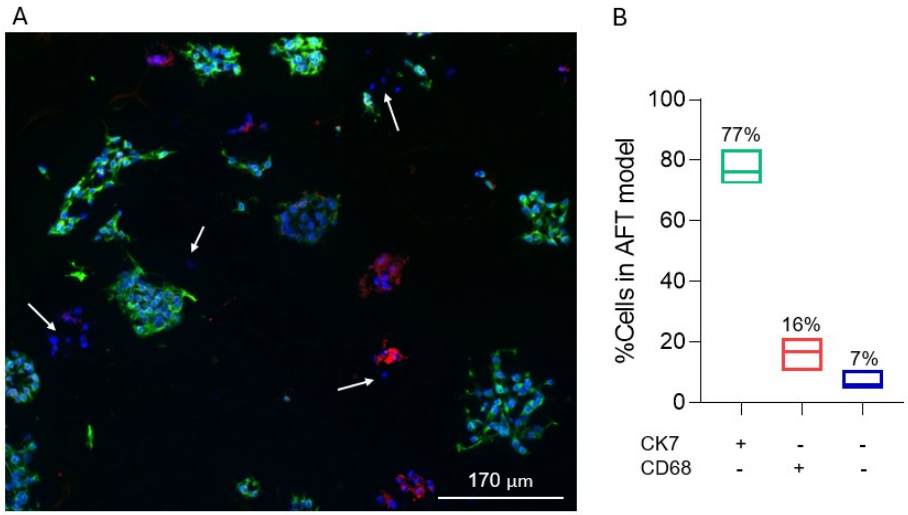

Figure S5.1. Cell type quantification in the AFT model. A) IHC images of 10 µm thick sections from the central region of the AFT model. Blue: Hoechst nuclei; green: $CK7^+$ cancer cells; red: $CD68^+$ THP-1-derived macrophages. Fibroblasts are identified as cells double negative to CK7 and CD68 staining ($CK7^-/CD68^-$, white arrows). Scale bars = 170 µm. B) Total cells quantified as the percentage of $CK7^+$ (cancer), $CD68^+$ (THP-1-derived macrophages) and $CK7^-/CD68^-$ (fibroblasts) cells relative to the total number of cells. Quantification was performed by analyzing three sections of three models from three independent biological replicates (n=3).

Macrophages polarization-associated gene expression (M0, M1, M2)

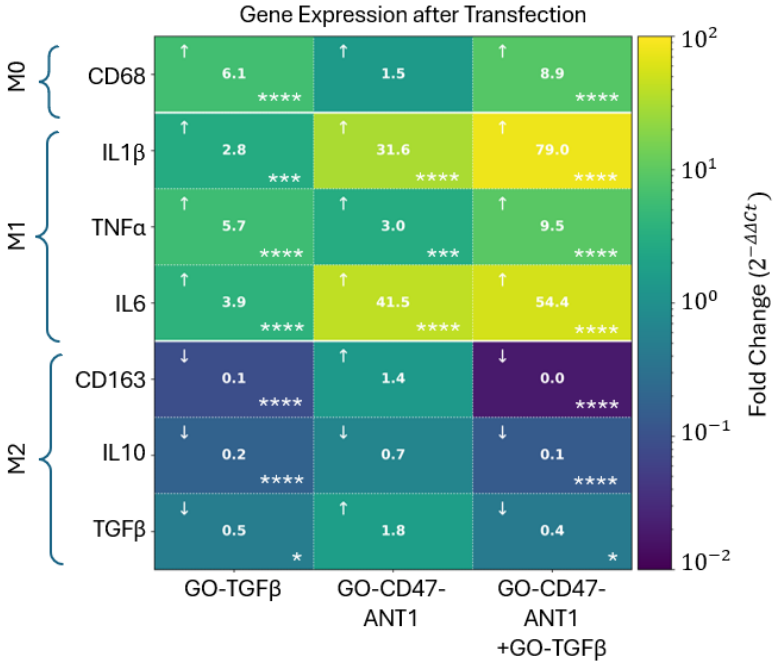

Figure S5.2. TGFβ involvement in macrophage activation. qPCR of macrophage polarization cytokines and markers after PMA treatment and 72 h transfection with GO-TGFβ, GO-CD47-ANT1 and GO-CD47-ANT1 + GO-TGFβ. Heatmap displays M0 (CD68), M1 (IL1β, TNFα, IL6) and M2 (CD163, IL10, TGFβ) gene expression. White arrows represent the upregulation or downregulation of mRNA levels related to untransfected control. Statistical significance was determined against the untransfected AFT model using two-way ANOVA (*P<0.05; **P<0.01; ***P<0.001; and ****P<0.0001; ns: P>0.05, not shown).

Gene expression regulation in DCs containing models

Table S5.1. Fold changes in CD47, ANT1 and TGFβ gene expression in AFDC and AFTDC models following transfection with GO-CD47-ANT1 + GO-TGFβ. Values are reported as mean ± SD. Statistical significance was assessed relative to the respective untransfected control, using two-way ANOVA, with **P< 0.01 considered significant. P> 0.05 was considered not significant.

Gene expression fold change	CD47	ANT1	TGFβ
AFDC	0.4 ± 0.1 (**)	2.1 ± 0.2	0.3 ± 0.1 (**)
AFTDC	0.7 ± 0.1 (**)	2 ± 0.3 (**)	0.5 ± 0.1 (**)

GO-based nanocarriers uptake

Table S5.2. CD47-ANT1 nanocarrier component uptake by $CK7^+$ cancer cells and $CK7^-$ non-cancer cells in the AFT model, following treatment with GO-CD47-ANT1 + GO-TGFβ and **GE11**/GO-CD47-ANT1 + GO-TGFβ in the absence or presence of EGFR blocking through incubation with extra GE11 free peptide. Values are reported as mean ± SD.

%Uptake	$CK7^+$	$CK7^-$
GO-CD47-ANT1 + GO-TGFβ	82 ± 1	35 ± 2
GO-CD47-ANT1 + GO-TGFβ + GE11 blocking	80 ± 2	36 ± 2
GE11/GO-CD47-ANT1 + GO-TGFβ	90 ± 1	14 ± 1
GE11/GO-CD47-ANT1 + GO-TGFβ + GE11 blocking	23 ± 2	14 ± 1

References

(1) Zhang, T.; Day, J. H.; Su, X.; Guadarrama, A. G.; Sandbo, N. K.; Esnault, S.; Denlinger, L. C.; Berthier, E.; Theberge, A. B. Investigating Fibroblast-Induced Collagen Gel Contraction Using a Dynamic Microscale Platform. *Front Bioeng Biotechnol,* **2019**, *7*, 196.
(2) Kessel, S.; Cribbes, S.; Bonasu, S.; Rice, W.; Qiu, J.; Chan, L. L.-Y. Real-time viability and apoptosis kinetic detection method of 3D multicellular tumor spheroids using the Celigo Image Cytometer. *Cytometry Part A* **2017**, *91*, 883-892.